

NORTHWESTERN UNIVERSITY

Design and Synthesis of Imine-Linked Two-Dimensional Covalent Organic Frameworks

A DISSERTATION

SUBMITTED TO THE GRADUATE SCHOOL
IN PARTIAL FULFILLMENT OF THE REQUIREMENTS

for the degree

DOCTOR OF PHILOSOPHY

Field of Chemistry

By

Woojung Ji

EVANSTON, ILLINOIS

June 2021

© Copyright by Woojung Ji 2021
All Rights Reserved

Design and Synthesis of Imine-Linked Two-Dimensional Covalent Organic Frameworks

Abstract

Two-dimensional (2D) covalent organic frameworks (COFs) are a class of crystalline polymer networks that polymerize and crystallize into layered structures, characterized by their atomically precise structure, permanent porosity and high modularity. Imine-linked COFs are one of the most important and promising classes of macromolecular sheets, which form by the condensation of polyfunctional amines with aldehydes. These materials exhibit one of the broadest structural diversity of 2D networks and are attractive partly because of their enhanced hydrolytic and oxidative stability compared to their boron-linked counterparts. This stability coupled with their immense structural versatility has led to their development with desirable properties for various applications. As such, the field has currently explored these stable frameworks by probing many testable properties of the polycrystalline COF powders. Major developments, however, are still needed. A key, currently unmet need that will provide morphological control as well as improved materials quality is better mechanistic understanding of the COF formation and growth. In this dissertation, I will discuss the design and synthesis, formation mechanisms, different morphologies, as well as molecular adsorption and separation applications of 2D imine-linked COFs. In chapter 1 I will discuss a broad overview of imine linkage chemistries and the 2D COFs generated by these strategies. This chapter will start with the outline of contemporary strategies used to successfully polymerize imine-linked macromolecular sheets and the exploration of the chemical and structural COF variants produced through each of these methods. Next, the chapter discusses the nano- and macroscale morphologies of COFs and molecular adsorption and separation applications using imine COFs. Finally, Chapter 1 will end by highlighting additional insight needed to address some of the major challenges in the field and identify opportunities for

continued study. Chapter 2 focuses on the design and synthesis of the amine-functionalized, 2D imine-linked COFs for perfluorinated alkyl substances (PFAS) removal from water. Chapter 3 is about thermal depolymerization and recrystallization of 2D imine-linked COFs, a novel phenomenon which can be used to improve and assess COF materials quality. Finally, Chapter 4 discusses a novel synthetic strategy for preparing imine-linked 2D COF single crystals of four different architectures.

Acknowledgements

Throughout my academic pursuits and construction of this dissertation there have been many contributions both scientifically and personally. I would first like to thank Prof. William R. Dichtel who has provided immense support, advice, and inspiration throughout my graduate school career. One of the best decisions I have ever made at Northwestern is to join DRG and work with Prof. Dichtel. I am thankful for having been able to grow alongside Will and Dichtelians who challenge me and inspire me to be better every day. Special gratitude is owed to Tory Helgeson, without whom we would all be at a loss. I would also like to express gratitude to my committee members, Prof. Joseph T. Hupp and Prof. Julia A. Kalow, for providing excellent instruction, insight and inspiration throughout my time at Northwestern.

I am also grateful for my mentors and friends whom I have had the privilege to meet and work with at Northwestern. I have special thanks to Dr. Michio Matsumoto who has provided unconditional support and advice since my early years at Northwestern. His belief in me is what keeps me going through hardship and I wish to make him proud. In my later years at Northwestern, I have struck immediate friendship with Dr. Anna Yang and Dr. Leslie Hamachi who, since then, have given me limitless advice, encouragement, and support. Anna especially aided in my personal growth, keeping my morale up and shedding light on the power of positivity. Leslie and I have been an excellent team in both science and personal life, always exchanging ideas and discussing projects out of pure joy. I would also like to thank Daylan Sheppard, Rebecca Li and Anushree Natraj for being great friends and the rest of Dichtelians for making my time at Northwestern special. They have all stuck by my side through thick and thin and for this I cannot be grateful enough.

I would also like to thank numerous scientific collaborators I have met who have expanded my perspectives and approach to science. This includes Prof. Damian E. Helbling, Dr. Yuhan Ling, and Casey Ching from Cornell University, Alexandra Brumberg from Northwestern University and Dr. Taylor Allen from National Renewable Energy Laboratory. I must also thank and acknowledge the staff scientist and facility managers whom I have worked with. Their unseen efforts are what catalyze the scientific discoveries. I owe a great deal of thanks to Dr. Christos D. Malliakas, Ms. Charlotte Stern, Dr. Yongbo Zhang, Dr. Yuyang Wu, Mr. Arsen Gaisin and Mr. Saman Shafaie at the Integrated Molecular Structure Education and Research Center (IMSERC), and Dr. Xinqi Chen at the Keck-II facility, Dr. Reiner Bleher at the BioCryo facility, and Ms. Tirzah Abbott and Ms. Elizabeth King at the EPIC facility of the NUANCE Center.

My studies would also not have been possible without the help of financial support provided by numerous grants. This work made use of the Army Research Office for a Multidisciplinary University Research Initiatives (MURI) award under grant number W911NF-15-1-0447, and the Strategic Environmental Research and Development Program (SERDP) under grant number ER18-1026. It made use of the IMSERC at Northwestern University, which has received support from the Soft and Hybrid Nanotechnology Experimental (SHyNE) Resource (NSF ECCS-1542205); the State of Illinois and International Institute for Nanotechnology (IIN), and the Keck-II facility and the EPIC facility of Northwestern University's NUANCE Center, which have received support from SHyNE Resource (NSF ECCS-1542205); the MRSEC program (NSF DMR-1720139) at the Materials Research Center; IIN; the Keck Foundation; and the State of Illinois. Parts of this work were performed at the DuPont-Northwestern-Dow Collaborative Access Team (DND-CAT) located at Sector 5 of the Advanced Photon Source (APS). DND-CAT is

supported by Northwestern University, E.I. DuPont de Nemours & Co., and the Dow Chemical Company. This research used resources of the Advanced Photon Source and Center for Nanoscale Materials, both U.S. Department of Energy (DOE) Office of Science User Facilities operated for the DOE Office of Science by Argonne National Laboratory under Contract No. DE-AC0206CH11357.

Lastly, I would like to express gratitude to my entire family, for their love, encouragement, and unwavering support, especially my mother Chaisun Oh, my father June Keun Ji, and my sister Heeseo Ji. We may be physically apart but are always together at heart. Special gratitude is owed to my boyfriend Gyeongwon Kang for his unconditional love and support. Thank you to all, I could not have done it without you.

List of Abbreviations and Symbols

2D	Two-dimensional
2DPs	Two-dimensional polymers
3D	Three-dimensional
AFFF	Aqueous film-forming foams
AFM	Atomic force microscopy
APPI	Atmospheric Pressure Photoionization
BET	Brunauer–Emmett–Teller
C	Carbon
CDCl ₃	Deuterated chloroform
COFs	Covalent organic frameworks
CuAAC	Cu-catalyzed azide-alkyne cycloadditions
DAPC	7-(diethylamino)-3-phenylcoumarin
DMTA	2,5-dimethoxyterephthaldehyde
ESI	Electrospray ionization
FFT	Fast Fourier transform
FT-IR	Fourier transform infrared spectroscopy
FWHM	Full width at half max
GAC	Granular activated carbon
GenX	ammonium perfluoro-2-propoxypropionate
H	Hydrogen
He	Helium
HRTEM	High-resolution transmission electron microscopy
ITO	Indium tin oxide
LC	Liquid chromatography
Methyl	2,5-dimethylterephthaldehyde
MOFs	Metal-organic frameworks
MS	Mass spectrometer
N	Nitrogen
Ne	Neon
NMR	Nuclear magnetic resonance
NR	Nile red
PAC	Powdered activated carbon
PDA	terephthalaldehyde
PFAS	Perfluorinated alkyl substances
PFAS	Per and polyfluorinated alkyl substances

PFBA	Perfluorobutanoic acid
PFBS	Perfluorobutanesulfonic acid
PFDA	Perfluorodecanoic acid
PFHpA	Perfluoroheptanoic acid
PFHxA	Perfluorohexanoic acid
PFHxS	Perfluorohexanesulfonic acid
PFNA	Perfluorononanoic acid
PFOA	Perfluorooctanoic acid
PFOS	Perfluorooctanesulfonic acid
PFTTrDA	Perfluorotridecanoic acid
PFUnA	Perfluoroundecanoic acid
PPh ₃	Triphenylphosphine
PXRD	Powder X-ray diffraction
q _e	Capacity at equilibrium
Q _{max}	Capacity
SEM	Scanning electron microscopy
S _{BET}	BET surface area
TAPB	1,3,5-tris(4-aminophenyl)benzene
TAPPy	1,3,5,8-tetra(4-aminophenyl)pyrene
Thiophene	thieno[3,2-b]thiophene-2,5-dicarboxaldehyde
TGS	Thermogravimetric analysis
VT	Variable temperature
WAXS	Wide angle X-ray scattering
XPS	X-ray photoelectron spectroscopy

This dissertation is dedicated to Bongsuk Choi, Chunhwan Ji, and Gilsoon Cho.

Contents

1. Design, Synthesis and Adsorptive Applications of Imine-Linked Two-Dimensional Covalent Organic Frameworks.....	21
1.1 Preface	21
1.2 Abstract.....	21
1.3 Introduction	22
1.4 Synthesis.....	25
1.5 Post-synthetic Modifications	28
1.6 Formation Mechanisms	31
1.7 Morphological Control	35
1.7.1 Polycrystalline Powder.....	36
1.7.2 Colloidal Nanoparticles.....	37
1.7.3 Nanosheets and Films	39
1.8 Molecular Adsorption and Separation Applications.....	42
1.8.1 Gas Storage and Separation.....	43
1.8.2 Membranes.....	43
1.8.3 Adsorbents	44
1.8.4 Chiral Separation.....	47
1.8.5 Molecular Recognition.....	48
1.8.6 Molecular Delivery	50
1.9 Outlook on Current Challenges and Future Opportunities	51
2. Synthesis of Amine-Functionalized Covalent Organic Frameworks to Remove Perfluorinated Alkyl Substances from Water	54
2.1 Preface	54
2.2 Abstract.....	55
2.3 Introduction	55
2.4 Results and Discussion	57
2.4.1 Amine-functionalized Covalent Organic Frameworks Synthesis and Characterization.....	57
2.4.2 GenX and Perfluorinated Alkyl Substances Removal.....	59
2.5 Conclusion	63
2.6 Acknowledgements	63
2.7 Chapter 2 Appendix.....	64
2.7.1 Materials and Instrumentation.....	64
2.7.2 Synthetic Procedures.....	69
2.7.3 Batch Adsorption Studies of GenX and Regeneration	76
2.7.4 Additional Characterization	81
2.7.5 Representative BET Plots for N ₂ Isotherm.....	103
2.7.6 ¹ H and ¹³ C NMR Spectra	111
3. Thermal Depolymerization and Recrystallization of Imine-Linked Two-Dimensional Covalent Organic Frameworks.....	114

3.1 Preface	114
3.2 Abstract.....	114
3.3 Introduction	115
3.4 Results and Discussion	118
3.5 Conclusion	128
3.6 Acknowledgments	129
3.7 Appendix	130
3.7.1 Materials and Instrumentation.....	130
3.7.2 Synthetic Procedures.....	132
3.7.3 Additional Images and Characterization	134
3.7.4 BET Plots for N ₂ Isotherm	139
4. Synthesis of Single-crystalline Imine-Linked Two-Dimensional Covalent Organic Frameworks.....	141
4.1 Preface	141
4.2 Abstract.....	141
4.3 Introduction	142
4.4 Results and Discussion	144
4.5 Conclusion	150
4.6 Appendix	151
4.6.1 Materials and Instrumentation.....	151
4.6.2 Synthetic Procedures.....	153
4.6.3 Additional Images and Characterization	156
4.6.4 BET Plots for N ₂ Isotherm	160
5. References.....	162
6. Vita.....	206
7. List of Publications	207

List of Figures

Figure 1.1 Timeline of solution-based chemistries used to prepare 2D covalent organic frameworks.	24
Figure 1.2 Catalyzed reversible condensation of amines and aldehydes to produce imines.	25
Figure 1.3 a) Formal transimination strategy used to polymerize imine-linked 2D COFs. b) <i>N</i> -aryl benzophenone-protected amine monomers demonstrated as amenable to this approach. Adapted with permission. ⁹ Copyright 2017 American Chemical Society.....	27
Figure 1.4 Representative post-synthetic modifications carried out on solution-synthesized 2D COFs.	29
Figure 1.5 General strategy of dynamic bond-forming reactions.	31
Figure 1.6 a) Synthesis of imine-linked COFs with a typical solvent mixture of 4 : 1 1,4-dioxane : mesitylene yields insoluble polycrystalline precipitates, whereas MeCN produces stable colloidal suspensions. b) SEM of drop-cast as synthesized colloidal suspensions c) higher magnification SEM. d) TEM of an individual COF nanoparticle. Adapted with permission. ¹⁰ Copyright 2019 The Royal Society of Chemistry.....	32
Figure 1.7 Chemical structure of the 2D COFs known as a) BDT TAPB COF and b) BDT-OMe TAPB COF. c) Transient reorganization of the COF layers during isolation and activation. X-ray diffraction patterns of either d) BDT TAPB COF or e) BDT-OMe TAPB COF that was immersed in a variety of solvents and then vacuum activated. ⁸ Adapted with permission. Copyright 2019 American Chemical Society.	34
Figure 1.8 a) c) e) and g) Four different 2D COF structures polymerized through different covalent bond-forming chemistries. b) d) f) and h) Transmission electron micrographs of these colloidal nanoparticles. Adapted with permission. ¹⁻³ Copyright 2018 American Association for the Advancement of Science. Copyright 2019 The Royal Society of Chemistry. Copyright 2019 American Chemical Society.	38
Figure 1.9 Acid exfoliation of 2D COF powders to produce suspensions of COFs and partially hydrolyzed oligomers that are then reconstituted into COF films. Adapted with permission. ⁵ Copyright 2020 John Wiley & Sons.	41
Figure 1.10 A representative sampling of 2D COF applications and some of their defining characteristics shown within the polymer structure.....	42
Figure 1.11 a) Synthesis a sulfur-functionalized 2D COF under solvothermal conditions. The COF exhibited strong fluorescence upon excitation at 390 nm. b) Upon the addition of Hg ²⁺ , the fluorescence of the COF was effectively quenched. c) Photographs of COF-LZU8 under a UV lamp ($\lambda_{\text{ex}} = 365 \text{ nm}$) visualize the significant change in the fluorescence emission before (left) and after (right) the adsorption of Hg ²⁺ and a chart showing the selectivity of Hg ²⁺ in fluorescence quenching versus other materials. Adapted with permission. ¹¹ Copyright 2016 American Chemical Society.	45

Figure 1.12 a) Chiral resolution of racemic mixtures using a 2D COF \square lysozyme and b) a representative chiral resolution chromatogram separating D- and L-tryptophan. Adapted with permission. ⁴ Copyright 2018 John Wiley & Sons.	47
Figure 1.13 a) Assembled tubule of Nile red (NR) dye molecules within the triangular pore of a multilayer 2D COF. b) Chemical structures of NR and DAPC ((7-diethylamino)-3-phenylcoumarin). c) Absorbance traces of a mixture of NR and DAPC in the presence of a 2D COF, where only the signals associated with the NR diminish over time. Adapted with permission. ⁷ Copyright 2019 John Wiley & Sons. ad) Scanning tunneling micrograph (image dimensions 2.1 nm \times 2.1 nm) of a 2D COF with an associated trichlorobenzene molecule. e-f) 3D rendering and chemical structure of this association complex. Adapted with permission. ¹² Copyright 2017 The Royal Society of Chemistry.....	49
Figure 1.14 a) Schematic of controlled molecular release from a 2D COF upon UV exposure as a function of azobenzene switching. b) Release profile of molecular dye as evaluated by UV-visible spectroscopy upon irradiation of the 2D COF with UV light. Adapted with permission. ⁶ Copyright 2019 American Chemical Society.	50
Scheme 2.1	57
Figure 2.1 (a) FT-IR spectra (2300–1900 cm^{-1}) of X% $[\text{N}_3]$ -COFs (bottom spectra) and X% $[\text{NH}_2]$ -COFs (top spectra), corresponding to the concentration of azides or amines (X) of 100% (red), 75% (orange), 50% (yellow), 28% (green), 20% (blue), 10% (indigo), and 1% (purple). (b) XPS of N 1s core level (392–408 eV) (c) PXRD patterns normalized at the (100) peak at 2.8° and (d) N_2 adsorption isotherm of 100% $[\text{N}_3]$ -COF (pink) and 100% $[\text{NH}_2]$ -COF (blue). For (d), solid and open circles indicate adsorption and desorption, respectively. Surface areas are reported as ± 1 standard deviation of 14 independently prepared samples of 100% $[\text{N}_3]$ -COF, and 3 independently prepared samples of 100% $[\text{NH}_2]$ -COF.	58
Figure 2.2 (a) Equilibrium GenX removal percentage at $[\text{GenX}]_0 = 200 \mu\text{g L}^{-1}$ and (b) equilibrium adsorption density at $[\text{GenX}]_0 = 50 \text{mg L}^{-1}$ by equal mass concentrations (100 mg L^{-1}) of 100% $[\text{N}_3]$ -COF (pink), X% $[\text{NH}_2]$ -COFs (blue), and 0% $[\text{N}_3]$ -COF (black) after the contact time of 22 hours. Q_e (mg g^{-1}) is the equilibrium adsorption density. Error bars: standard deviation of 3 experiments.....	60
Figure 2.3 (a) Kinetics of PFAS adsorption by 28% $[\text{NH}_2]$ -COF ($[\text{PFAS}]_0 = 1 \mu\text{g L}^{-1}$; $[\text{COF}] = 10 \text{mg L}^{-1}$) at 23 $^\circ\text{C}$. (b) PFAS equilibrium removal percentage on 28% $[\text{NH}_2]$ -COF after 30 min. PFCAs: perfluoroalkyl carboxylic acids; PFSAs: perfluoroalkyl sulfonic acids. (c) GenX adsorption after 30 min by GAC, PAC, and 28% $[\text{NH}_2]$ -COF using $[\text{GenX}]_0 = 1 \mu\text{g L}^{-1}$; $[\text{Adsorbent}] = 10 \text{mg L}^{-1}$. Error bars: standard deviation of 3 experiments.	61
Scheme 2.S1	72
Scheme 2.S2	72
Scheme 2.S3	73
Scheme 2.S4	74
Table 2.S1 The C, H, and N elemental analysis of X% $[\text{N}_3]$ -COFs.....	81

Table 2.S2 The C, H, and N elemental analysis of X%[NH₂]-COFs	82
Table 2.S3 Surface areas and pore sizes of X%[N₃]-COFs and X%[NH₂]-COFs . The errors in the BET surface areas were determined from the standard deviation of independently prepared samples.....	83
Table 2.S4 Zeta potential measurements.....	84
Table 2.S5 Langmuir and Freundlich Parameters Derived from Plots of the GenX Binding Isotherm.	84
Table 2.S6 Comparison of GenX kinetic and thermodynamic adsorption parameters by other adsorbents in literature. For this paper, the kinetic and adsorption parameters were determined at 23 °C.....	85
Table 2.S7 Desorption observed between the 60-minute and the 24-hour time points using [PFAS] ₀ of 1 µg L ⁻¹ and [COF] of 10 mg L ⁻¹	86
Table 2.S8 Incorporation ratios estimated from quantitative IR analysis. Normalized azide absorbance at 2098 cm ⁻¹ to the imine at 1618 cm ⁻¹ was used for estimation. Errors show the standard deviation of three independent measurements.	87
Figure 2.S1 PXRD patterns of 100%[N₃]-COF using 6M CH ₃ CO ₂ H (pink) or Sc(OTf) ₃ (purple) ³¹⁹ as a catalyst. The patterns are normalized at the (100) peak at 2.8°	88
Figure 2.S2 N ₂ adsorption isotherm of 100%[N₃]-COF using 6M CH ₃ CO ₂ H (pink) or Sc(OTf) ₃ (purple) ³¹⁹ as a catalyst. Solid and open circles represent the adsorption and desorption branches, respectively.	88
Figure 2.S3 Fourier transform-infrared (FT-IR) spectra of 100%[N₃]-COF (red) and 100%[NH₂]-COF after the Staudinger reaction in CH ₃ OH (orange), CH ₂ Cl ₂ (yellow), DMF (green), THF (blue), CH ₃ CN (indigo), and toluene (purple). The traces of the colors are being described from top-to-bottom.	89
Figure 2.S4 Fourier transform-infrared (FT-IR) spectra of X%[N₃]-COFs corresponding to the concentration of azides or amines (X) of 75% (orange), 50% (yellow), 28% (green), 20% (blue), 10% (indigo), 1% (purple). The traces of the colors are being described from bottom-to-top.	90
Figure 2.S5 Fourier transform-infrared (FT-IR) spectra of X%[NH₂]-COFs corresponding to the concentration of azides or amines (X) of 75% (orange), 50% (yellow), 28% (green), 20% (blue), 10% (indigo), 1% (purple). The traces of the colors are being described from bottom-to-top.	90
Figure 2.S6 X-ray photoelectron spectra of 100%[N₃]-COF (pink) and 100%[NH₂]-COF (blue). Left shows X-ray photoelectron spectra of P 2p core level.....	91
Figure 2.S7 Scanning electron microscopy (SEM) images of 100%[N₃]-COF (pink) and 100%[NH₂]-COF (blue).....	91
Figure 2.S8 Representative PXRD patterns of X%[N₃]-COFs and X%[NH₂]-COFs corresponding to the concentration of azides or amines (X) of 100% (red), 75% (orange), 50%	

(yellow), **28%** (green), **20%** (blue), **10%** (indigo), and **1%** (purple) normalized at the (100) peak at 2.8° 92

Figure 2.S9 Representative N_2 adsorption isotherms of **X%[N₃]-COFs** and **X%[NH₂]-COFs** corresponding to the concentration of azides or amines (**X**) of **100%** (red), **75%** (orange), **50%** (yellow), **28%** (green), **20%** (blue), **10%** (indigo), and **1%** (purple). Solid and open circles represent the adsorption and desorption processes, respectively..... 93

Figure 2.S10 Representative pore size distributions (determined from nonlocal density functional theory analysis of each nitrogen adsorption isotherm) of **X%[N₃]-COFs** and **X%[NH₂]-COFs** corresponding to the concentration of azides or amines (**X**) of **100%** (red), **75%** (orange), **50%** (yellow), **28%** (green), **20%** (blue), **10%** (indigo), and **1%** (purple)..... 94

Figure 2.S11 PXRD pattern of **0%[N₃]-COF**..... 95

Figure 2.S12 N_2 adsorption isotherm of **0%[N₃]-COF**. Solid and open circles represent the adsorption and desorption processes, respectively. 95

Figure 2.S13 Thermogravimetric Analysis (TGA) of **2** (yellow), **100%[N₃]-COF** (pink) and **100%[NH₂]-COF** (blue)..... 96

Figure 2.S14 GenX removal percentage ($[GenX]_0 = 200 \mu g L^{-1}$) by equal mass concentrations ($400 mg L^{-1}$) of **100%[N₃]-COF** (pink), **100%[NH₂]-COF** (blue) and **0%[N₃]-COF** (black) after the contact time of 22 h. Figures show average GenX removal percentages, and error bars show the standard deviation of three experiments..... 97

Figure 2.S15 Kinetics of GenX adsorption by **100%[N₃]-COF** (pink) and **100%[NH₂]-COF** (blue) ($[GenX]_0 = 200 \mu g L^{-1}$; $[COF] = 400 mg L^{-1}$). Figures show average GenX removal percentages, and error bars show the standard deviation of three experiments..... 97

Figure 2.S16 Kinetics of GenX adsorption by **X%[NH₂]-COF** ($[GenX]_0 = 200 \mu g L^{-1}$; $[COF] = 100 mg L^{-1}$). Figures show average GenX removal percentages, and error bars show the standard deviation of three experiments..... 98

Figure 2.S17 The molar ratio of GenX to amines in **X%[NH₂]-COFs** ($[GenX]/[NH_2]$) calculated from Figure 2(b) at $[GenX]_0 = 50 mg L^{-1}$ by equal mass concentrations ($100 mg L^{-1}$) of **X%[NH₂]-COFs** after the contact time of 22 h. 98

Figure 2.S18 A list of GenX and 12 perfluorinated alkyl substances (PFAS) tested in an adsorption experiment ($[PFAS]_0 = 1 \mu g L^{-1}$; $[COF] = 10 mg L^{-1}$)..... 99

Figure 2.S19 GenX adsorption isotherm of **28%[NH₂]-COF** ($[GenX]_0 = 0.2-100 mg L^{-1}$; $[COF] = 100 mg L^{-1}$). Dotted lines show fits to Langmuir (blue) and Freundlich (orange) models. Error bars show the standard deviation of three experiments..... 100

Figure 2.S20 GenX adsorption isotherm of **100%[NH₂]-COF** ($[GenX]_0 = 0.2-100 mg L^{-1}$; $[COF] = 100 mg L^{-1}$). Dotted lines show fits to Langmuir (blue) and Freundlich (orange) models. Error bars show the standard deviation of three experiments..... 100

Figure 2.S21 Kinetics of GenX and PFAS adsorption by **100%[NH₂]-COF** (Each $[PFAS]_0 = 1 \mu g L^{-1}$; $[COF] = 10 mg L^{-1}$). Figure shows average PFAS removal percentages, and error bars show the standard deviation of three experiments..... 101

Figure 2.S22 Kinetics of GenX and PFAS adsorption by 1%[NH₂]-COF (Each [PFAS] ₀ = 1 μg L ⁻¹ ; [COF] = 10 mg L ⁻¹). Figure shows average PFAS removal percentages, and error bars show the standard deviation of three experiments.	101
Figure 2.S23 Regeneration and reuse of 28%[NH₂]-COF by washing with CH ₃ OH. Adsorption experiments: [GenX] ₀ = 10 mg L ⁻¹ , [COF] = 2 mg, 10 sec. Desorption: COF was washed with CH ₃ OH for 10 sec. Error bars: standard deviation of 3 experiments.....	102
Figure 2.S24 BET plot for 100%[N₃]-COF using Sc(OTf) ₃ as a catalyst.....	103
Figure 2.S25 BET plot for 100%[N₃]-COF using 6M CH ₃ CO ₂ H as a catalyst.	103
Figure 2.S26 BET plot for 75%[N₃]-COF	104
Figure 2.S27 BET plot for 50%[N₃]-COF	104
Figure 2.S28 BET plot for 28%[N₃]-COF	105
Figure 2.S29 BET plot for 20%[N₃]-COF	105
Figure 2.S30 BET plot for 10%[N₃]-COF	106
Figure 2.S31 BET plot for 1%[N₃]-COF	106
Figure 2.S32 BET plot for 0%[N₃]-COF	107
Figure 2.S33 BET plot for 100%[NH₂]-COF	107
Figure 2.S34 BET plot for 75%[NH₂]-COF	108
Figure 2.S35 BET plot for 50%[NH₂]-COF	108
Figure 2.S36. BET plot for 28%[NH₂]-COF	109
Figure 2.S37 BET plot for 20%[NH₂]-COF	109
Figure 2.S38 BET plot for 10%[NH₂]-COF	110
Figure 2.S39 BET plot for 1%[NH₂]-COF	110
Figure 2.S40 ¹ H NMR spectrum of 2 in CDCl ₃	111
Figure 2.S41 Zoomed-in ¹ H NMR spectrum (4.45–3.30 ppm) of 2 in CDCl ₃	112
Figure 2.S42 ¹³ C NMR spectrum of 2 in CDCl ₃	113
Figure 3.1 a) Amounts of Free Aldehyde (green diamond) and Imine 1 (orange triangle) present in solution when Imine 1 was subjected to the heating and cooling cycle, condition that mimic COF recrystallization. b) Representative VT-NMR spectra and the equilibrium between the monomers (PDA and aniline) and Imine 1 . Concentration of each species was estimated <i>via</i> peak area integration using 1,4-dinitrobenzene was as an internal standard.	118
Figure 3.2 Schematic of TAPB-PDA COF recrystallization.....	119
Figure 3.3 a) Representative VT-NMR spectra during the first cycle of TAPB-PDA COF recrystallization. b) Equilibrium between the TAPB-PDA COF , Imines 1 and 2 , and monomers (TAPB and PDA) during the COF recrystallization.	121

Figure 3.4 Amounts of TAPB (blue square), Free Aldehyde (green diamond), Imines 1 and 2 (orange and purple triangles), and both aldehyde and imines combined (black circle) present in solution during the a) first and d) second cycle of TAPB-PDA COF recrystallization. Change in domain sizes of TAPB-PDA COF during the b) first and e) second cycle of COF recrystallization. Domain sizes are determined from the Scherrer analysis of the (100) diffraction peak. Representative WAXS patterns of TAPB-PDA COF , centered at its (100) diffraction peak, upon heating (red) and cooling (blue) during the c) first and f) second cycle of recrystallization.....	123
Figure 3.5 a) PXRD patterns and b) N ₂ adsorption isotherms of TAPB-PDA COF before (black) and after (blue) the first cycle of COF recrystallization.	124
Figure 3.6 Schematic representations of proposed COF recrystallization mechanisms	125
Figure 3.7 a) Amounts of TAPB (blue square), Free Aldehyde (green diamond), Imines 1 and 2 (orange and purple triangles), and both aldehyde and imines combined (black circle) present in solution during the first cycle of TAPB-DMTA COF recrystallization. b) Change in domain sizes of TAPB-DMTA COF during the first cycle of COF recrystallization. Domain sizes are determined from the Scherrer analysis of the (100) diffraction peak. c) Representative WAXS patterns of TAPB-DMTA COF , centered at its (100) diffraction peak, upon heating (red) and cooling (blue) during the first cycle of recrystallization. d) Synthesis of TAPB-DMTA COF colloids e) PXRD patterns and f) N ₂ adsorption isotherms of TAPB-DMTA COF before (black) and after (blue) the first cycle of COF recrystallization.	127
Figure 3.S1 FT-IR Spectra of colloidal (red) and recrystallized (orange) TAPB-PDA COF , and colloidal (yellow) and recrystallized (green) TAPB-DMTA COF	134
Figure 3.S2 Pore size distributions of colloidal (yellow) and recrystallized (red) TAPB-PDA COF , and colloidal (green) and recrystallized (purple) TAPB-DMTA COF	135
Figure 3.S3 Representative VT-NMR spectrum (0–12 ppm) of TAPB-PDA COF reaction mixture at 90 °C in benzonitrile- <i>d</i> ₅	136
Figure 3.S4 Soluble imine-linked species in the representative VT-NMR spectrum in Figure 3.7a	137
Figure 3.S5 SEM images of colloidal TAPB-PDA COFs	138
Figure 3.S6 SEM images of colloidal TAPB-DMTA COFs	138
Figure 3.S7 BET Plot for colloidal TAPB-PDA COF	139
Figure 3.S8 BET Plot for recrystallized TAPB-PDA COF	139
Figure 3.S9 BET Plot for colloidal TAPB-DMTA COF	140
Figure 3.S10 BET Plot for Recrystallized TAPB-DMTA COF	140
Figure 4.1 Schematic of single-crystalline imine-linked 2D COF synthesis. Four different COFs structures, TAPB-DMTA , TAPB-Methyl , TAPPy-PDA and TAPPy-Thiophene COFs , are shown.	144

- Figure 4.2.** (a) SEM and (b) AFM images, (c) PXRD and (d) N₂ adsorption isotherms of 1 μm sized **TAPB-DMTA COF** single crystals. (e) Lattice-resolution HRTEM images of a **TAPB-DMTA COF** crystal with consistent lattice fringes extending across the entire particle. (f) Region of interest at higher magnification and (g) FFT of the boxed region in (e), showing the predominant, color-coded fringe spacing of ~31.5 Å, *d*₁₀₀. (h) Magnified image in (f) after applying a bandpass filter. 145
- Figure 4.3.** SEM and AFM images, and histogram size analysis for **TAPB-DMTA COF** crystals synthesized under the monomer concentration of 8 mM and aniline loading of 0.8 equiv [(a), (b), and (c)], 0.6 equiv [(d), (e), and (f)] or 0.4 equiv [(g), (h), and (i)], and monomer concentration of 12 mM [(j), (k), and (l)] or 16 mM [(m), (n), and (o)] and aniline loading of 0.8 equiv with respect to the aldehyde functional group. 146
- Figure 4.4.** (a) Evolution of **TAPB-DMTA COF** crystal sizes with time and (b) final **TAPB-DMTA COF** crystal sizes with respect to increasing reaction temperature under the monomer concentration of 8 mM (red square), 12 mM (yellow square), and 16 mM (green square). For (a) and (b) 0.8 equiv of aniline per aldehyde functional group are added for each concentration. (c) SEM images of 20 μm sized **TAPB-DMTA COF** crystals. 147
- Figure 4.5.** SEM and AFM images, and histogram size analysis for **TAPPy-PDA COF** crystals synthesized under the monomer concentration of 8 mM and aniline loading of 1.3 equiv [(a), (b), and (c)], 1.2 equiv [(d), (e), and (f)] or 1.0 equiv [(g), (h), and (i)]. (j) Lattice-resolution HRTEM images of a **TAPPy-PDA COF** crystal with uniform lattice fringes extending across the entire particle. (k) FFT of the boxed region number in (j). 148
- Figure 4.6** Low- and high-magnification SEM images and size analysis histograms of 720 nm sized **TAPB-Methyl COF** [(a), (b), and (c)] and 400 nm sized **TAPPy-Thiophene COF** single crystals [(i), (j), and (k)]. Lattice-resolution HRTEM images of a (d) **TAPPy-PDA COF** and (l) **TAPPy-Thiophene COF** crystal with consistent lattice fringes extending across the entire particle. FFT of the (e) larger and (g) smaller boxed region number in (d). (f) Region of interest at higher magnification corresponding to the smaller boxed region in (d). (h) Magnified image in (f) after applying a bandpass filter. FFT of the (m) larger and (o) smaller boxed region number in (l). (n) Region of interest at higher magnification corresponding to the smaller boxed region in (l). (p) Magnified image in (n) after applying a bandpass filter. 149
- Figure 4.S1** Pore size distributions of **TAPB-DMTA COF** (red), **TAPB-Methyl COF** (yellow), **TAPPy-PDA COF** (green), and **TAPPy-Thiophene COF** (blue). 156
- Figure 4.S2** FFT patterns of the various boxed regions of the lattice-resolution HRTEM image of a **TAPB-DMTA COF** crystal on the left, showing the predominant fringe spacing of ~31.5 Å, *d*₁₀₀. 157
- Figure 4.S3** (a) PXRD and (b) N₂ adsorption isotherm of **TAPB-Methyl COF**. 158
- Figure 4.S4** (a) PXRD and (b) N₂ adsorption isotherm of **TAPPy-PDA COF**. 158
- Figure 4.S5** (a) PXRD and (b) N₂ adsorption isotherm of **TAPPy-Thiophene COF**. 159
- Figure 4.S6** BET plot of **TAPB-DMTA COF**. 160
- Figure 4.S7** BET plot of **TAPB-Methyl COF**. 160

Figure 4.S8 BET plot of **TAPPy-PDA COF**. 161

Figure 4.S9 BET plot of **TAPPy-Thiophene COF**. 161

1. Design, Synthesis and Adsorptive Applications of Imine-Linked Two-Dimensional Covalent Organic Frameworks

1.1 Preface

In this chapter, I will cover imine linkage chemistries and the two-dimensional (2D) covalent organic frameworks (COFs) generated by these strategies. I will begin by outlining contemporary strategies used to successfully polymerize imine-linked macromolecular sheets. I will then explore the chemical and structural COF variants produced through each of these methods. For each of these, I emphasize design principles, formation mechanisms and experimentally realized COF structures through direct condensations and post-synthetic modifications. Next, I discuss the nano- and macroscale morphologies of COFs produced with a focus on the advantages and disadvantages of each morphology. Finally, I describe the emergent properties and potential applications of imine COFs on molecular adsorption and separation. In all cases, I describe current limitations and opportunities for advancement. As the field of 2D polymerization continues to mature, these materials will find intended technological uses in society, as has already occurred for linear and network polymers.

1.2 Abstract

Synthetic chemists have developed robust methods to synthesize discrete molecules, linear and branched polymers, and disordered cross-linked networks. However, two-dimensional polymers (2DPs) prepared from designed monomers have been long missing from these capabilities, both as objects of chemical synthesis and in Nature. Recently, new polymerization strategies and characterization methods have enabled the unambiguous realization of covalently linked

macromolecular sheets. Here we discuss the synthesis, formation mechanisms, nanoscale and macroscale morphologies, and molecular adsorption and separation applications of imine-linked 2D covalent organic frameworks (COFs), one of the broadest and the most important classes of 2DPs. Imine COFs are desirable because of their high structural versatility and their enhanced hydrolytic and oxidative stability relative to their boron-linked counterpart. Throughout, we highlight achievements in the imine COF chemistries and identify opportunities for continued study. The continued development of COF and 2DP chemistry, along with improved understanding of their formation and growth mechanisms, will provide a means to access their molecularly precise structures for intended purposes.

1.3 Introduction

The irreversible bond-forming reactions established for linear polymerizations, in the absence of molecular preorganization or templation, are largely unamenable to the production of large-area macromolecular sheets. Largely, this restriction originates from the enormous entropic penalty incurred by polymerizing monomers into a 2D monolayer. If these entropic penalties lead to even a small number of intersheet defects, an amorphous network is more likely to be obtained than a topologically planar molecular sheet. This fundamental limitation hindered the development of 2D polymerization for many years and led some researchers to speculate that 2D polymers (2DPs) might be a synthetic impossibility. However, developments in areas outside of traditional polymer science, such as supramolecular chemistry,¹³⁻²⁵ coordination networks,^{19, 26-35} two-dimensional materials,³⁶⁻⁴⁶ and crystal engineering,^{33, 47-54} have led to the coevolution of 2D polymerization approaches that would have been challenging to envision from controlled linear or network

polymerizations. As such, contemporary 2D polymerization strategies largely emerge and continue to draw inspiration from many synthetic traditions.

In 2005, Yaghi and coworkers polymerized and subsequently characterized the formation of 2DPs for the first time.⁵⁵ The authors speculated that by using reversible condensation reactions between aromatic boronic acids and polyfunctional catechols, structural defects were annealed during the production of these layered, periodic, macromolecular sheets. This strategy takes clear inspiration from the chemistries used to prepare crystalline, porous coordination polymers— often known as metal-organic frameworks (MOFs).³⁰ The structural similarity and traditions that produced these 2DPs led researchers to name these macromolecular sheets 2D covalent organic frameworks (2D COFs). Since these early reports, the term COF has been used widely to describe hundreds of 2DP structures, which at the outset were speculated to require reversible bond-forming chemistries.⁵⁶⁻⁵⁸ However, as the COF subfield has matured, irreversible reactions have provided polycrystalline, layered 2DPs with sufficiently large domains for characterization by powder X-ray diffraction (PXRD).⁵⁹ It is therefore conceivable that solution-based, irreversible- and reversible-chemistries take advantage of self-templated formation, which blurs the distinction between 2DPs prepared this way and those produced through strategies that rely on explicit monomer preorganization.

Imine-linked COFs are one of the most important and promising classes of macromolecular sheets. Imine COFs, form by the condensation of polyfunctional amines with aldehydes, exhibit the broadest structural diversity of 2D networks. These materials are attractive partly because of their enhanced hydrolytic and oxidative stability compared to their boron-linked counterparts. This stability coupled with their immense structural versatility has led to their development with desirable properties for various applications. As such, the field has currently explored these stable

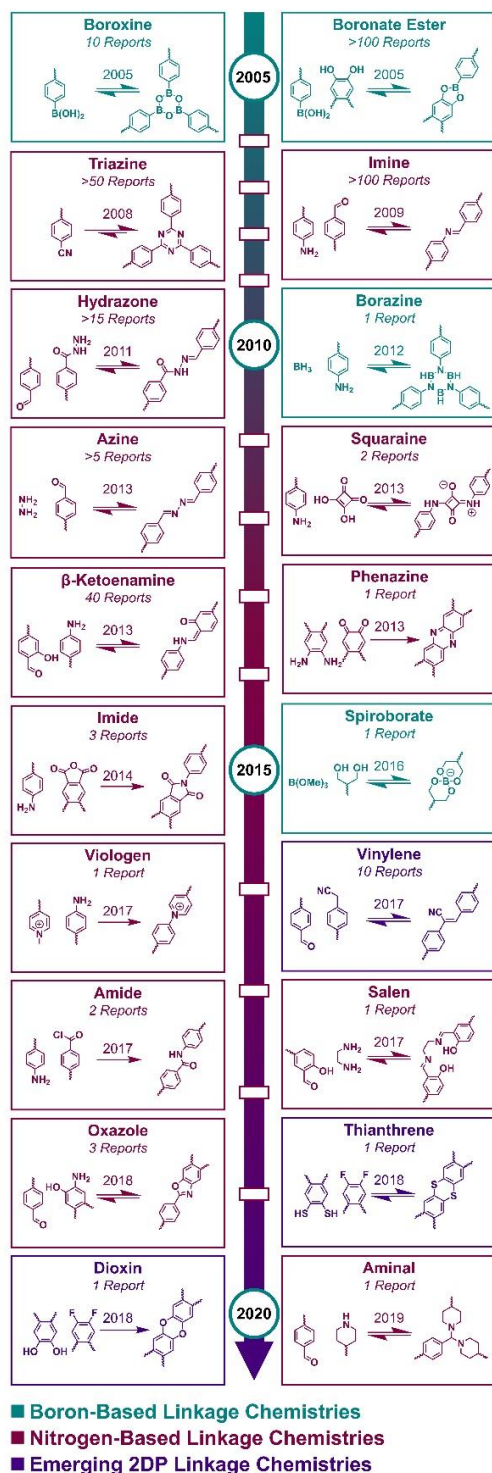


Figure 1.1 Timeline of solution-based chemistries used to prepare 2D covalent organic frameworks.

frameworks by probing many testable properties of the polycrystalline COF powders. Major developments, however, are still needed. Control over morphology, including the ability to grow oriented, highly crystalline thin films, free-standing membranes, colloids, and single crystals with increased crystallite size will all be needed before these properties and rational design strategies are fully leveraged. A key, currently unmet need that will provide morphological control as well as improved materials quality is better mechanistic understanding of the COF formation and growth. The appropriate rates of bond formation and exchange for imine-linked COFs are still poorly understood, making their discovery and optimization empirical and predisposed to uncontrolled nucleation. Gaining additional insight needed to address these challenges in the field, thereby unlocking the full potential of these materials, represents an exciting yet challenging undertaking at the interfaces of physical organic chemistry, polymer science, and crystal engineering.

1.4 Synthesis

Solvothermal COF synthesis is conducted by reacting solubilized topologically regular monomers at elevated temperatures to produce macromolecular sheets.⁵⁷ Typically, this produces insoluble polycrystalline COF powders or films that can be characterized by powder X-ray diffraction or grazing-incidence X-ray diffraction. Early iterations of this strategy assumed that dynamic bond-forming events were required to effectively produce crystalline macromolecular sheets. However, as solution-based strategies have matured, several irreversible polymerization chemistries have been demonstrated to produce COFs.⁵⁹⁻⁶³ Successful solution-based COF synthesis likely relies on a confluence of factors including the efficiency of bond-forming reactions, topological regularity of monomers, and the energetic landscape of particular COF systems. Regardless of these ambiguities, solution-based COF synthesis can be fine-tuned to successfully yield macromolecular sheets. For this reason, solution-based approaches are the most synthetically accessible in preparing 2D COFs, with more than 500 distinct structures produced through over 20 different polymerization chemistries, including linkages that rely on B-O, B-N, N-N, C-N, and C-C bond formation (**Figure 1.1**).^{56-58, 64, 65} Many of these functionalities are a direct result of the reaction between monomers, though others are more easily accessed through post-synthetic modification of pre-polymerized COFs.⁶⁶

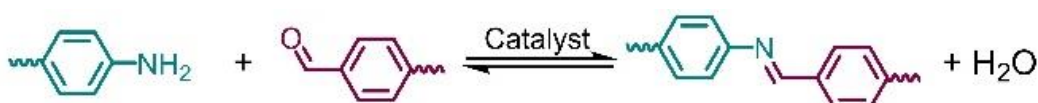


Figure 1.2 Catalyzed reversible condensation of amines and aldehydes to produce imines.

Imine formation occurs by the condensation of an aldehyde and an amine (**Figure 1.2**) and is the first and most well-studied Schiff-base 2D polymerization. Imine-linked systems have several advantages that have led to their expansion into the largest and most actively investigated 2DP

classes. First, imine linkages are highly stable in neutral water and most organic solvents, unlike their boron-linked counterparts.¹⁶ Second, a vast array of polyfunctional amines and aldehydes are available from commercially available sources or short synthetic routes, providing efficient access to numerous structures. As a result, more than 200 imine-linked COFs have been reported.^{56-58, 67-}

71

The first use of dynamic imine formation to prepare topologically regular polymers was the synthesis of a 3D framework, COF-300, through the condensation of tetra-(4-anilyl)methane and terephthalaldehyde.⁷² Soon after this study demonstrated that dynamic imine chemistry could yield periodic 3D networks, Wang and coworkers condensed 1,3,5-triformylbenzene and 1,4-diaminobenzene into a crystalline COF.⁷³ This network's high hydrolytic stability allowed for its post-synthetic metallation with palladium acetate, which was used as a solid-state Suzuki-Miyaura catalytic support. This preliminary report demonstrated that imine-linked COFs form under catalyzed dynamic polymerization reaction conditions and are stable under a wide range of post-polymerization conditions, including exposure to water. This reasonable hydrolytic stability has driven the rapid expansion and investigation of imine-linked 2D COFs. As such, the strategy used to prepare imine-linked 2D COFs was quickly found to be general for the polymerization of other aromatic monomers including benzene,^{1, 73-85} anthracene,⁸⁶ thiadiazoline, pyrene,^{86, 87} triazine,⁸⁸ tetrathiafulvalene,⁸⁹ hexaphenylbenzene,⁹⁰ hexabenzocoronene,⁹⁰ pyridine,⁹¹⁻⁹⁶ hexaazatriphenylene,⁹⁷ tetraphenylethylene,⁹⁸ thiophene,^{87, 99-102} porphyrin,¹⁰³⁻¹¹¹ and many functionalized derivatives.

Recently, Dichtel and coworkers developed a solvothermal transimination strategy to prepare highly crystalline imine-linked COFs (**Figure 1.3**).⁹ Amines protected by *N*-aryl benzophenones

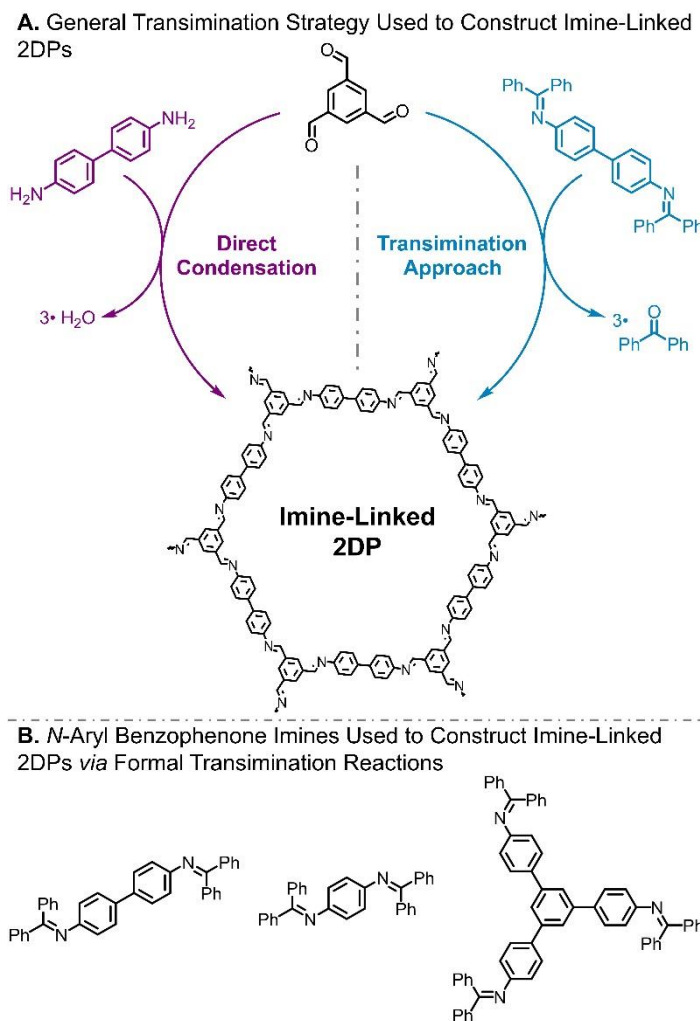


Figure 1.3 a) Formal transimination strategy used to polymerize imine-linked 2D COFs. b) *N*-aryl benzophenone-protected amine monomers demonstrated as amenable to this approach. Adapted with permission.⁹ Copyright 2017 American Chemical Society.

are generally more soluble and oxidatively stable than their free-amine counterparts. Additionally, because *N*-aryl benzophenone imines are sometimes produced as synthetic precursors of aryl amines, using them directly as monomers is also desirable. Similarly, the protection of aldehyde-functionalized monomers as acetals has also been explored to increase their solubility.¹¹² Taken together, the nearly limitless number of amine- and formyl-functionalized molecules, the diverse synthetic conditions suitable for their polymerization, and the enhanced hydrolytic stability of the resultant networks have enabled the

broad investigation of imine-linked 2D COFs. As mechanistic understanding of 2D imine polymerizations improves to the point where large-domain 2D COFs can be generated as single crystals, these materials have potential to be examined for their fundamental properties and will find applied use.

1.5 Post-synthetic Modifications

Post-synthetic modification represents a versatile approach to diversify the chemical structures of 2D COFs.¹¹³ Many studies have demonstrated that the linkages themselves play a large role in determining the chemical and physical properties of the 2D COFs, primarily by determining the system's planarity, stability, and, in some cases, conjugation. While dynamic polymerization chemistries are beneficial for obtaining high-quality 2D COFs, they do not necessarily provide the desired combination of properties. Recently, Yaghi and coworkers showed that dynamic imine linkages could be converted into more-stable amide linkages through a post-synthetic oxidation performed on a prepolymerized 2D imine-linked COFs.⁶⁶ These 2D COFs were highly crystalline, derived from their reversible imine-forming polymerizations, and chemically stable, due to their amide linkages. This approach has since been expanded to realize benzoxazole-,¹¹⁴⁻¹¹⁸ quinoline-,¹¹⁹ imidazole-,¹²⁰ amine-,¹²¹ cyclic-carbamate-,¹²² and cyclic-thiocarbamate-linked 2D COFs.^{117, 123} These synthetic strategies result in chemically robust, functionalized structures with emergent properties and functions challenging to access by direct polymerization. Furthermore, Lotsch and coworkers demonstrated the topochemical conversion of an imine-linked 2D COF into a structurally similar thiazole-linked COF through thermal treatment with elemental sulfur.¹²³ The higher conjugation and larger electron density contrast of this COF allowed for its structural characterization by electron diffraction and TEM, which was challenging with the parent imine-linked COF. These representative examples demonstrate that post-synthetic modification enables the preparation of 2D COFs with unique properties that would be challenging to install through direct polymerization.¹¹³

Post-synthetic linkage transformations based on monomer exchange reactions have also been realized. Dichtel and coworkers recently transformed imine-linked 2D COFs to their corresponding β -ketoenamine analogues by substituting their aldehyde component with structurally similar *o*-hydroxybenzaldehydes.⁸⁰ Upon this exchange, irreversible tautomerization occurs, thus generating higher-quality β -ketoenamine-linked 2D COFs than are accessible by direct condensation. Building off of this approach, other linkage chemistries have also been accessed that are challenging *via* direct synthetic methods. For instance, Yaghi and coworkers

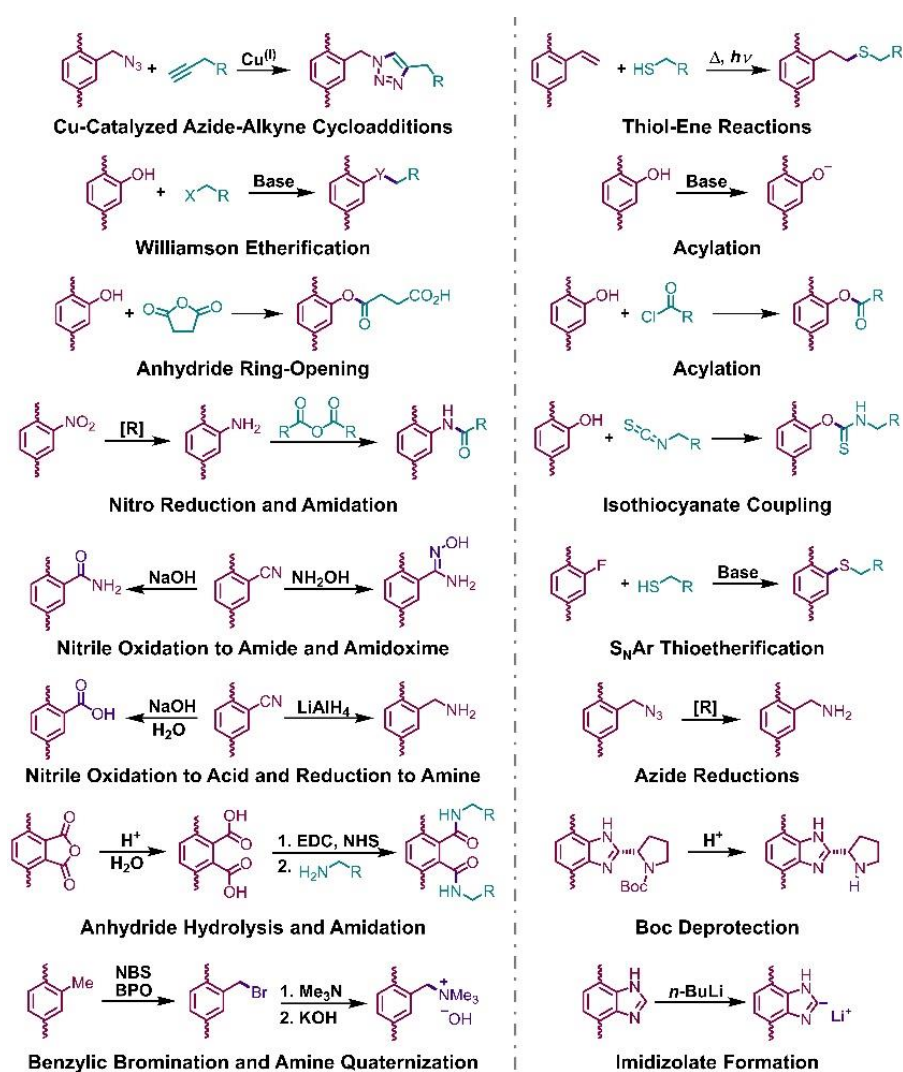


Figure 1.4 Representative post-synthetic modifications carried out on solution-synthesized 2D COFs.

demonstrated that monomer species flanked by phenolic or thiophenolic moieties could be quantitatively exchanged into the network.^{66, 117, 122} Subsequent cyclization and oxidative reactions manifested in 2D COFs containing thiazole or oxazole linkages.^{66, 117, 122} These results demonstrate that the imine linkages of 2D

COFs can serve as a traceless templating agent for preparing high quality COFs with linkages that are challenging to attain *via* direct polymerization.

In addition to modifying the backbone of the COF through linkage transformations, pendant moieties can post-synthetically be installed on the 2D COF pores. These reactions include Cu-catalyzed azide-alkyne cycloadditions (CuAAC), thiol-ene reactions, Michael additions, Williamson etherifications, and Staudinger reductions (**Figure 1.4**).¹¹³ One of the major advantages of these approaches is that the degree of pore functionalization can be tuned by varying monomer feed ratios or by only partially reacting the pendant moieties. For instance, Helbling, Dichtel and coworkers installed pendant azide moieties on a functionalized terephthalaldehyde derivative, which was subsequently incorporated into an imine-linked 2D COF in a variety of ratios. The pendant azide moieties were then reduced to the corresponding amines by Staudinger reduction, and this material was used to remove anionic fluorinated alkyl substances from water.¹²⁴ This report established that pendant moieties thought to interfere with polymerization can be masked, and subsequently revealed in a post-synthetic fashion. Azide groups are also commonly used as coupling partners in CuAAC reactions. For instance, Jiang and coworkers prepared a 1,4-benzene bis(boronic acid) derivative with pendant azide moieties, which were incorporated into a phthalocyanine-based electron-donating 2D COF. These 2D COFs were then reacted with an ethynyl-functionalized fullerene to generate a photoelectric 2D COF with segregated donor-acceptor segments.¹²⁵ Similarly, ethynyl-functionalized monomers have been incorporated into 2D COFs and subsequently transformed into functionalized triazines suitable for organo-catalysis. Significant opportunities remain to develop highly functionalized structures from a small number of strategically designed monomers. As 2D COFs increase in chemical complexity, the reactions

used to functionalize their surfaces are likely to evolve as well. The continued diversification of 2D COFs prepared by dynamic polymerization will undoubtedly drive the continued exploration of emergent properties and device potential in 2D COFs accessed through *de novo* and post-synthetic modification approaches.

1.6 Formation Mechanisms

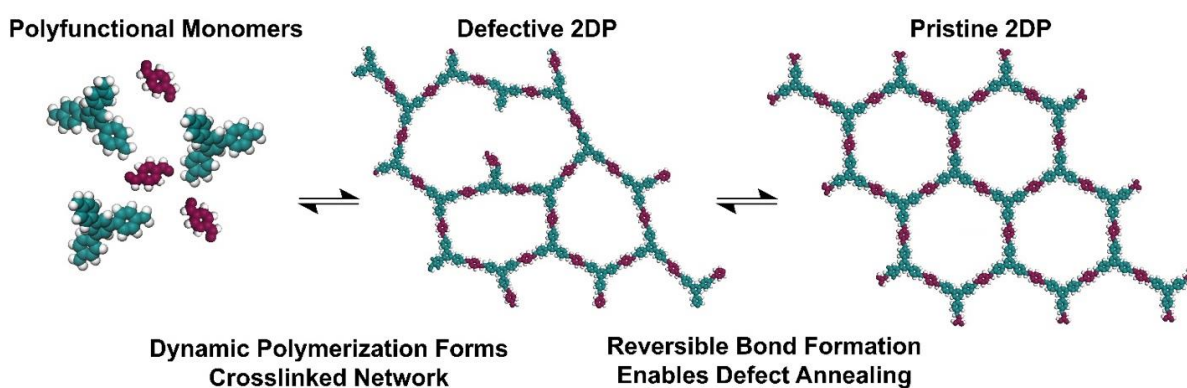


Figure 1.5 General strategy of dynamic bond-forming reactions.

The solvothermal synthesis of 2D COFs enables chemists to tune polymerization conditions (e.g. solvent, catalysts, temperature), ultimately manifesting in a suite of chemically and structurally diverse polymer architectures. Similarly, solution-phase polymerization has proven to be the most synthetically general approach to prepare 2D COFs, with hundreds of chemically distinct COF structures prepared to-date.^{56, 57, 68, 126-129} Inspired by the use of dynamic coordination bonds for preparing crystalline coordination polymers, Yaghi and coworkers developed a dynamic polymerization strategy for the solvothermal synthesis of 2D COFs.^{26, 30, 65, 130-132} All early solution-based synthesis for 2D COFs used reversible chemistries^{13, 14, 17, 133-135} and long reaction times that were speculated to produce COFs as the thermodynamic product (**Figure 1.5**). Recent mechanistic investigations have revealed that an interplay of reversible and irreversible processes

is likely operative in the solvothermal synthesis, which are more complex than simple defect annealing. Using synthetic designs based off of this mechanistic understanding, several researchers have produced large-area 2D COFs through dynamic polymerization chemistries. As solution-based 2D polymerization has developed, researchers have found that solution-based irreversible chemistries can also produce layered, crystalline, aggregated 2D COFs, as characterized by powder X-ray diffraction. These materials indicate that monomer rigidity and undesigned templation effects can also give rise to crystalline layers with lateral dimensions on the scale of tens of nanometers. These chemistries greatly broaden the scope of solution-based 2D polymerization but will likely require additional monomer preorganization strategies to produce larger sheets.

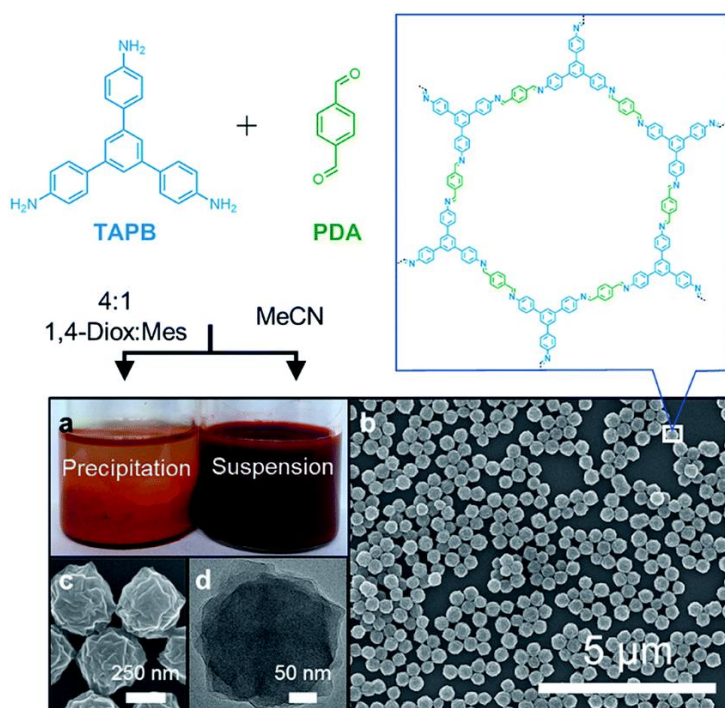


Figure 1.6 a) Synthesis of imine-linked COFs with a typical solvent mixture of 4:1 1,4-dioxane:mesitylene yields insoluble polycrystalline precipitates, whereas MeCN produces stable colloidal suspensions. b) SEM of drop-cast as synthesized colloidal suspensions c) higher magnification SEM. d) TEM of an individual COF nanoparticle. Adapted with permission.¹⁰ Copyright 2019 The Royal Society of Chemistry.

Early mechanistic studies of imine-linked COF formation reported that polymerization of monomer species occurred rapidly to produce an initially amorphous, cross-linked gel.⁸² It was then observed that this amorphous network polymer transiently reorganized through reversible transimination reactions to produce a thermodynamically preferred crystalline 2D COF. Several follow-up reports also isolated

amorphous low-surface-area networks that became more crystalline with higher surface areas after multiday reaction times.^{81, 83} This slow transition was then expedited from days to minutes by replacing a traditional Brønsted acid catalyst with a more active Lewis acid catalyst.^{81, 136} Furthermore, amorphous-to-crystalline transitions were observed in imine-linked macrocycles that were designed as 2D COF analogues.¹³⁷ However, the irreversible precipitation of 2D COFs from solution makes the evaluation of dynamic processes in amorphous-to-crystalline transitions challenging. Recently, it was found that imine-linked 2D COFs could be prepared as stable colloidal suspensions in acetonitrile (**Figure 1.6**).¹ By studying the COF formation *via in situ* small- and wide-angle X-ray scattering, the polymerization of COFs was observed to proceed by a slightly faster rate than the crystallization.¹ These differential rates led the authors to conclude that amorphous particles formed initially would crystallize slowly over the course of the reaction. This conclusion was in agreement with other observations of transient amorphous phases in nitrogen-based 2D COFs.^{82, 138-145} Recently, Marder,¹⁴⁶ Bein,⁸ and their coworkers have found that workup protocols used widely in 2DP syntheses can damage the isolated polymer structure, including the 2D COFs that have been studied extensively for their formation mechanisms (**Figure 1.7**). Both studies noted that by avoiding damaging workup conditions, high-quality 2D COFs could be isolated more rapidly than initially reported. A subsequent report found that 2D imine-linked **TAPB-PDA COF**, previously reported to proceed through an amorphous-to-crystalline mechanism initially polymerized as disorganized few-layer 2D sheets, when activated using gentler conditions. These species then slowly reorganized to produce well-layered stacks of 2D COF sheets, which were more robust to conventional activation procedures.^{147, 148} These results demonstrate that careful isolation of these early species may be critical to the preparation and

exfoliation of few-layer 2D COFs, which remain as important frontiers in 2D polymerization. These reports demonstrate the enormous value of *in situ* characterization techniques and that great care must be taken when generating mechanistic conclusions by analysis of isolated products, especially those subjected to extensive workup protocols. Further development of *in situ* 2D polymerization monitoring techniques are likely to provide additional mechanistic insight and improved synthetic control. Likely, a combination of mechanisms is active in all dynamic 2D

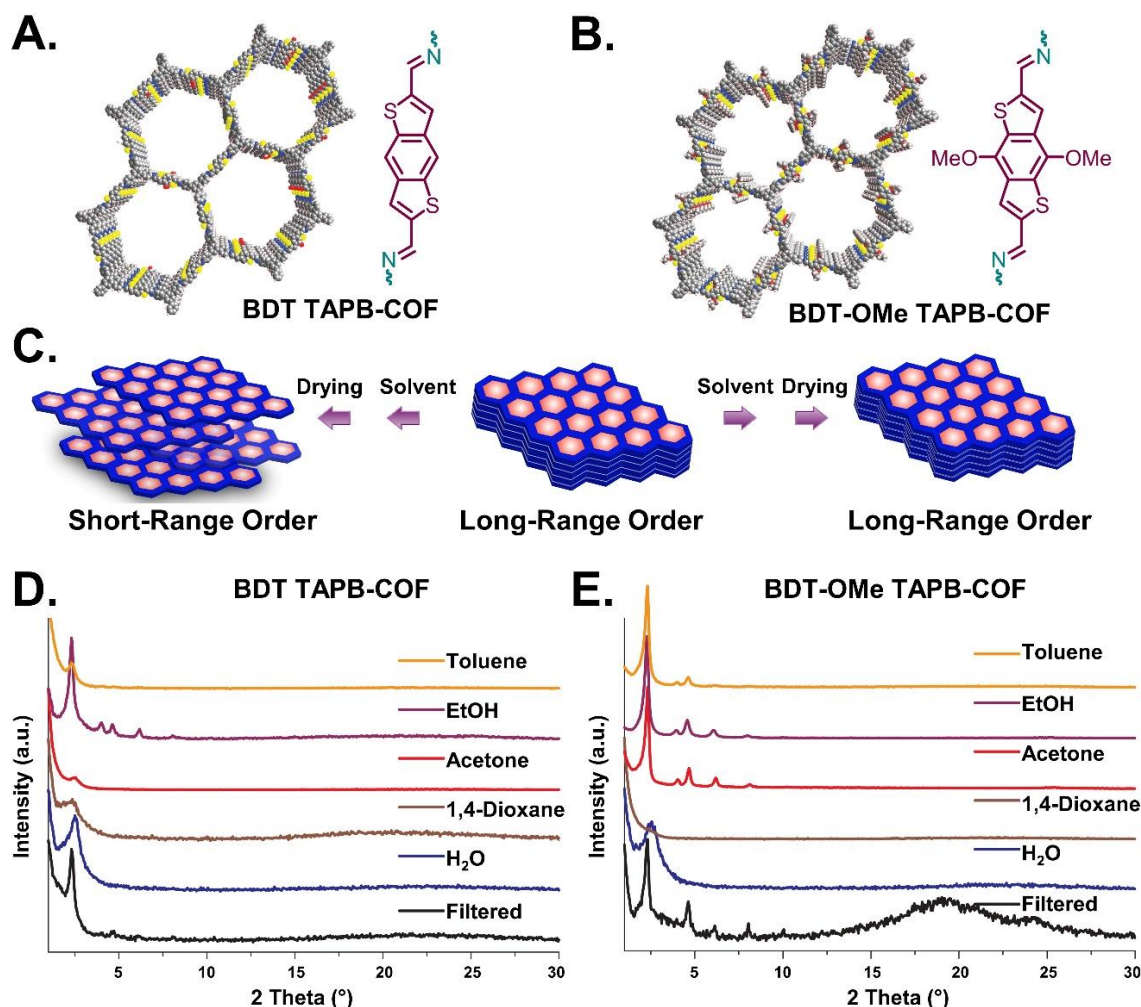


Figure 1.7 Chemical structure of the 2D COFs known as a) BDT TAPB COF and b) BDT-OMe TAPB COF. c) Transient reorganization of the COF layers during isolation and activation. X-ray diffraction patterns of either d) BDT TAPB COF or e) BDT-OMe TAPB COF that was immersed in a variety of solvents and then vacuum activated.⁸ Adapted with permission. Copyright 2019 American Chemical Society.

polymerizations, the extent of which depends greatly on the synthetic conditions and COF system studied. As an array of monomer systems and synthetic conditions has not been routinely studied for their mechanistic behavior, broad conclusions about the polymerization mechanism remain elusive.⁵⁶⁻⁵⁸

1.7 Morphological Control

Two-dimensional COFs have been obtained in a variety of forms including single crystals, polycrystalline powders, exfoliated sheets, colloidal nanoplatelets, films, and composited materials. Moving forward, each of these morphologies is likely to contribute important understanding for 2D COF syntheses, properties, and potential applications. Currently, the vast majority of 2D COFs are obtained as polycrystalline powders due to the inherent insolubility of rigid, cross-linked polymer networks. This represents a fundamental challenge in the field, as poorly defined polycrystalline aggregates are generally not well suited for property measurements or integration into many promising devices, such as membranes, organo-electronics, or solid-state electrolytes. This realization has inspired many researchers to pursue a variety of strategies to process 2D COFs into more useful forms. Ultimately, it is desirable to develop methods to prepare 2D COFs as any morphology and sheet size, which has yet to be achieved. As such, there exists substantial opportunity to overcome synthetic and fabrication limitations that currently restrict 2D COF property measurements and subsequent device integration. Here, we survey the 2D COF morphologies obtained to date, including their synthesis, characterization, and uses.

1.7.1 Polycrystalline Powder

Solution-based 2D polymerizations are most often associated with the production of polycrystalline powders, which arise as a function of aggregation processes operative in the production of densely cross-linked 2D COFs.⁵⁶⁻⁵⁸ Aggregated 2D COFs are evaluated by PXRD and through finite-crystal size line-broadening analysis are proposed to have approximately 50 nm lateral domain sizes.^{3, 55, 149, 150} In many cases, these findings are supported by other ensemble measurements such as infrared spectroscopy, N₂ porosimetry, or solid-state NMR, which can also indirectly evaluate the quality of these materials. As one early example, Lavigne and coworkers polymerized boron-linked 2D COFs as polycrystalline powders.¹⁵¹ In this report, all of the ensemble techniques described above were used to confirm the COF structure. Moreover, these techniques were applied after the COFs were exposed to water, which revealed that the COFs functionalized with alkyl chains retained their original structure to a greater extent than those that were unfunctionalized. In some cases, polycrystalline 2D COF powders exhibit features such as broad diffraction signals, less than ideal BET surface areas, or convoluted infrared spectra, which suggests that these 2D COFs are either defective, have interlayer arrangements that are not well-defined, or that they are contaminated by other chemical species. Due to challenges in characterizing insoluble polycrystalline powders, however, these nonideal features are often not characterized. For this reason, it is difficult to distinguish between 2D polymerizations that produce small-domain-sized crystallites with weak diffraction patterns, and those that yield large-area, defect-free, few-layered 2D sheets. As mechanistic insight and the characterization toolkit coevolve, resolving this uncertainty will be of major interest.

The random particle size, domain orientations, grain boundaries, and defects present in polycrystalline 2D COFs also makes characterizing their intrinsic thermomechanical or optoelectronic properties challenging. Likewise, polycrystalline powders are notoriously challenging to fabricate into devices that may benefit from the incorporation of COFs, such as electronic circuits or nanofiltration membranes.¹⁵² However, several proof-of-principle applications of 2D COFs have been explored using polycrystalline powders including adsorbents,¹⁵³⁻¹⁵⁵ chemical indicators,^{156, 157} photocatalysts,^{158, 159} gas separation media,¹⁶⁰⁻¹⁶² optical emitters,^{163, 164} and energy storage devices.^{165, 166} Going forward, polycrystalline 2DP powders are likely to find continued use in proof-of-principle applications due to their relative synthetic accessibility. Though studies of polycrystalline 2DPs expedite the exploration and rapid assessment of 2DP properties and applications, we note that these findings may suffer from convoluting factors due to the structural ambiguities of this form.

1.7.2 Colloidal Nanoparticles

Colloidal 2D COF nanoparticles are one of the few forms through which COF single crystals can be obtained. Recently, nitrile-containing cosolvents were found to prevent polycrystalline aggregation in boron-based 2D COFs.^{2, 167} By preventing aggregation, nucleation and elongation processes were temporally resolved and micron-sized 2D boron COF single crystals were obtained through continued monomer addition (**Figure 1.8**).^{168, 169} In addition to enhanced reactivity control, colloidal 2D COFs are compatible with many solution-based characterization techniques that require homogeneous suspensions of material, which inherently limits the use of polycrystalline powders, including *in situ* X-ray diffraction,^{1, 2, 167, 168} liquid-cell TEM,¹⁶⁷ transient absorption spectroscopy,¹⁷⁰ solution fluorescence spectroscopy,² and dynamic light scattering.^{1, 2,}

^{167, 168} For example, *in situ* X-ray scattering measurements in conjunction with kinetic Monte Carlo

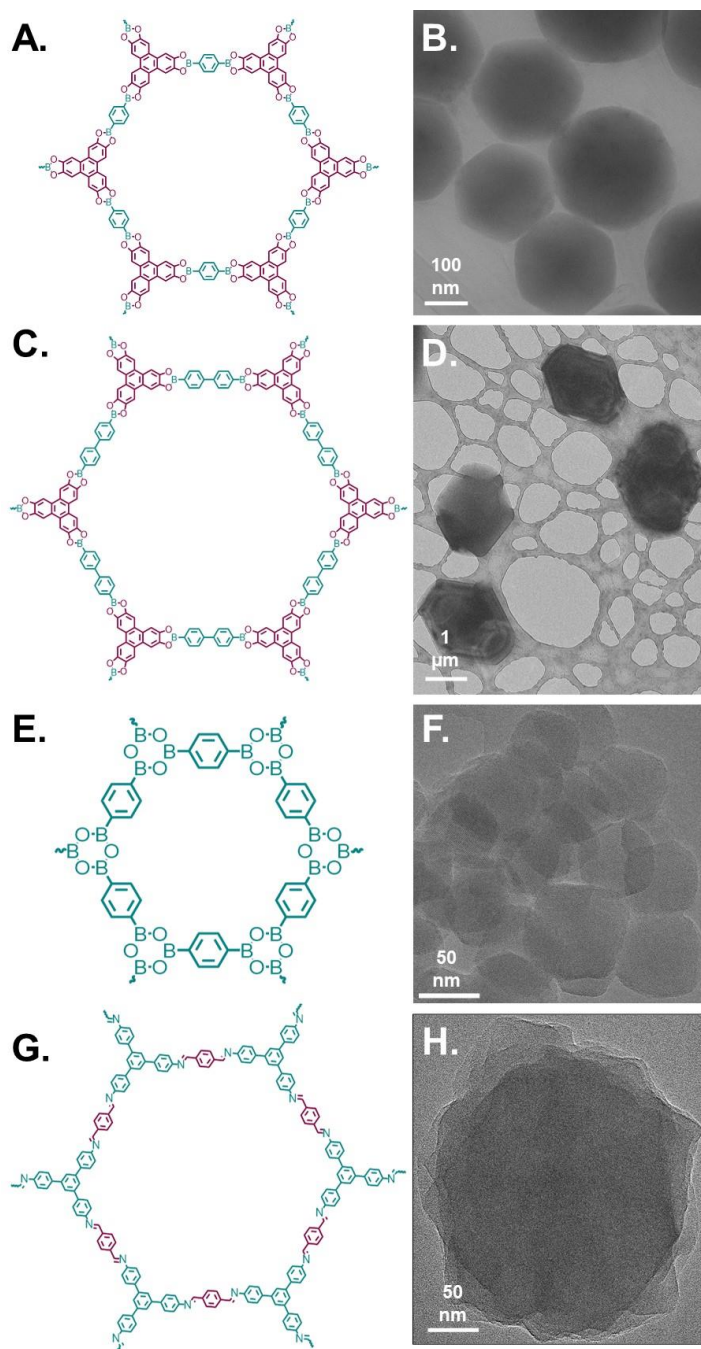


Figure 1.8 a) c) e) and g) Four different 2D COF structures polymerized through different covalent bond-forming chemistries. b) d) f) and h) Transmission electron micrographs of these colloidal nanoparticles. Adapted with permission.¹⁻³ Copyright 2018 American Association for the Advancement of Science. Copyright 2019 The Royal Society of Chemistry. Copyright 2019 American Chemical Society.

simulations were used to probe the nucleation and growth processes of boronate-ester-linked 2D COF colloids in the presence of monofunctional modulators.¹⁶⁸ These results revealed that nucleation was suppressed in the presence of monofunctional modulators, due to oligomer sizes insufficient for nucleation, which allowed higher steady-state monomer concentrations to be used for growth.¹⁷¹ Dichtel and coworkers exploited these findings to expedite a previously multi-week polymerization to under two days of reaction time, which was possible due to suppressed nucleation. Under these conditions, anisotropic out-of-plane elongation of 2D COF nanoparticles was observed *via* TEM. These results reveal that monofunctional additives can be used to control 2D COF

formation, which is an exciting frontier in 2D polymerization. Furthermore, exploring the properties of 2D COF colloids of various sizes and shapes is likely to produce a deeper understanding of their fundamental properties and application potential, as has already been realized in other nanomaterials.¹⁷²

Unlike boronate-ester-linked colloids, which exhibit a hexagonally layered structure, imine-linked colloids are typically irregularly shaped.¹ One possible explanation for this difference is that the lower interlayer interactions in imine-linked 2D COFs lead to mesoscale structural deformation that precludes faceted crystals. Another hypothesis is that imine-linked 2D COFs first produce an amorphous cross-linked polymer that then transiently reorganizes to yield polycrystalline particles with irregularly shaped domains (**Figure 1.8g**).⁸² So far, it has been unclear how strategies used to successfully synthesize boronate-ester-linked 2D COF nanocrystals can be generalized to synthesize high-quality 2D COFs with other dynamic covalent linkages.^{173, 174} Regardless, we expect that the lessons learned from boron-based COF systems will inform the long-standing goal of synthesizing large-area single-crystalline COF sheets of virtually any chemical composition.

1.7.3 Nanosheets and Films

The preparation of 2D COFs into few- or single-layer sheets is of immense interest.¹⁷⁵⁻¹⁸⁰ Generally, there are two routes to obtain 2D COF as nanosheets: 1) A top-down approach where multilayer 2D COFs are exfoliated and 2) a bottom-up approach where few-layer macromolecular sheets are synthesized directly. The most common method to prepare 2D COF films is by direct polymerization onto a solid support. This approach was first conducted as conventional solution-phase 2D polymerization in the presence of a graphene-coated substrate.¹⁸¹ Direct growth

frequently produces 2D COF films with their layers oriented parallel to the substrate.¹⁸¹ This approach has been found to be largely general, with many 2D COFs prepared as films on graphene substrates.¹⁸¹⁻¹⁸³ However, the use of bulk reaction conditions to produce 2D COF films results in significant contamination by insoluble powder aggregates that are also produced during the polymerization. Historically, the films produced by this method are composed of COF sheets of limited sizes, with crystallographic dimensions similar to those produced by bulk powder syntheses (approximately 50 nm lateral domain size).

Medina and coworkers recently optimized bulk imine-linked 2D COF synthesis conditions to reduce the amount of powder contamination, which generated 2D COF films suitable for optoelectronic characterization, on a variety of substrates including silicon and indium tin oxide (ITO).¹⁸⁴⁻¹⁸⁶ Similarly, Dichtel and coworkers found that 2D COFs could be grown in flow conditions, which enabled the formation of smooth, oriented, thickness-controlled COF films.¹⁸⁷ By growing the films in flow under low steady-state monomer conditions, bulk COF nucleation and precipitation were suppressed, both of which were identified as critical for the formation of smooth films. Interestingly, film crystallinity is detected only at longer monomer residence times, which suggests that oligomeric and polymeric species may play a role in the boronate ester-linked COF film formation and growth. Collectively, these studies also suggest that the heterogeneous nucleation barrier is lower than the homogenous nucleation barrier, in some cases.

More recently, 2D COF films were grown under colloidal synthetic conditions that restricted powder precipitation altogether. This approach allows for trivial separation of COF films and nanoparticles, which are formed simultaneously. The films prepared by this approach had practically no powder contamination, which enabled their detailed optoelectronic and

thermomechanical characterization as well as their direct imaging *via* TEM. These recent developments indicate that the conditions that prevent bulk 2D COF formation and precipitation are likely also optimal for the synthesis of high-quality films *via* direct growth approaches. Taken together, direct growth is routinely used to prepare well-oriented 2D COF films but has obvious limitations in scale-up and substrate compatibility. However, its relative simplicity and compatibility with developed bulk-reaction chemistry will drive the prevalence of direct growth methods for producing 2D COF films at the lab scale.

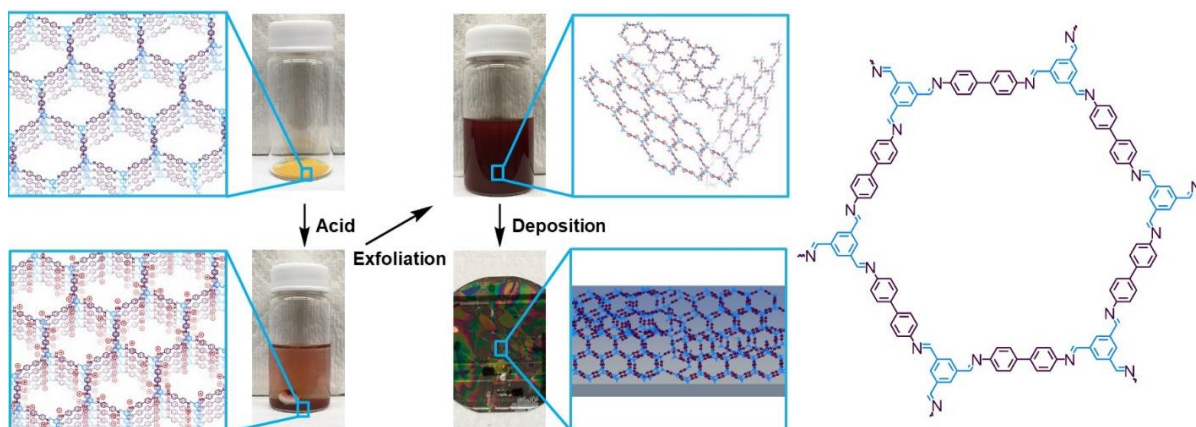


Figure 1.9 Acid exfoliation of 2D COF powders to produce suspensions of COFs and partially hydrolyzed oligomers that are then reconstituted into COF films. Adapted with permission.⁵ Copyright 2020 John Wiley & Sons.

Another strategy to prepare 2D COF films is to exfoliate bulk COF materials and reconstitute them as films. For example, Banerjee and coworkers have shown how 2D COFs prepared *in solvo* and then cast as suspended particles can generate large-area freestanding COF films.¹⁸⁸ Because the catalyst is not removed in this case it is likely that as the solvent is evaporated, crosslinks evolve between the COF sheets, which can impart mechanical strength to the millimeter thick 2D COF membranes. Dichtel and coworkers exfoliated 2D COFs by protonating the imine linkages with trifluoroacetic acids, which yielded stable suspensions (**Figure 1.9**).⁵ These suspensions could then be solvent cast to produce crystalline large-area thin films. Similar to the example above, the

trifluoroacetic acid was not removed during this procedure, which was shown by NMR spectroscopy to partially depolymerize the COF structure into soluble monomers and oligomers. Presumably, the depolymerization-repolymerization aspect of this strategy is partly responsible for the homogeneity of films obtained by this method. This strategy is particularly appealing for a broad class of 2D COFs linked through imines, which could be protonated to drive exfoliation and subsequently reconstituted as homogenous films.

1.8 Molecular Adsorption and Separation Applications

Two-dimensional COFs have a unique combination of properties including permanent porosity, mechanical strength, chemical stability, low density, and atomic scale precision which, when coupled with their vast synthetic modularity, make them ideal materials platforms for a host of applications. So far, challenges related to device integration and processability have limited COF

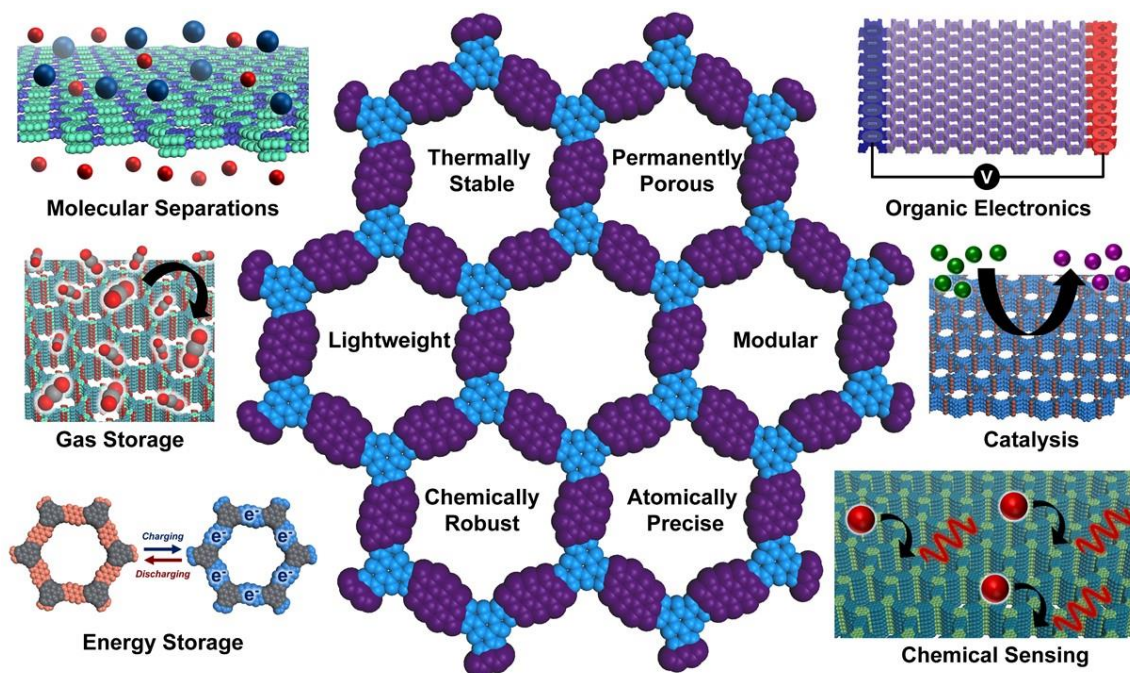


Figure 1.10 A representative sampling of 2D COF applications and some of their defining characteristics shown within the polymer structure.

device-fabrication efforts and therefore, their real-world deployment. Despite these complications, numerous reports suggest that 2D COFs hold considerable promise to exhibit many properties that would be valuable in a suite of applications. Here, we will discuss the emergent properties and application potential of 2D COFs.

1.8.1 Gas Storage and Separation

Since their earliest syntheses, researchers have speculated that 2D COFs might be promising gas storage and separation materials due to their immense permanent porosities and low gravimetric densities.⁵⁵ Moreover, the structural regularity of COFs yields homogeneous binding sites with high tunability and selectivity, compared to conventional porous polymers.¹⁸⁹⁻²⁰⁰ This structural regularity also enables the investigation and screening of 2D COFs by computational methods, which is far more challenging in amorphous polymers systems.²⁰¹ As such, many theoretical investigations have suggested that pristine COF materials will have high selectivities and capacities, characteristics that support the promise of 2D COFs as gas storage and separation materials.^{65, 79, 127, 128, 189, 191, 193, 194, 196, 198-200, 202-246} Finally, these applications are some of the most experimentally studied because they can be investigated using polycrystalline powders, which is the most commonly isolated 2DP morphology.

1.8.2 Membranes

Atomically thin COF membranes linked entirely through stable covalent bonds with precisely engineered pore chemistries and sizes have potential provide near-ideal membrane performance. This realization has spurred researchers to explore 2D COFs for a wide array of separations and membrane-based applications. However, to date, membrane applications have been restricted by

the challenge of synthesizing precisely aligned, mechanically robust 2D sheets. Despite this synthetic challenge, several researchers have performed preliminary investigations into 2D COFs as nanofiltration membranes and have obtained promising separation performances.²⁴⁷⁻²⁴⁹ This area is an important and fast-moving frontier in the field, and many leading reviews highlight the success of rationally designed 2D COF nanofiltration membranes.²⁴⁷⁻²⁴⁹ While 2D COFs are undoubtedly promising as liquid-phase membranes, caution is warranted that membranes derived from these materials have not yet unambiguously demonstrated size-selective behavior that is clearly distinguishable from removal by other mechanisms. In fact, a recent study indicates that polycrystalline COF films act more as adsorbents than size-sieving membranes in which the authors ask for a careful reexamination of the COF membrane literature, as separations based on differential transport through 2D COF pores is an important yet unrealized frontier.²⁵⁰

1.8.3 Adsorbents

The synthetic modularity, structural regularity, and permanent porosity of 2D COFs endow them with high adsorption selectivity and capacity for various adsorbate species. This realization has inspired 2D COFs to be developed for a host of molecular capture and delivery applications. In regard to molecular capture, 2D COFs have been studied extensively in the removal of heavy metal ions from water.²⁵¹ For example, high-sulfur-containing 2D COFs, such as those functionalized with sulfides,²⁵² thiols,¹¹ and thioethers,²⁵³ have been shown to be highly selective for Hg²⁺ capture and removal.^{11, 252-257} In addition to their pollutant removal capabilities, the fluorescence of a 2D COF sorbent was quenched upon binding mercury ions, providing a simple means to detect its presence (**Figure 1.11**).¹¹ Fluorescence “turn-on” sensors for radioactive elements were also reported based on the binding to Eu³⁺ within the pores of the COFs.²⁵⁸ These results show that 2D

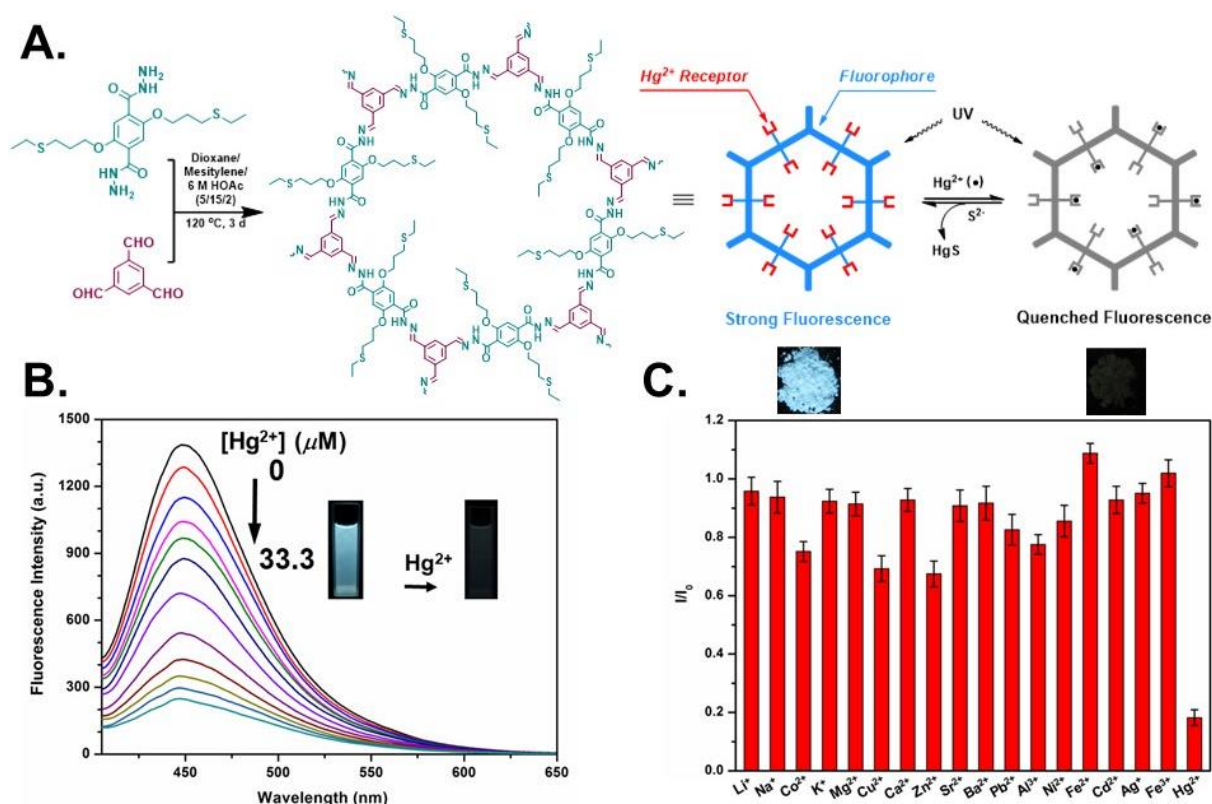


Figure 1.11 a) Synthesis a sulfur-functionalized 2D COF under solvothermal conditions. The COF exhibited strong fluorescence upon excitation at 390 nm. b) Upon the addition of Hg^{2+} , the fluorescence of the COF was effectively quenched. c) Photographs of COF-LZU8 under a UV lamp ($\lambda_{\text{ex}} = 365 \text{ nm}$) visualize the significant change in the fluorescence emission before (left) and after (right) the adsorption of Hg^{2+} and a chart showing the selectivity of Hg^{2+} in fluorescence quenching versus other materials. Adapted with permission.¹¹ Copyright 2016 American Chemical Society.

COFs are a compelling platform for the simultaneous detection and removal of inorganic contaminants. This may be particularly valuable for identifying and removing persistent, low levels of contamination. In another recent study, Ma and coworkers developed amidoxime-based 2D COFs that were capable of removing valuable inorganics from water, such as uranium.^{259, 260} Due to the high porosity and amidoxime functionality in these networks, these materials reported high capacities (127 mg g^{-1}) and rapid kinetics of removal for uranium (<10 min equilibration time). Similarly, Yu and coworkers showed how 2D COFs functionalized with thioether pendant side chains can remove Au metal (560 mg g^{-1}) from water at micromolar concentrations.²⁶¹ These reports show that COF adsorbents are promising candidates for materials that capture valuable

species from low-concentration sources. We expect this area will garner greater interest as primary sources of valuable metals become scarce.

Similar to the removal of inorganic contaminants, 2D COFs can be engineered to remove organic micropollutants from water. For example, researchers have shown that 2D COFs functionalized with ionic bonding, hydrogen bonding, or hydrophobic motifs can capture ionic dyes, nanoparticles, polymers, or other species of interest from water.^{109, 212, 214, 230, 255, 262-275} Typically, these adsorbents are used as microcrystalline powders with high surface areas. The high porosity and small crystallite sizes make these materials efficient platforms for the rapid removal of organic pollutants. Similarly, their immense surface areas allow them to have notable gravimetric capacities. In one example, Dichtel and coworkers reported amine-functionalized 2D COFs that effectively bind anionic perfluorinated alkyl substances (PFAS).¹²⁴ This is an exciting development as it showed how monomers that included chemistries incompatible with the COF formation could be post-synthetically installed for the efficient removal of PFAS.¹²⁴

Outside of pollutant remediation, the uniform pore size and high surface area of 2D COFs have attracted interest for the selective removal of endogenous peptides from biosamples.²⁷⁶ The presence of these endogenous peptides, such as neuropeptides and peptide hormones, albeit in low quantities, greatly interferes with the analysis of the biosamples. Liang, Li, and coworkers reported an imine-linked 2D COF that facilitated the extraction and identification of 416 peptides from human serum, and demonstrated the exclusion of larger proteins, presumably due to the limited pore size (2.5 nm) of the COF.²⁷⁷ This demonstrated the utility of 2D COFs as selective adsorbents in peptidomics research, and further tuning of the COF properties can potentially increase their selectivity for specific peptide residues. While the cost of these COF adsorbents is considerably

larger than that of the conventional adsorbents, their large capacities and rapid removal efficiencies make them highly attractive as point-of-use adsorbents. Taken together, these results demonstrate that 2D COFs can be synthetically engineered to remove target analytes from water in laboratory settings. Immediate next steps should be taken to establish the utility of these materials as adsorbents, such as studying their long-term stability and efficacy in complex, environmentally relevant matrices.

1.8.4 Chiral Separation

Chiral separations are driven by the differential interaction energies of enantiomers with a chiral

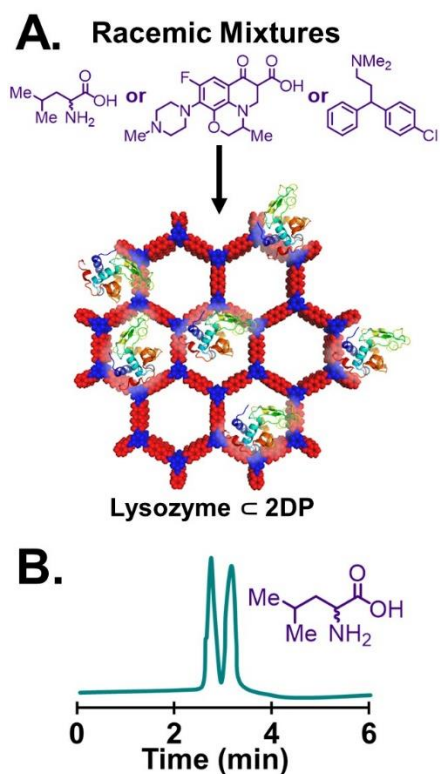


Figure 1.12 a) Chiral resolution of racemic mixtures using a 2D COF @lysozyme and b) a representative chiral resolution chromatogram separating D- and L-tryptophan. Adapted with permission.⁴ Copyright 2018 John Wiley & Sons.

stationary phase.²⁷⁸ Chiral 2D COFs have been formed by covalently immobilizing chiral species (amino acids, peptides, enzymes) onto achiral COF network.^{4, 247, 279} Inheriting the specific chiral interactions of these immobilized biomolecules, the afforded 2D COF@biomolecules serve as versatile and highly efficient chiral stationary phases toward various racemates in both the normal and reverse phase of high-performance liquid chromatography.^{4, 280} For example, Ma and coworkers showed that racemic mixtures of amino acids could be separated by immobilizing lysozymes onto 2D COF scaffolds (**Figure 1.12**).⁴ The different interactions between enzyme secondary structure and racemates were revealed by surface-enhanced Raman scattering studies,

and were speculated to be the origin of the observed stereoselectivity. Presumably, as morphological control of 2D COFs improves, these materials will be more promising for real-world chiral separation applications. A promising avenue of research will be to leverage the well-defined structural aspects of 2D COFs for adsorbent applications. It is, for instance, feasible that ultrahigh selectivity for a particular analyte could be designed within a 2D COF pore structure. We expect that these studies will be on the cutting edge of COF adsorbent research in the coming years.

1.8.5 Molecular Recognition

The tailored, persistent pore sizes of 2D COFs make them ideal candidates for molecular recognition if suitable binding pockets can be installed into the network. In addition, the periodicity of 2D COFs along their 1D channels allows for cooperative molecular recognition to minimize the loss of crystalline registry between the 2D sheets. These opportunities were realized by Jiang and coworkers when they prepared an imine-linked 2D COF containing triangular pores (**Figure 1.13**).⁷ In this work, structurally similar molecules (Nile red (NR), 7-(diethylamino)-3-phenylcoumarin (DAPC), and Coumarin 6) were shown to dock into the notches at the vertices of the triangular pore. This binding process of Nile red was characterized by ultraviolet-visible spectroscopy and shown to be cooperative, which resulted in its rapid removal from solution (**Figure 1.13c**). This cooperativity allowed for the authors to rapidly separate mixtures of these molecules, differing only by a single atom.

MacLeod, Rosei, and coworkers studied the adsorption of trichlorobenzene to 2D COFs synthesized on-surface (**Figure 1.13d-f**).¹² Scanning tunneling microscopy used in this study

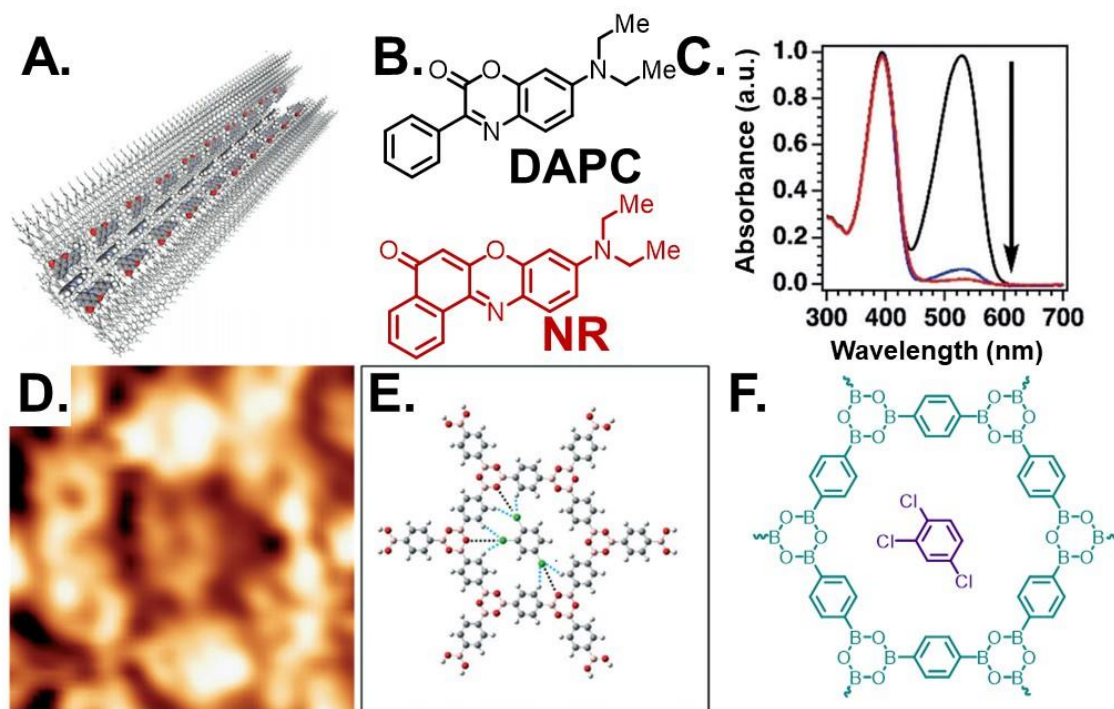


Figure 1.13 a) Assembled tubule of Nile red (NR) dye molecules within the triangular pore of a multilayer 2D COF. b) Chemical structures of NR and DAPC ((7-diethylamino)-3-phenylcoumarin). c) Absorbance traces of a mixture of NR and DAPC in the presence of a 2D COF, where only the signals associated with the NR diminish over time. Adapted with permission.⁷ Copyright 2019 John Wiley & Sons. ad) Scanning tunneling micrograph (image dimensions 2.1 nm × 2.1 nm) of a 2D COF with an associated trichlorobenzene molecule. e-f) 3D rendering and chemical structure of this association complex. Adapted with permission.¹² Copyright 2017 The Royal Society of Chemistry.

showed the precise binding location, which yielded important information about the highly selective adsorption of trichlorobenzene to the COF pore.¹² This example reveals that direct imaging techniques, such as STM, can provide unambiguous evidence for particular binding geometries and mechanisms. While this is an underexplored area of research for COFs, this report highlights opportunities to leverage cooperative binding mechanisms in structurally regular networks for precise molecular recognition and separations. Importantly, combinations of computational and experimental approaches will be valuable to the design and iterative testing of cooperative phenomena in 2D COFs.

1.8.6 Molecular Delivery

In addition to molecular capture and storage, 2D COFs can be engineered to adsorb and transport chemical species. In one example of this, the tunable hydrolysis rate of imine linkage allowed the degradation of the COF, along with release of its molecular cargo, to be controlled.^{11, 155, 252-254, 257}

This behavior has enabled further exploration of 2D COFs that can carry common pharmaceuticals, such as ibuprofen and captopril, at high loadings *in vitro*.²⁸¹ When the 2D COFs were endocytosed and hydrolyzed by cancer cells, these analytes were effectively released inside the cells. In that report, the drug loading capacity and release profiles were tuned based on their different pore sizes, highlighting the design potential of 2D COFs for drug delivery. In another report of COF drug

carriers, a mechanically exfoliated 2D COF effectively delivered 5-fluorouracil to breast cancer cells. Given the operationally simple transformation of 2D COFs into functionalized delaminated sheets, they are of growing interest for targeted drug delivery to a wide variety of cells. Trabolsi and coworkers prepared an imine-linked 2D COF with azobenzene units that under photoirradiation could undergo *cis-trans* isomerizations.⁶ Upon the

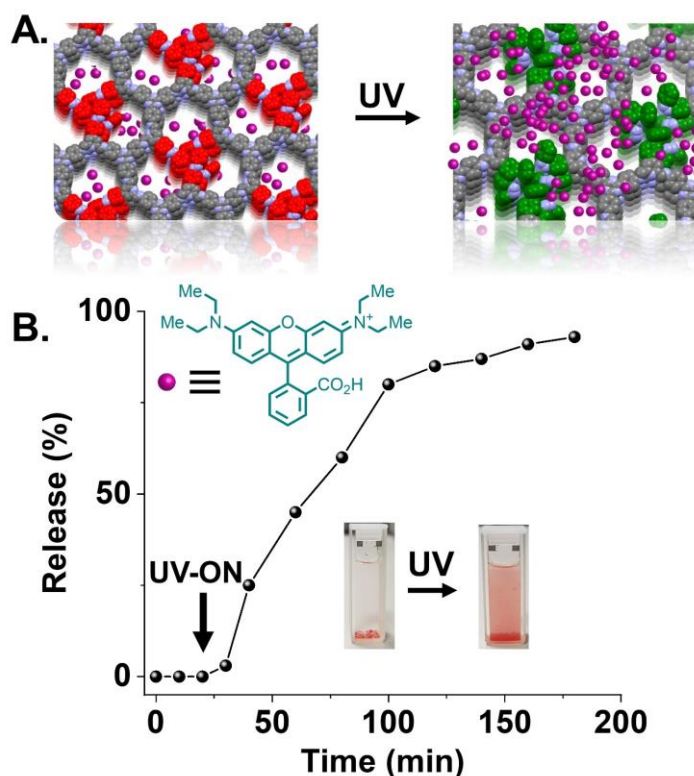


Figure 1.14 a) Schematic of controlled molecular release from a 2D COF upon UV exposure as a function of azobenzene switching. b) Release profile of molecular dye as evaluated by UV-visible spectroscopy upon irradiation of the 2D COF with UV light. Adapted with permission.⁶ Copyright 2019 American Chemical

irradiation, the adsorbed rhodamine-B molecules were released into solution (**Figure 1.14**). Presumably, future designs could take advantage of photoinduced structural transformation for many molecular capture and release applications. As with many 2D COF applications, however, other classes of materials are also promising for the controlled transport and release of molecular compounds. Likely the success of 2D COFs in this space will require more thorough investigation of additional properties related to device performance across a wide swath of 2D COFs, which is yet to be demonstrated.

1.9 Outlook on Current Challenges and Future Opportunities

The long-standing goal of polymerizing macromolecular sheets has recently been realized. The emergence of this new branch of polymer chemistry has been enabled by scientific contributions from many fields including supramolecular chemistry, framework chemistry, and crystal engineering. To date, solution-based 2D polymerization strategies using dynamic bond-forming reactions have emerged as one of the most common approaches to the synthesis of macromolecular sheets. The ingenuity of polymer chemists has expanded these strategies immensely, which has resulted in the polymerization of more than 500 discrete 2D COF structures. Despite major advances in 2D polymerization over the last two decades, however, methods to prepare large-area, defect-free macromolecular sheets of arbitrary composition are by no means mature. Many challenges in 2D polymerization can be traced to a lack of foundational mechanistic understanding. Therefore, the continued investigation of COF formation and growth mechanisms is paramount for the continued development of this field. Polymer chemists have also not yet developed the vernacular to discuss 2DPs at the same depth as other polymer architectures. For example, terms such as dispersity and molecular weight are not currently well defined for 2DPs, nor are they

routinely measured or reported. These limitations make discussion and characterization of 2D COFs and their emergent properties challenging. As the synthesis and characterization toolkits become more refined for 2DPs, it will be important that the language used to describe them also evolves. Ultimately, as the scientific understanding and descriptive vocabulary surrounding 2D polymerization coevolve, so too will the quality and complexity of 2DPs.

The synthesis of chemically diverse, high-quality 2D COFs will likely produce materials with unique combinations of properties not available in other materials. However, due to the synthetic challenges outlined above, many of these properties have yet to be studied or rationally manipulated. This challenge predominantly arises as a consequence of the relatively uncontrolled polymerization strategies used to prepare many 2D COFs. As these synthetic obstacles are overcome, it will become commonplace to unambiguously characterize the COF structure, leading to meaningful structure-property relationships in these materials. For instance, as large-area macromolecular sheets are reliably produced it will become possible to examine the intrinsic thermomechanical and optoelectronic properties of these materials, with confidence that measurements are not confounded by limited domain size or defects. Additionally, many properties of 2D COFs are likely determined by their thickness. Therefore, as methods to prepare large-area mono- and few-layer COFs using bottom-up and top-down approaches are developed, we expect that explorations of layer-dependent phenomena in 2D COFs will be a fruitful area of study. These findings will certainly guide further development of 2D COFs for real-world applications.

Toward this end, examples of molecular adsorption and separation applications for 2D COFs are provided, many of which show promise. Care is needed when characterizing 2D COFs integrated

into membranes or device-relevant platforms, since many of these COF materials have been prepared using less-than-ideal polymerization strategies that introduce molecular defects and significant edge and surface sites not found in the bulk materials. It is also frequently unclear whether the COF structure and properties are maintained within a device environment. Though just as linear polymers were improved through decades of study and are now incorporated into our everyday lives, we anticipate that 2DPs will do so as well. We foresee a promising future in 2D polymerization. In the near term, the constantly accelerating rate of research into 2D COFs and their properties is certain to continue. This expansion of interest will drive innovations regarding their synthesis, properties, and eventual applications. Ultimately, particular applications are likely to emerge as promising for real-world deployment. This will mark the beginning of the next generation of COF and 2DP science. In 1993, Roald Hoffman described synthetic 2D chemistry as an uncharted wasteland.²⁸² Here, we hope to have convinced the reader that the grounds of 2D organic chemistry have now been cultivated, are beginning to blossom, and will soon be ripe for harvesting.

2. Synthesis of Amine-Functionalized Covalent Organic Frameworks to Remove Perfluorinated Alkyl Substances from Water

2.1 Preface

In this chapter, I discuss the design and synthesis of the amine-functionalized, two-dimensional (2D) imine-linked covalent organic frameworks (COFs) for perfluorinated alkyl substances (PFAS) removal from water. I will briefly highlight current PFAS contamination and limitations of current PFAS removal technologies. I will then outline the advantages of covalent organic frameworks over conventional activated carbon-based adsorbents. COFs are relatively unexplored but hold promise as adsorbents due to their high surface area and tunable pore sizes. Herein, we present our design and synthesis of 2D imine-linked COFs functionalized with primary amines that remove GenX and 12 other PFAS at environmentally relevant concentrations.

This work was done in collaboration with Dr. Yuhan Ling, Casey Ching and Prof. Damian Helbling from the School of Civil and Environmental Engineering at Cornell University, and Dr. Leilei Xiao, Dr. Michio Matsumoto, and Dr. Ryan P. Bisbey Chemistry from the Chemistry Department at Cornell University. This work is reprinted with permission from Ji, W.; Xiao, L.; Ling, Y.; Ching, C.; Matsumoto, M.; Bisbey, R. P.; Helbling, D. E.; Dichtel, W. R., *J. Am. Chem. Soc.* **2018**, *140*, 12677-12681. Copyright (2018) American Chemical Society.

2.2 Abstract

Per- and polyfluorinated alkyl substances (PFAS), such as perfluorooctanoic acid (PFOA), perfluorooctane sulfonate (PFOS), and ammonium perfluoro-2-propoxypropionate (GenX), contaminate ground and surface waters throughout the world. The cost and performance limitations of current PFAS removal technologies motivate efforts to develop selective and high affinity adsorbents. Covalent organic frameworks (COFs) are unexplored yet promising adsorbents because of their high surface area and tunable pore sizes. Here we show that imine-linked two-dimensional (2D) COFs bearing primary amines adsorb GenX rapidly at environmentally relevant concentrations. COFs with partial amine incorporation showed the highest capacity and fastest removal, suggesting that the synergistic combination of the polar group and hydrophobic surfaces are responsible for GenX binding. A COF with 28% amine loading also removed more than 90% of 12 out of 13 PFAS. These results demonstrate the promise of COFs for PFAS removal and suggest design criteria for maximizing adsorbent performance.

2.3 Introduction

Covalent organic frameworks (COFs) are crystalline, porous polymers whose monomers are organized using directional bonding principles.^{221, 283-285} Several features of COFs enable them to function as adsorbents with fast uptake and high capacity: their crystallinity positions functional groups into precise arrangements and their few-nanometer 1D channels are readily accessible.²⁸⁶⁻²⁸⁸ COFs have been demonstrated for binding technologically relevant gases, such as CH₄,²⁸⁹ H₂,^{289, 290} NH₃,²⁹¹ and CO₂,^{286, 292} and heavy metals,^{287, 293, 294} but they are unexplored for sequestering organic micropollutants. Here we reduce azide-functionalized COFs to the

corresponding amine-functionalized networks and demonstrate their promise as adsorbents for per- and polyfluorinated alkyl substances (PFAS).

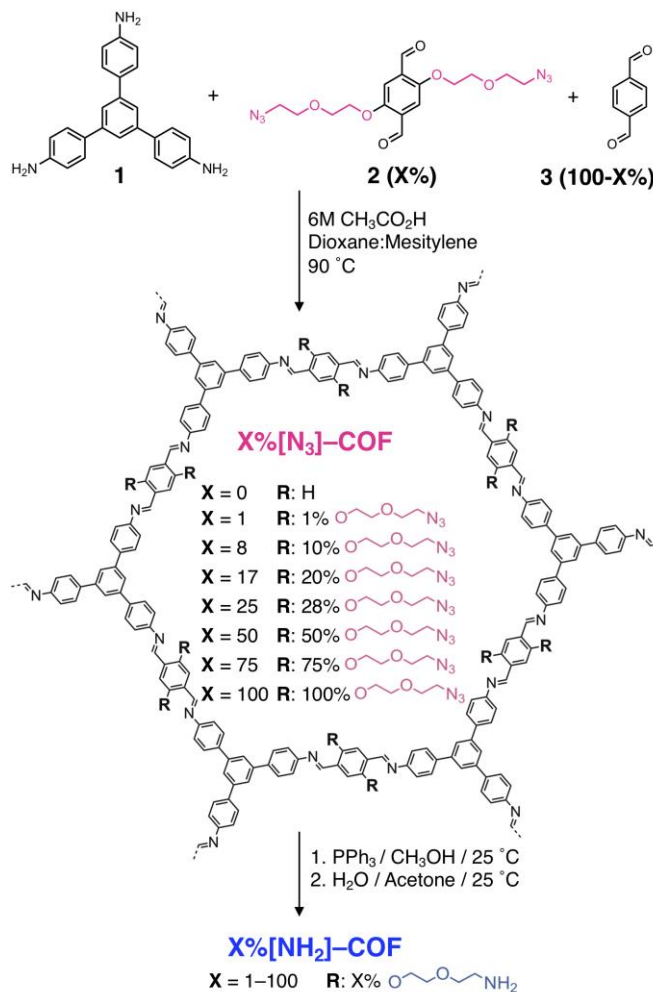
The contamination of ground and surface water by PFAS affects hundreds of millions of people world-wide.²⁹⁵⁻²⁹⁷ PFAS are used in the production of fluoropolymers, water and stain repellents, and as components of aqueous film-forming foams (AFFF) used to suppress fires.²⁹⁸ Thousands of airports and military installations are contaminated by PFAS found in AFFF,²⁹⁹ and several communities in the US declared states of emergency for PFOA and PFOS in 2016. Concerns about PFOA's ecological persistence, bioaccumulation,³⁰⁰⁻³⁰³ and health effects prompted its phase-out in the United States, but it was replaced by other PFAS, such as GenX, that are also emerging contaminants.³⁰⁴⁻³⁰⁶ GenX was found in the Cape Fear River in North Carolina,^{295, 307} and its removal by conventional and advanced treatment processes was negligible.²⁹⁵ Therefore, developing effective treatment and remediation strategies is essential. Granular activated carbon is presently used by affected communities, but its modest affinity and effectiveness against short-chain PFAS compounds^{295, 308, 309} have motivated studies of alternatives. The COFs studied here present amine groups that interact with the anionic head group of PFAS, along with ample hydrophobic surface area that further support adsorption. The optimized materials, with amine loadings of 20–28%, bind 13 PFAS with high affinity and rapid kinetics.

We targeted a hexagonal imine-linked 2D COF bearing amine functionalities to provide high affinity for anionic PFAS. The loading of amine functional groups into the final COF was controlled by condensing 1,3,5-tris(4-aminophenyl)benzene (**1**, **Scheme 2.1**) with a mixture of terephthalaldehyde (**3**) and a dialdehyde bearing azide-functionalized ethylene glycol side chains (**2**). **2** and **3** were polymerized in various molar ratios to synthesize COFs (X%**[N₃]**-COFs) that

average 6, 4.5, 3, 1.5, 1, 0.5, and 0.06 azides, respectively, per layer within each hexagonal pore.

$X\%[\text{N}_3]\text{-COFs}$ were prepared in a 4:1 mixture of 1,4-dioxane and mesitylene with 6M $\text{CH}_3\text{CO}_2\text{H}$ at 90 °C for 72 hours.

The resulting precipitates were collected and purified by Soxhlet extraction with CH_3OH and activated by supercritical CO_2 drying. $X\%[\text{N}_3]\text{-COFs}$ were reduced to the corresponding $X\%[\text{NH}_2]\text{-COFs}$ by PPh_3 in CH_3OH . The amine-functionalized imine COFs ($X\%[\text{NH}_2]\text{-COFs}$) were washed with 4% (v/v) H_2O in acetone followed by CH_3OH , and subsequently activated by supercritical CO_2 drying.



Scheme 2.1

2.4 Results and Discussion

2.4.1 Amine-functionalized Covalent Organic Frameworks Synthesis and

Characterization. The complete reduction of azides to amines was characterized by spectroscopy. Fourier-transform infrared spectroscopy (FT-IR) revealed that the azides in $X\%[\text{N}_3]\text{-COFs}$ were reduced, based on the disappearance of the azide stretch at 2098 cm^{-1} (Figure S.1a) and the appearance of a broad amine N–H stretch at 3356 cm^{-1} (Figure 2.S3–2.S5).

The incorporation ratios of the COFs with lower azide and amine loadings were slightly higher

than the feed ratios, as judged from the quantitative IR analysis (**Table 2.S8**), indicating that **2** is slightly more reactive than **3**. X-ray photoelectron spectroscopy (XPS) also indicated the conversion of azides to amines (**Figure 2.1b**, **Figure 2.S6**). The spectrum of the **100%[N₃]-COF** shows characteristic azide N 1s peaks at 400.0 and 403.7 eV with an area ratio of 2:1.^{310, 311} The spectrum of the **100%[NH₂]-COF** instead shows a new N 1s peak at 398.6 eV, which was fit to a 1:1 combination of imines and aliphatic amines.^{310, 311} Zeta potentials of **100%[N₃]-COF** and **100%[NH₂]-COF** at pH 7 were -7 mV and +13 mV (**Table 2.S4**), whose change in sign is attributed to protonation of the amines. Collectively, these measurements and elemental analysis

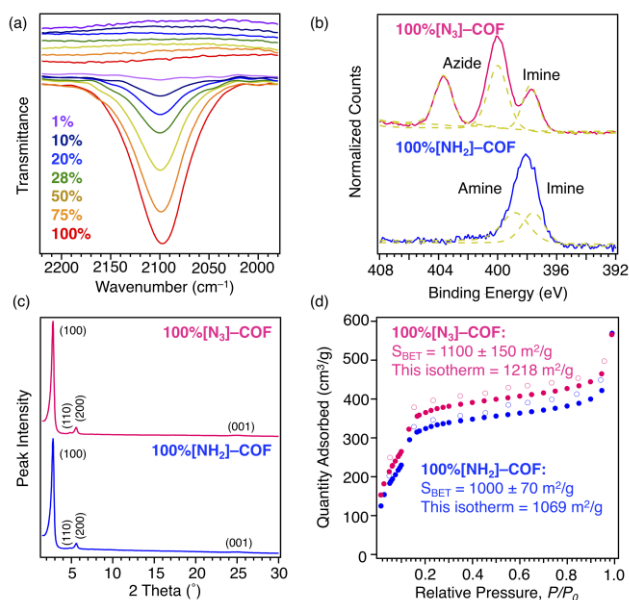


Figure 2.1 (a) FT-IR spectra (2300–1900 cm⁻¹) of X%[N₃]-COFs (bottom spectra) and X%[NH₂]-COFs (top spectra), corresponding to the concentration of azides or amines (X) of 100% (red), 75% (orange), 50% (yellow), 28% (green), 20% (blue), 10% (indigo), and 1% (purple). (b) XPS of N 1s core level (392–408 eV) (c) PXRD patterns normalized at the (100) peak at 2.8° and (d) N₂ adsorption isotherm of 100%[N₃]-COF (pink) and 100%[NH₂]-COF (blue). For (d), solid and open circles indicate adsorption and desorption, respectively. Surface areas are reported as ± 1 standard deviation of 14 independently prepared samples of 100%[N₃]-COF, and 3 independently prepared samples of 100%[NH₂]-COF.

(**Table 2.S1–S2**) indicate the quantitative conversion of azides to amines.

The crystallinity and porosity of X%[NH₂]-COFs were retained after the reduction, as confirmed by powder X-ray diffraction (PXRD, **Figure 2.1c**, **Figure 2.S8**) and N₂ adsorption isotherms (**Figure 2.1d**, **Figure 2.S9**, **Table 2.S3**). The PXRD pattern of **100%[N₃]-COF** exhibited an intense (100) diffraction peak at 2.8°, along with the (110), (200), and (001) diffraction peaks at 4.8°, 5.6°, and 25.2°, respectively, which is consistent with the reported eclipsed pattern for

imine-linked COFs containing dimethoxy side groups.³¹² **100%[NH₂]-COF** exhibited an identical PXRD pattern to that of **100%[N₃]-COF**, indicating that the 2D hexagonal structure of **100%[N₃]-COF** was retained upon reduction. Each **X%[NH₂]-COF** also exhibited the same PXRD pattern to that of the corresponding **X%[N₃]-COF** (**Figure 2.S8**). The permanent porosity of **X%[N₃]-COFs** and **X%[NH₂]-COFs** was measured by N₂ adsorption isotherms at 77 K (**Figure 2.1d, Figure 2.S9**). The Brunauer–Emmett–Teller (BET) surface area of **100%[N₃]-COF** was $1100 \pm 150 \text{ m}^2/\text{g}$, and that of **100%[NH₂]-COF** was $1000 \pm 70 \text{ m}^2/\text{g}$. The BET surface areas of other **X%[NH₂]-COFs** were also retained upon reduction (**Table 2.S3**). Nonlocal density functional theory analysis of each isotherm provided narrow pore size distributions centered around 2.6 nm (**Figure 2.S10**). As the concentration of azides and amines (**X**) decreased, the BET surface areas and average pore sizes of **X%[N₃]-COFs** and **X%[NH₂]-COFs** increased (**Table 2.S3**). These results confirm the formation of a broad range of 2D imine-linked COFs with pendant amine loadings ranging from 1 to 100% of the terephthalaldehyde monomers.

2.4.2 GenX and Perfluorinated Alkyl Substances Removal. Each of the **X%[NH₂]-COFs** exhibited superior equilibrium removal of GenX compared to both **100%[N₃]-COF** and **0%[N₃]-COF**. The equilibrium Gen-X removal by **X%[NH₂]-COFs**, **100%[N₃]-COF** and **0%[N₃]-COF** was first evaluated in a batch experiment using [GenX]₀ of $200 \mu\text{g L}^{-1}$, and [COF] of 100 mg L^{-1} (**Figure 2.2a**). GenX removal was inversely correlated to amine loading for **100%[NH₂]-COF** (56%) through **20%[NH₂]-COF** (97%). At lower amine loadings, GenX adsorption decreased slightly for **10%[NH₂]-COF** (94%) and **1%[NH₂]-COF** (73%). The trend of increasing GenX removal from 0% to 20% amine loading and the poor removal by **100%[N₃]-COF** and **0%[N₃]-COF** indicate that the

amines are essential for GenX binding. The trend of decreasing GenX removal from 20% to 100% amine loading suggests that dispersing the amines in the network is essential for maximum affinity, either to allow for sufficient space within the pores or adsorption of the hydrophobic tails to the pore walls.

The GenX binding capacity as a function of amine loading was probed further at higher $[\text{GenX}]_0$ (50 mg L^{-1}), still with a COF loading of 100 mg L^{-1} (Figure 2.2b).

20% $[\text{NH}_2]$ -COF again exhibited the highest capacity for GenX of 240 mg g^{-1} (Figure 2.2b), and **0% $[\text{N}_3]$ -COF** adsorbed the least GenX (3 mg g^{-1}). The molar ratio of GenX to amines in **X% $[\text{NH}_2]$ -COFs** ($[\text{GenX}]/[\text{NH}_2]$) is approximately 2:1 from **1%** to **20% $[\text{NH}_2]$ -COFs** and 1:1 for **28% $[\text{NH}_2]$ -COF** (Figure 2.S17). The

GenX:amine ratio then drops below 1:1 as the amine loading is increased from 28% to 100%, indicating that not every amine

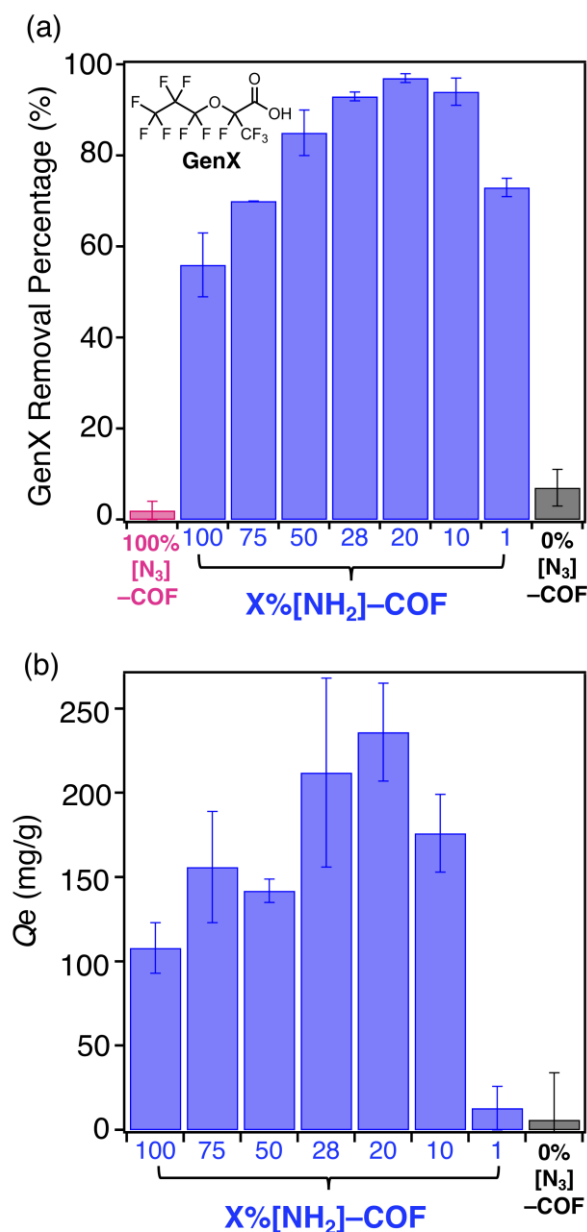


Figure 2.2 (a) Equilibrium GenX removal percentage at $[\text{GenX}]_0 = 200 \text{ } \mu\text{g L}^{-1}$ and (b) equilibrium adsorption density at $[\text{GenX}]_0 = 50 \text{ mg L}^{-1}$ by equal mass concentrations (100 mg L^{-1}) of 100% $[\text{N}_3]$ -COF (pink), X% $[\text{NH}_2]$ -COFs (blue), and 0% $[\text{N}_3]$ -COF (black) after the contact time of 22 hours. Q_e (mg g^{-1}) is the equilibrium adsorption density. Error bars: standard deviation of 3 experiments.

can interact with GenX at these higher loadings.

These results suggest that the amines in the network create a microenvironment that is conducive for GenX binding and that each amine can bind a maximum of two GenX molecules when distributed sparsely in the network.

To better understand the removal of GenX by $X\%[\text{NH}_2]\text{-COFs}$, we constructed a GenX binding isotherm for **28% $[\text{NH}_2]\text{-COF}$** (Figure 2.S19) and **100% $[\text{NH}_2]\text{-COF}$** (Figure 2.S20) using $[\text{COF}] = 100 \text{ mg L}^{-1}$ and $[\text{GenX}]_0$ ranging from 0.2 to 100 mg L^{-1} . The isotherm was best fit by the Langmuir model, which provided an affinity coefficient, K_L , of $6.3 \cdot 10^4 \text{ M}^{-1}$ and the estimated maximum capacity, Q_m , of 200 mg g^{-1} for **28% $[\text{NH}_2]\text{-COF}$** and K_L of $7.2 \cdot 10^4 \text{ M}^{-1}$ and Q_m of 130 mg g^{-1} for **100% $[\text{NH}_2]\text{-COF}$** (Table 2.S6). The high affinity coefficients and capacities of **28% $[\text{NH}_2]\text{-COF}$** and **100% $[\text{NH}_2]\text{-COF}$** explain their remarkable removal of GenX from water.

Based on the GenX removal experiments, the 28%, 1%, and 100% amine-loaded COFs were evaluated

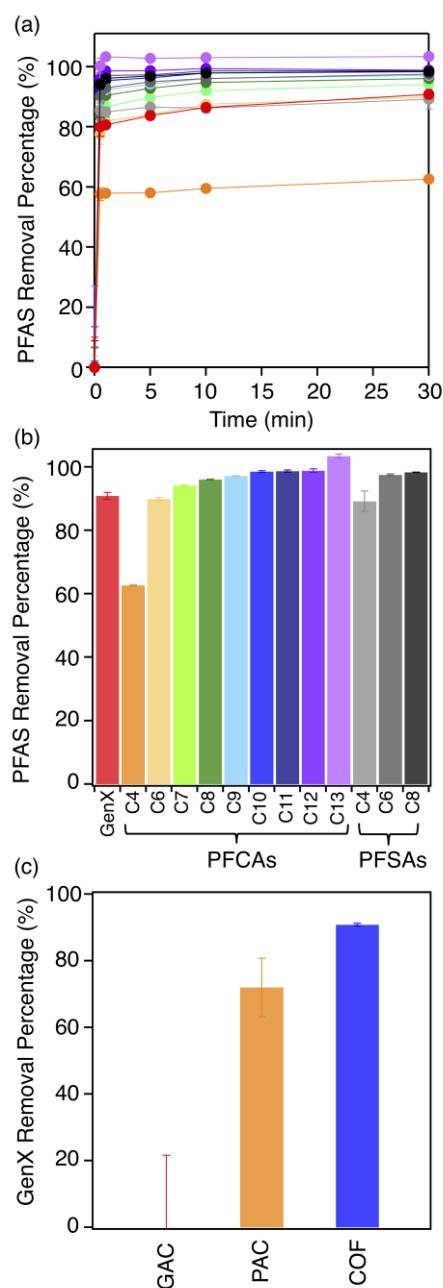


Figure 2.3 (a) Kinetics of PFAS adsorption by 28% $[\text{NH}_2]\text{-COF}$ ($[\text{PFAS}]_0 = 1 \mu\text{g L}^{-1}$; $[\text{COF}] = 10 \text{ mg L}^{-1}$) at 23 °C. (b) PFAS equilibrium removal percentage on 28% $[\text{NH}_2]\text{-COF}$ after 30 min. PFCAs: perfluoroalkyl carboxylic acids; PFSA: perfluoroalkyl sulfonic acids. (c) GenX adsorption after 30 min by GAC, PAC, and 28% $[\text{NH}_2]\text{-COF}$ using $[\text{GenX}]_0 = 1 \mu\text{g L}^{-1}$; $[\text{Adsorbent}] = 10 \text{ mg L}^{-1}$. Error bars: standard deviation of 3 experiments.

for their ability to remove a mixture of thirteen PFAS (**Figure 2.S18**) with different chain lengths and functional groups at environmentally relevant concentrations (**Figure 2.3**, **Figure 2.S21–2.S22**). Following exposure of nanopure water solutions containing $1 \mu\text{g L}^{-1}$ (1 ppb) of each PFAS to 10 mg L^{-1} of each COF, equilibrium binding was observed within 30 minutes, and each COF exhibited broad spectrum removal and high affinity for nearly all of the PFAS. Among the three COFs, **28% $[\text{NH}_2]$ –COF** performed the best and removed more than 90% of 12 PFAS and 63% of perfluorobutanoic acid (PFBA). These observations suggest that **28% $[\text{NH}_2]$ –COF** has the highest affinity for 13 PFAS compared to **1% $[\text{NH}_2]$ –COF** and **100% $[\text{NH}_2]$ –COF**, consistent with the GenX studies performed at higher concentration. We also observed that the **1% $[\text{NH}_2]$ –COF** and **100% $[\text{NH}_2]$ –COF** exhibited partial desorption of the bound PFAS between the 1- and the 24- hour time points. This effect was less pronounced for **28% $[\text{NH}_2]$ –COF** (**Table 2.S7**). Partial desorption was also observed in experiments conducted only with GenX (**Figure 2.S15**), ruling out competitive adsorption as an explanation. We are currently investigating the nature of these effects, which indicate a slow, dynamic change to these COFs that is not observed in the **28% $[\text{NH}_2]$ –COF** adsorbent. Finally, we benchmarked the GenX adsorption by **28% $[\text{NH}_2]$ –COF** against a granular activated carbon (GAC, particle size $>1000 \mu\text{m}$) and a powdered activated carbon (PAC, particle size $10\text{--}75 \mu\text{m}$) at environmentally relevant concentrations (**Figure 2.3c**). **28% $[\text{NH}_2]$ –COF** outperformed both GAC and PAC in these experiments, in which GAC removed 0%, PAC removed 72%, and **28% $[\text{NH}_2]$ –COF** removed 91% of GenX after 30 min. These combined observations indicate that amine-functionalized 2D COFs are outstanding candidates for GenX and broad-spectrum PFAS removal.

2.5 Conclusion

In conclusion, we incorporated a varying density of amine functionalities into the pores of imine-linked COFs while maintaining high surface areas ($\geq 1000 \text{ m}^2/\text{g}$). The amine-functionalized COFs show rapid uptake and high affinity for adsorbing GenX and other PFAS that is strongly influenced by the amine loading. Among the amine-functionalized imine COFs, **20% $[\text{NH}_2]$ -COF** showed the highest uptake of GenX at high concentrations ($[\text{GenX}]_0 = 0.2$ and 50 mg L^{-1}) and **28% $[\text{NH}_2]$ -COF** showed the most rapid and the highest uptake of GenX and twelve other PFAS at environmentally relevant concentrations, suggesting that the ideal composition of amines for removing PFAS is in this range. The well-defined COF structure and relationships between amine loading and PFAS binding also suggest general design criteria to improve the performance of other adsorbent classes.

2.6 Acknowledgements

The study was supported by the Strategic Environmental Research and Development Program (ER18-1026). It made use of the IMSERC at Northwestern University, which has received support from the Soft and Hybrid Nanotechnology Experimental (SHyNE) Resource (NSF ECCS-1542205); the State of Illinois and International Institute for Nanotechnology (IIN), and the Keck-II facility and the EPIC facility of Northwestern University's NUANCE Center, which have received support from SHyNE Resource (NSF ECCS-1542205); the MRSEC program (NSF DMR-1720139) at the Materials Research Center; IIN; the Keck Foundation; and the State of Illinois.

2.7 Chapter 2 Appendix

2.7.1 Materials and Instrumentation

Materials. Reagents were purchased in reagent grade from commercial suppliers and used without further purification, unless otherwise described. Anhydrous solvents (CH_2Cl_2 , DMF, THF, CH_3CN , toluene, and CH_3OH) were obtained from a solvent purification system (JC Myer System). 2-(2-Azido-ethoxy)-ethanol (**S2**),³¹³ 2-(2-azido-ethoxy)-ethyl 4-methylbenzenesulfonate (**S3**),³¹⁴ and 2,5-hydroxy-1,4-dibenzaldehyde (**S5**)³¹⁴ were prepared using literature procedures.

Instrumentation. Infrared spectra were recorded using a Nicolet iS10 FT-IR spectrometer equipped with a ZnSe ATR.

Sonication was performed with a Branson 3510 ultrasonic cleaner with a power output of 100W and a frequency of 42 kHz.

Proton nuclear magnetic resonance (^1H NMR) spectra and carbon nuclear magnetic resonance (^{13}C NMR) spectra were recorded at 25 °C on Bruker AvanceIII-500 MHz. The spectra were calibrated using residual solvent as internal reference (CDCl_3 : 7.26 ppm for ^1H NMR, 77.00 for ^{13}C NMR).

High-resolution mass spectra were acquired on Agilent 6210A LC-TOF mass spectrometer, with Atmospheric Pressure Photoionization (APPI) as an ionization source. The instrument is equipped with an Agilent Series 1200 HPLC binary pump, and autosampler, using Mass Hunter software. The samples were run using direct injection.

Elemental analyses were performed on an Elementar Vario Cube EL CHNS elemental analyzer by Integrated Molecular Structure Education and Research Center (IMSERC) at Northwestern University.

The supercritical CO₂ drying was performed in Tousimis Samdri-795 critical point dryer. Prior to the supercritical drying process, all samples were placed in tea bags (ETS Drawstring Tea Filters, sold by English Tea Store) while wet. The tea bags containing the samples were then placed in the drying chamber. The drying chamber was first sealed, cooled, and filled with liquid CO₂, and after 2 min, the samples were vented quickly. This fill-vent cycle was repeated 20 times after which the CO₂ source was turned off and the temperature was raised to 30 °C resulting in a chamber pressure of around 1300 psi, which is well above the critical point of CO₂. The chamber was held above the critical point for 5 min, and the pressure was released over a period of 5 min.

Powder X-ray diffraction (PXRD) patterns were obtained at room temperature on a STOE-STADI MP powder diffractometer equipped with an asymmetric curved Germanium monochromator (CuK α_1 radiation, $\lambda = 1.54056 \text{ \AA}$) and one-dimensional silicon strip detector (MYTHEN2 1K from DECTRIS). The line focused Cu X-ray tube was operated at 40 kV and 40 mA. The as-obtained powder samples were sandwiched between two acetate foils (polymer sample with neither Bragg reflections nor broad peaks above $10^\circ 2\theta$) mounted in flat plates with a disc opening diameter of 8 mm and measured in transmission geometry in a rotating holder. The patterns were recorded in the 2θ range of $0\text{--}32^\circ$ for an overall exposure time of 24 min. The instrument was calibrated against a NIST Silicon standard (640d) prior to the measurement.

Gas adsorption isotherms were conducted on a Micromeritics ASAP 2420 Accelerated Surface Area and Porosity Analyzer using 15–50 mg samples in dried and tared analysis tubes equipped with filler rods and capped with a Transeal. Two different degassing procedures were performed for $X\%[\text{N}_3]\text{-COFs}$ and $X\%[\text{NH}_2]\text{-COFs}$. For $X\%[\text{N}_3]\text{-COFs}$, samples were heated to 40 °C at a rate of 1 °C/min and evacuated at 40 °C for 20 min, then heated to 100 °C at a rate of 1 °C/min heat and evacuated at 100 °C for 5 h. For $X\%[\text{NH}_2]\text{-COFs}$, samples were evacuated at 25 °C for 15 h. After degassing, each tube was weighed again to determine the mass of the activated sample and transferred to the analysis port of the instrument. UHP-grade (99.999% purity) N_2 was used for all adsorption measurements. N_2 isotherms were generated by incremental exposure to nitrogen up to 760 mmHg (1 atm) in a liquid nitrogen (77 K) bath. Oil-free vacuum pumps and oil-free pressure regulators were used for all measurements. Brunauer-Emmett-Teller (BET) surface areas were calculated from the linear region of the N_2 isotherm at 77 K within the pressure range P/P_0 of 0.05–0.20.

X-ray photoelectron spectroscopy (XPS) was performed on an ESCALAB 250Xi (ThermoFisher Scientific). COF powder samples were prepared on a carbon tape. A 500 μm spot size was used to illuminate the sample with monochromatic Al $K\alpha$ radiation (1486.6 eV) and an electron flood gun was used for charge compensation. Survey and high-resolutions scans were performed at 150 and 50 eV pass energies respectively. Spectra were processed and analyzed using the native Advantage Software. All peaks were referred to with the C 1s peak binding energy (284.8 eV). A SMART background was subtracted before peak deconvolution and integration.

Thermogravimetric analysis (TGA) was performed on a Mettler Toledo SDTA 851

Thermogravimetric Analysis System using 10–15 mg of sample. The samples were heated to

designated temperature at a rate of 10 °C/min and held at that temperature for 10 min under a nitrogen atmosphere.

Scanning electron microscopy (SEM) images of the osmium-coated **100%[N₃]-COF** and **100%[NH₂]-COF** samples were taken on a Hitachi S4800 cFEG SEM.

Zeta potential measurements were performed at 25 °C on a Nano Zetasizer (Malvern Instruments Ltd.) with a He-Ne laser (633 nm, Max 5 mW). 10 mg of a COF sample was added into a polypropylene vial with 1 mL 0.1 M phosphate buffer and 9 mL Milli-Q water to yield a 1 g L⁻¹ suspension. The suspension was sonicated for 1 minute and then stirred on a multi-position stirrer for 2 h at 500 rpm to disperse small aggregates. The suspension was then diluted by putting 1 mL of the 1 g L⁻¹ stock into a polypropylene vial with 0.9 mL 0.1 M phosphate buffer and 8.1 mL Milli-Q water to yield a 0.1 g L⁻¹ suspension.

GenX removal experiments were performed at 25 °C on a stir plate with a 500 rpm stirring rate. Aqueous samples from high concentration GenX adsorption experiments (200 µg L⁻¹ to 100 mg L⁻¹) were filtered with a 0.2 µm inorganic syringe filter (Whatman). Low concentration (1 µg L⁻¹) PFAS kinetic and equilibrium experiments were performed at 23 °C on a stir plate with a 460 rpm stirring rate. Aqueous samples from low concentration adsorption experiments were filtered with a 0.45 µm cellulose acetate filter (Restek). Control experiments were performed in the exact same procedure with the absence of COF. All experiments were performed in triplicate.

Quantification of GenX (200 µg L⁻¹ to 100 mg L⁻¹) from the adsorption studies (kinetic experiments at [GenX]₀ = 200 µg L⁻¹ and isotherm experiments) was conducted using Agilent 1200 Series high performance liquid chromatography (LC) coupled with an ESI-ion trap mass

spectrometer (MS) Bruker Amazon X (USA). The mobile phase consisted of (A) Milli-Q water and (B) HPLC-grade methanol: water = 85:15 (Sigma Aldrich, USA), each amended with 10 mM ammonium acetate (Sigma Aldrich, USA). Samples were injected at 5 μL volumes and were loaded onto a ZORBAX Eclipse Plus (Agilent, Santa Clara, CA) C18 column (2.1mm x 50 mm, particle size 3.5 μm) with a loading pump delivering 400 $\mu\text{L min}^{-1}$ of a mobile phase consisting of 85% B. The column temperature was held constant at 40 $^{\circ}\text{C}$. The HPLC-MS was operated with electrospray ionization in negative polarity mode. Matrix-matched calibration standards ($n = 7$) were prepared with concentrations ranging between 10 $\mu\text{g L}^{-1}$ to 200 $\mu\text{g L}^{-1}$ for external calibration. Analytes were quantified from calibration standards based on the GenX responses by S-3 linear least-squares regression. Calibration curves were run at the beginning of the analytical run. Instrument blanks were run before and after the calibration curve and each batch of triplicate samples.

Quantification of PFAS from the adsorption studies at $[\text{PFAS}]_0 = 1 \mu\text{g L}^{-1}$ was conducted using large volume injection and high performance liquid chromatography (LC) coupled with a quadrupole-orbitrap mass spectrometer (QExactive, ThermoFisher Scientific) according to EPA Method 537. Briefly, the mobile phase consisted of (A) Milli-Q water amended with 20 mM ammonium acetate and (B) HPLC-grade methanol. Samples were injected at 5 mL volumes onto a Hypersil Gold C18 12 μm 2.1 x 20mm trap column (ThermoFisher Scientific) and were eluted onto an Atlantis C18 5 μm 2.1 x 150mm analytical column (Waters) with a gradient pump delivering 300 $\mu\text{L min}^{-1}$ of a mobile phase gradient starting at 40% B. The column temperature was held constant at 25 $^{\circ}\text{C}$. The HPLC-MS was operated with electrospray ionization in negative polarity mode. Matrix-matched calibration standards ($n = 9$) were prepared with concentrations

ranging between 1 ng L^{-1} to 1000 ng L^{-1} for external calibration. Analytes were quantified from calibration standards based on the PFAS responses by linear least-squares regression. Calibration curves were run at the beginning of the analytical run. Instrument blanks were run before and after the calibration curve and each batch of triplicate samples.

2.7.2 Synthetic Procedures

Brief Guidelines for the Safe Handling of Azides

Organic azides are potentially explosive and shock sensitive under external energy sources, such as light, heat, friction, and pressure. Therefore, azides require precaution during preparation, storage, handling and disposal.

Stability of Organic Azides

Carbon to Nitrogen Ratio

- With few exceptions, the number of nitrogen atoms should not exceed the number of carbon atoms in an organic azide ($C/N \geq 3$).

Rule of Six

- “Rule of Six” is another method of assessing the stability of an organic azide, which states that there should be no less than six carbons (or other atoms about the same size) per energetic functional group (azide, diazo, nitro, ...).³¹⁵ Less than six carbons per functional group can result in the material being explosive.

Preparation and Handling

Acidic and Aqueous Materials

- Azides should never be mixed with acidic and aqueous materials. The mixture can lead to the formation of hydrazoic acid, which is highly toxic and explosive.

Metals

- Azides should never be mixed with metals. The mixtures can lead to the formation of

Halogenated Solvents

- Halogenated solvents, such as dichloromethane and chloroform, should never be used for reactions or workup procedures in the presence of azides as their mixing can result in the formation of di- and tri- azidomethane, which are explosive.

Storage

- Azides should be stored separately from bromine, carbon disulfide, chromyl chloride, dimethyl sulfate, acids, and heavy metals and their salts.
- Azides should be stored in plastic amber containers and away from light.

Disposal

- Azide-containing waste must be collected separately and labelled clearly detailing the specific azide and any additional compatible chemical substituents.
- Organic azides should be converted to a stable derivative, such as amines, prior to the disposal.

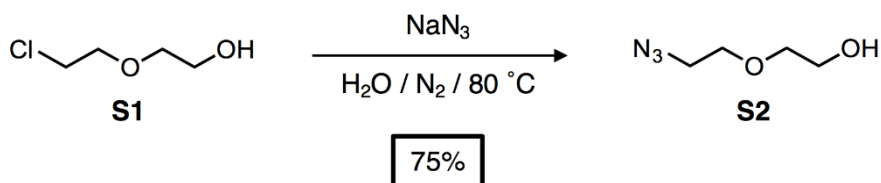
- All azide-containing materials should be disposed through university or corporate chemical waste system.
- DO NOT combine azide and acidic wastes – this can produce highly toxic and explosive hydrazoic acid.

More resources:

ACS C&E News safety portal: <http://pubs.acs.org/cen/safety/>

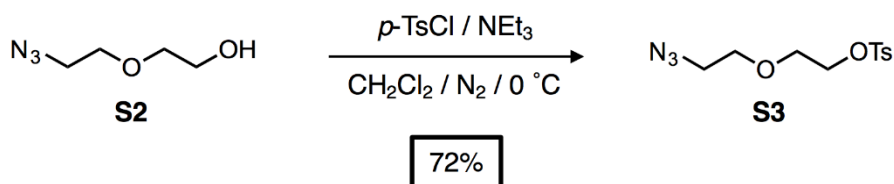
Kolb, H. C.; Finn, M. G.; Sharpless, K. B., Click Chemistry: Diverse Chemical Function from a Few Good Reactions. *Angew. Chem. Int. Ed.* **2001**, *40*, 2004-2021.³¹⁵

Scheme 2.S1



Synthesis of 2-(2-azido-ethoxy)-ethanol (S2): To a 500 mL flame-dried round bottom flask, a solution of 2-(2-chloro-ethoxy)-ethanol (**S1**, 35.4 g, 284 mmol) in deionized H_2O (180 mL) and NaN_3 (46.2 g, 710 mmol, 2.5 equiv) were added. The reaction mixture was stirred at $80\text{ }^\circ\text{C}$ under a nitrogen atmosphere for 18 h then poured into a NaOH solution (5% (w/v), 300 mL) and extracted with diethyl ether (5 x 300 mL). The organic layer was dried over MgSO_4 and evaporated to dryness to afford **S2** as a colorless oil (27.7 g, 75%). NMR data was consistent with those previously reported.³¹³

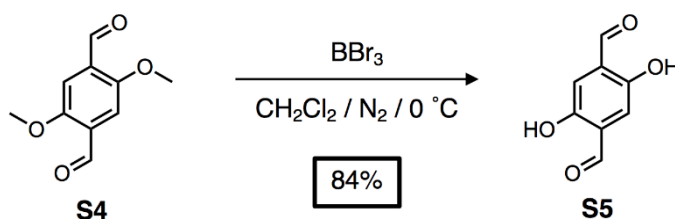
Scheme 2.S2



Synthesis of 2-(2-azido-ethoxy)-ethyl 4-methylbenzenesulfonate (S3): To a 1000 mL flame-dried round bottom flask, a solution of 2-(2-azido-ethoxy)-ethanol (**S2**, 20.0 g, 153 mmol) in dry CH_2Cl_2 (600 mL) and Et_3N (27 mL, 184 mmol, 1.5 equiv) were added. The reaction mixture was cooled to $0\text{ }^\circ\text{C}$ and $p\text{-TsCl}$ (34.8 g, 184 mmol, 1.2 equiv) was added. The solution was stirred at $0\text{ }^\circ\text{C}$ for 1 h, allowed to warm to room temperature and stirred for another 17 h under a nitrogen

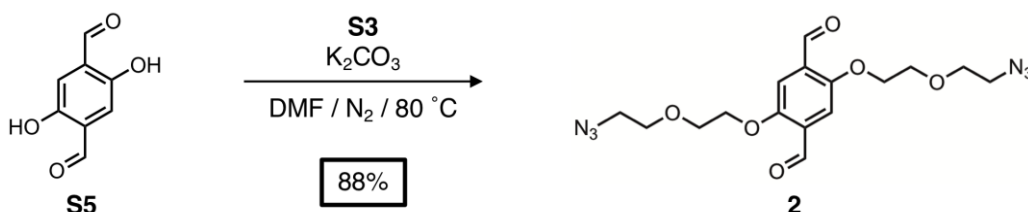
atmosphere. The solution was washed with NaHCO_3 (3 x 800 mL), H_2O (3 x 800 mL), and brine (3 x 800 mL), dried over MgSO_4 , and evaporated to dryness to afford **S3** as a colorless oil (31.3 g, 72%). NMR data was consistent with those previously reported.³¹³

Scheme 2.S3



Synthesis of 2,5-hydroxy-1,4-dibenzaldehyde (S5): To a flame-dried 250 mL round bottom flask, a solution of 2,5-dimethoxy-1,4-dibenzaldehyde (**S4**, 3.0 g, 15 mmol) in dry CH_2Cl_2 (100 mL) was added. The reaction mixture was cooled to $0\text{ }^\circ\text{C}$ and BBr_3 (1.0 M in CH_2Cl_2 , 42 mL) was added dropwise. The solution was stirred at $0\text{ }^\circ\text{C}$ for 3 h and diluted with H_2O (150 mL), and the organic layer was separated. The aqueous layer was extracted with hot EtOAc (3 x 120 mL) and the combined organic layer was dried over MgSO_4 , filtered, and evaporated to dryness. Recrystallization from boiling EtOAc afforded **S5** as an orange crystal (2.2 g, 84%). NMR data was consistent with those previously reported.³¹⁴

Scheme 2.S4



Synthesis of 2: As per a similar literature procedure,³¹⁴ to a flame-dried 1000 mL round bottom flask, a solution of 2,5-hydroxy-1,4-dibenzaldehyde (**S5**, 4.0 g, 24 mmol) and 2-(2-azido-ethoxy)-ethyl 4-methylbenzenesulfonate (**S3**, 16.4 g, 57 mmol, 2.4 equiv) in dry DMF (400 mL) was added, followed by K₂CO₃ (26.0 g, 193 mmol). The reaction mixture was stirred at 80 °C for 18 h, diluted with water (1000 mL), and extracted with hot EtOAc (5 x 600 mL). The combined organic layer was dried over MgSO₄, filtered and evaporated to dryness. Silica gel column chromatography (hexane/EtOAc = 3/2) afforded **2** as a yellow crystal (8.2 g, 88%). **2**: ¹H NMR (500 MHz, CDCl₃) δ 10.51 (s, 2H), 7.46 (s, 2H), 4.28-4.26 (m, 4H), 3.90-3.88 (m, 4H), 3.73-3.71 (t, *J* = 4.9 Hz, 4H), 3.40-3.38 (t, *J* = 5.0 Hz, 4H) ¹³C NMR (126 MHz, CHCl₃) δ 189.11, 155.10, 129.48, 112.17, 70.34, 69.45, 68.76, 50.65 ppm. IR (solid, ATR) 3347, 2934, 2881, 2858, 2137, 2115, 2081, 1678, 1485, 1445, 1427, 1399, 1386, 1358, 1339, 1278, 1244, 1237, 1213, 1122, 1091, 1071, 1058, 990, 954, 942, 878, 857, 830, 703 cm⁻¹. HRMS calculated for [C₁₆H₂₀NaN₆O₆Na⁺] 415.1337, found: 415.1348.

Synthesis of X%[N₃]-COFs: A 20 mL scintillation vial was charged with 1,3,5-tris(4-aminophenyl)benzene (**1**, 105 mg, 0.3 mmol) and **2/3**(total of 0.45 mmol) at different molar ratios of 100/0, 75/25, 50/50, 25/75, 17/83, 8/92, 1/99, and 0/100. A 1,4-dioxane / mesitylene solution

(4:1 v/v, 12 mL) was added, and the resulting suspension was sonicated at room temperature until the monomers were fully dissolved. Glacial $\text{CH}_3\text{CO}_2\text{H}$ (3.6 mL) and H_2O (2.4 mL) were added, and the resulting solution was heated at $90\text{ }^\circ\text{C}$ for 72 h. The reaction mixture was transferred to a tea bag and washed with methanol in a Soxhlet extractor for 18 h. The material was then activated by supercritical CO_2 followed by drying under vacuum at room temperature for 5 h that afforded **X% $[\text{N}_3]$ -COFs** as a yellow solid in isolated yields of **100% $[\text{N}_3]$ -COF** (200 mg, 75%), **75% $[\text{N}_3]$ -COF** (142 mg, 60%), **50% $[\text{N}_3]$ -COF** (117 mg, 56%), **28% $[\text{N}_3]$ -COF** (87 mg, 48%), **20% $[\text{N}_3]$ -COF** (81 mg, 48%), **10% $[\text{N}_3]$ -COF** (71 mg, 45%), **1% $[\text{N}_3]$ -COF** (56 mg, 37%), and **0% $[\text{N}_3]$ -COF** (51 mg, 34%).

Synthesis of X% $[\text{NH}_2]$ -COFs: To a flame-dried 25 mL round bottom flask, a suspension of **X% $[\text{N}_3]$ -COF** (100 mg, 0.34 mmol by imine) in dry CH_3OH (10 mL) was added, followed by PPh_3 (1.3 g, 5.1 mmol, 15 equiv). After 24 h at $25\text{ }^\circ\text{C}$, the suspension was filtered in a tea bag and immersed in 4% (v/v) H_2O in acetone for 18 h and in methanol for 3 h. The material was subjected to the supercritical CO_2 drying followed by the vacuum drying at room temperature for 5 h that afforded **X% $[\text{NH}_2]$ -COFs** as a yellow solid in isolated yields of **100% $[\text{NH}_2]$ -COF** (89 mg, 97%), **75% $[\text{NH}_2]$ -COF** (91 mg, 98%), **50% $[\text{NH}_2]$ -COF** (83 mg, 88%), **28% $[\text{NH}_2]$ -COF** (95 mg, 98%), **20% $[\text{NH}_2]$ -COF** (93 mg, 95%), **10% $[\text{NH}_2]$ -COF** (89 mg, 90%), and **1% $[\text{NH}_2]$ -COF** (87 mg, 87%).

2.7.3 Batch Adsorption Studies of GenX and Regeneration

I. Batch adsorption studies

The batch adsorption experiments at $200 \mu\text{g L}^{-1}$ and 50 mg L^{-1} of GenX (**Figure 2.2**) were performed in 20 mL polypropylene scintillation vials with magnetic stir bars. The experiments were conducted at 23–24 °C on a stirring hot plate with the stirring rate at 500 revolutions per minute (rpm). The adsorbent dose was 100 mg L^{-1} and GenX stock solution was spiked to generate an initial concentration of $200 \mu\text{g L}^{-1}$ or 50 mg L^{-1} .

Prior to GenX adsorption experiments, vacuum-dried adsorbents were rehydrated. 20 mg of adsorbent was added to a polypropylene vial with 20 mL Milli-Q water to yield a 1 g L^{-1} suspension. The suspensions were sonicated for 1 min and stirred on a multi-position stirrer for 1 h at 500 rpm to disperse small aggregates. Following this procedure, adsorbent solution (2 mL, 1 g L^{-1}), GenX solution (4 mL, 1 mg L^{-1}) and Milli-Q water (14 mL) were added to a 20 mL polypropylene scintillation vial to generate an initial GenX concentration of $200 \mu\text{g L}^{-1}$ and adsorbent concentration of 100 mg L^{-1} . To generate an initial GenX concentration of 50 mg L^{-1} and adsorbent concentration of 100 mg L^{-1} , adsorbent solution (2 mL, 1 g L^{-1}), GenX solution (0.5 mL, 2 g L^{-1}) and Milli-Q water (17.5 mL) were added to a 20 mL polypropylene scintillation vial. Samples were collected in 1 mL volumes after 22 h and filtered with a $0.2 \mu\text{m}$ inorganic syringe filter (Whatman). Control experiments to account for GenX losses were performed in the same condition except for the addition of adsorbents, and samples were collected after 22 h. All batch experiments were performed with triplicates.

The efficiency of GenX removal by adsorbents was determined by **Eq. 2.S1**:

Equation 2.S1:

$$\text{GenX Removal} = \frac{C_0 - C_t}{C_0} * 100$$

where C_0 ($\mu\text{g L}^{-1}$) and C_t ($\mu\text{g L}^{-1}$) are the initial and residual concentration of GenX in the stock solution and filtrate, respectively.

The amount of pollutant bound to the sorbent was determined by **Eq. 2.S2**:

Equation 2.S2:

$$q_t = \frac{C_0 - C_t}{C_A}$$

where q_t (mg g^{-1}) is the amount of GenX adsorbed on the solid phase at any time t (h); C_0 ($\mu\text{g L}^{-1}$) is the average concentration of GenX in the samples of the control experiments; C_t ($\mu\text{g L}^{-1}$) is the concentration of GenX in the liquid phase at any sample time t (h); and C_A (mg L^{-1}) is the concentration of adsorbent. The batch kinetics can be described with Ho and McKay's pseudo-second-order adsorption model in a linearized form by **Eq. 2.S3**:

Equation 2.S3:

$$\frac{t}{q_t} = \frac{t}{q_e} + \frac{1}{k_{obs}q_e^2}$$

where q_e (mg g^{-1}) is the amount of GenX adsorbed on the solid phase at equilibrium; and k_{obs} ($\text{g}/(\text{mg}^2\text{h})$) is the rate constant of adsorption.

II. Kinetic adsorption studies

The batch kinetic experiments at $200 \mu\text{g L}^{-1}$ of GenX (**Figure 2.S15**) were performed in 20 mL polypropylene scintillation vials with magnetic stir bars. The experiments were conducted at 23–24 °C on a stirring hot plate with the stirring rate at 500 revolutions per minute (rpm). The adsorbent dose was 400 mg L^{-1} and GenX stock solution was spiked to generate an initial concentration of 0.2 mg L^{-1} .

Prior to GenX adsorption experiments, vacuum-dried adsorbents were rehydrated. 8 mg of adsorbent was added into a polypropylene vial with 16 mL Milli-Q water to yield a 500 mg L^{-1} suspension. The suspensions were sonicated for 1 minute and stirred on a multi-position stirrer for 2 h at 500 rpm to disperse small aggregates. Following this procedure, GenX solution (4 mL, 1 mg L^{-1}) was added to each suspension. Samples were collected in 1 mL volumes at predetermined sampling times (0, 0.5, 1, 5, 10 min and 22 h) and filtered with a $0.2 \mu\text{m}$ inorganic syringe filter (Whatman). Control experiments to account for GenX losses were performed in the same condition except for the addition of adsorbents, and samples were collected after 22 h. All batch experiments were performed with triplicates.

III. Isotherm adsorption studies.

The batch isotherm experiments (**Figure 2.S19–2.S20**) were performed in 20 mL polypropylene vials with magnetic stir bars. The experiments were conducted at 23–24 °C on a stirring hot plate with the stirring rate at 500 revolutions per minute (rpm). The adsorbent dose was 100 mg L^{-1} and GenX stock solution was spiked to generate initial concentrations of 0.2, 1, 10, 20, 30, 50, 100 mg L^{-1} . The suspensions were stirred for 22 h to reach the equilibrium, then filtered by $0.2 \mu\text{m}$

inorganic syringe filters (Whatman) to remove any remaining solid. Control experiments to account for GenX losses were performed in the same condition except for the addition of adsorbents, and samples were collected at 22 h. All batch experiments were performed with triplicates.

Langmuir adsorption and Freundlich isotherm fits were generated by Non-linear Least Square Regression in **Eq. 2.S4** and **2.S5**:

Equation 2.S4:

$$\frac{1}{q_e} = \frac{1}{q_m} + \frac{1}{C_e \times q_m \times K_L}$$

where q_e (mg g^{-1}) is the amount of GenX adsorbed at equilibrium. q_m (mg g^{-1}) is the maximum adsorption capacity of adsorbent at equilibrium. C_e (mg L^{-1}) is the residual GenX concentration at equilibrium. K_L (L mg^{-1}) is the equilibrium constant.

Equation 2.S5:

$$q_e = K_F C_e^{\frac{1}{n}}$$

where q_e (mg g^{-1}) is the amount of GenX adsorbed at equilibrium. C_e (mg L^{-1}) is the residual GenX concentration at equilibrium. K_F ($\text{mg g}^{-1}(\text{L mg}^{-1})^{1/n}$) is the Freundlich constant. n is an indicator of the intensity of the adsorption.

IV. Low concentration kinetics and equilibrium studies

The batch experiments at $1 \mu\text{g L}^{-1}$ of PFAS (**Figure 2.3**) were performed in 125 mL polypropylene flasks with magnetic stir bars. The experiments were conducted at $23 \text{ }^{\circ}\text{C}$ on a stirring hot plate with the stirring rate at 460 revolutions per minute (rpm). The adsorbent dose was 10 mg L^{-1} and PFAS stock solution was spiked to generate an initial concentration of $1 \mu\text{g L}^{-1}$.

Prior to experiments, vacuum-dried adsorbents were rehydrated as described in the preceding. Samples were collected in 8 mL volumes at predetermined sampling times (0, 0.5, 1, 5, 10, 30, 60 min and 24 h) and filtered with a $0.45 \mu\text{m}$ cellulose acetate filter (Restek). Control experiments to account for PFAS losses were performed in the same condition except for the addition of adsorbents, and samples were collected at each time point. All batch experiments were performed with triplicates.

V. Regeneration Studies

Adsorption Experiments: 20 mg of adsorbent (**28% $[\text{NH}_2]$ -COF**) was added to a polypropylene vial with 20 mL Milli-Q water to yield a 1 g L^{-1} suspension. The suspensions were sonicated for 1 min and stirred on a multi-position stirrer for 1 h at 500 rpm to disperse small aggregates. Following this procedure, adsorbent solution (2 mL, 1 g L^{-1}) was passed through a 10 mL syringe fitted with a $0.2 \mu\text{m}$ hydrophilic PTFE filter (Chromafil) to pack the adsorbent into the filter. A GenX solution (2 mL, 10 mg L^{-1}) was then passed through the syringe for 10 seconds and the GenX concentration of the filtrate was measured by LC-MS.

Desorption Experiments: GenX-loaded adsorbent in the syringe filter was regenerated by washing the adsorbent in the filter with 2 mL of Milli-Q water and by passing 10 mL of CH₃OH through the filter for 10 seconds. The CH₃OH filtrate was concentrated under vacuum, and the residual solid was dissolved in Milli-Q water and measured by LC-MS to determine the concentration of recovered GenX.

2.7.4 Additional Characterization

Table 2.S1 The C, H, and N elemental analysis of X%[N₃]-COFs

COF (Type)		C [%]	N [%]	H [%]
100%[N₃]-COF	Theoretical	65.07	18.97	5.12
	Experimental	64.10 ± 0.07	17.9 ± 0.2	5.33 ± 0.01
75%[N₃]-COF	Theoretical	68.49	17.31	4.91
	Experimental	67.6 ± 0.2	16.4 ± 0.2	5.26 ± 0.06
50%[N₃]-COF	Theoretical	72.81	15.17	5.02
	Experimental	70.38 ± 0.03	14.7 ± 0.2	5.22 ± 0.06
28%[N₃]-COF	Theoretical	77.87	12.74	4.96
	Experimental	74.4 ± 0.4	11.90 ± 0.2	5.2 ± 0.1
20%[N₃]-COF	Theoretical	80.06	11.67	4.93
	Experimental	78.6 ± 0.2	11.2 ± 0.4	5.2 ± 0.4
10%[N₃]-COF	Theoretical	83.15	10.17	4.90
	Experimental	79.3 ± 0.1	9.7 ± 0.1	5.2 ± 0.1
1%[N₃]-COF	Theoretical	86.34	8.61	4.86
	Experimental	82.9 ± 0.4	8.5 ± 0.1	5.1 ± 0.1

Table 2.S2 The C, H, and N elemental analysis of **X%[NH₂]-COFs**

COF (Type)		C [%]	N [%]	H [%]
100%[NH₂]-COFs	Theoretical	71.35	10.40	6.36
	Experimental	70.3 ± 0.4	9.35 ± 0.04	6.56 ± 0.05
75%[NH₂]-COFs	Theoretical	73.89	10.06	6.10
	Experimental	71.84 ± 0.06	9.20 ± 0.09	6.5 ± 0.1
50%[NH₂]-COFs	Theoretical	77.22	9.65	5.79
	Experimental	74.4 ± 0.2	9.12 ± 0.08	5.97 ± 0.04
28%[NH₂]-COFs	Theoretical	80.78	9.19	5.44
	Experimental	78.22 ± 0.06	9.1 ± 0.1	5.53 ± 0.03
20%[NH₂]-COFs	Theoretical	82.29	9.00	5.29
	Experimental	79.8 ± 0.2	8.86 ± 0.04	5.4 ± 0.1
10%[NH₂]-COFs	Theoretical	84.38	8.73	5.08
	Experimental	81.44 ± 0.04	8.8 ± 0.1	5.11 ± 0.06
1%[NH₂]-COFs	Theoretical	86.47	8.46	4.88
	Experimental	83.0 ± 0.2	8.5 ± 0.2	5.01 ± 0.06

Table 2.S3 Surface areas and pore sizes of **X%[N₃]-COFs** and **X%[NH₂]-COFs**. The errors in the BET surface areas were determined from the standard deviation of independently prepared samples.

COF (Type)	S _{BET} (m ² /g)	Pore Size (nm)	Pore Volume (cm ³ /g)	Number of Samples
100%[N₃]-COF	1100 ± 150	2.6	0.66	14
75%[N₃]-COF	1200 ± 200	2.7	0.75	3
50%[N₃]-COF	1450 ± 30	2.7	0.90	3
28%[N₃]-COF	1600 ± 100	3.0	0.95	2
20%[N₃]-COF	1600 ± 80	3.0	1.03	3
10%[N₃]-COF	1900 ± 100	3.1	1.08	2
1%[N₃]-COF	2000 ± 400	3.2	1.69	2
0%[N₃]-COF	2000 ± 20	3.4	1.44	2
100%[NH₂]-COF	1000 ± 70	2.6	0.59	3
75%[NH₂]-COF	1500 ± 100	2.6	0.87	3
50%[NH₂]-COF	1600 ± 100	3.0	0.93	3
28%[NH₂]-COF	1900 ± 200	3.0	1.06	3
20%[NH₂]-COF	1800 ± 50	3.0	1.22	2
10%[NH₂]-COF	1900 ± 20	3.2	1.25	2
1%[NH₂]-COF	2033	3.2	1.44	1

Table 2.S4 Zeta potential measurements

COF (Type)	Zeta Potential (mV)
100%[N₃]-COF	- 7 ± 3
0%[N₃]-COF	- 6 ± 4
100%[NH₂]-COF	13 ± 5
75%[NH₂]-COF	6 ± 3
50%[NH₂]-COF	2 ± 7
28%[NH₂]-COF	5 ± 3

Table 2.S5 Langmuir and Freundlich Parameters Derived from Plots of the GenX Binding Isotherm.

COF	Langmuir Fit			Freundlich Fit		
	K _L (M ⁻¹)	Q _m (mg/g)	R ²	K _F (mg/g)(L/mg) ^{1/n}	n	R ²
100%[NH₂]-COF	7.2·10 ⁴	130	0.96	40	3.7	0.87
28%[NH₂]-COF	6.3·10 ⁴	200	0.99	64	3.6	0.97

Table 2.S6 Comparison of GenX kinetic and thermodynamic adsorption parameters by other adsorbents in literature. For this paper, the kinetic and adsorption parameters were determined at 23 °C.

Reference	Adsorbent	Matrix	Kinetic			Langmuir Isotherm	
			[Adsorbent] (mg L ⁻¹)	[PFAS] ₀ (mg L ⁻¹)	<i>k</i> _{obs} (g mg ⁻¹ h ⁻¹)	<i>Q</i> _m (mg g ⁻¹)	<i>K</i> _L (L mmol ⁻¹)
This Paper	100%[NH₂]-COF	Milli-Q	10	[GenX] ₀ = 0.001	8530	130	72
		Milli-Q	10	[PFHpA] ₀ = 0.001	9710	N/A	N/A
	28%[NH₂]-COF	Milli-Q	10	[GenX] ₀ = 0.001	16400	200	63
		Milli-Q	10	[PFHpA] ₀ = 0.001	6300	N/A	N/A
	1%[NH₂]-COF	Milli-Q	10	[GenX] ₀ = 0.001	1300	N/A	N/A
		Milli-Q	10	[PFHpA] ₀ = 0.001	3300	N/A	N/A
<i>Water Sci. Technol.</i> 2011 , <i>63</i> , 2106-2113. ³¹⁶	GAC	Milli-Q	1000	[PFHpA] ₀ = 5	0.457	N/A	N/A
<i>Chemosphere</i> 2016 , <i>144</i> , 2336-2342. ³¹⁷	GAC	Milli-Q	200	[PFHpA] ₀ = 10	5.10	41.3	15

The rates of adsorption were best described by Ho and McKay's pseudo second-order adsorption model,³¹⁸ which provides a figure-of-merit for how quickly an adsorbent reaches equilibrium, *k*_{obs}. Since there are no reported kinetics of GenX adsorption by other adsorbents, we compared the kinetics of perfluoroheptanoic acid (PFHpA) adsorption, which was the most similar to GenX among our chosen PFAS in terms of removal kinetics and equilibrium removal, with those by granular activated carbon (GAC) in literature. The *Q*_m of **28%[NH₂]-COF** is more than 2.7

times higher and K_L is more than 7.2 times greater than those of granular activated carbon (GAC) for PFHpA.³¹⁷

Table 2.S7 Desorption observed between the 60-minute and the 24-hour time points using $[PFAS]_0$ of $1 \mu\text{g L}^{-1}$ and $[COF]$ of 10 mg L^{-1} .

COF	PFAS	Removal % at 60 min	Removal % at 24 h	Desorption %
100%$[\text{NH}_2]$-COF	PFBA	47	35	12
	PFDoA	97	92	5
	PFTTrDA	97	90	7
1%$[\text{NH}_2]$-COF	PFBS	85	81	4
	PFBA	23	0	23
	PFHxA	63	0	63
	GenX	57	0	57
	PFHpA	81	28	53
	PFOA	90	51	39
	PFNA	93	69	24
	PFDA	95	73	22
	PFDoA	96	68	28
	PFBS	70	19	51
	PFHxS	93	65	28
	PFOS	96	89	7

Table 2.S8 Incorporation ratios estimated from quantitative IR analysis. Normalized azide absorbance at 2098 cm^{-1} to the imine at 1618 cm^{-1} was used for estimation. Errors show the standard deviation of three independent measurements.

Feed Ratios (%)	Calculated Incorporation Ratios (%)
75	75 ± 2
50	50 ± 3
25	28 ± 2
17	20 ± 2
8	10 ± 2
1	1 ± 1

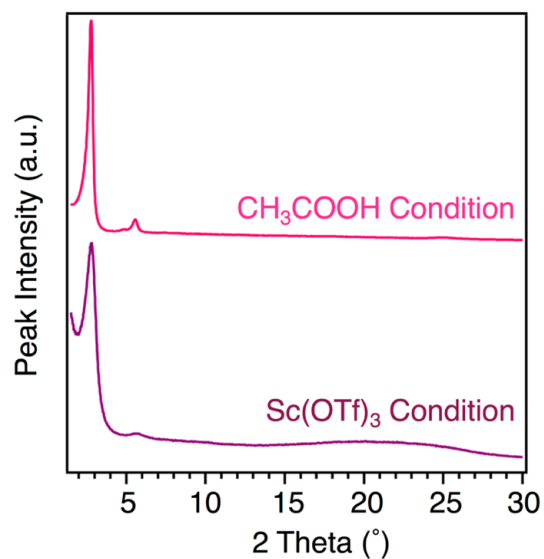


Figure 2.S1 PXRD patterns of **100%[N₃]-COF** using 6M CH₃CO₂H (pink) or Sc(OTf)₃ (purple)³¹⁹ as a catalyst. The patterns are normalized at the (100) peak at 2.8°.

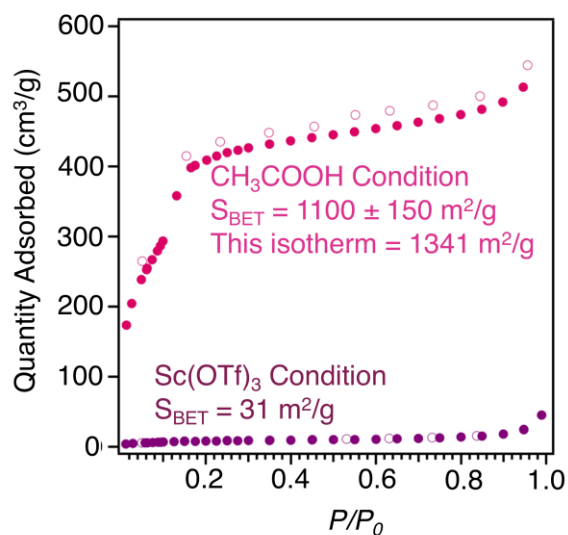


Figure 2.S2 N₂ adsorption isotherm of **100%[N₃]-COF** using 6M CH₃CO₂H (pink) or Sc(OTf)₃ (purple)³¹⁹ as a catalyst. Solid and open circles represent the adsorption and desorption branches, respectively.

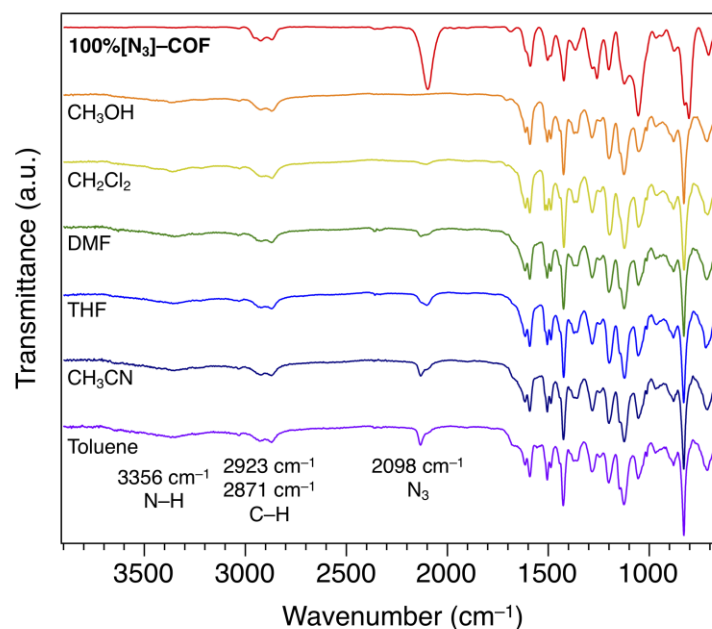


Figure 2.S3 Fourier transform-infrared (FT-IR) spectra of **100% $[N_3]$ -COF** (red) and **100% $[NH_2]$ -COF** after the Staudinger reaction in CH_3OH (orange), CH_2Cl_2 (yellow), DMF (green), THF (blue), CH_3CN (indigo), and toluene (purple). The traces of the colors are being described from top-to-bottom.

The extent of reduction in **X% $[NH_2]$ -COFs** was highly solvent-dependent. The reduction performed in CH_2Cl_2 , DMF, THF, CH_3CN , and toluene did not go to completion after 24 hours, as evidenced by the small azide stretch (**Figure 2.S3**). Quantitative conversion of azides to amines was achieved only in CH_3OH , consistent with previous reports.^{320, 321}

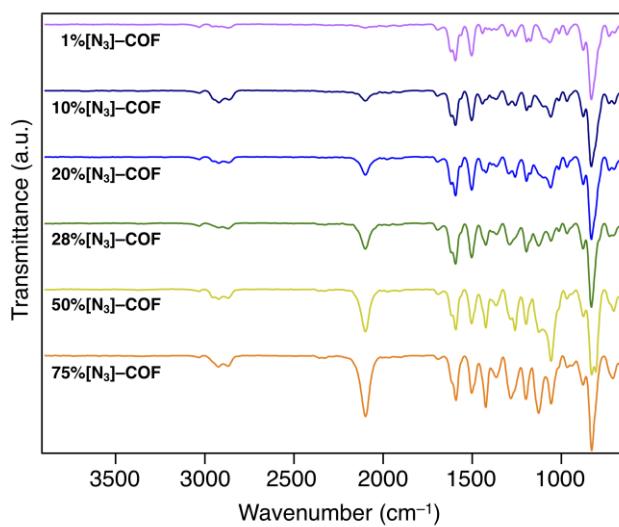


Figure 2.S4 Fourier transform-infrared (FT-IR) spectra of $X\%[\text{N}_3]\text{-COFs}$ corresponding to the concentration of azides or amines (X) of **75%** (orange), **50%** (yellow), **28%** (green), **20%** (blue), **10%** (indigo), **1%** (purple). The traces of the colors are being described from bottom-to-top.

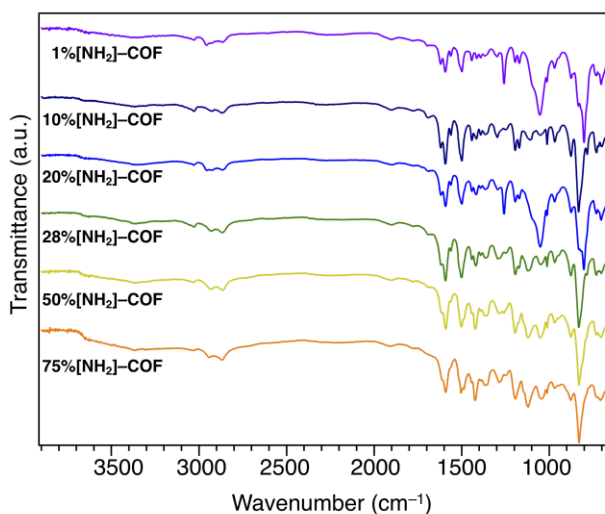


Figure 2.S5 Fourier transform-infrared (FT-IR) spectra of $X\%[\text{NH}_2]\text{-COFs}$ corresponding to the concentration of azides or amines (X) of **75%** (orange), **50%** (yellow), **28%** (green), **20%** (blue), **10%** (indigo), **1%** (purple). The traces of the colors are being described from bottom-to-top.

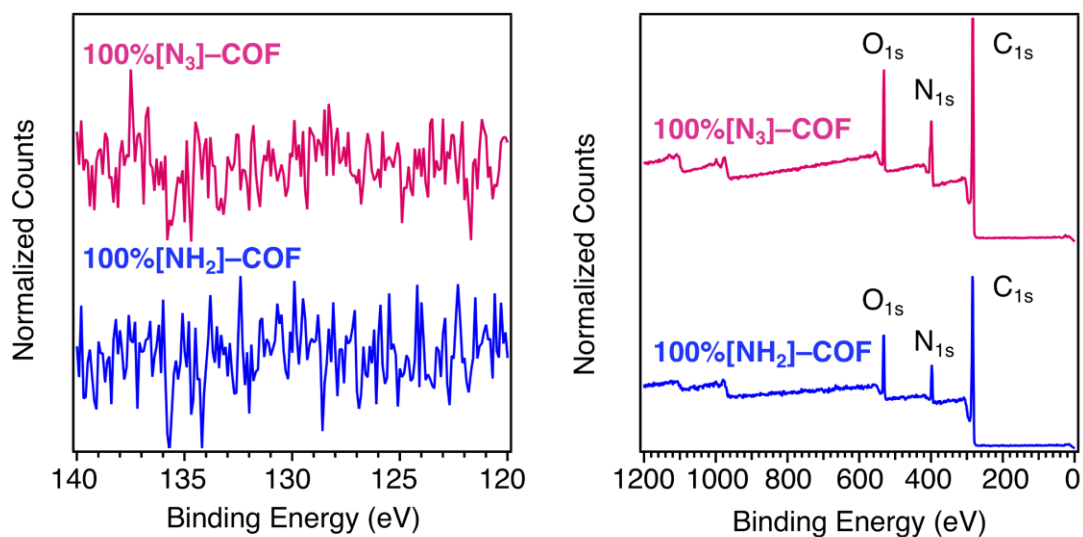


Figure 2.S6 X-ray photoelectron spectra of **100%[N₃]-COF** (pink) and **100%[NH₂]-COF** (blue).

Left shows X-ray photoelectron spectra of P 2p core level.

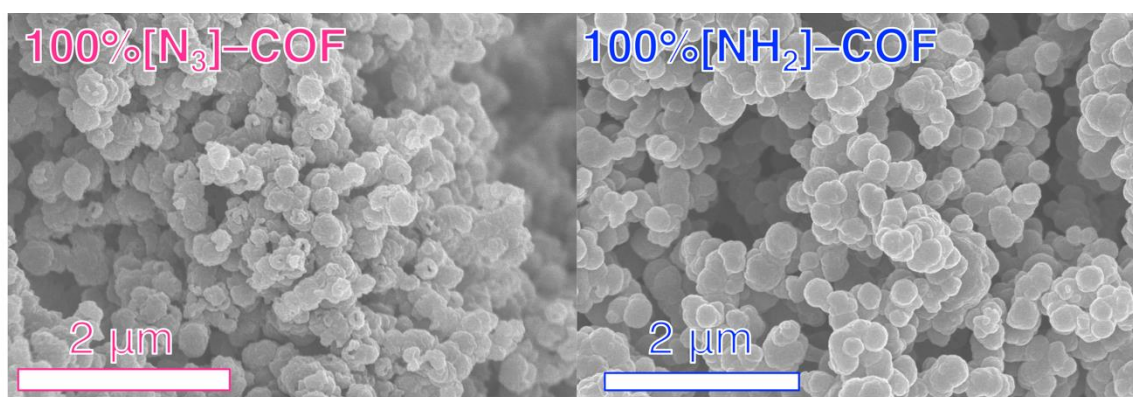


Figure 2.S7 Scanning electron microscopy (SEM) images of **100%[N₃]-COF** (pink) and **100%[NH₂]-COF** (blue).

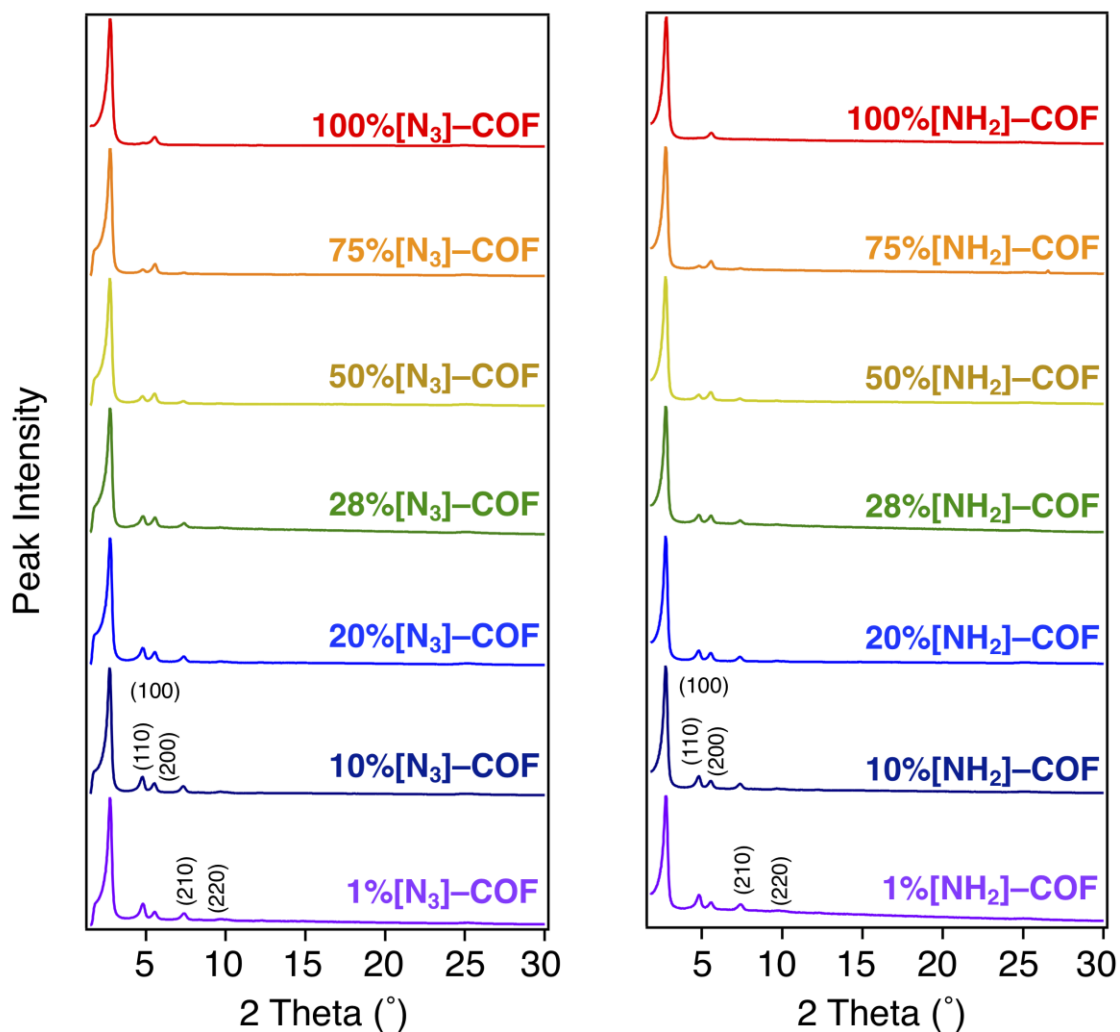


Figure 2.S8 Representative PXRD patterns of $X\%[N_3]$ -COFs and $X\%[NH_2]$ -COFs corresponding to the concentration of azides or amines (X) of **100%** (red), **75%** (orange), **50%** (yellow), **28%** (green), **20%** (blue), **10%** (indigo), and **1%** (purple) normalized at the (100) peak at 2.8° .

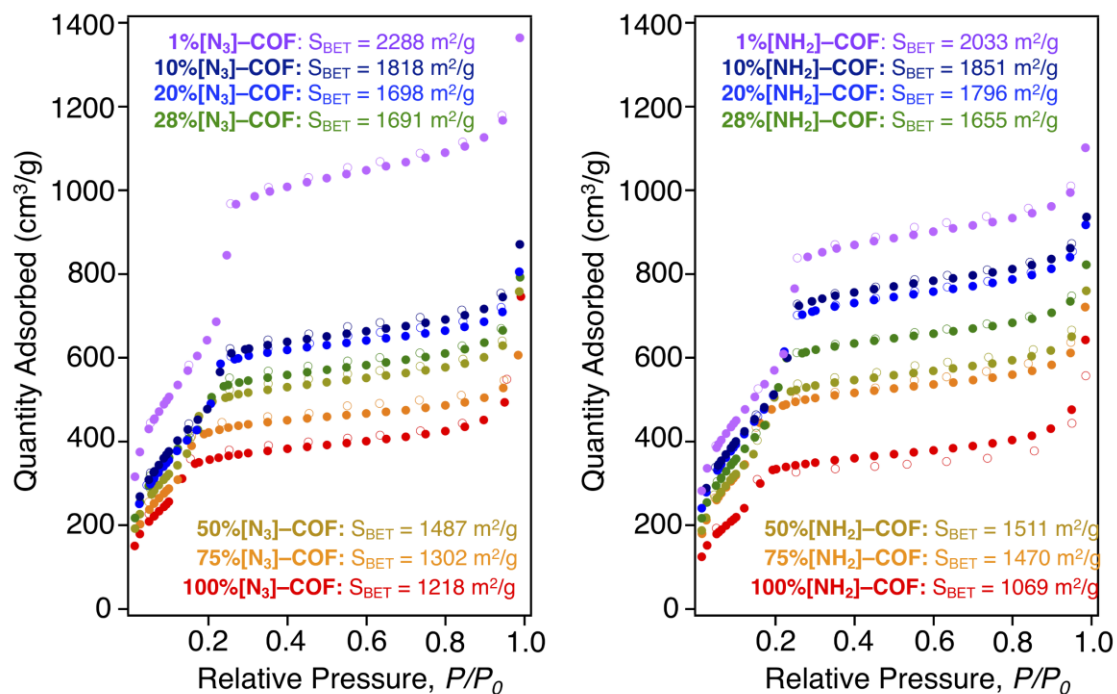


Figure 2.S9 Representative N_2 adsorption isotherms of $X\%[N_3]$ -COFs and $X\%[NH_2]$ -COFs corresponding to the concentration of azides or amines (X) of 100% (red), 75% (orange), 50% (yellow), 28% (green), 20% (blue), 10% (indigo), and 1% (purple). Solid and open circles represent the adsorption and desorption processes, respectively.

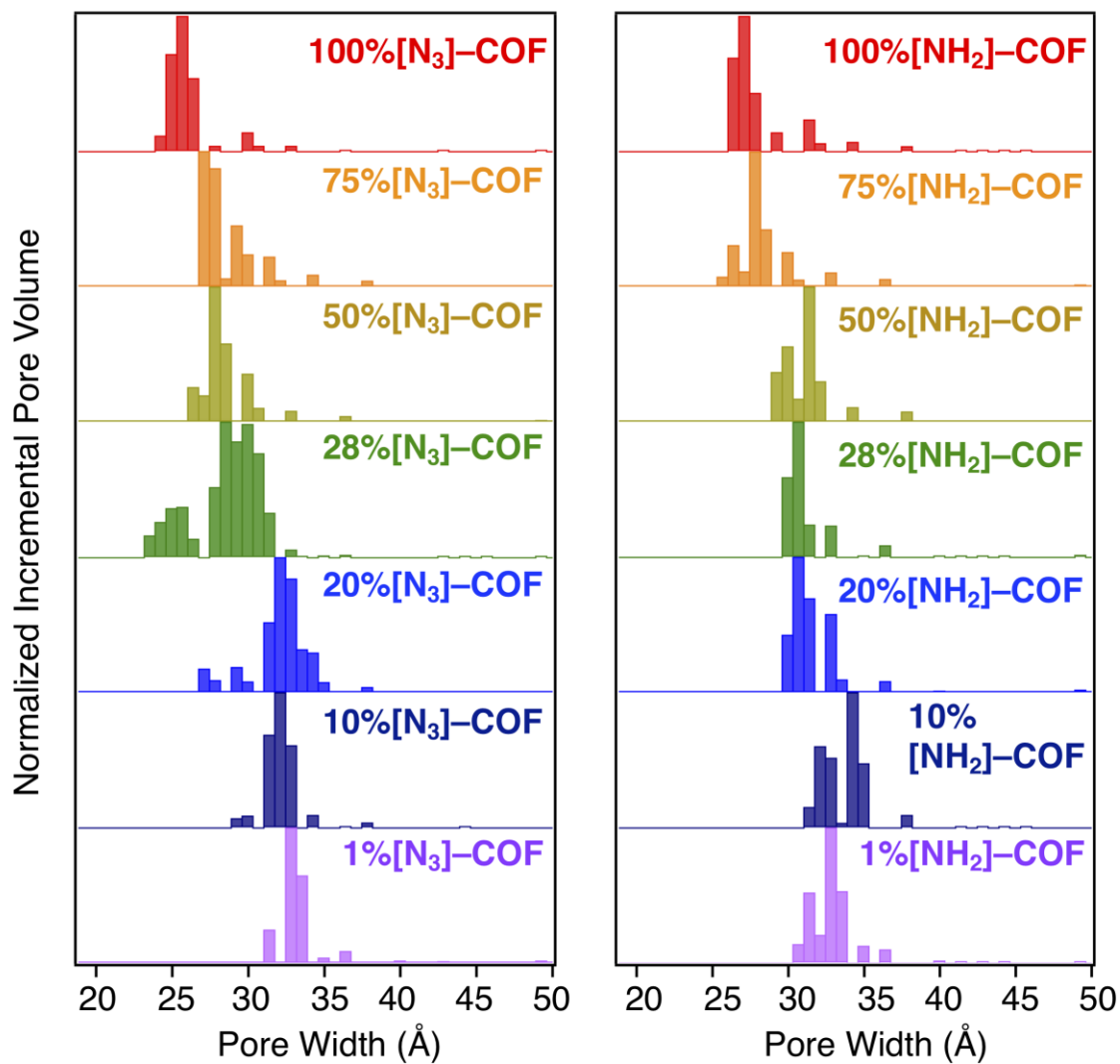


Figure 2.S10 Representative pore size distributions (determined from nonlocal density functional theory analysis of each nitrogen adsorption isotherm) of $X\%[\text{N}_3]\text{-COFs}$ and $X\%[\text{NH}_2]\text{-COFs}$ corresponding to the concentration of azides or amines (X) of 100% (red), 75% (orange), 50% (yellow), 28% (green), 20% (blue), 10% (indigo), and 1% (purple).

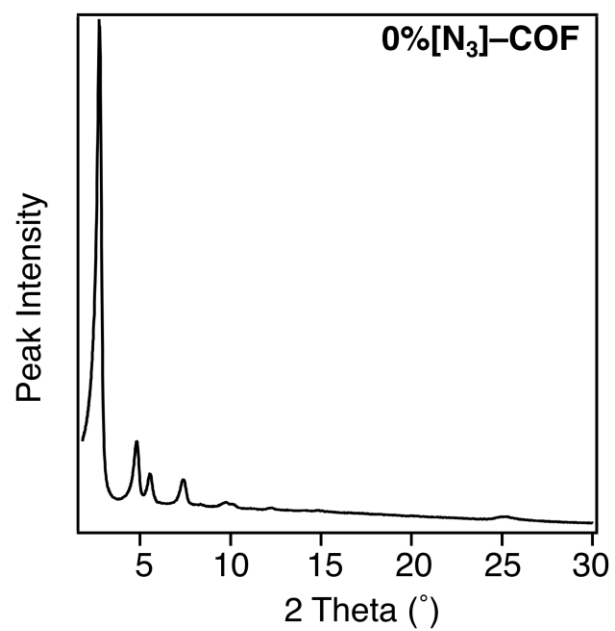


Figure 2.S11 PXRD pattern of 0%[N₃]-COF.

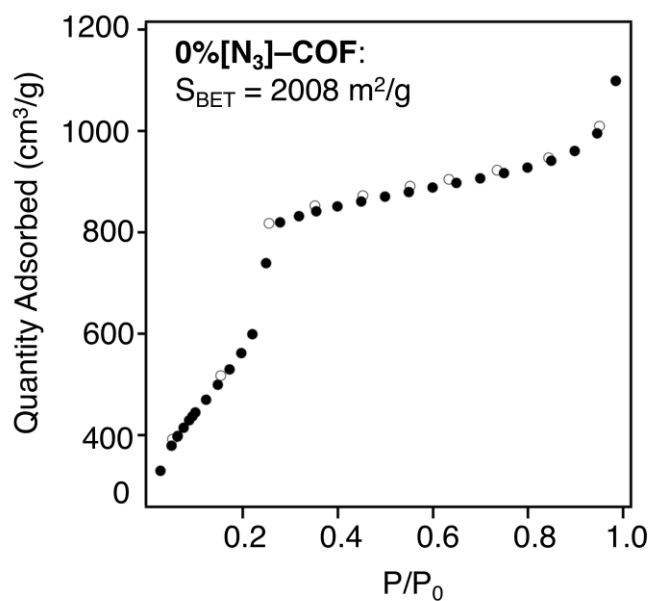


Figure 2.S12 N₂ adsorption isotherm of 0%[N₃]-COF. Solid and open circles represent the adsorption and desorption processes, respectively.

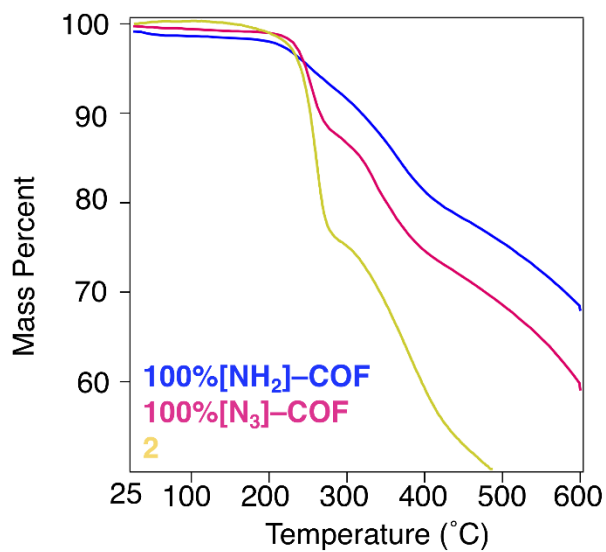


Figure 2.S13 Thermogravimetric Analysis (TGA) of **2** (yellow), **100% $[\text{N}_3]$ -COF** (pink) and **100% $[\text{NH}_2]$ -COF** (blue).

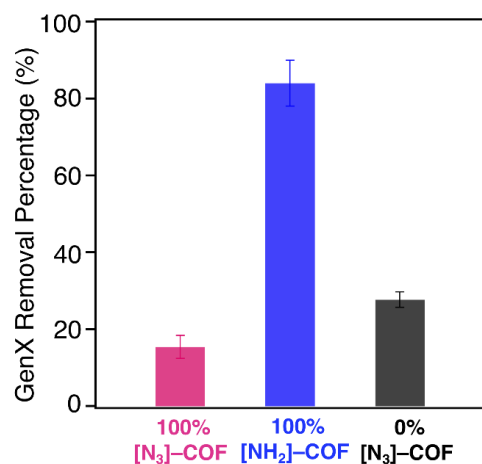


Figure 2.S14 GenX removal percentage ($[\text{GenX}]_0 = 200 \mu\text{g L}^{-1}$) by equal mass concentrations (400 mg L^{-1}) of **100% [N₃]-COF** (pink), **100% [NH₂]-COF** (blue) and **0% [N₃]-COF** (black) after the contact time of 22 h. Figures show average GenX removal percentages, and error bars show the standard deviation of three experiments.

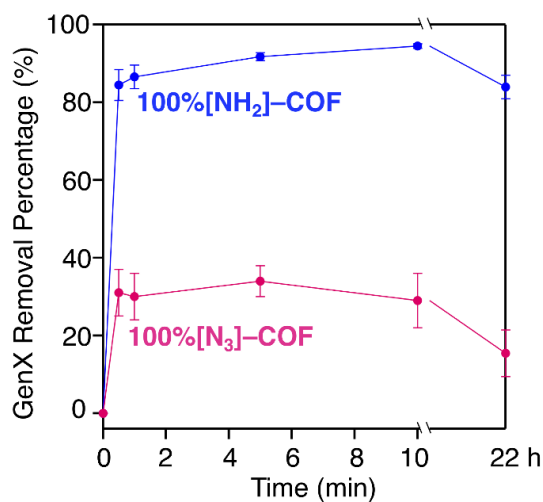


Figure 2.S15 Kinetics of GenX adsorption by **100% [N₃]-COF** (pink) and **100% [NH₂]-COF** (blue) ($[\text{GenX}]_0 = 200 \mu\text{g L}^{-1}$; $[\text{COF}] = 400 \text{ mg L}^{-1}$). Figures show average GenX removal percentages, and error bars show the standard deviation of three experiments.

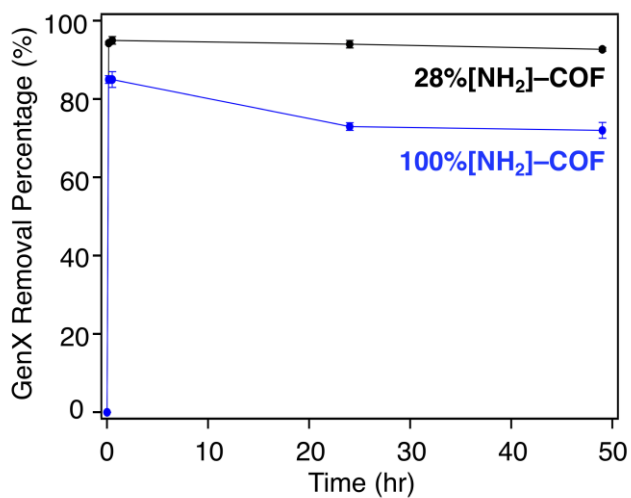


Figure 2.S16 Kinetics of GenX adsorption by $X\%[\text{NH}_2]\text{-COF}$ ($[\text{GenX}]_0 = 200 \mu\text{g L}^{-1}$; $[\text{COF}] = 100 \text{mg L}^{-1}$). Figures show average GenX removal percentages, and error bars show the standard deviation of three experiments.

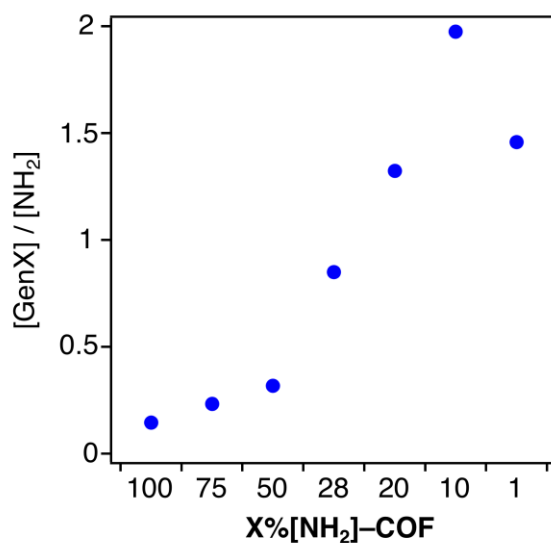


Figure 2.S17 The molar ratio of GenX to amines in $X\%[\text{NH}_2]\text{-COFs}$ ($[\text{GenX}]/[\text{NH}_2]$) calculated from Figure 2(b) at $[\text{GenX}]_0 = 50 \text{mg L}^{-1}$ by equal mass concentrations (100mg L^{-1}) of $X\%[\text{NH}_2]\text{-COFs}$ after the contact time of 22 h.

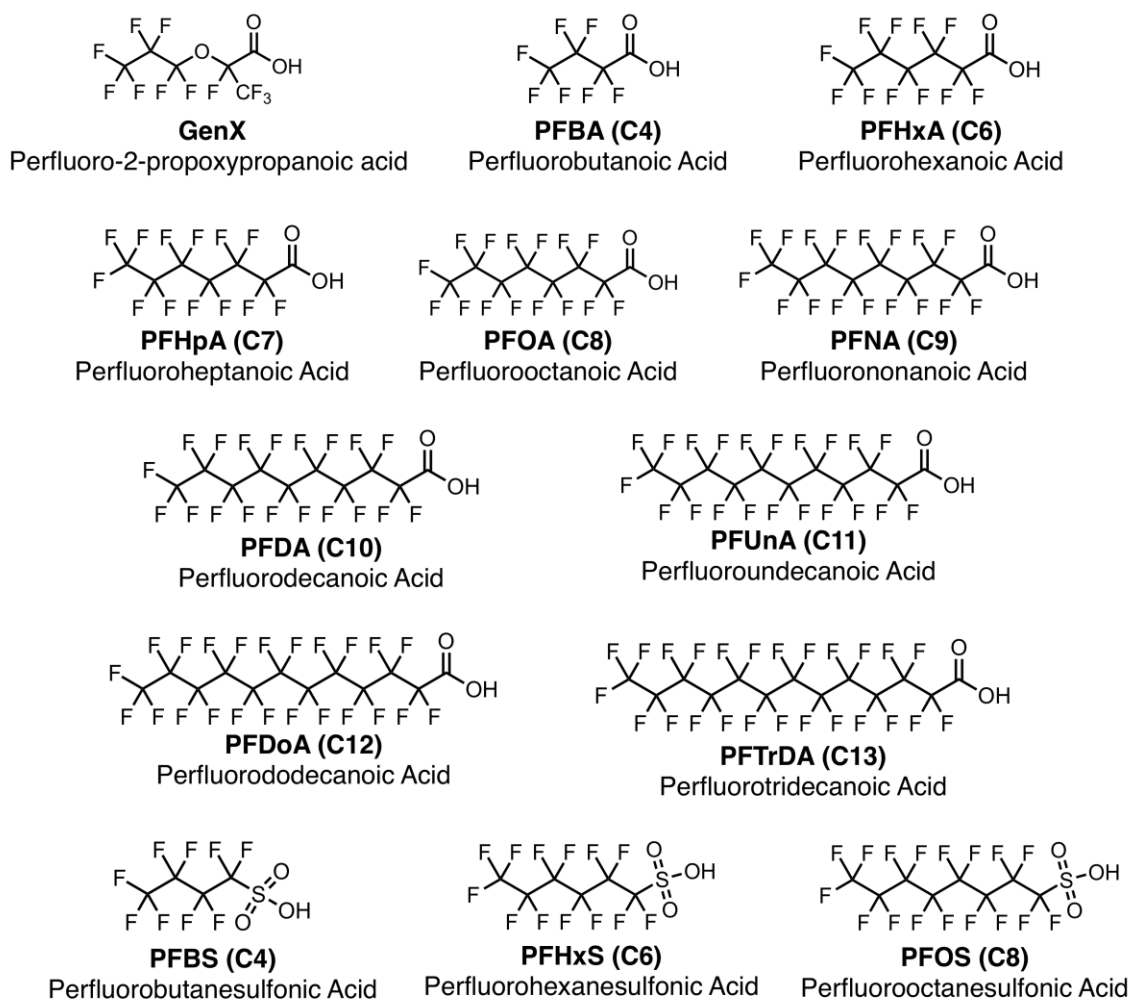


Figure 2.S18 A list of GenX and 12 perfluorinated alkyl substances (PFAS) tested in an adsorption experiment ($[\text{PFAS}]_0 = 1 \mu\text{g L}^{-1}$; $[\text{COF}] = 10 \text{mg L}^{-1}$).

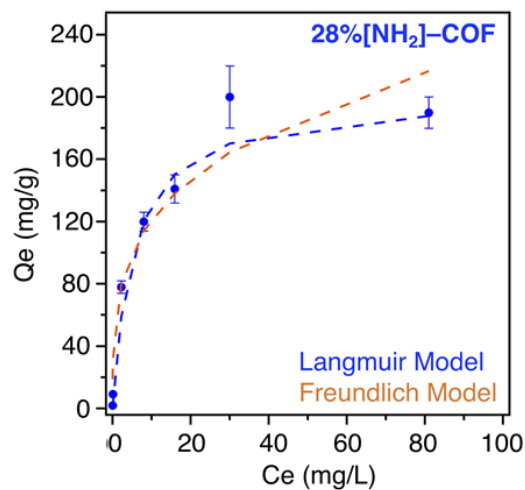


Figure 2.S19 GenX adsorption isotherm of **28%[NH₂]-COF** ($[\text{GenX}]_0 = 0.2\text{--}100 \text{ mg L}^{-1}$; $[\text{COF}] = 100 \text{ mg L}^{-1}$). Dotted lines show fits to Langmuir (blue) and Freundlich (orange) models. Error bars show the standard deviation of three experiments

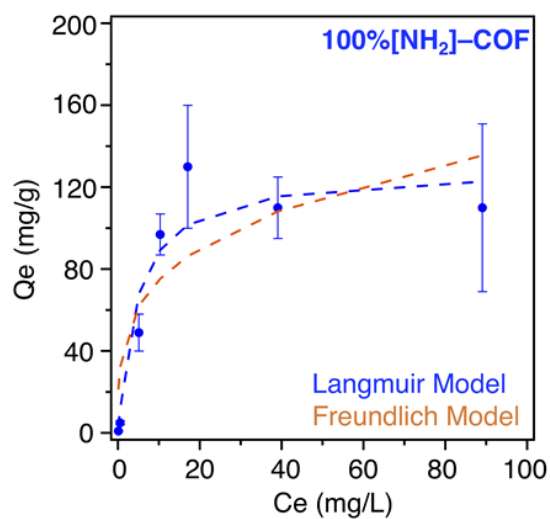


Figure 2.S20 GenX adsorption isotherm of **100%[NH₂]-COF** ($[\text{GenX}]_0 = 0.2\text{--}100 \text{ mg L}^{-1}$; $[\text{COF}] = 100 \text{ mg L}^{-1}$). Dotted lines show fits to Langmuir (blue) and Freundlich (orange) models. Error bars show the standard deviation of three experiments.

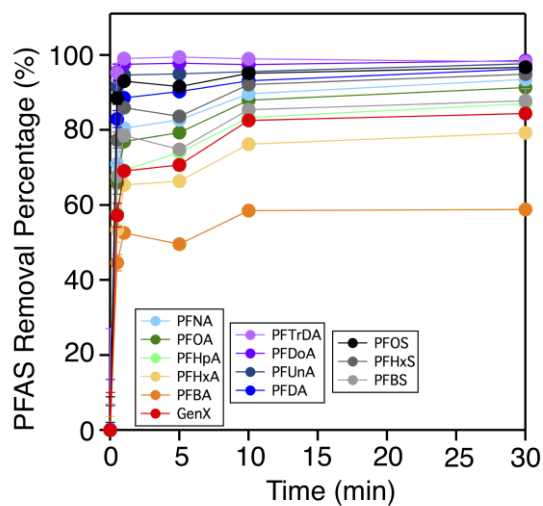


Figure 2.S21 Kinetics of GenX and PFAS adsorption by **100% $[\text{NH}_2]$ -COF** (Each $[\text{PFAS}]_0 = 1 \mu\text{g L}^{-1}$; $[\text{COF}] = 10 \text{ mg L}^{-1}$). Figure shows average PFAS removal percentages, and error bars show the standard deviation of three experiments.

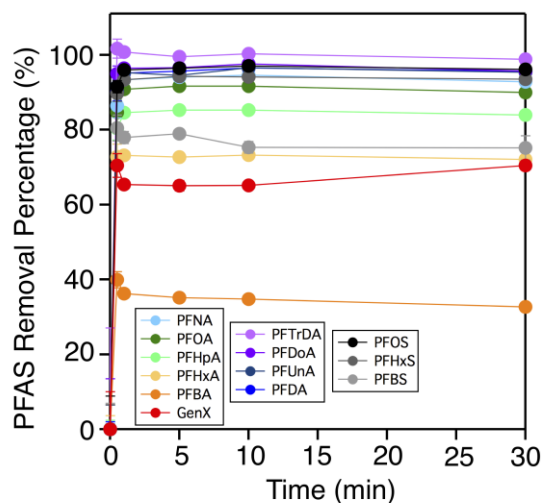


Figure 2.S22 Kinetics of GenX and PFAS adsorption by **1% $[\text{NH}_2]$ -COF** (Each $[\text{PFAS}]_0 = 1 \mu\text{g L}^{-1}$; $[\text{COF}] = 10 \text{ mg L}^{-1}$). Figure shows average PFAS removal percentages, and error bars show the standard deviation of three experiments.

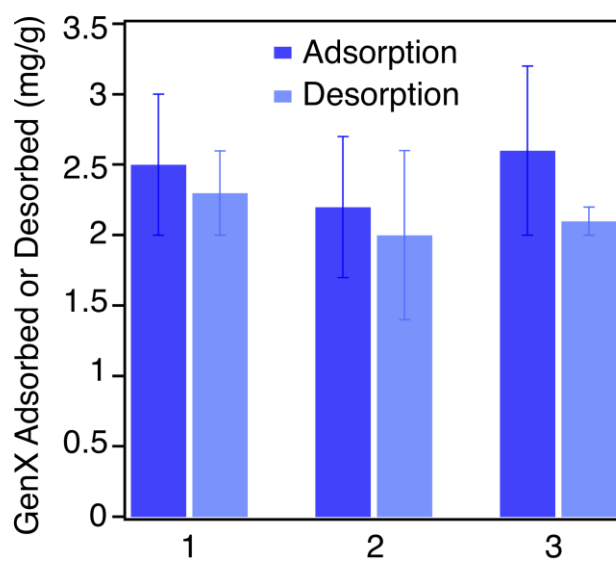


Figure 2.S23 Regeneration and reuse of 28% $[\text{NH}_2]$ -COF by washing with CH_3OH . Adsorption experiments: $[\text{GenX}]_0 = 10 \text{ mg L}^{-1}$, $[\text{COF}] = 2 \text{ mg}$, 10 sec. Desorption: COF was washed with CH_3OH for 10 sec. Error bars: standard deviation of 3 experiments.

2.7.5 Representative BET Plots for N₂ Isotherm

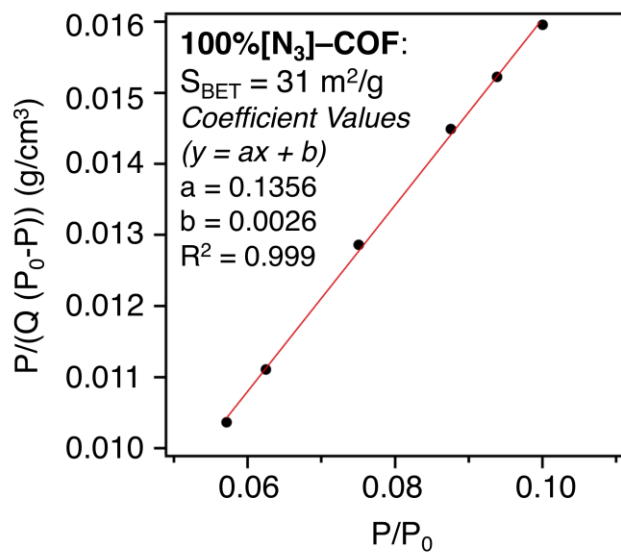


Figure 2.S24 BET plot for **100%[N₃]-COF** using $\text{Sc}(\text{OTf})_3$ as a catalyst.

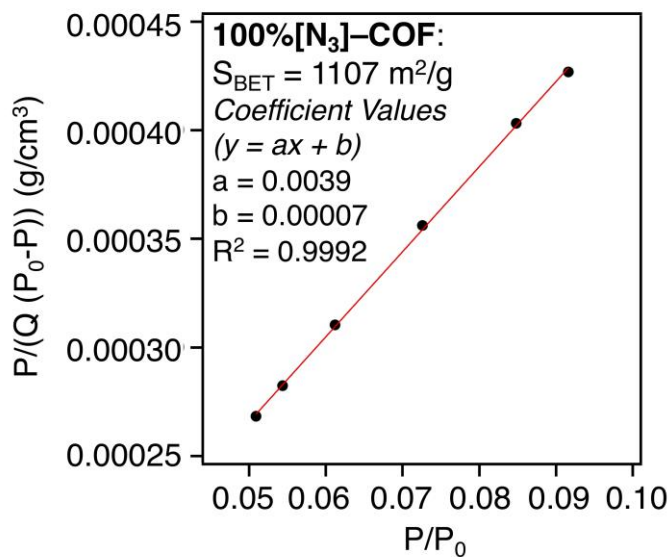


Figure 2.S25 BET plot for **100%[N₃]-COF** using 6M $\text{CH}_3\text{CO}_2\text{H}$ as a catalyst.

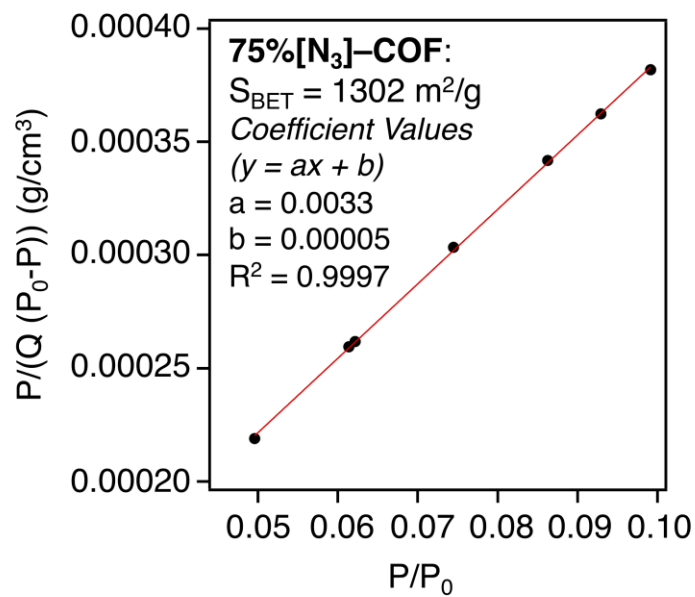


Figure 2.S26 BET plot for 75%[N₃]-COF.

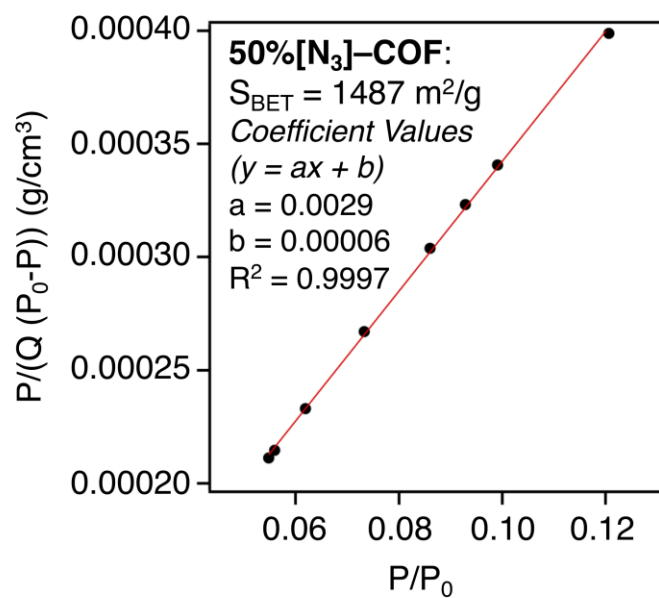


Figure 2.S27 BET plot for 50%[N₃]-COF.

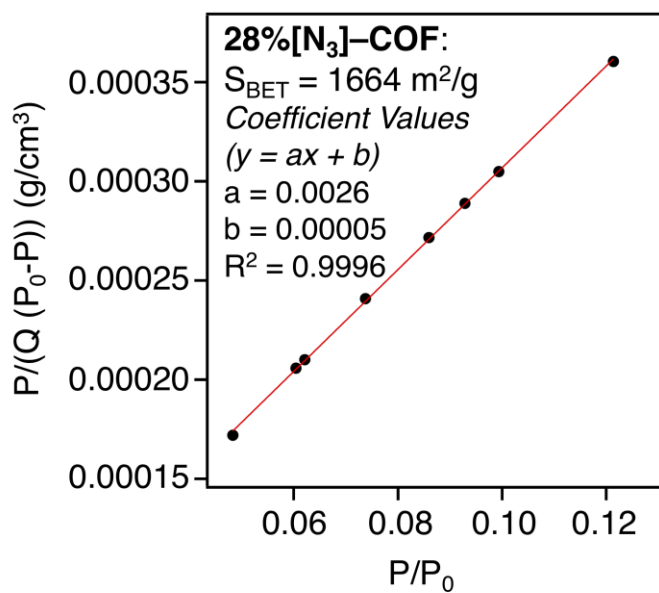


Figure 2.S28 BET plot for 28%[N₃]-COF.

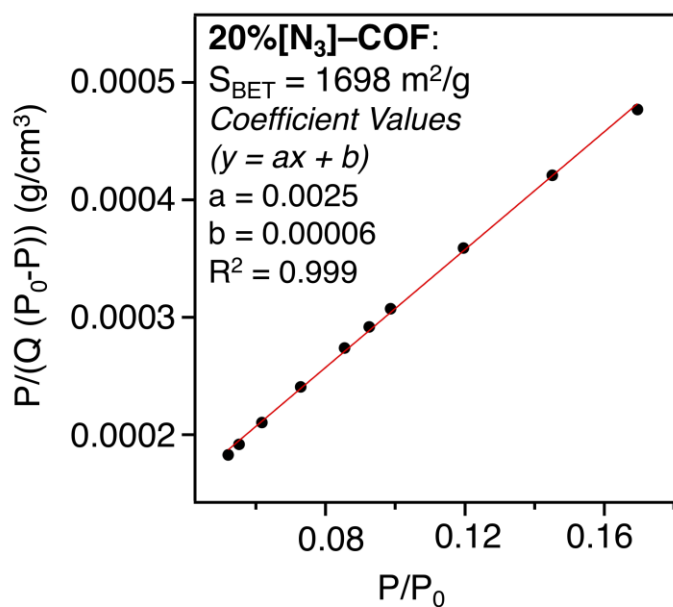


Figure 2.S29 BET plot for 20%[N₃]-COF.

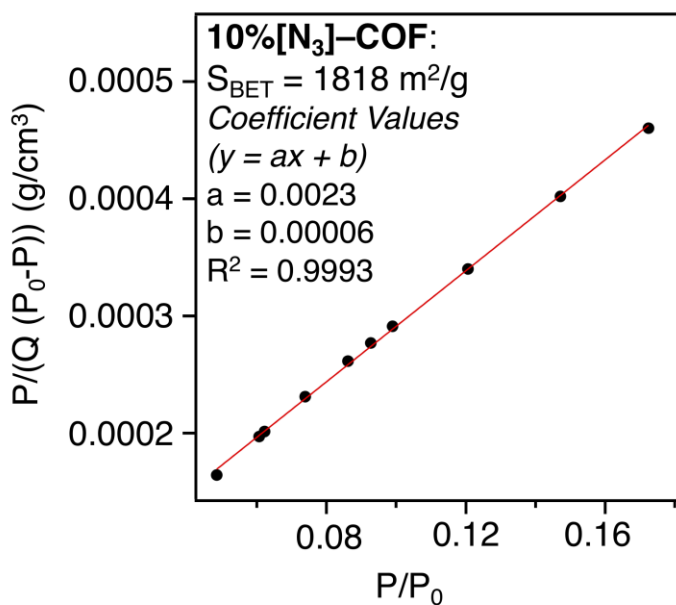


Figure 2.S30 BET plot for 10%[N₃]-COF.

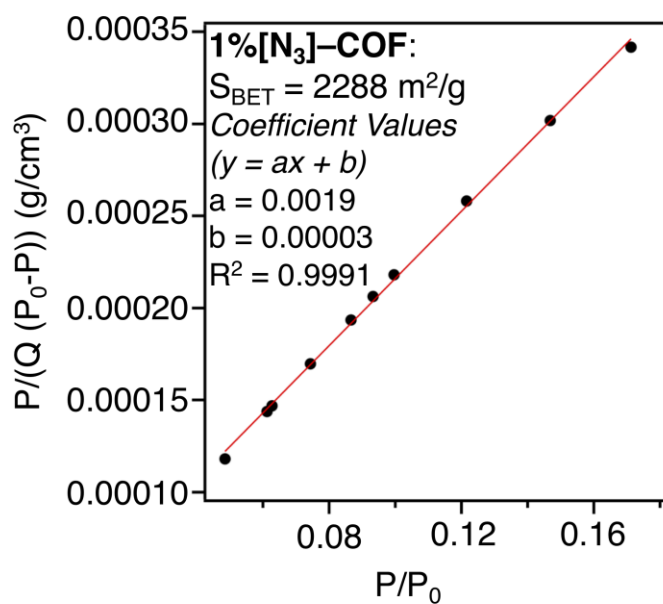


Figure 2.S31 BET plot for 1%[N₃]-COF.

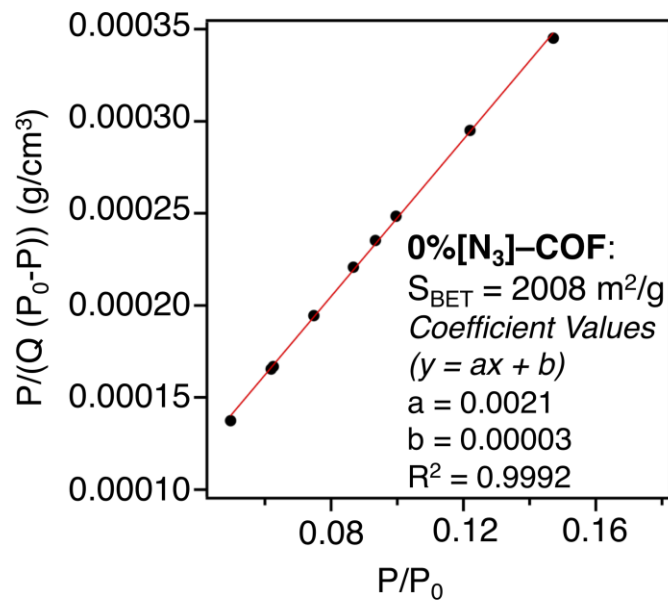


Figure 2.S32 BET plot for 0%[N₃]-COF.

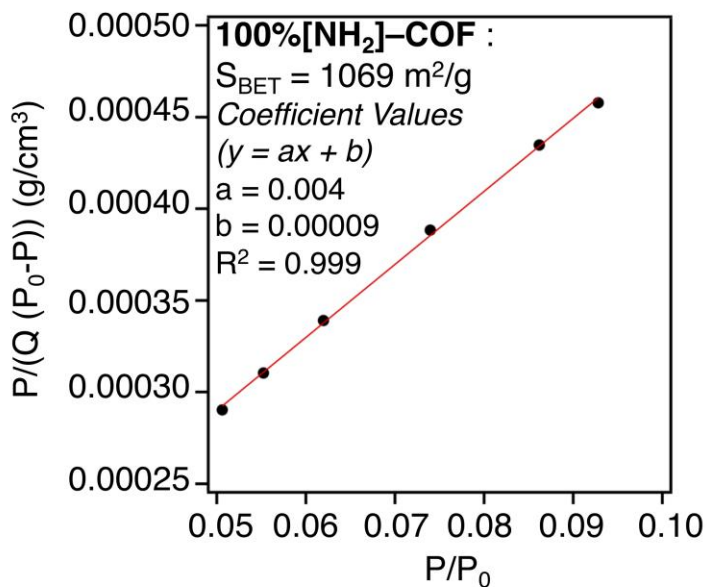


Figure 2.S33 BET plot for 100%[NH₂]-COF.

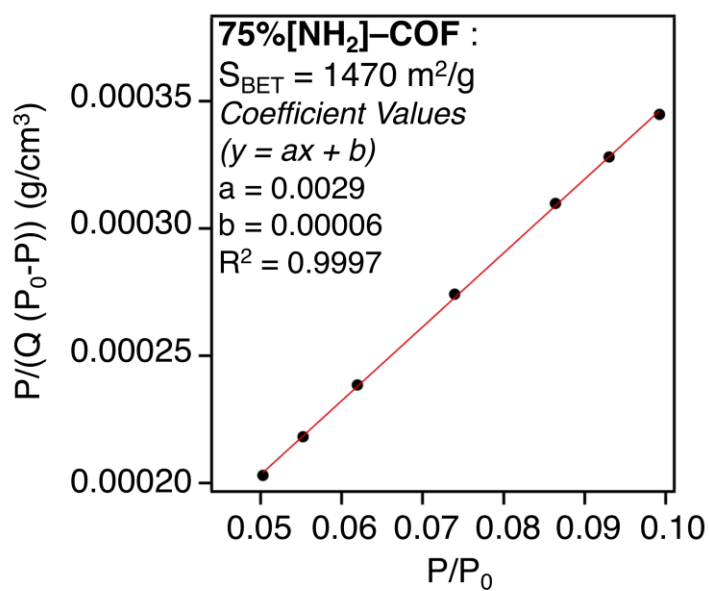


Figure 2.S34 BET plot for 75% $[\text{NH}_2]$ -COF.

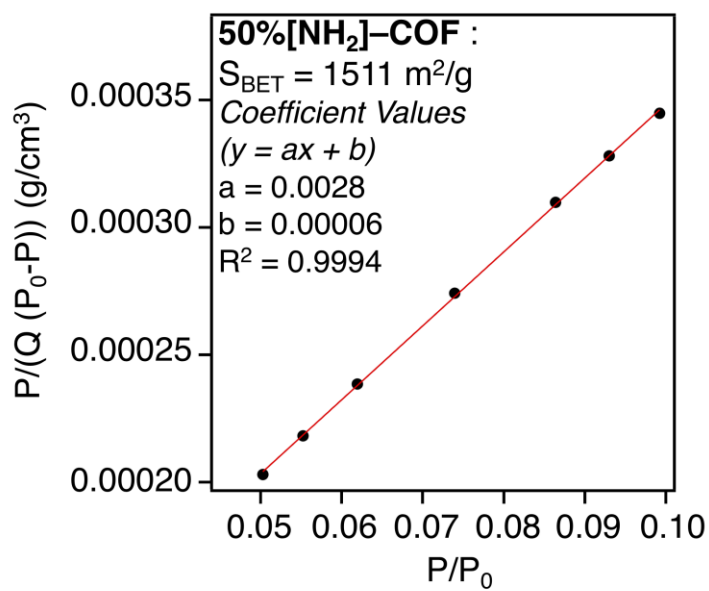


Figure 2.S35 BET plot for 50% $[\text{NH}_2]$ -COF.

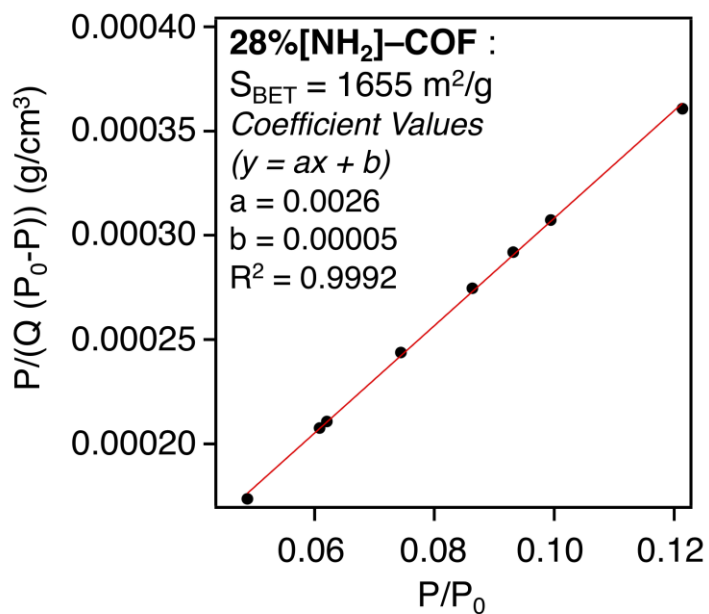


Figure 2.S36. BET plot for 28%[NH₂]-COF.

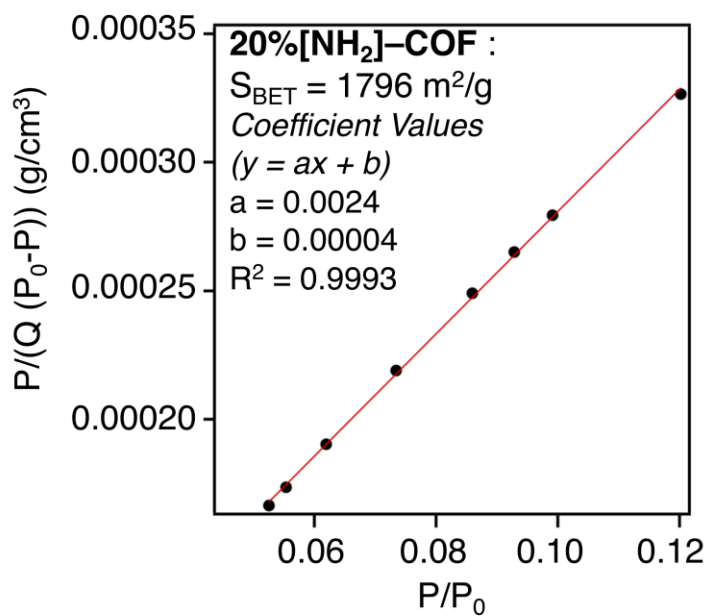


Figure 2.S37 BET plot for 20%[NH₂]-COF.

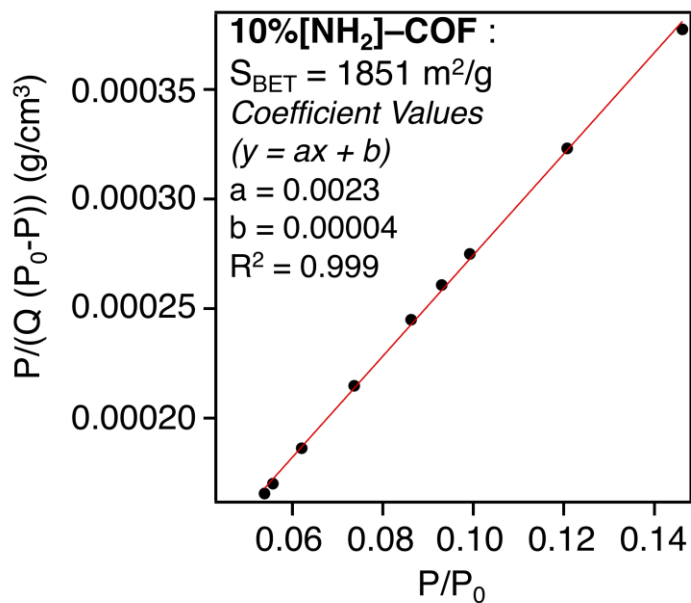


Figure 2.S38 BET plot for 10% $[\text{NH}_2]$ -COF.

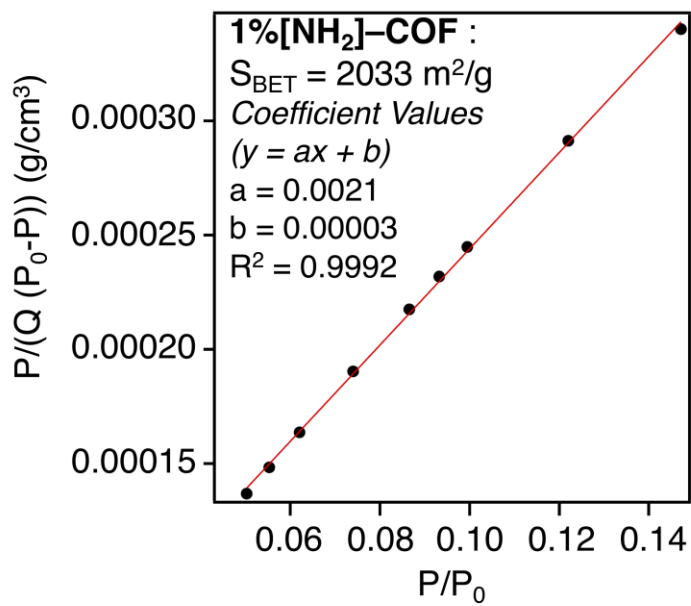


Figure 2.S39 BET plot for 1% $[\text{NH}_2]$ -COF.

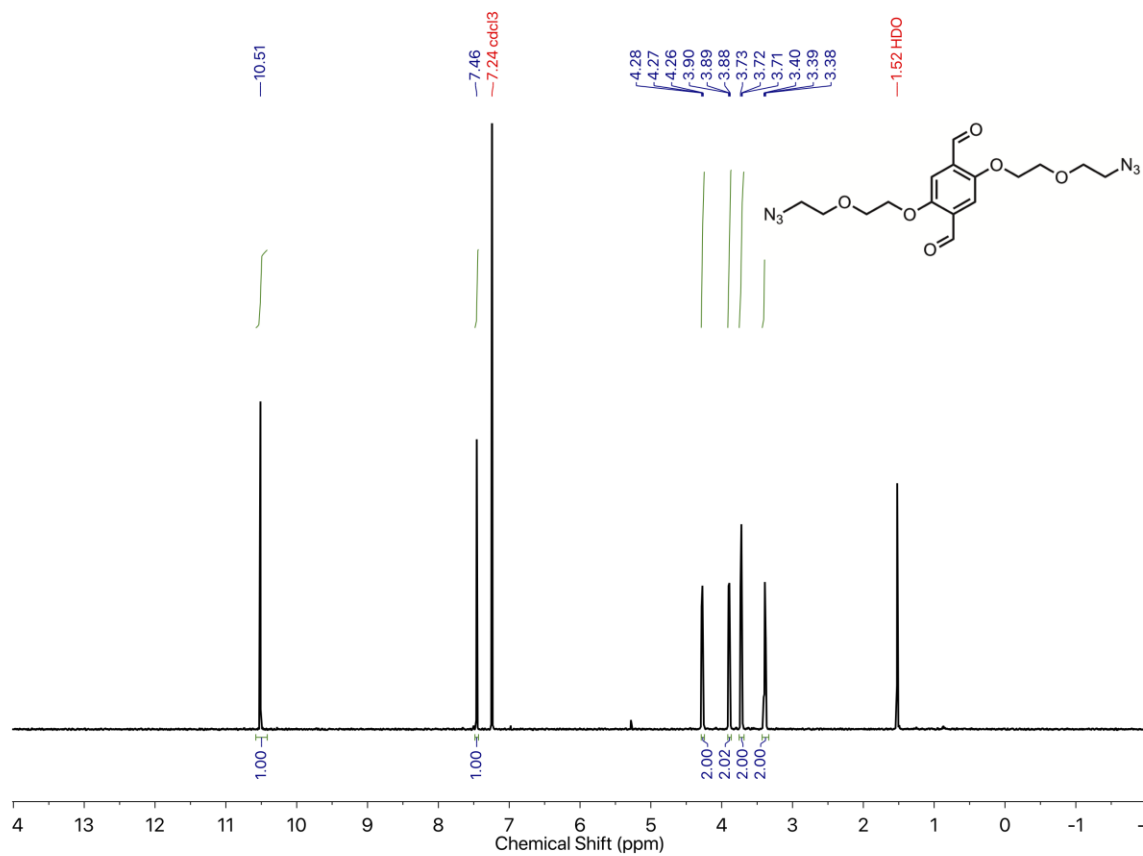
2.7.6 ^1H and ^{13}C NMR Spectra

Figure 2.S40 ^1H NMR spectrum of **2** in CDCl_3 .

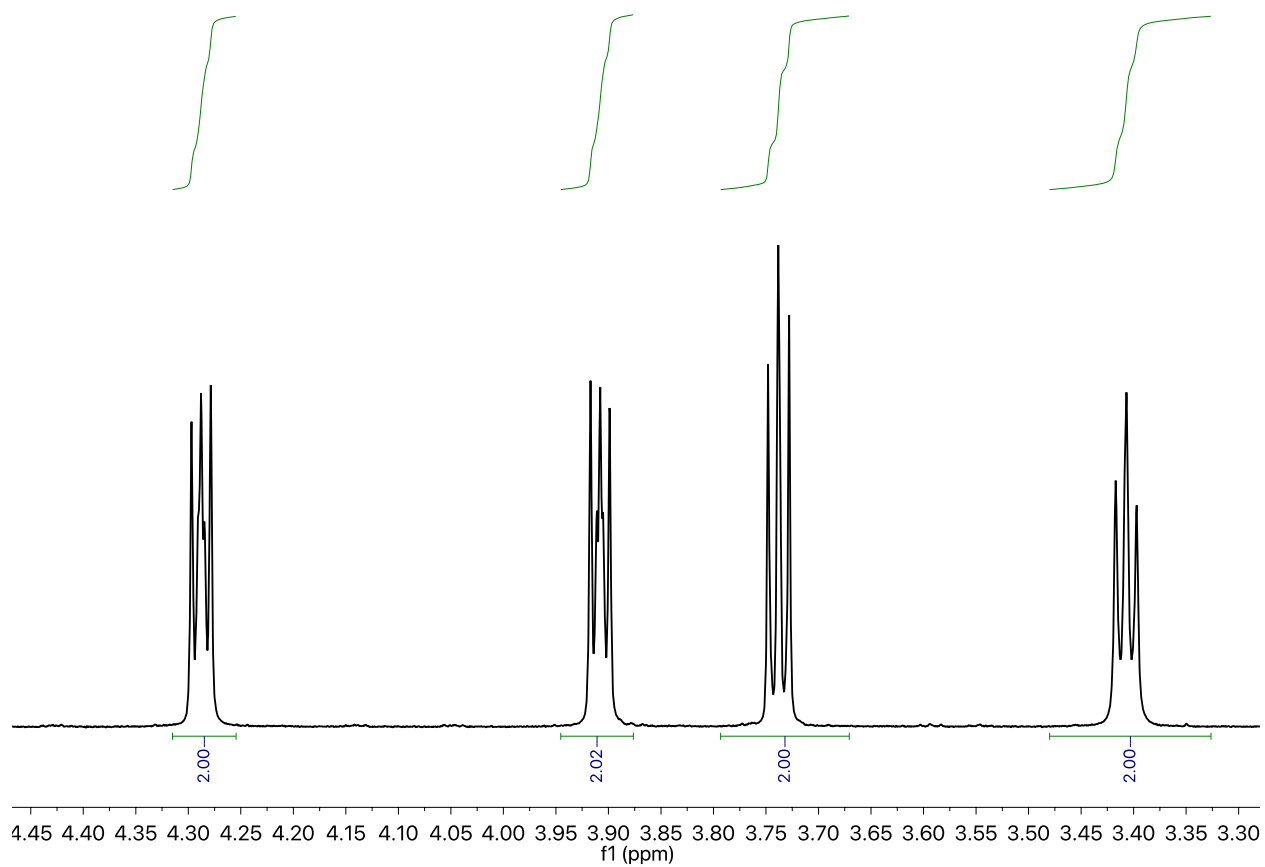


Figure 2.S41 Zoomed-in ^1H NMR spectrum (4.45–3.30 ppm) of **2** in CDCl_3 .

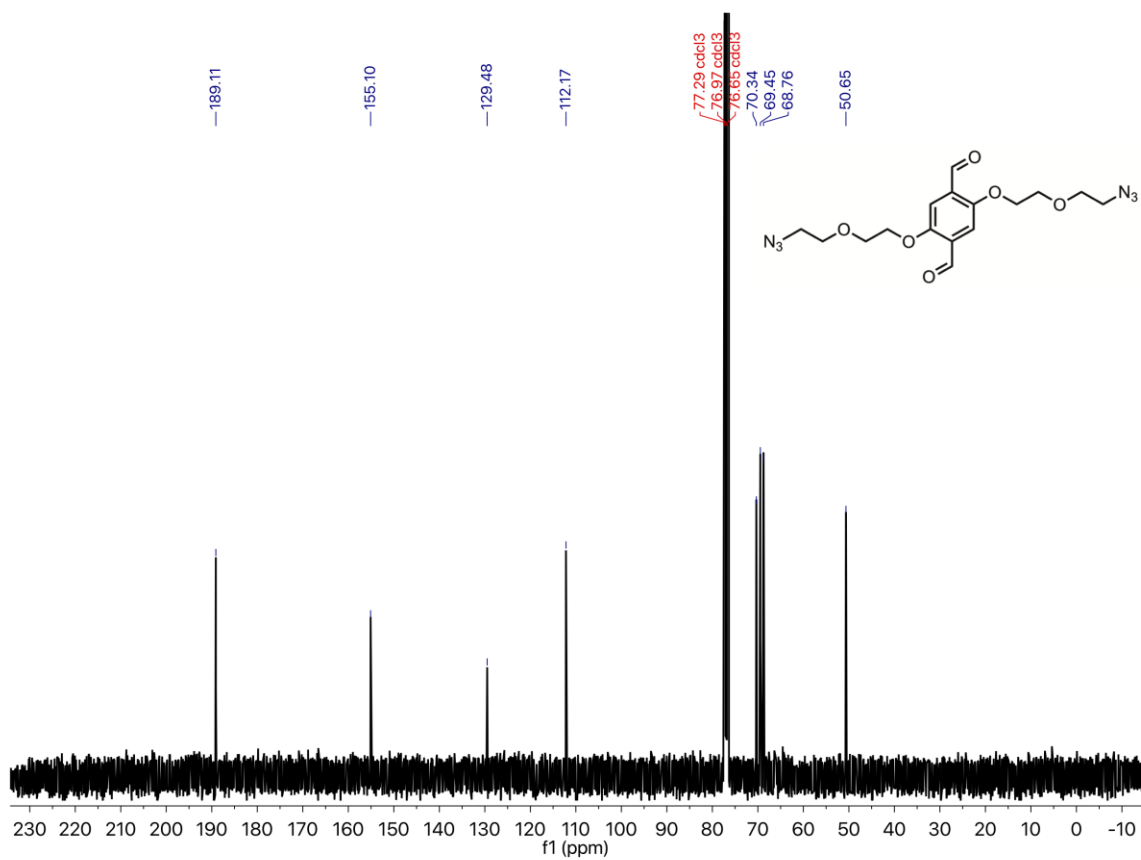


Figure 2.S42 ^{13}C NMR spectrum of **2** in CDCl_3 .

3. Thermal Depolymerization and Recrystallization of Imine-Linked Two-Dimensional Covalent Organic Frameworks

3.1 Preface

In this chapter, I discuss thermal depolymerization and recrystallization of imine-linked two-dimensional (2D) covalent organic frameworks (COFs) that can be employed to improve and assess COF materials quality. I will briefly outline previous COF mechanistic works reported in the literature and highlight the need for further studies on the formation and growth of imine COFs for better understanding of the processes and ultimately improving their qualities. I will then discuss the advantages of depolymerizing and recrystallizing defective COF networks using temperature and solubility effects, which draws on inspiration from the thermal dissociation of molecular imines. This novel synthetic strategy imine COFs results in COF materials of higher crystallinity and porosity and sheds light on the relationship between the COF crystallinity and stability.

This work was performed in collaboration with Dr. Leslie Hamachi, Rebecca Li, Nathan Flanders and Anushree Natraj in the Dichtel group.

3.2 Abstract

A more robust and better mechanistic insight into the formation and growth of imine-linked two-dimensional (2D) covalent organic frameworks (COFs) is needed to improve their materials quality and small crystallite sizes, both of which limit the promise of 2D COFs and 2D polymerization in general. Here we identify the temperature-dependent depolymerization and

recrystallization of colloidal imine-linked 2D COFs, offering a new means to improve their crystallinity and overall materials quality. 2D COF colloids prepared at room temperature depolymerize when their polymerization mixtures are heated to 90 °C. As the solutions are cooled back to room temperature, the 2D COFs repolymerize and crystallize with improved crystallinity and porosity, as characterized by XRD, FT-IR and N₂ adsorption isotherms. The evolution of COF crystallinity during thermal depolymerization and repolymerization processes was characterized by *in situ* wide angle X-ray scattering (WAXS), and the concentrations of free COF monomers as a function of temperature were quantified by variable temperature (VT) H¹ NMR spectroscopy. The ability of a 2D COF to depolymerize under these conditions depends on both the identity of the COF itself and its overall materials quality. For one network formed at room temperature (**TAPB-PDA COF**), a first depolymerization process is nearly complete, and the repolymerization yields materials with dramatically enhanced crystallinity and surface area. These recrystallized materials only partially depolymerize upon heating the solution a second time. A related 2D COF (**TAPB-DMTA COF**) forms initially with improved crystallinity compared to **TAPB-PDA COF** and does not depolymerize fully upon heating. These results suggest that crystallinity and network-dependent properties (e.g., interlayer interaction strength) allow some 2D COFs to resist depolymerization. These findings offer a new means to recrystallize or solvent anneal 2D COFs and may ultimately inspire improved methods for forming large imine-linked two-dimensional polymers from solution.

3.3 Introduction

Two-dimensional (2D) covalent organic frameworks (COFs) are crystalline and permanently porous polymer networks that polymerize and crystallize into layered structures.^{283, 322-324} COFs

are highly modular in their topology, pore sizes, composition and functionality,^{325, 326} which can be selected to produce materials with properties of interest for gas storage and separation,^{289, 327, 328} catalysis,³²⁹⁻³³² sensing,³³³⁻³³⁶ membranes,³³⁷⁻³⁴⁰ adsorbents^{155, 293} and organic electronic devices.³⁴¹⁻³⁴³ Despite this promise, many of the above potential applications for COFs remain limited by the quality of synthetically accessible crystals.³⁴⁴ To date, isolation of large, single-crystalline COF crystallites remains rare, with isolated reports of boron-linked 2D COFs,³⁴⁵ imine-linked 3D COFs,³⁴⁶ and more exotic 3D COFs based on the dimerization of polyfunctional nitroso compounds.³⁴⁷ Improving the quality of imine-linked 2D COFs remains one of the most important frontiers in 2D polymerization. Conventionally, imine-linked COFs are synthesized solvothermally at an elevated temperature (90-120 °C) in sealed reaction vials.^{348, 349} During synthesis, heterogeneous COF mixtures are rapidly produced, whose precipitates are unable to fully participate in reversible bond formation reactions. To address this shortcoming and access COF materials of higher quality, a deeper mechanistic understanding of 2D polymerization is needed.

Previous mechanistic studies on the synthesis and activation of imine-linked 2D COFs produced notable advances in COF materials quality.^{319, 348, 349} Feriante *et al.* demonstrated that imine COFs form more rapidly than previously thought, and that the previously common practice of isolating and desolvating the COF product *via* vacuum activation often negatively impacts its bulk crystallinity and porosity.^{349, 350} Improved imine-linked 2D COF polymerizations, remain an important frontier, as nucleation and growth processes remain difficult to control and poorly understood. Under typical solvothermal reaction conditions, imine-linked COFs precipitate rapidly,³⁴⁸ and this fast rate of formation is suspected to yield COF materials with numerous

defects. Indeed, *in situ* mechanistic studies on imine-linked COF formation showed that the imine COFs first proceed through an amorphous polymer intermediate instead of a direct crystallization process such as the boron-based COF systems.^{348, 351} It remains an open question whether development of different reaction conditions could lead to the direct crystallization of imine-linked COFs, or if the crystallization mechanism of these two materials is inherently different. Various additional strategies that rely on slowing down COF polymerization rates have been successfully implemented towards improved COF synthesis, such as the slow addition of monomers,³⁴⁵ nitrile solvents^{10, 351} and the inclusion of monofunctional modulators, which are usually aniline in imine-linked COF systems.^{346, 352, 353} Upon exploring the role of modulators and nitrile solvents in the synthesis of 2D COF colloids, we unexpectedly found that the COFs underwent temperature-dependent depolymerization. These results led us to explore thermal depolymerization and repolymerization of COFs under similar conditions as a potential means to better control COF formation and improve materials quality.

Here, we report a novel synthetic condition in which defective 2D imine COFs thermally depolymerize and recrystallize into COF materials of higher crystallinity and porosity. Analogous to the temperature-dependent hydrolysis of an imine model compound (**1**) under similar conditions, colloidal **TAPB-PDA COF** prepared at room temperature depolymerizes when heated to 90 °C. Upon cooling the solution, soluble monomers and oligomers repolymerize to provide the COF material with improved crystallinity and increased surface area, both common markers of materials quality. These thermal depolymerization and recrystallization process result in the formation of larger and highly ordered COF crystallites, which is reminiscent of small molecule recrystallization. The COF depolymerization and recrystallization processes are characterized by *in situ* wide-angle X-ray scattering (WAXS) and variable temperature (VT) NMR experiments,

while COF qualities before and after recrystallization are assessed by powder X-ray diffraction (PXRD), Fourier-transform infrared spectroscopy (FTIR), and N₂ adsorption isotherms.

3.4 Results and Discussion

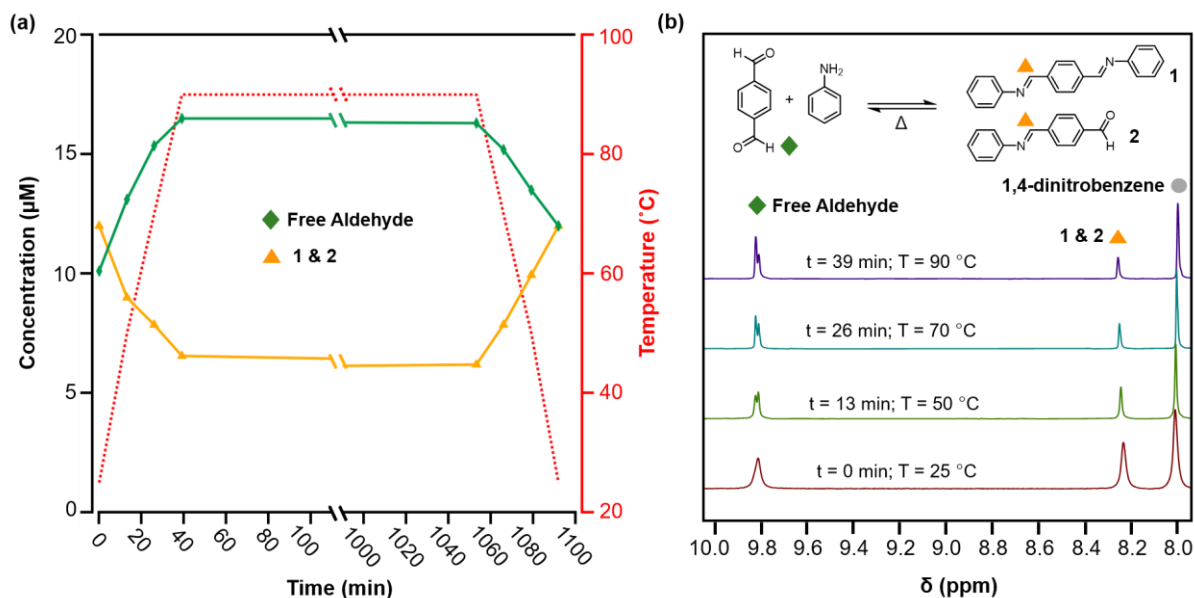


Figure 3.1 a) Amounts of **Free Aldehyde** (green diamond) and **Imine 1** (orange triangle) present in solution when **Imine 1** was subjected to the heating and cooling cycle, condition that mimic COF recrystallization. b) Representative VT-NMR spectra and the equilibrium between the monomers (**PDA** and aniline) and **Imine 1**. Concentration of each species was estimated *via* peak area integration using 1,4-dinitrobenzene as an internal standard.

The position of the equilibrium that interconverts the diimine **1** and H₂O with terephthalaldehyde (**PDA**) and two equivalents of aniline is highly temperature dependent. A pure sample of **1** was dissolved in a mixture of deuterated solvents (benzonitrile-*d*₅:D₂O; 16:1 *v/v*) along with aniline-*d*₅ (1 equiv with respect to **1**) and benzoic acid-*d*₅ (76 equiv with respect to **1**) and heated to 90 C in an NMR spectrometer for 17h and then cooled to room temperature, with spectra obtained at various reaction times (**Figure 3.1**). In the NMR spectra, aldehyde functional groups show up as singlets at δ(CH) = 9.8 ppm and imines as a singlet at δ(CH) = 8.25 ppm (**Figure 3.1b**). The overall concentrations of aldehydes (from **PDA** and its single condensation with aniline **2**) and imines

(from **1** and **2**) were quantified as a function of temperature and reaction time (**Figure 3.1a**). Prior to heating, 42% of the imines of **1** dissociated to provide a 1:1.2 ratio of aldehydes (10 μM) and imines (12 μM). Upon heating to 90 $^{\circ}\text{C}$, the aldehyde concentration increased to 16.5 μM and the imine concentration decreased to 7.5 μM , a 2.2:1 ratio (**Figure 3.1a**). This new equilibrium was established rapidly relative to the rate of thermal equilibration in the spectrometer, and the concentrations of imine and aldehydes did not change significantly when held at 90 $^{\circ}\text{C}$ for 17 hours. Subsequently, upon cooling back to 25 $^{\circ}\text{C}$, the equilibrium shifts towards imine formation, as the aldehyde concentration decreased to 14 μM and the imine concentration increased to 10 μM , which are close to those established at the beginning of the experiment. These findings demonstrate that the equilibrium of imine condensation and hydrolysis is highly temperature dependent under conditions similar to those used for 2D COF formation (see below). It is also important to note that equilibration is rapid at all temperatures studied, as evidenced by the rapid partial hydrolysis of **1** prior to heating. These studies on **PDA**, a monomer used often in 2D COFs, suggest that the driving force for COF formation might be similarly temperature dependent.

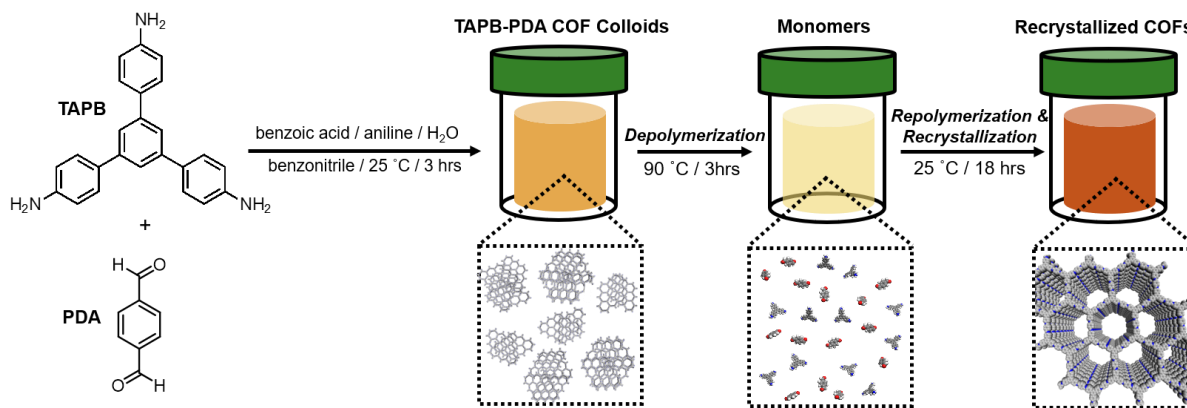


Figure 3.2 Schematic of TAPB-PDA COF recrystallization

To investigate how the temperature-dependent nature of imine formation under these conditions might influence the 2D polymerization process, it was first necessary to polymerize **TAPB-PDA**

COF at room temperature, where the driving force for imine-formation is relatively high. **TAPB-PDA COF** was first synthesized at room temperature by condensing 1,3,5-tris(4-aminophenyl)benzene (**TAPB**) and **PDA** in the presence of aniline and benzoic acid in a mixture of solvents (benzonitrile:H₂O; 16:1 v/v) (**Figure 3.2**; see Supporting Information for detailed procedures). Within 3 hours, a yellow colloidal suspension formed, which was comprised of 2 μm-sized spheres, as determined by scanning electron microscopy (SEM) images of the drop-casted solution (**Figure 3.S5**). The colloids were precipitated from solution by adding saturated aqueous NaCl and methanol, washed by Soxhlet extraction using methanol, and activated by supercritical CO₂ drying. The resulting powder product was characterized as a crystalline sample of the imine-linked **TAPB-PDA COF**, as confirmed by PXRD, N₂ adsorption isotherms and FT-IR spectrum of the isolated colloids (**Figure 3.2, 5a and b**). The PXRD pattern of the COF exhibited sharp <100>, <110>, <200>, and <210> Bragg diffraction peaks, consistent with an eclipsed model of the COF and reported powder patterns.³¹⁹ FT-IR spectroscopy showed the characteristic imine stretch at 1624 cm⁻¹, along with the absence of both the **PDA** aldehyde stretch at 1687 cm⁻¹ and the **TAPB** amine stretches at the range of 3300—3500 cm⁻¹ (**Figure 3.S1**). Analysis of the N₂ adsorption isotherm provided a Brunauer–Emmett–Teller (BET) surface area of 1740 m² g⁻¹, from which nonlocal density functional theory analysis provided a narrow pore width distribution centered at 3.4 nm (**Figure 3.5b and S2**). In considering the BET surface area as a metric of the **TAPB-PDA COF** materials quality, this value is sufficiently high to describe the material as a successfully activated 2D COF, yet lower than the theoretical value and other literature reports. These bulk characterization techniques collectively indicate that polymerization of **TAPB-PDA**

COF under these conditions at room temperature provides the target material in good but not superior materials quality.

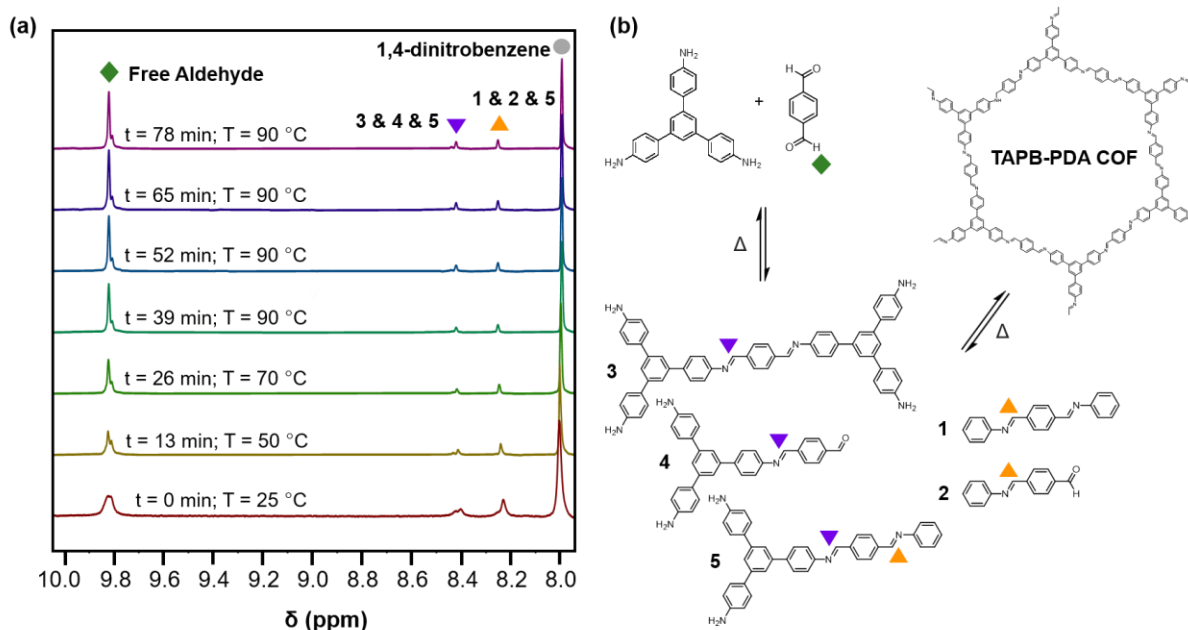


Figure 3.3 a) Representative VT-NMR spectra during the first cycle of **TAPB-PDA COF** recrystallization. b) Equilibrium between the **TAPB-PDA COF**, **Imines 1 and 2**, and monomers (**TAPB** and **PDA**) during the COF recrystallization.

Similar to the model compound study described above, imine-linked 2D COFs show a temperature-dependent equilibrium that enables their depolymerization and repolymerization in a manner reminiscent of molecular recrystallization. The depolymerization of **TAPB-PDA COF** colloids prepared at room temperature was characterized by variable-temperature NMR spectroscopy, *in situ* wide-angle x-ray scattering, as well as product analysis following repolymerization. For the VT-NMR spectroscopy experiments, **TAPB-PDA COF** was prepared as described above in the presence of deuterated solvents and reagents. The monomers were combined in aniline-*d*5 and benzoic acid-*d*6 in a mixture of deuterated solvents (benzonitrile-*d*5:D₂O; 16:1 v/v) and heated to 90 °C in an NMR spectrometer as the temperature was varied. The overall concentrations of aldehyde functional groups (from **PDA** and its single condensation with

aniline (**2**), **TAPB** (**4**), and other oligomers), as well as imine functional groups (from **1**, **2**, **3**, **4**, **5** and other oligomers, **Figure 3.3b**) were quantified as a function of temperature and reaction time (**Figure 3.4a**). Imines **1**, **2**, and **5** from the condensation between **PDA** and aniline appear as a single peak centered at 8.25 ppm, and imines **3**, **4** and **5** from a condensation between **PDA** and **TAPB** show up as a singlet at $\delta(\text{CH}) = 8.4$ ppm (**Figure 3.3a**). Prior to heating, the COF reaction mixture contained approximately 61% of the free COF monomers of aldehydes (4.5 μM), **TAPB** (3.9 μM), and imines (2.8 μM). Upon heating to 90 °C, the equilibrium shifted rapidly towards COF depolymerization and imine dissociation, as the aldehyde and **TAPB** concentrations instantly increased to 7.2 μM and 5.9 μM , respectively, and the imine concentrations decreased to 1.5 μM . When held at 90 °C for 14.5 hours, the concentrations of both aldehydes and imines, and **TAPB** further increased to 12 μM and 8 μM , respectively, reaching 100 % of COF depolymerization (**Figure 3.4a**). Upon cooling back to 25 °C, the equilibrium shifted back towards imine and COF formation, as the aldehyde and **TAPB** concentrations rapidly decreased to 6.4 μM and 6.2 μM , respectively, and the total imine concentrations increased to 4.4 μM . After sitting room temperature for 18 hours, the concentrations of aldehyde, **TAPB** and imines all decreased to 1.5 μM , 0.9 μM , and 0.9 μM , respectively, which suggest further repolymerization overnight (**Figure 3.4d**). Overall, **TAPB-PDA** COF colloids were observed to quantitatively depolymerize at 90 °C and slowly repolymerize at 25 °C. These findings demonstrate that the driving force for COF formation is highly temperature dependent, similar to the established equilibrium between diamine **1** and **PDA**.

In situ WAXS of **TAPB-PDA** COF obtained during the thermal depolymerization and repolymerization processes were consistent with depolymerization at an elevated temperature,

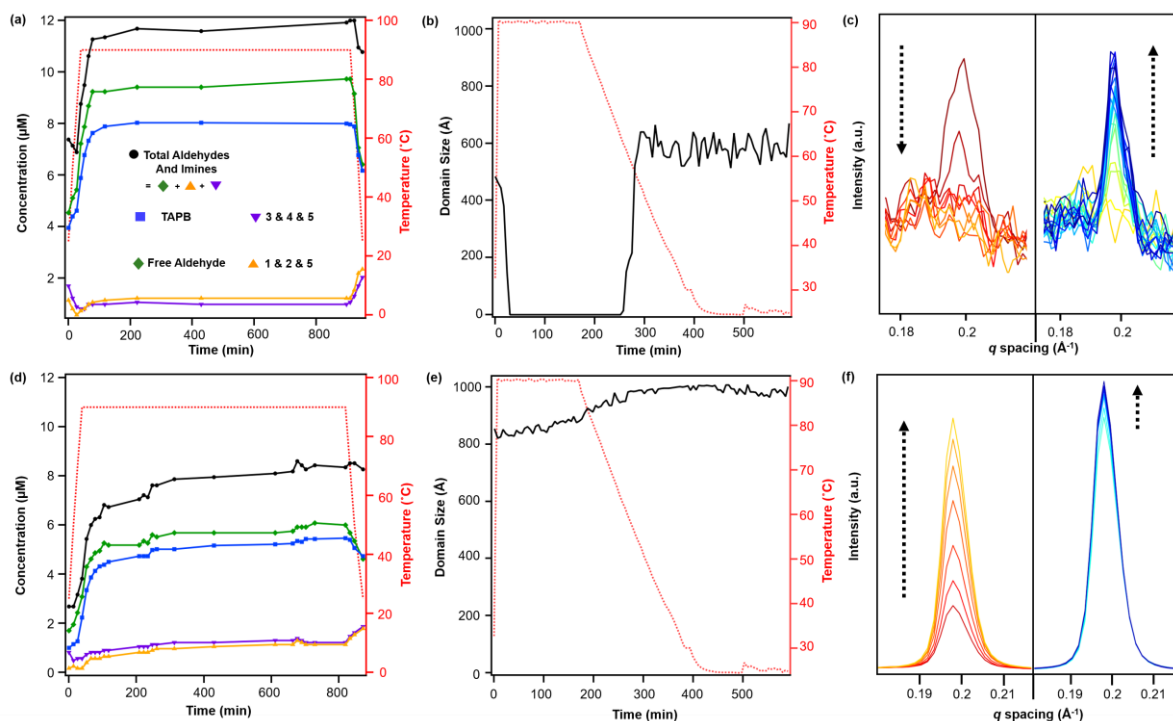


Figure 3.4 Amounts of **TAPB** (blue square), **Free Aldehyde** (green diamond), **Imines 1 and 2** (orange and purple triangles), and both aldehyde and imines combined (black circle) present in solution during the a) first and d) second cycle of **TAPB-PDA COF** recrystallization. Change in domain sizes of **TAPB-PDA COF** during the b) first and e) second cycle of COF recrystallization. Domain sizes are determined from the Scherrer analysis of the (100) diffraction peak. Representative WAXS patterns of **TAPB-PDA COF**, centered at its (100) diffraction peak, upon heating (red) and cooling (blue) during the c) first and f) second cycle of recrystallization.

followed by the formation of a more crystalline material upon repolymerization (**Figure 3.4b**). A colloidal suspension of **TAPB-PDA COF** formed at room temperature was heated to 90 °C in a capillary for 3 hours and cooled to room temperature for 7 hours, with WAXS spectra obtained at various reaction times. The WAXS pattern of the COF exhibited peaks at $q = 0.20, 0.35,$ and 0.54 \AA^{-1} , corresponding to the $\langle 100 \rangle, \langle 110 \rangle,$ and $\langle 200 \rangle$ Bragg diffraction peaks (**Figure 3.4c** and **S6a**). The average crystalline domain size of the COF was determined by applying the Scherrer equation to the full width at half max (FWHM) of the $\langle 100 \rangle$ diffraction peak.¹⁰ Prior to heating, the COF has an initial domain size of 44 nm. As the sample was held at 90 °C for 3 hours, the $\langle 100 \rangle$ diffraction peak decreases in intensity and eventually disappears completely, consistent with depolymerization. Upon cooling to room temperature over X h, the domain size increases to

64 nm ($t = 292$ min and $T = 48$ °C), approximately 20 nm higher than the initial COF domain size. After sitting overnight at room temperature, the COF domain size increased to 85 nm, indicating further crystallization at room temperature (**Figure 3.4e**). Overall, the changes in the crystallinity and domain sizes of **TAPB-PDA COF** suggest that the COFs initially formed at room temperature depolymerize at 90 °C and repolymerize/recrystallize into higher quality COFs upon cooling.

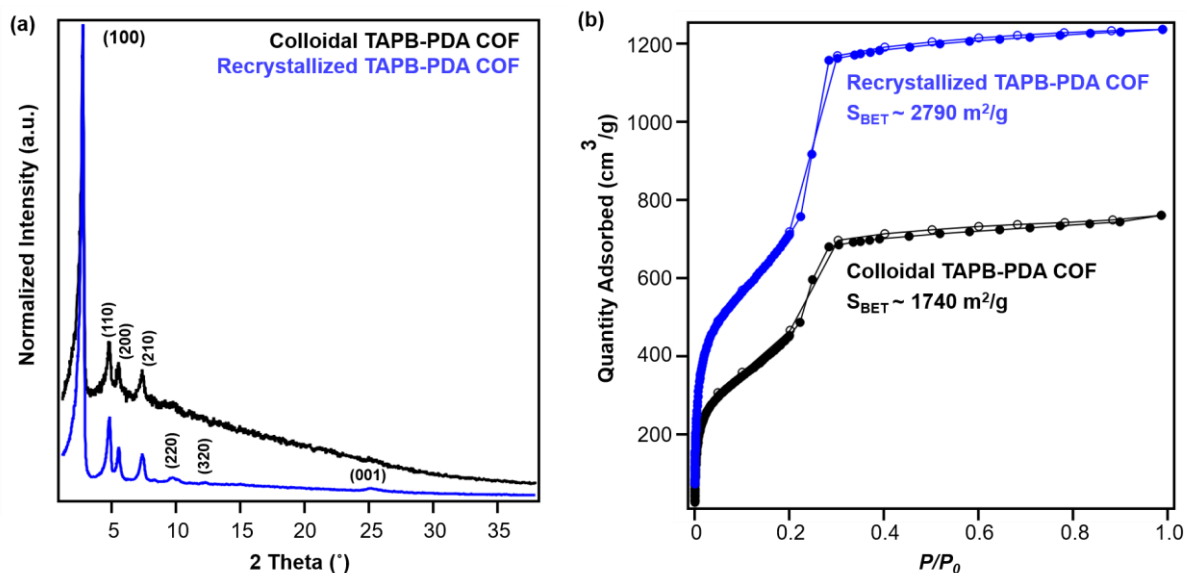


Figure 3.5 a) PXRD patterns and b) N₂ adsorption isotherms of **TAPB-PDA COF** before (black) and after (blue) the first cycle of COF recrystallization.

Recrystallized **TAPB-PDA COF** exhibited enhanced crystallinity and porosity compared to the COF colloids prepared at room temperature, as characterized by PXRD and N₂ adsorption isotherms (**Figure 3.5a** and **b**). Visually, heating the **TAPB-PDA COF** colloids in its reaction mixture to 90 °C turned the initial milky suspension into a clear yellow solution within a few minutes (**Figure 3.2**). The solution was heated at 90°C for 3 hours and remained homogeneous. Upon removing the reaction vessel and allowing it to cool to room temperature and stand overnight, the solution slowly turned opaque and yielded dark red precipitates. Recrystallized

TAPB-PDA COF after isolation exhibited much sharper and more well-defined $\langle 100 \rangle$, $\langle 110 \rangle$, $\langle 200 \rangle$, and $\langle 210 \rangle$ Bragg diffraction peaks as well as $\langle 220 \rangle$, $\langle 320 \rangle$ and $\langle 001 \rangle$ higher order peaks than the COF colloids (**Figure 3.5a**) along with a much higher BET surface area from $1740 \text{ m}^2 \text{ g}^{-1}$ to $2790 \text{ m}^2 \text{ g}^{-1}$ (**Figure 3.5b**). The IR spectrum of the recrystallized COF was identical to that of the COF colloids, with the presence of imine stretch at 1624 cm^{-1} , and the absence of both the aldehyde stretch at 1687 cm^{-1} and the amine stretches at the range of $3300\text{--}3500 \text{ cm}^{-1}$ (**Figure 3.S1**). Similar observations and materials quality were obtained by cooling the solution more slowly by turning the hot plate off but not removing the reaction vessel from the heating bath. Overall, the crystallinity and porosity of **TAPB-PDA COF** were improved after recrystallization, consistent with the increased domain sizes observed from *in situ* WAXS analysis (**Figure 3.4e**).

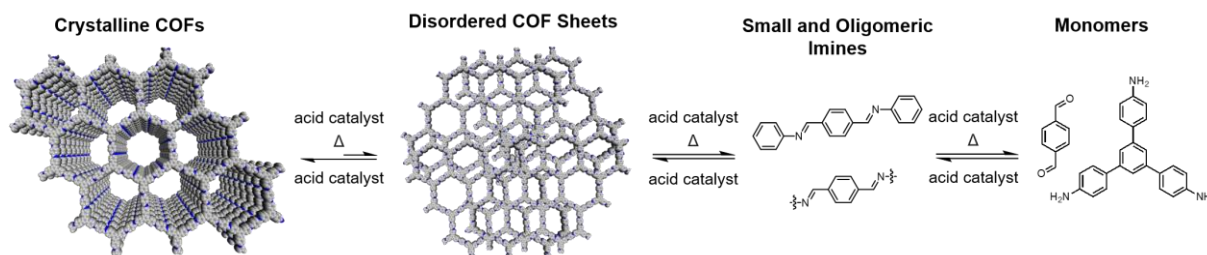


Figure 3.6 Schematic representations of proposed COF recrystallization mechanisms

After one depolymerization/repolymerization cycle, **TAPB-PDA COF** samples will partially depolymerize again upon reheating to 90 C , but a smaller percentage of the imine bonds are hydrolyzed (**Figure 3.4d, e, f** and **6**). After repolymerization, the reaction solution contains 22% of molecular species in the forms of aldehydes ($1.7 \text{ }\mu\text{M}$), **TAPB** ($1.0 \text{ }\mu\text{M}$), and imines ($1.0 \text{ }\mu\text{M}$). Upon reheating to $90 \text{ }^\circ\text{C}$, the aldehyde and **TAPB** concentrations increase to $3.1 \text{ }\mu\text{M}$ and $2.2 \text{ }\mu\text{M}$, respectively, and the imine concentrations decrease to $0.8 \text{ }\mu\text{M}$, all of which are approximately 13% lower than those observed during the first cycle of COF recrystallization. When held at $90 \text{ }^\circ\text{C}$ for

10.6 hours, the concentrations of both aldehydes and imines, and **TAPB** increase to 8.6 μM and 5.4 μM , respectively, corresponding to 72% of the available monomers being present in solution rather than incorporated into the COF (**Figure 3.4d**). Simultaneously, *in situ* WAXS analysis of this solution indicated that the average domain size of the COF network that remained had increased from 82 nm to 104 nm when held at 90 °C (**Figure 3.4e and f**). These observations suggest that a 2D COFs crystallinity make it more or less susceptible to this thermal depolymerization process. Defect-rich COFs, such as the initially synthesized **TAPB-PDA COF** colloids, are more susceptible to depolymerization; whereas more crystalline samples of the same material, including the recrystallized **TAPB-PDA COF**, are less susceptible (**Figure 3.6**). These observations may form the basis of procedures to solvent-anneal or otherwise upgrade the materials quality of COFs. However, it is important to note that further explorations of these conditions are needed, as the bulk crystallinity and porosity of the twice-recrystallized **TAPB-PDA COF** were similar to those of the samples isolated after one recrystallization cycle. These observations suggest that the repolymerization process may proceed through the nucleation of new COFs instead of the monomers adding exclusively to the residual COF crystallites. Together, these results suggest that lower quality or smaller COF crystallites are more susceptible to depolymerization than larger, more well ordered 2D COF domains.

In evaluating the depolymerization/repolymerization of a related imine-linked 2D COF, derived from 2,5-dimethoxyterephthaldehyde (**DMTA**), different degrees of depolymerization but a similar dependence on materials quality are observed (**Figure 3.7**). The initial formation of **TAPB-DMTA COF** colloids provides more highly crystalline samples that can be isolated and activated to provide a higher BET surface area of 2250 $\text{m}^2 \text{g}^{-1}$ as compared to the initially isolated **TAPB-**

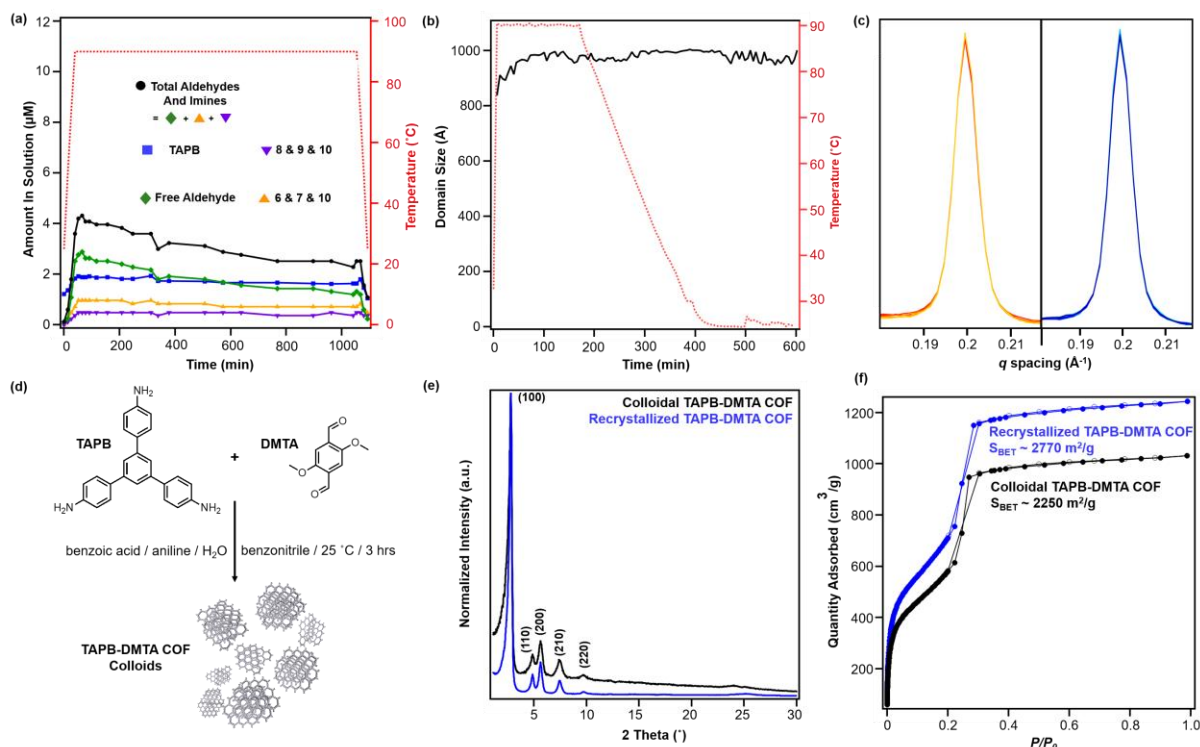


Figure 3.7 a) Amounts of TAPB (blue square), Free Aldehyde (green diamond), Imines 1 and 2 (orange and purple triangles), and both aldehyde and imines combined (black circle) present in solution during the first cycle of TAPB-DMTA COF recrystallization. b) Change in domain sizes of TAPB-DMTA COF during the first cycle of COF recrystallization. Domain sizes are determined from the Scherrer analysis of the (100) diffraction peak. c) Representative WAXS patterns of TAPB-DMTA COF, centered at its (100) diffraction peak, upon heating (red) and cooling (blue) during the first cycle of recrystallization. d) Synthesis of TAPB-DMTA COF colloids e) PXRD patterns and f) N_2 adsorption isotherms of TAPB-DMTA COF before (black) and after (blue) the first cycle of COF recrystallization.

PDA COF colloids with a BET surface area of $1740 \text{ m}^2 \text{ g}^{-1}$. TAPB DMTA COF colloids were synthesized at room temperature under the same conditions as TAPB-PDA COF colloids. These provided colloidal COFs with superior crystallinity compared to the TAPB-PDA COF colloids, as determined by the sharp Bragg diffraction peaks and the Scherer analysis (Figure 3.7e and f). The TAPB-DMTA COF colloids underwent partial depolymerization upon heating to 90°C in the presence of benzoic acid, aniline, and water. Heating the TAPB DMTA COF colloids in its reaction mixture to 90°C for 3 hours and cooling to room temperature yielded recrystallized TAPB DMTA COF, which exhibited enhanced crystallinity and porosity with a modest increase in BET surface area from $2250 \text{ m}^2 \text{ g}^{-1}$ to $2770 \text{ m}^2 \text{ g}^{-1}$ (Figure 3.7e and f). Prior to heating, the colloidal

TAPB DMTA COF reaction mixture contained free COF monomers of **DMTA** (0.12 μM) and **TAPB** (1.0 μM) (**Figure 3.7a**). Upon heating to 90 $^{\circ}\text{C}$, approximately 36% of the COF depolymerized to aldehydes (2.9 μM), **TAPB** (1.9 μM) and imines (1.5 μM), which is much lower compared to 94% depolymerization for the room-temperature synthesized **TAPB-PDA COF** colloids. When held at 90 $^{\circ}\text{C}$ for 16.5 hours, however, the concentrations of both aldehydes and imines, and **TAPB** slowly decreased to 2.3 μM and 1.6 μM , respectively, indicating repolymerization of **TAPB-DMTA COF** even at this elevated temperature. Simultaneously, *in situ* WAXS analysis of this solution clearly showed **TAPB-DMTA COF** colloids are highly crystalline at 90 $^{\circ}\text{C}$ with domain sizes exceeding 80 nm (**Figure 3.7b** and **c**). These results are in stark contrast to the continuous thermal depolymerization of **TAPB-PDA COF** observed during the first and second cycles of COF recrystallization (**Figure 3.4b** and **d**). We hypothesize that the larger crystalline domains and/or stronger interlayer interactions of **TAPB-DMTA COF**^{329, 354} compared to **TAPB-PDA COF** are responsible for this material's increased ability to resist depolymerization. Moreover, for both networks, we speculate that less ordered regions of the materials are more susceptible to hydrolysis under these conditions, which explains why materials of improved crystallinity depolymerize to lesser extents.

3.5 Conclusion

We identified a previous unknown, temperature-based depolymerization and repolymerization/recrystallization process for imine-linked 2D COFs. Mirroring the temperature-dependent hydrolysis of the soluble imine-containing model compound **1**, the 2D COFs depolymerize in their polymerization solutions and recrystallize into higher quality COF materials upon cooling. *In situ* WAXS and VT-NMR experiments reported on the crystallinity and extent of

depolymerization of the COFs in solution at various temperatures. PXRD, FTIR and N₂ adsorption isotherms of the isolated materials were used to assess their quality before and after recrystallization. While **TAPB-PDA COF** colloids first prepared at room temperature fully depolymerize to soluble monomers and oligomers at 90 °C, recrystallized **TAPB-PDA COF** colloids with larger domain sizes (> 80nm) only partially depolymerize under the same conditions. Likewise, **TAPB-DMTA COF** is initially formed as a more crystalline network, and it likewise depolymerizes to a lesser extent. These observations suggest that larger and more ordered COF crystallites are more resistant to thermal depolymerization. Taken together, this study reports a series of novel phenomena in which 2D imine COFs undergo temperature-dependent depolymerization and recrystallization and provides an efficient synthetic strategy to improve and assess COF materials quality. These findings provide a new means to improve 2D COF materials quality from as-synthesized materials, as well as intriguing insight into their formation that may inform improved 2D polymerizations in the future.

3.6 Acknowledgments

We acknowledge the Army Research Office for a Multidisciplinary University Research Initiatives (MURI) award under grant number W911NF-15-1-0447. Parts of this work were performed at the DuPont-Northwestern-Dow Collaborative Access Team (DND-CAT) located at Sector 5 of the Advanced Photon Source (APS). DND-CAT is supported by Northwestern University, E.I. DuPont de Nemours & Co., and the Dow Chemical Company. This research used resources of the Advanced Photon Source and Center for Nanoscale Materials, both U.S. Department of Energy (DOE) Office of Science User Facilities operated for the DOE Office of Science by Argonne National Laboratory under Contract No. DE-AC0206CH11357. This work has also made use of

the IMSERC, EPIC, and Keck II facility of NUANCE Center at Northwestern University, which has received support from the Soft and Hybrid Nanotechnology Experimental (SHyNE) Resource (NSF ECCS1542205), the MRSEC program (NSF DMR-1720139) at the Materials Research Center, the Keck Foundation, the State of Illinois and International Institute for Nanotechnology (IIN). N. C. F. and L. X. C. are partially supported by Basic Energy Science, CBG Division, US Department of Energy through Argonne National Laboratory under Contract No. DE-AC02-06CH11357.

3.7 Appendix

3.7.1 Materials and Instrumentation

Materials. Reagents were purchased in reagent grade from commercial suppliers and used without further purification, unless otherwise described. Borosilicate capillaries (1.5 mm in diameter and a wall thickness of 0.01 mm) were purchased from Charles Supper.

Instrumentation. Infrared spectra were recorded using a Nicolet iS10 FT-IR spectrometer equipped with a ZnSe ATR.

Various temperature proton nuclear magnetic resonance (VT-¹H NMR) spectra were recorded on Bruker AvanceIII-600 MHz.

The supercritical CO₂ drying was performed on Leica EM CPD 300. Prior to the supercritical drying process, all samples were placed in tea bags (ETS Drawstring Tea Filters, sold by English Tea Store) while wet. The tea bags containing the samples were then placed in the drying chamber. The drying chamber was first sealed, cooled, and filled with liquid CO₂, and after 2 min, the

samples were vented quickly. This fill-vent cycle was repeated 99 times, after which the temperature was raised to 40 °C resulting in a chamber pressure of around 1300 psi, which is well above the critical point of CO₂. The chamber was held above the critical point for 5 min, after which the CO₂ source was turned off, and the pressure was released over a period of 5 min.

Powder X-ray diffraction (PXRD) patterns were obtained at room temperature on a STOE-STADIMP powder diffractometer equipped with an asymmetric curved Germanium monochromator (CuK α_1 radiation, $\lambda = 1.54056 \text{ \AA}$) and one-dimensional silicon strip detector (MYTHEN2 1K from DECTRIS). The line focused Cu X-ray tube was operated at 40 kV and 40 mA. The as-obtained powder samples were sandwiched between two acetate foils (polymer sample with neither Bragg reflections nor broad peaks above 10° 2 θ) mounted in flat plates with a disc opening diameter of 8 mm and measured in transmission geometry in a rotating holder. The patterns were recorded in the 2 θ range of 0–32° for an overall exposure time of 24 min. The instrument was calibrated against a NIST Silicon standard (640d) prior to the measurement.

Wide-angle X ray scattering (WAXS) patterns were collected at sector 5-ID-D of the Advanced Photon Source at Argonne National Lab. A beam energy 13.3 keV was used at 5-ID-D. Each pattern was obtained by collecting ten one second frames on a Pilatus 2D detector and then averaged and radially integrated using software available at APS.

Gas adsorption isotherms were conducted on a Micromeritics ASAP 2420 Accelerated Surface Area and Porosity Analyzer using 15–50 mg samples in dried and tared analysis tubes equipped with filler rods and capped with a Transeal. Samples were heated to 40 °C at a rate of 1 °C/min and evacuated at 40 °C for 20 min, then heated to 100 °C at a rate of 1 °C/min heat and evacuated

at 100 °C for 18 h. After degassing, each tube was weighed again to determine the mass of the activated sample and transferred to the analysis port of the instrument. UHP-grade (99.999% purity) N₂ was used for all adsorption measurements. N₂ isotherms were generated by incremental exposure to nitrogen up to 760 mmHg (1 atm) in a liquid nitrogen (77 K) bath. Oil-free vacuum pumps and oil-free pressure regulators were used for all measurements. Brunauer-Emmett-Teller (BET) surface areas were calculated from the linear region of the N₂ isotherm at 77 K within the pressure range P/P_0 of 0.10–0.20.

Scanning electron microscopy (SEM) images of TAPB-PDA and TAPB-DMTA COFs samples were taken on a Hitachi S4800 cFEG SEM. The samples were coated with 8 nm of Osmium using SPI OPC-60A osmium plasma coater.

3.7.2 Synthetic Procedures

COF Synthesis at Room Temperature: A 20 mL scintillation vial was charged with benzoic acid (675 mg, 5.5 mmol) and corresponding aldehyde (0.072 mmol of **PDA**, **DMTA** or **BDA**) in benzonitrile (6 mL) and heated to 90 °C for a few minutes to ensure dissolution of each species. The solution was cooled to room temperature and added water (0.375 mL, 21 mmol), aniline (0.1 mL of 0.7 M stock in benzonitrile, 0.07 mmol), and 1,3,5-tris(4-aminophenyl)benzene (**TAPB**, 17 mg, 0.048 mmol). The resulting reaction mixture was let stand at room temperature for 3 hours until it turned opaque to serve as room temperature control COFs (**RT Control COFs**). These COFs were then precipitated out by the addition of 0.2 mL brine and 10 mL methanol, centrifuged for 10 minutes, transferred to a tea bag, and washed with methanol in a Soxhlet extractor for 18 h.

The materials were activated by supercritical CO₂ that afforded **RT Control COFs** as yellow solids in isolated yields of 75%.

COF Recrystallization: The colloidal solution of **RT Control COFs** in a 20 mL scintillation vial was used right after their 3-hour reaction time at room temperature and was heated to 90 °C for **TAPB-PDA** and **TAPB-BDA COFs** and to 140 °C for **TAPB-DMTA COF** for 3 hours, after which the solution was observed to turn clear red. The COF solution was then cooled to room temperature and let sit for 18 hours to be transferred to a tea bag, and washed with methanol in a Soxhlet extractor for 18 h. The materials were activated by supercritical CO₂ that afforded **Recrystallized COFs** as yellow solids in isolated yields of 85%.

3.7.3 Additional Images and Characterization

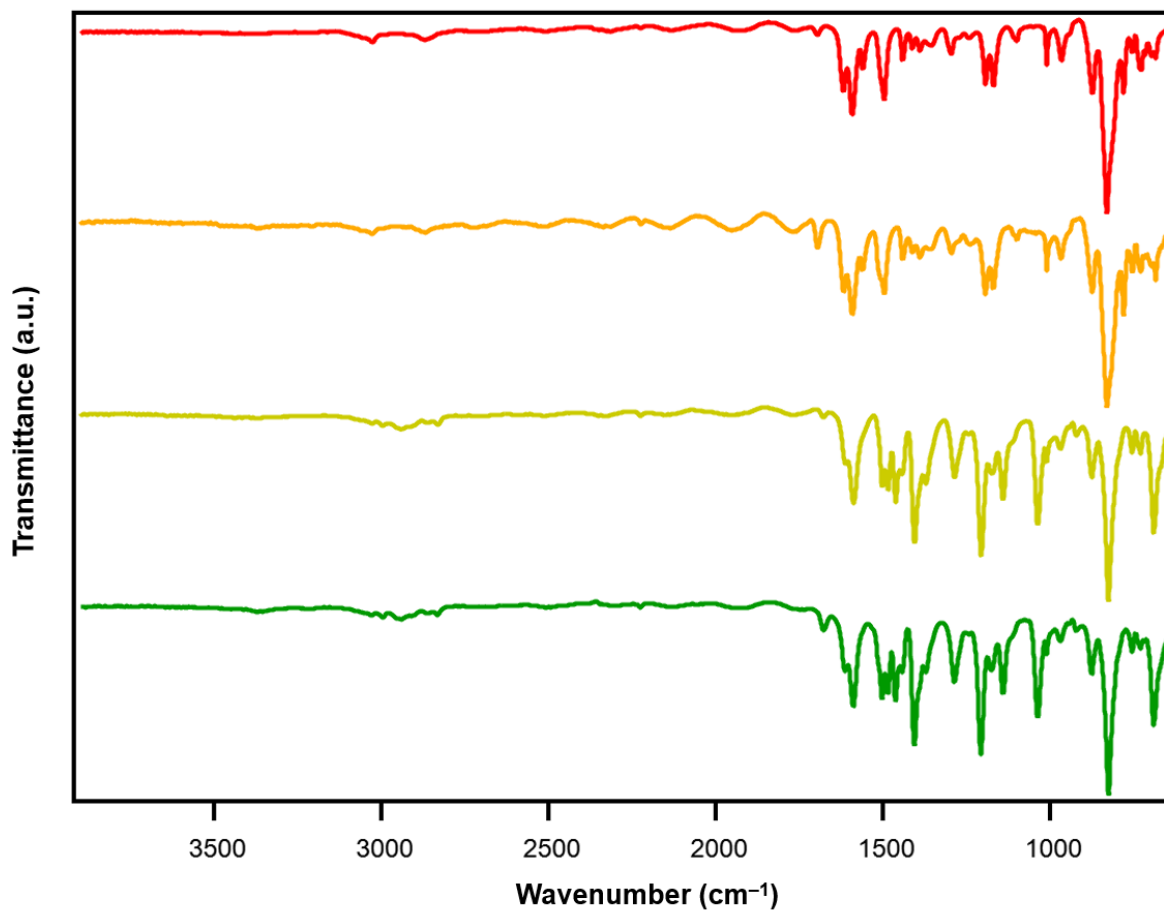


Figure 3.S1 FT-IR Spectra of colloidal (red) and recrystallized (orange) **TAPB-PDA COF**, and colloidal (yellow) and recrystallized (green) **TAPB-DMTA COF**.

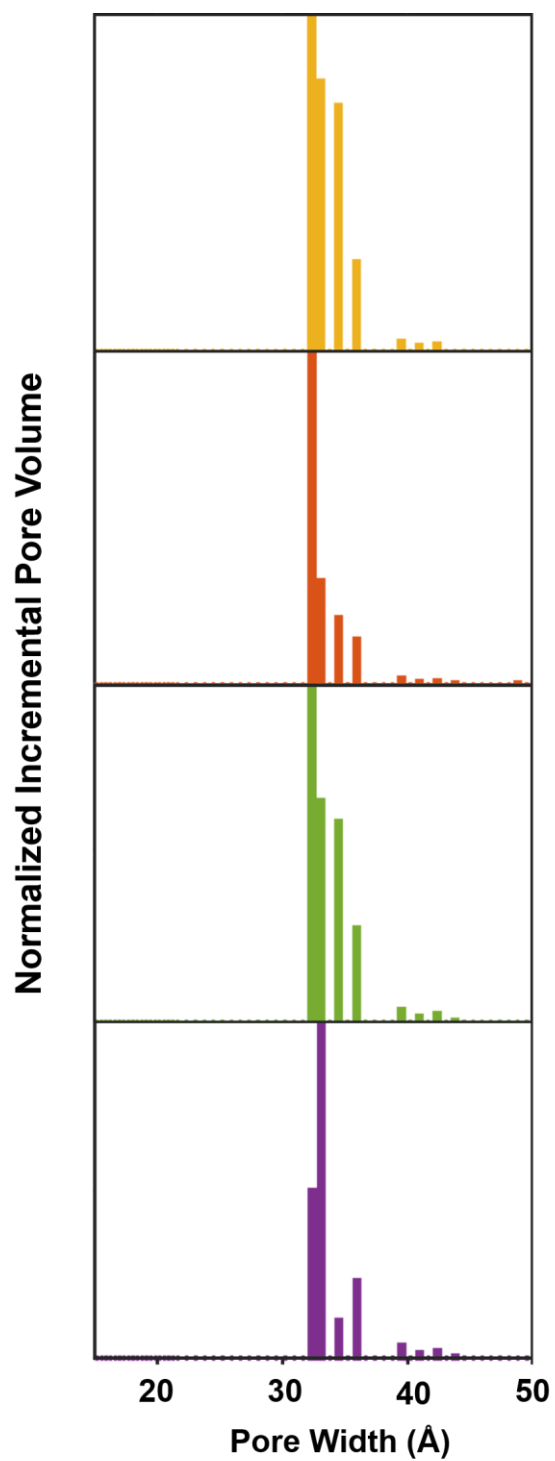


Figure 3.S2 Pore size distributions of colloidal (yellow) and recrystallized (red) **TAPB-PDA COF**, and colloidal (green) and recrystallized (purple) **TAPB-DMTA COF**.

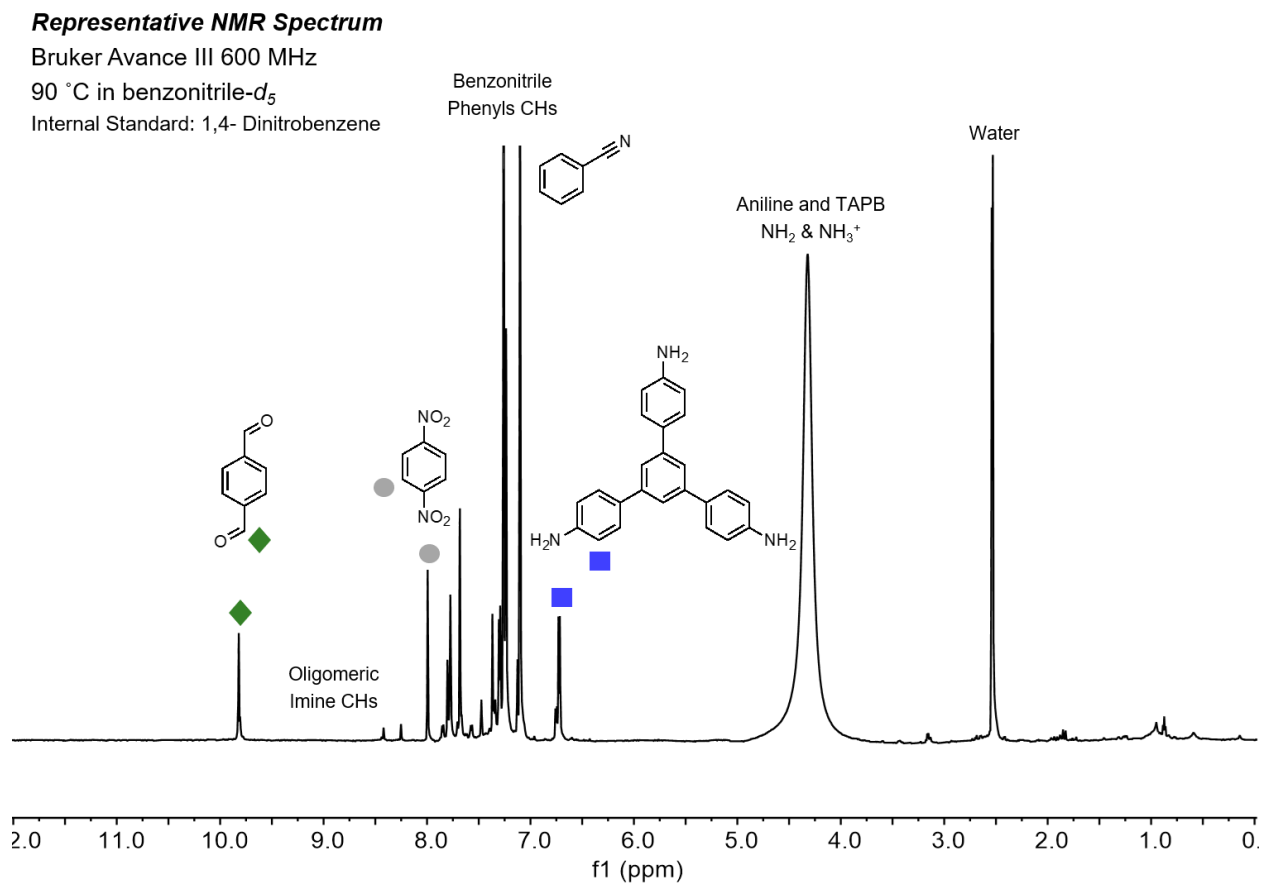


Figure 3.S3 Representative VT-NMR spectrum (0–12 ppm) of **TAPB-PDA COF** reaction mixture at 90 °C in benzonitrile- d_5 .

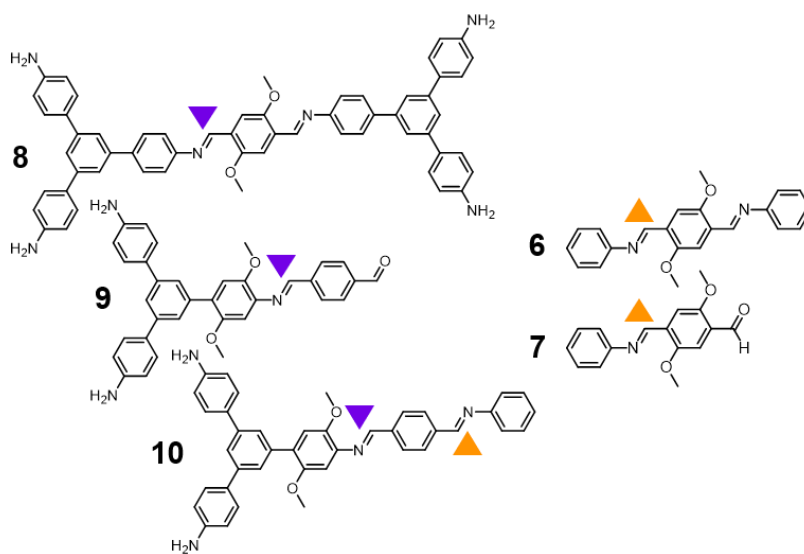


Figure 3.S4 Soluble imine-linked species in the representative VT-NMR spectrum in **Figure 3.7a**.

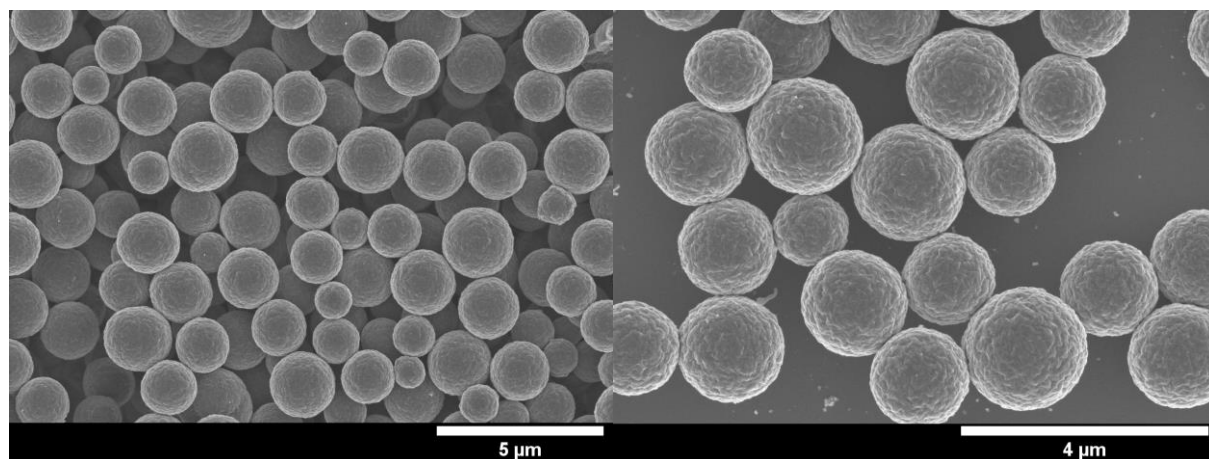


Figure 3.S5 SEM images of colloidal TAPB-PDA COFs.

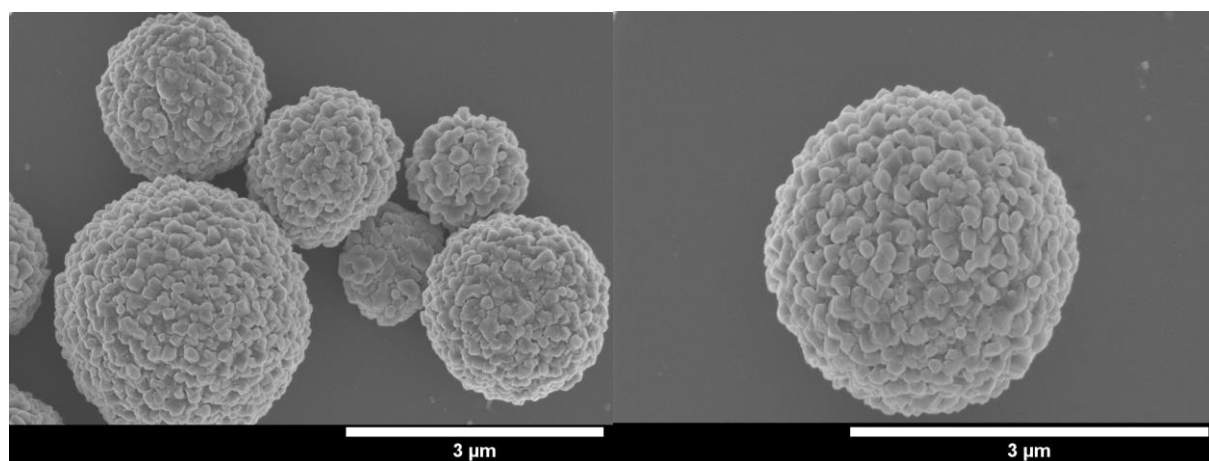


Figure 3.S6 SEM images of colloidal TAPB-DMTA COFs.

3.7.4 BET Plots for N₂ Isotherm

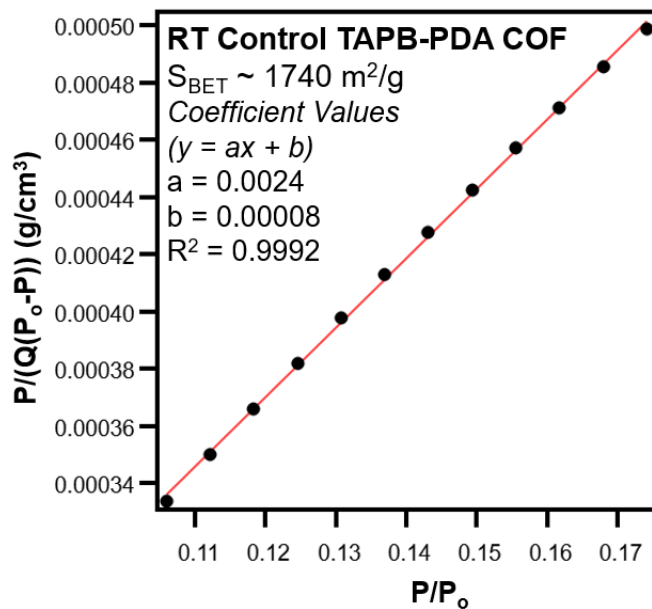


Figure 3.S7 BET Plot for colloidal TAPB-PDA COF.

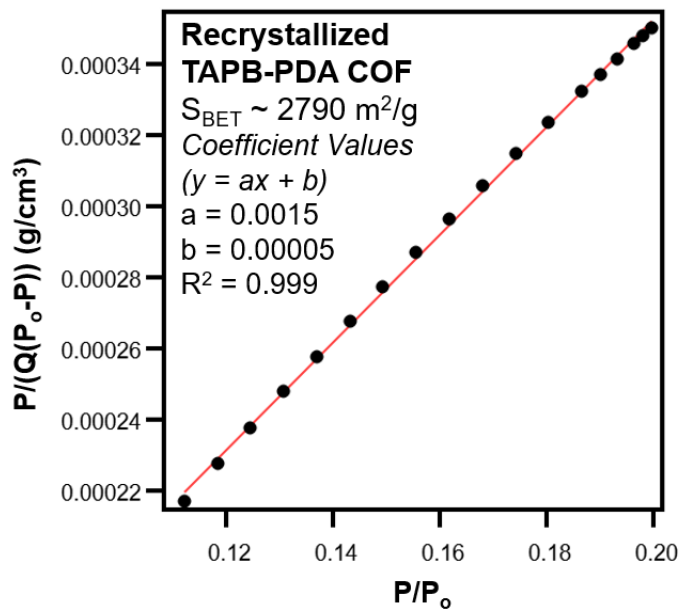


Figure 3.S8 BET Plot for recrystallized TAPB-PDA COF.

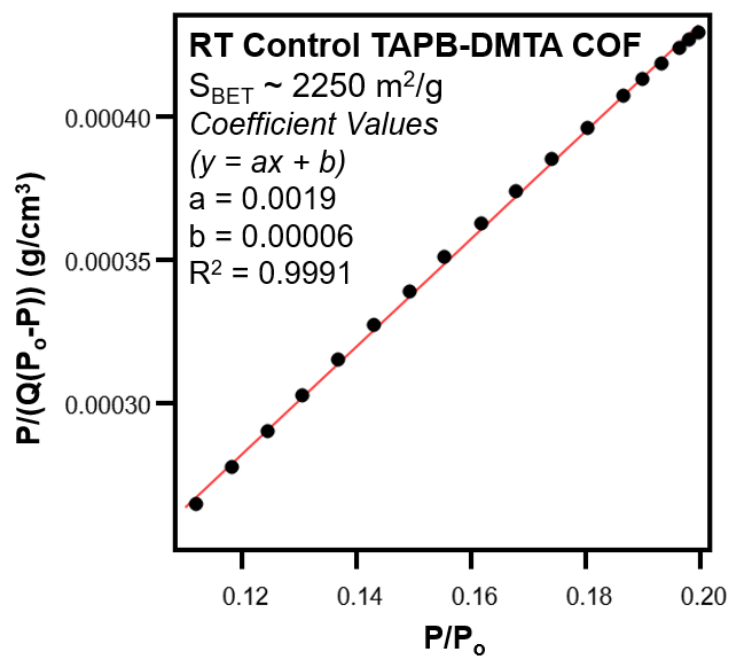


Figure 3.S9 BET Plot for colloidal TAPB-DMTA COF.

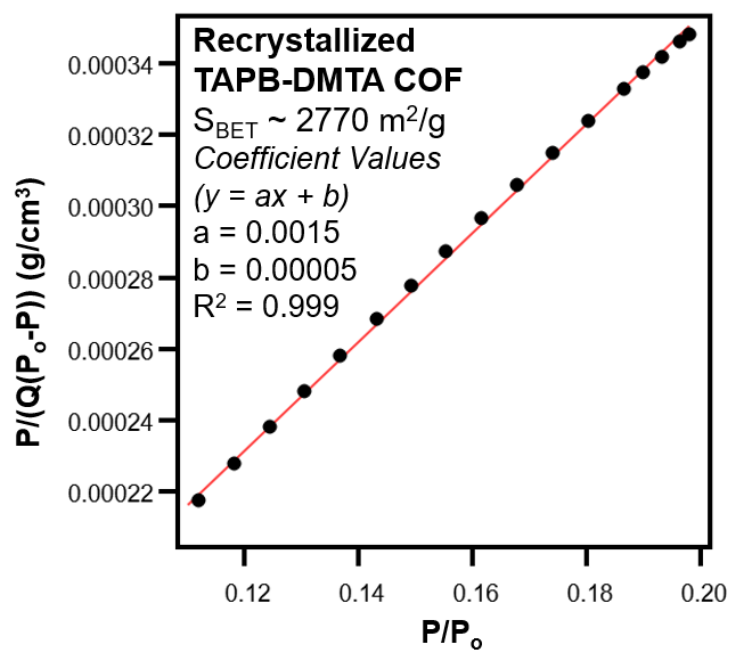


Figure 3.S10 BET Plot for Recrystallized TAPB-DMTA COF.

4. Synthesis of Single-crystalline Imine-Linked Two-Dimensional Covalent Organic Frameworks

4.1 Preface

In the final chapter I discuss a novel synthetic strategy for preparing imine-linked 2D COF single crystals of four different architectures. I briefly discuss the motivation behind this project and highlight the three key components leveraged in the synthesis. In particular, both the reaction temperature and modulator species were shown to be efficient at inhibiting nucleation and promoting COF growth, such that the sizes of the imine-linked 2D COF crystals reported here can be fine-tuned from hundreds of nanometers to tens of micrometers. This approach represents the first example of synthetically realizing imine-linked 2D COF single crystals and we anticipate that these findings will be highly impactful in enabling the synthesis of a broader and newer class of 2D polymer structures and exploration of their properties.

This work was performed in collaboration with Ioannina Castano, Anushree Natraj, Dr. Leslie S. Hamachi and Dr. Austin M. Evans in the Dichtel group.

4.2 Abstract

Two-dimensional (2D) covalent organic frameworks (COFs) are composed of structurally precise, permanently porous, layered macromolecular sheets, which have traditionally been synthesized as polycrystalline aggregates with small crystalline domains of less than 50 to 100 nm. Only recently have a small number of synthetic strategies been reported to prepare boron-linked 2D and imine-linked 3D COF single crystals. Here, we report a novel synthetic condition in which single-

crystalline imine-linked 2D COFs of four different structures are prepared, consisting of two hexagonal **TAPB-DMTA** and **TAPB-Dimethyl COFs** and two tetragonal **TAPPy-PDA** and **TAPPy-Thiophene COFs**. The condition leverages both the reaction temperature and modulator species to inhibit nucleation and promote COF growth, such that the sizes of **TAPB-DMTA** and **TAPPy-PDA COF** crystals can be fine-tuned from 450 nm to 20 μm , and 720 nm to 1.3 μm in diameter, respectively. All of the COF crystals exhibit excellent crystallinity and porosity, as judged from PXRD and N_2 adsorption isotherms, and are single-crystalline, as corroborated by high-resolution TEM characterization. This approach represents the first example of synthetically realizing imine-linked 2D COF single crystals and we anticipate that these findings will enable the synthesis of a broader and newer class of 2D polymer structures and exploration of their properties.

4.3 Introduction

Polymerization of monomers into ordered two-dimensional (2D) networks yields covalently linked macromolecular sheets, which yields novel polymer architectures and distinct combinations of properties. 2D covalent organic frameworks (COFs),^{283, 322-324} for instance, are of interest for numerous applications, including catalysis,³²⁹⁻³³² sensing,³³³⁻³³⁶ membranes,³³⁷⁻³⁴⁰ gas storage and separation,^{289, 327, 328} adsorbents^{155, 293} and organic electronic devices³⁴¹⁻³⁴³ due to their modularity, precise monomer arrangements and permanent porosity.^{325, 326} However, most 2D COFs are isolated as aggregated polycrystalline powders with small domain sizes of less than 50 nm, which limit their utility in otherwise promising applications. To date, isolation of large, single-crystalline COF crystallites remains quite rare, with limited reports on 2D boron based COFs³⁴⁵ and imine-linked 3D COFs,^{346, 347} such that improving the quality of imine-linked 2D COFs is a rich area of opportunity.

Here, we report a novel synthetic condition in which single-crystalline 2D imine COFs of four different architectures can be prepared. In this condition, nitrile solvents, monofunctional modulator and reaction temperature are identified as key components and leveraged accordingly. First, nitrile solvents are thought to prevent aggregation and have been shown to provide colloidal suspensions of boron-linked 2D COF single crystals^{345, 352, 355} and imine-linked 2D COF colloids.¹⁰ Upon screening various nitrile solvents, benzonitrile was employed as a solvent for the COF synthesis. 2) The addition of monofunctional modulator in the synthesis of framework materials has been shown to inhibit undesirable nucleation events and promote growth, ultimately increasing the crystallinity of the resulting networks.^{346, 352} Thus, we incorporated varying loadings of aniline, which is a common modulator species in the synthesis of imine-linked COFs, in the reaction mixture. 3) In inorganic nanocrystal synthesis, temperature plays another important role in controlling nucleation and promoting growth, which has yet to be systematically studied in the COF synthesis. In this study we leverage all three key parameters and synthesize varying sizes of four different imine-linked 2D COF single crystals. The COF crystals exhibit excellent crystallinity and porosity, as determined from PXRD and N₂ adsorption isotherms, and are single-crystalline, as corroborated by HRTEM characterization. This approach represents the first example of synthetically realizing single-crystalline imine-linked 2D COFs of four different structures and rationally controlling their sizes through fine-tuning the reaction parameters.

4.4 Results and Discussion

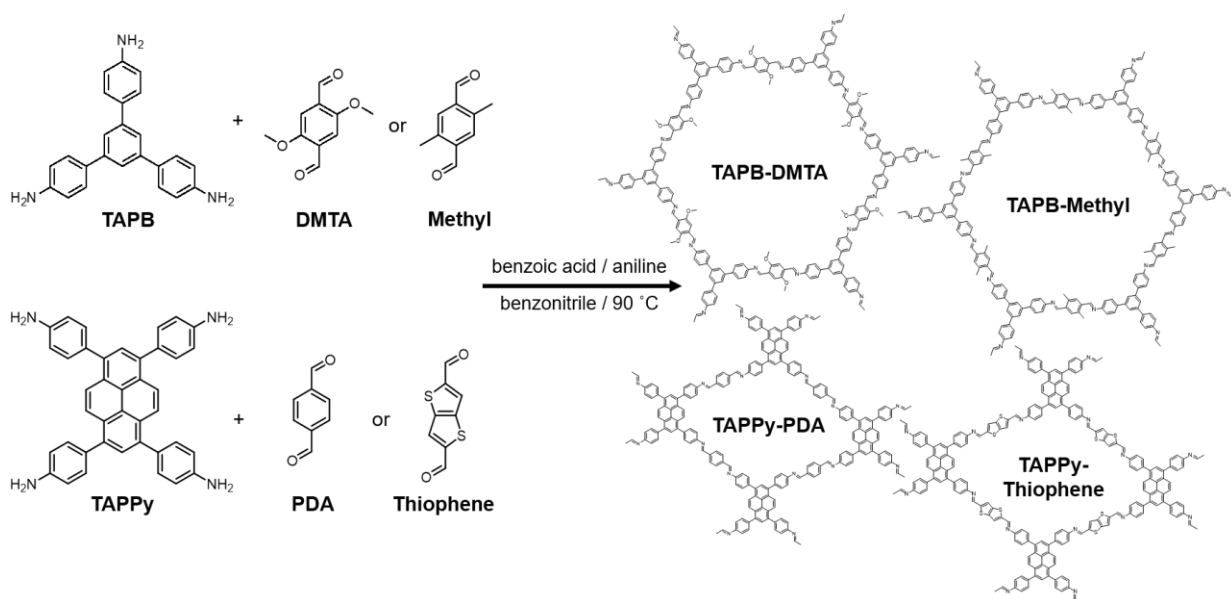


Figure 4.1 Schematic of single-crystalline imine-linked 2D COF synthesis. Four different COFs structures, **TAPB-DMTA**, **TAPB-Methyl**, **TAPPy-PDA** and **TAPPy-Thiophene** COFs, are shown.

As a model system we first targeted an imine-linked 2D COF derived from 2,5-dimethoxyterephthalaldehyde (**DMTA**). **TAPB-DMTA** COFs was first synthesized at 90 °C by condensing 1,3,5-tris(4-aminophenyl)benzene (**TAPB**) and **DMTA** in the presence of aniline and benzoic acid in benzonitrile (**Figure 4.1**; see Supporting Information for detailed procedures). Within minutes, a red colloidal suspension formed, which was comprised of 2 μm -sized hexagonal platelets, as determined by scanning electron microscopy (SEM) and atomic force microscopy (AFM) images of the drop-casted solution (**Figure 4.2a** and **b**). The colloids were precipitated from solution by adding saturated aqueous NaCl and methanol, washed by Soxhlet extraction using methanol, and activated by supercritical CO₂ drying. The resulting powder product was exceptionally crystalline and porous, as confirmed by PXRD and N₂ adsorption isotherms of the isolated colloids (**Figure 4.2c** and **d**). The PXRD pattern of the COF exhibited sharp <100> as

well as $\langle 110 \rangle$, $\langle 200 \rangle$, $\langle 210 \rangle$, $\langle 220 \rangle$ and $\langle 001 \rangle$ higher order Bragg diffraction peaks, consistent with an eclipsed model of the COF and reported powder patterns.³²⁹ Analysis of the N_2 adsorption isotherm provided a Brunauer–Emmett–Teller (BET) surface area of $3500 \text{ m}^2 \text{ g}^{-1}$, from which nonlocal density functional theory analysis provided a narrow pore width distribution centered at 3.2 nm (**Figure 4.2d** and **S1**). In considering the BET surface area as a metric of COF materials quality, this value one of the highest for **TAPB-DMTA COF** reported thus far. These bulk characterization techniques collectively indicate that polymerization of **TAPB-DMTA COF** under this condition provides the target material in excellent quality.

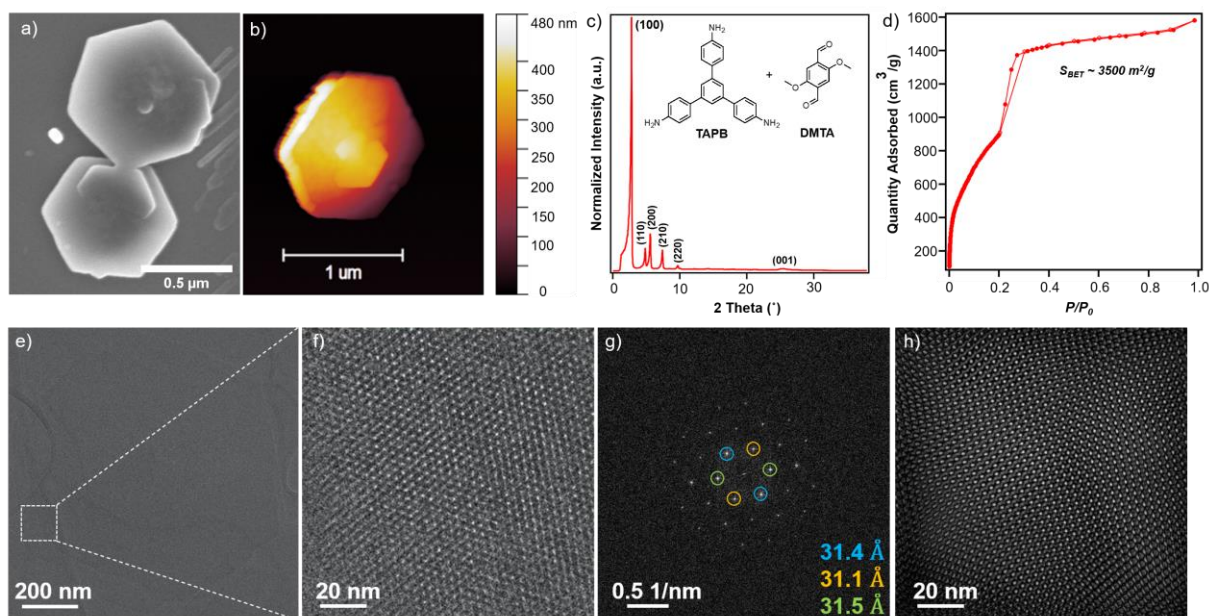


Figure 4.2. (a) SEM and (b) AFM images, (c) PXRD and (d) N_2 adsorption isotherms of 1 μm sized **TAPB-DMTA COF** single crystals. (e) Lattice-resolution HRTEM images of a **TAPB-DMTA COF** crystal with consistent lattice fringes extending across the entire particle. (f) Region of interest at higher magnification and (g) FFT of the boxed region in (e), showing the predominant, color-coded fringe spacing of $\sim 31.5 \text{ \AA}$, d_{100} . (h) Magnified image in (f) after applying a bandpass filter.

The 1 μm -sized **TAPB-DMTA COF** hexagonal platelets were subsequently analyzed by low-dose, high-resolution transmission electron microscopy (HRTEM) to further visualize their morphology, size, aspect ratio, and crystallinity (**Figure 4.2e-h**). TEM imaging at low magnification revealed that the COF platelets have uniform six-fold symmetry and are hexagonally faceted, consistent

with their SEM and AFM images (**Figure 4.2**). The COF crystals seemed to preferentially orient with their intersheet stacking dimension normal to the TEM substrate, which is likely due to their z-dimension (particle thickness) being smaller than their lateral dimension (**Figure 4.2b**). Furthermore, lattice-resolution images of individual COF particle show that they are single-crystalline (**Figure 4.2e-h**), as consistent and continuous lattice fringes extend throughout the particles. For the particle selected in **Figure 4.2e**, the fringe spacing is ~ 31.5 Å (fitting d_{100} for **TAPB-DMTA COF**), as measured by fast Fourier transform (FFT; **Figure 4.2g**). The FFT patterns of additionally highlighted center and edges of the particle in **Figure 4.S2** also exhibited clear d_{100} features at 31.5 Å. Taken together, HRTEM images and the FFT pattern of the **TAPB-DMTA COF** crystals corroborated their single crystalline nature.

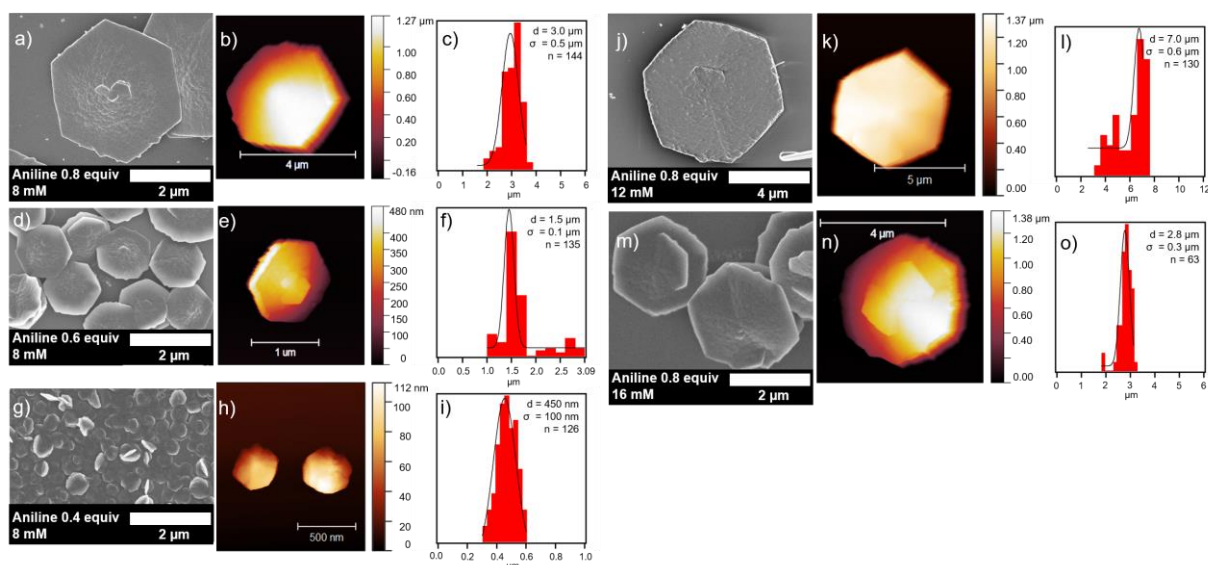


Figure 4.3. SEM and AFM images, and histogram size analysis for **TAPB-DMTA COF** crystals synthesized under the monomer concentration of 8 mM and aniline loading of 0.8 equiv [(a), (b), and (c)], 0.6 equiv [(d), (e), and (f)] or 0.4 equiv [(g), (h), and (i)], and monomer concentration of 12 mM [(j), (k), and (l)] or 16 mM [(m), (n), and (o)] and aniline loading of 0.8 equiv with respect to the aldehyde functional group.

The **TAPB-DMTA COF** crystals sizes can further grow to reach 20 μm in diameter by optimizing the monomer concentration, aniline loadings, and temperature of the reaction mixture (**Figure 4.3** and **4**; see Supporting Information for detailed procedures). As shown in **Figure 4.3**, changing the

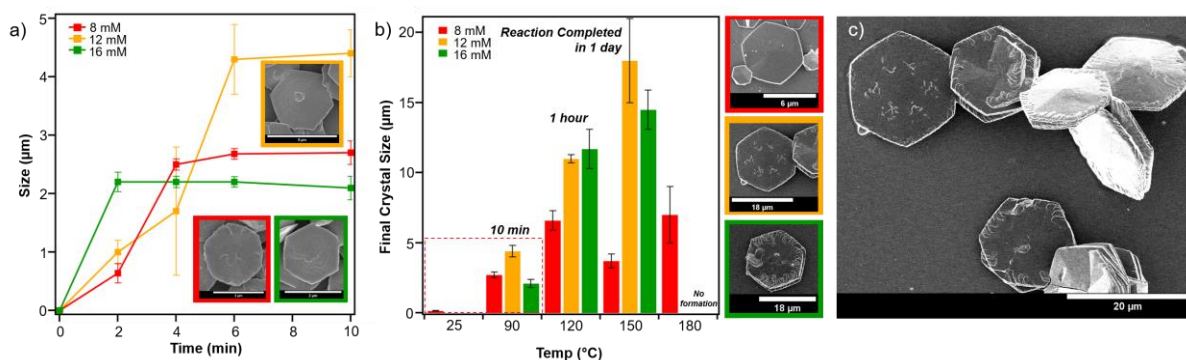


Figure 4.4. (a) Evolution of **TAPB-DMTA COF** crystal sizes with time and (b) final **TAPB-DMTA COF** crystal sizes with respect to increasing reaction temperature under the monomer concentration of 8 mM (red square), 12 mM (yellow square), and 16 mM (green square). For (a) and (b) 0.8 equiv of aniline per aldehyde functional group are added for each concentration. (c) SEM images of 20 µm sized **TAPB-DMTA COF** crystals.

monomer concentration and the aniline loadings at the initial reaction temperature of 90 °C results in a broad range of final **TAPB-DMTA COF** crystal sizes from 450 nm to 7.0 µm in diameter and 100 nm to 1.4 µm in thickness. In general, increasing the monomer concentration from 8 to 12 mM and the aniline loading from 0.4 to 0.8 equiv with respect to the aldehyde functional group results in a larger crystal. As such a 12 mM monomer solution with the aniline loading of 0.8 equiv in benzonitrile at 90 °C yielded the largest **TAPB-DMTA COF** crystal of 7.0 µm in diameter and 1.4 µm in thickness. While monitoring the COF synthesis at 90 °C, however, we observed that the COF particles nucleated and stopped growing within the first few minutes of the reaction. Specifically, upon isolating and imaging **TAPB-DMTA COF** crystals in the initial stages of the reaction, the COF growth in the 8 mM, 12 mM and 16 mM reaction mixture was observed to stop in 4, 6 and 2 minutes, respectively (**Figure 4.4a**). This was undesirable as it indicated that the rate of nucleation was much faster than the rate of COF growth at 90 °C. We hypothesized that increasing the reaction temperature would shift the equilibrium towards promoting COF growth. Consistent with our hypothesis, the growth of the COFs was completed at a much later time point and the final crystal sizes increased with higher temperature, such that the largest 20-µm sized

TAPB-DMTA COF crystals were obtained at 150 °C. No COF formation occurred at 180 °C, at which both nucleation and growth may be too slow (**Figure 4.4b** and **c**). Taken together, the size of **TAPB-DMTA COF** crystals can be fine-tuned by varying the monomer concentration, aniline loadings, and temperature of the reaction mixture, which emphasizes the high modularity of the reaction condition.

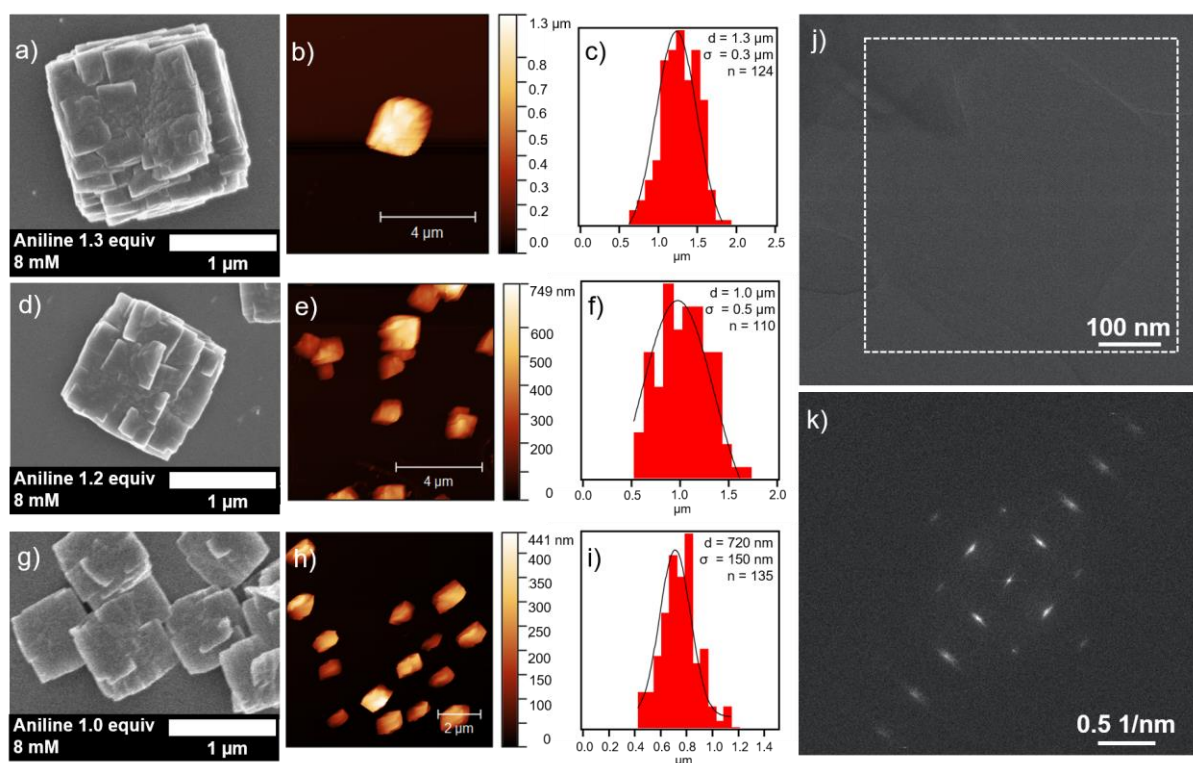


Figure 4.5. SEM and AFM images, and histogram size analysis for **TAPPy-PDA COF** crystals synthesized under the monomer concentration of 8 mM and aniline loading of 1.3 equiv [(a), (b), and (c)], 1.2 equiv [(d), (e), and (f)] or 1.0 equiv [(g), (h), and (i)]. (j) Lattice-resolution HRTEM images of a **TAPPy-PDA COF** crystal with uniform lattice fringes extending across the entire particle. (k) FFT of the boxed region number in (j).

To probe the generality of the synthetic methodology, we prepared another hexagonal net, **TAPB-Methyl COF** derived from 2,5-dimethylterephthalaldehyde (**Methyl**) and two square nets, **TAPPy-PDA** and **TAPPy-Thiophene COFs** derived from 1,3,5,8-tetra(4-aminophenyl)pyrene (**TAPPy**) and terephthalaldehyde (**PDA**), and thieno[3,2-b]thiophene-2,5-dicarboxaldehyde (**Thiophene**), respectively. The COFs were synthesized under the similar reaction conditions as **TAPB-DMTA**

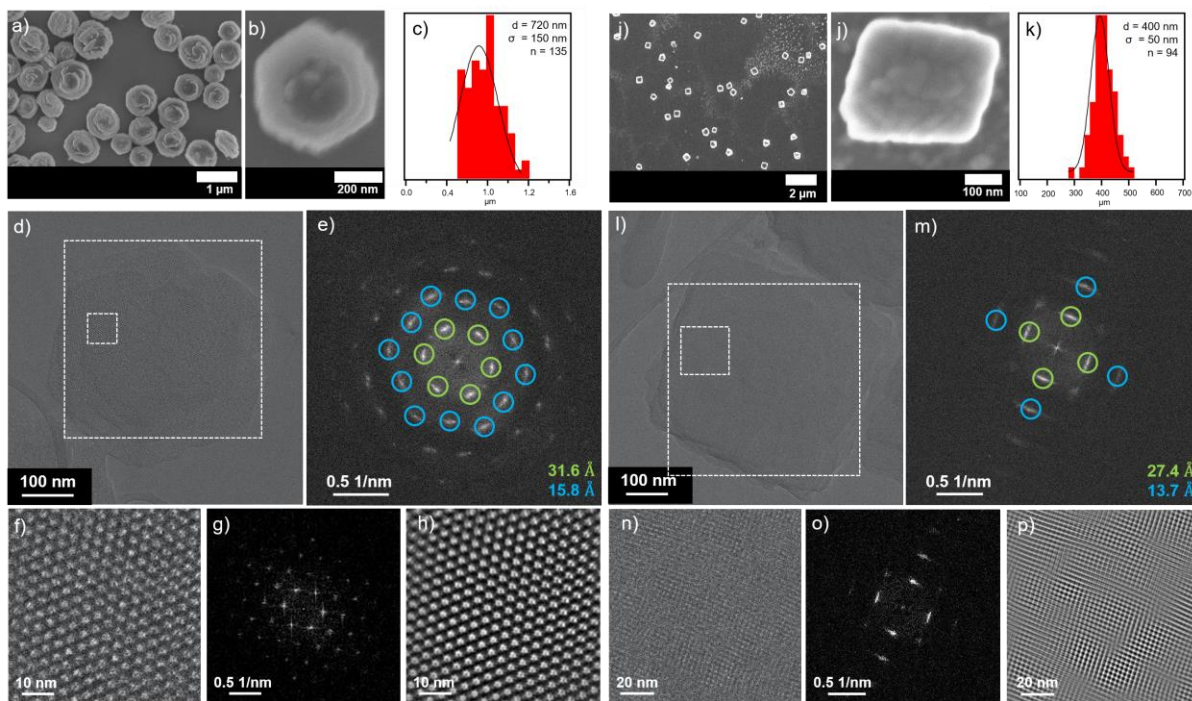


Figure 4.6 Low- and high-magnification SEM images and size analysis histograms of 720 nm sized **TAPB-Methyl COF** [(a), (b), and (c)] and 400 nm sized **TAPPy-Thiophene COF** single crystals [(i), (j), and (k)]. Lattice-resolution HRTEM images of a (d) **TAPPy-PDA COF** and (l) **TAPPy-Thiophene COF** crystal with consistent lattice fringes extending across the entire particle. FFT of the (e) larger and (g) smaller boxed region number in (d). (f) Region of interest at higher magnification corresponding to the smaller boxed region in (d). (h) Magnified image in (f) after applying a bandpass filter. FFT of the (m) larger and (o) smaller boxed region number in (l). (n) Region of interest at higher magnification corresponding to the smaller boxed region in (l). (p) Magnified image in (n) after applying a bandpass filter.

COF with minor optimization (**Figure 4.5** and **6**; see Supporting Information for detailed procedures). These yielded **TAPPy-PDA COF** crystals of varying diameters from 720 nm to 1.3 μm with increasing aniline loadings from 1.0 to 1.3 equiv with respect to the aldehyde functional group, and **TAPB-Methyl** and **TAPPy-Thiophene COF** crystals of 720 nm and 400 nm in diameter, respectively (**Figure 4.5** and **6**). All of the COF crystals were highly crystalline and porous, as characterized by the PXRD patterns and N_2 adsorption isotherms with the BET surface areas of $2220 \text{ m}^2 \text{ g}^{-1}$, $1640 \text{ m}^2 \text{ g}^{-1}$, and $1070 \text{ m}^2 \text{ g}^{-1}$ for **TAPB-Methyl**, **TAPPy-PDA** and **TAPPy-Thiophene COFs**, respectively (**Figure 4.S3-5**). Furthermore, HRTEM characterization indicated that all three COF networks were single-crystalline, as consistent and continuous lattice fringes

extended throughout the particles (**Figure 4.5** and **6**). The FFT patterns of **TAPB-Methyl**, **TAPPy-PDA** and **TAPPy-Thiophene COF** exhibited preeminent d_{100} and d_{110} features at 31.6 Å and 15.8 Å, 24 Å and 12 Å, and 27.4 Å and 13.7 Å, respectively. Overall, these results demonstrate that the synthetic strategy is generalizable for three different imine-linked 2D COF and highlight the versatile nature of the strategy in preparing large single crystalline imine-linked 2D COF crystals in a facile and efficient manner.

4.5 Conclusion

In conclusion, we demonstrated the synthesis of single-crystalline imine-linked 2D COF particles of four different **architectures**, composed of two hexagonal TAPB-DMTA and TAPB-Dimethyl COFs and two tetragonal TAPPy-PDA and TAPPy-Thiophene COFs. The synthetic strategy leverages both the monomer concentration, modulator loadings and reaction temperature to fine-tune the sizes of TAPB-DMTA and TAPPy-PDA COFs from 450 nm to 20 µm, and 720 nm to 1.3 µm in diameter, respectively. All of the COF crystals **reported here** exhibit excellent crystallinity and porosity, as determined from PXRD and N₂ adsorption isotherms, are faceted, as imaged by SEM and AFM, and are single-crystalline, as corroborated by HRTEM characterization. Taken together, these results demonstrate a novel synthetic strategy in which **large, single-crystalline** imine-linked 2D COFs are prepared in a highly facile and **versatile** manner. Ultimately, this work will enable the synthesis of a much broader and newer class of 2D polymer structures and exploration of their properties.

4.6 Appendix

4.6.1 Materials and Instrumentation

Materials. Reagents were purchased in reagent grade from commercial suppliers and used without further purification, unless otherwise described. Borosilicate capillaries (1.5 mm in diameter and a wall thickness of 0.01 mm) were purchased from Charles Supper.

Instrumentation.

The supercritical CO₂ drying was performed on Leica EM CPD 300. Prior to the supercritical drying process, all samples were placed in tea bags (ETS Drawstring Tea Filters, sold by English Tea Store) while wet. The tea bags containing the samples were then placed in the drying chamber. The drying chamber was first sealed, cooled, and filled with liquid CO₂, and after 2 min, the samples were vented quickly. This fill-vent cycle was repeated 99 times, after which the temperature was raised to 40 °C resulting in a chamber pressure of around 1300 psi, which is well above the critical point of CO₂. The chamber was held above the critical point for 5 min, after which the CO₂ source was turned off, and the pressure was released over a period of 5 min.

Powder X-ray diffraction (PXRD) patterns were obtained at room temperature on a STOE-STADIMP powder diffractometer equipped with an asymmetric curved Germanium monochromator (CuK α_1 radiation, $\lambda = 1.54056 \text{ \AA}$) and one-dimensional silicon strip detector (MYTHEN2 1K from DECTRIS). The line focused Cu X-ray tube was operated at 40 kV and 40 mA. The as-obtained powder samples were sandwiched between two acetate foils (polymer sample with neither Bragg reflections nor broad peaks above $10^\circ 2\theta$) mounted in flat plates with a disc

opening diameter of 8 mm and measured in transmission geometry in a rotating holder. The patterns were recorded in the 2θ range of $0\text{--}32^\circ$ for an overall exposure time of 24 min. The instrument was calibrated against a NIST Silicon standard (640d) prior to the measurement.

Gas adsorption isotherms were conducted on a Micromeritics ASAP 2420 Accelerated Surface Area and Porosity Analyzer using 15–50 mg samples in dried and tared analysis tubes equipped with filler rods and capped with a Transeal. Samples were heated to $40\text{ }^\circ\text{C}$ at a rate of $1\text{ }^\circ\text{C}/\text{min}$ and evacuated at $40\text{ }^\circ\text{C}$ for 20 min, then heated to $100\text{ }^\circ\text{C}$ at a rate of $1\text{ }^\circ\text{C}/\text{min}$ heat and evacuated at $100\text{ }^\circ\text{C}$ for 18 h. After degassing, each tube was weighed again to determine the mass of the activated sample and transferred to the analysis port of the instrument. UHP-grade (99.999% purity) N_2 was used for all adsorption measurements. N_2 isotherms were generated by incremental exposure to nitrogen up to 760 mmHg (1 atm) in a liquid nitrogen (77 K) bath. Oil-free vacuum pumps and oil-free pressure regulators were used for all measurements. Brunauer-Emmett-Teller (BET) surface areas were calculated from the linear region of the N_2 isotherm at 77 K within the pressure range P/P_0 of 0.10–0.20.

Scanning electron microscopy (SEM) images of TAPB-PDA and TAPB-DMTA COFs samples were taken on a Hitachi S4800 cFEG SEM. The samples were coated with 8 nm of Osmium using SPI OPC-60A osmium plasma coater.

Atomic force microscopy (AFM) images were collected using a Bruker Dimension Fastscan AFM in tapping mode.

Transmission electron microscopy (TEM) of the COF crystals was performed using a JEOL (JEOL USA, Inc., Peabody, MA) ARM300F GrandARM TEM operating at 300 keV equipped with a

Gatan (Gatan, Inc., Pleasanton, CA) K3-IS “direct electron” detector (FEG Emission: 15 μ A, spot size 5, 150 μ m CL aperture). The ARM300F was aligned for low-dose imaging, measuring the dose rate on the K3 detector through vacuum (no grid inserted). The dose rate used was $0.61 \text{ e}^- \text{ \AA}^{-2} \text{ s}^{-1}$ for low magnification images (5760 x 4092 pixels, binning 2), with an image exposure time of 1 s ($0.61 \text{ e}^- \text{ \AA}^{-2}$ cumulative dose per image). All image acquisition was done using the Gatan Microscopy Suite (GMS), Digital Micrograph (Gatan, Inc., Pleasanton, CA).

4.6.2 Synthetic Procedures

TAPB-DMTA COF Synthesis (450 nm – 7 μ m): A 40 mL scintillation vial was charged with benzoic acid (1.35 g, 11 mmol) and 2,5-dimethoxyterephthaldehyde (**DMTA**, 28 mg, 0.144 mmol) in benzonitrile (12, 8 or 6 mL for 8, 12 and 16 mM, respectively) and heated to 90 °C for a few minutes to ensure dissolution of each species. To the solution was added aniline (0.2, 0.3 or 0.4 mL of 0.7 M stock in benzonitrile for 0.4, 0.6 or 0.8 equiv aniline per aldehyde functional group), and 1,3,5-tris(4-aminophenyl)benzene (**TAPB**, 34 mg, 0.096 mmol). The resulting reaction mixture was held at 90 °C for 10 minutes and used for imaging with 10-fold dilution in benzonitrile. Alternatively, the COFs can be precipitated out by the addition of 0.2 mL brine and 10 mL methanol, centrifuged for 10 minutes, transferred to a tea bag or a dialysis tubing, and washed with methanol in a Soxhlet extractor for 18 h. The materials were activated by supercritical CO₂ that afforded **TAPB-DMTA COF** as yellow solids in isolated yields of 80%.

TAPB-DMTA COF Synthesis (20 μ m): A 40 mL scintillation vial was charged with benzoic acid (1.35 g, 11 mmol) and **DMTA** (28 mg, 0.144 mmol) in benzonitrile (8 mL) and heated to 150 °C for a few minutes to ensure dissolution of each species. To the solution was added aniline (0.4

mL of 0.7 M stock in benzonitrile, 0.28 mmol), and 1,3,5-tris(4-aminophenyl)benzene (**TAPB**, 34 mg, 0.096 mmol). The resulting reaction mixture was held at 150 °C for 2 days and cooled to room temperature. The COFs can be used for imaging with 10-fold dilution in benzonitrile. Alternatively, the COFs can be precipitated out by the addition of 0.2 mL brine and 10 mL methanol, centrifuged for 10 minutes, transferred to a tea bag or a dialysis tubing, and washed with methanol in a Soxhlet extractor for 18 h. The materials were activated by supercritical CO₂ that afforded **TAPB-DMTA COF** as yellow solids in isolated yields of 70%.

TAPB-Methyl COF Synthesis (720 nm): A 20 mL scintillation vial was charged with benzoic acid (0.675 g, 5.5 mmol) and 2,5-dimethylterephthaldehyde (**Methyl**, 15 mg, 0.072 mmol) in benzonitrile (3 mL) and heated to 90 °C for a few minutes to ensure dissolution of each species. To the solution was added aniline (0.1 mL of 0.7 M stock in benzonitrile, 0.07 mmol), and 1,3,5-tris(4-aminophenyl)benzene (**TAPB**, 17 mg, 0.048 mmol). The resulting reaction mixture was held at 90 °C for 10 minutes and used for imaging with 10-fold dilution in benzonitrile. Alternatively, the COFs can be precipitated out by the addition of 0.2 mL brine and 10 mL methanol, centrifuged for 10 minutes, transferred to a tea bag or a dialysis tubing, and washed with methanol in a Soxhlet extractor for 18 h. The materials were activated by supercritical CO₂ that afforded **TAPB-Methyl COF** as yellow solids in isolated yields of 80%.

TAPPy-PDA COF Synthesis (720 nm – 1.3 μm): A 40 mL scintillation vial was charged with benzoic acid (0.938 g, 7.7 mmol) and terephthaldehyde (**PDA**, 12 mg, 0.089 mmol) in benzonitrile (6 mL) and heated to 90 °C for a few minutes to ensure dissolution of each species. To the solution was added aniline (0.280, 0.340 or 0.370 mL of 0.7 M stock in benzonitrile for 1.0, 1.2 or 1.3 equiv aniline per aldehyde functional group), and 1,3,5,8-tetra(4-aminophenyl)pyrene (**TAPPy**, 28 mg,

0.050 mmol). The resulting reaction mixture was held at 90 °C for 10 minutes and used for imaging with 10-fold dilution in benzonitrile. Alternatively, the COFs can be precipitated out by the addition of 0.2 mL brine and 10 mL methanol, centrifuged for 10 minutes, transferred to a tea bag or a dialysis tubing, and washed with methanol in a Soxhlet extractor for 18 h. The materials were activated by supercritical CO₂ that afforded **TAPPy-PDA COF** as red solids in isolated yields of 90%.

TAPPy-Thiophene COF Synthesis (720 nm): A 40 mL scintillation vial was charged with benzoic acid (0.938 g, 7.7 mmol) and thieno[3,2-b]thiophene-2,5-dicarboxaldehyde (**Thiophene**, 17 mg, 0.089 mmol) in benzonitrile (6 mL) and heated to 90 °C for a few minutes to ensure dissolution of each species. To the solution was added aniline (0.230 mL of 0.7 M stock in benzonitrile, 0.16 mmol), and 1,3,5,8-tetra(4-aminophenyl)pyrene (**TAPPy**, 28 mg, 0.050 mmol). The resulting reaction mixture was held at 90 °C for 10 minutes and used for imaging with 10-fold dilution in benzonitrile. Alternatively, the COFs can be precipitated out by the addition of 0.2 mL brine and 10 mL methanol, centrifuged for 10 minutes, transferred to a tea bag or a dialysis tubing, and washed with methanol in a Soxhlet extractor for 18 h. The materials were activated by supercritical CO₂ that afforded **TAPPy-Thiophene COF** as dark red solids in isolated yields of 90%.

4.6.3 Additional Images and Characterization

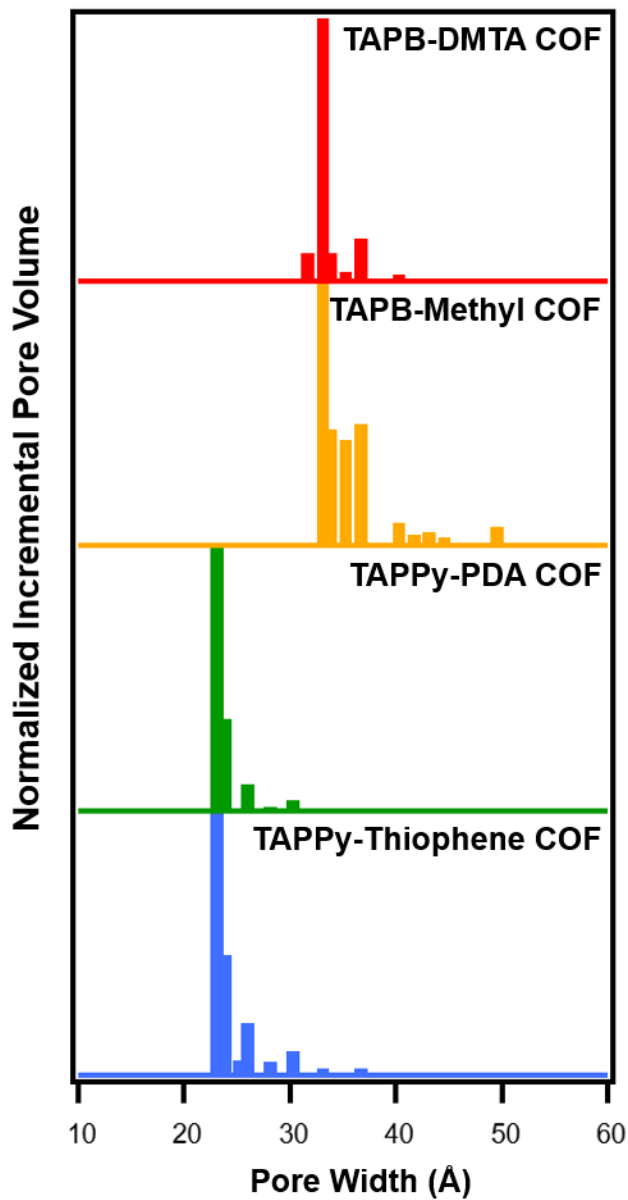


Figure 4.S1 Pore size distributions of **TAPB-DMTA COF** (red), **TAPB-Methyl COF** (yellow), **TAPPy-PDA COF** (green), and **TAPPy-Thiophene COF** (blue).

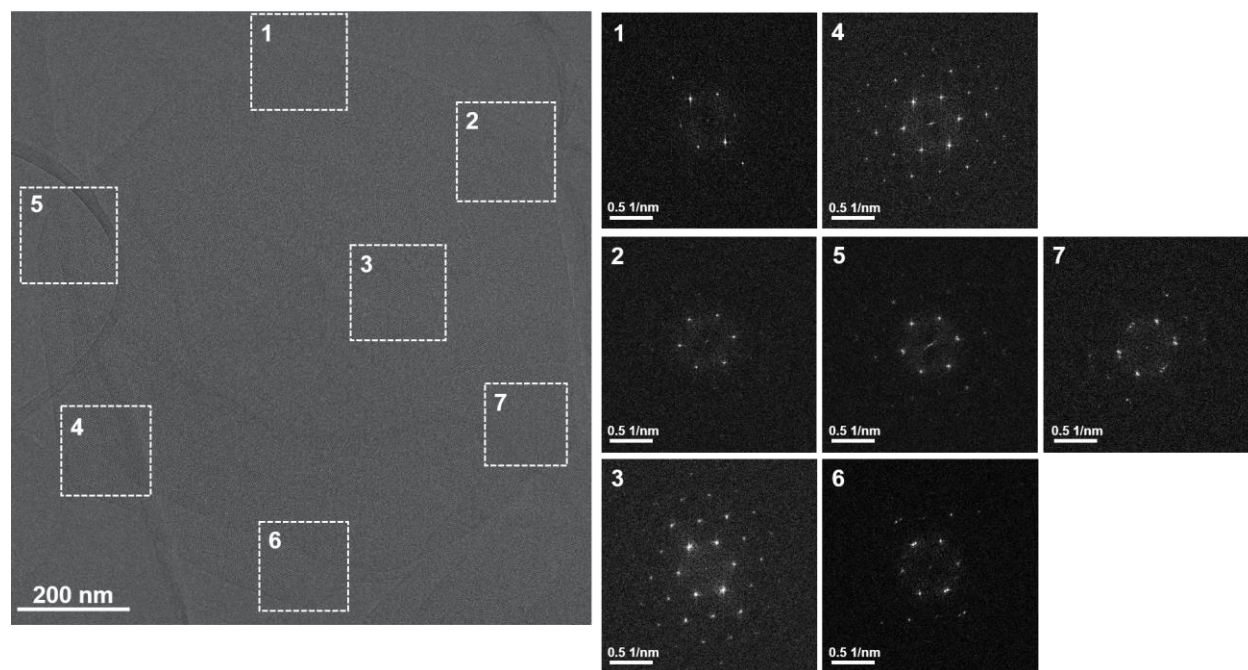


Figure 4.S2 FFT patterns of the various boxed regions of the lattice-resolution HRTEM image of a **TAPB-DMTA COF** crystal on the left, showing the predominant fringe spacing of $\sim 31.5 \text{ \AA}$, d_{100} .

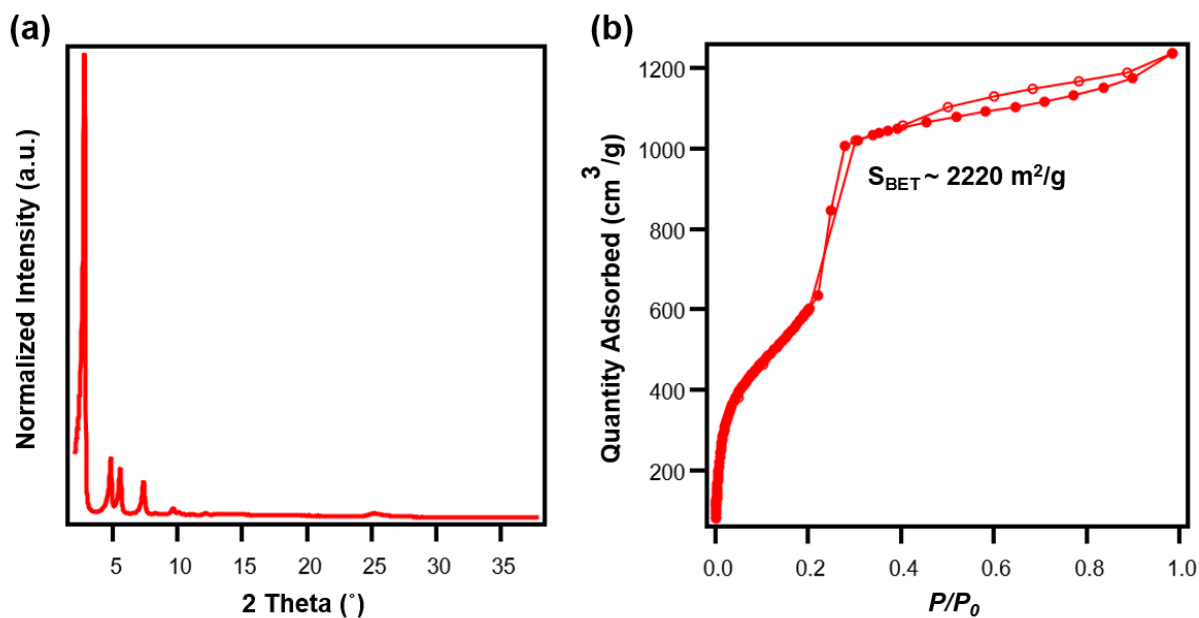


Figure 4.S3 (a) PXRD and (b) N₂ adsorption isotherm of TAPB-Methyl COF.

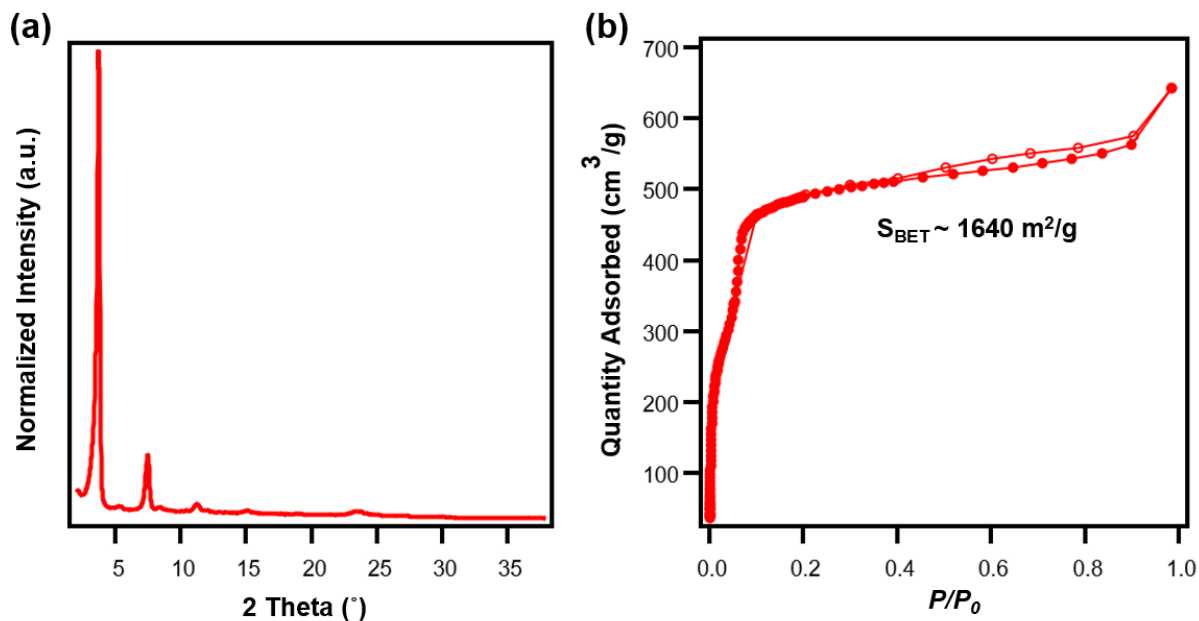


Figure 4.S4 (a) PXRD and (b) N₂ adsorption isotherm of TAPPy-PDA COF.

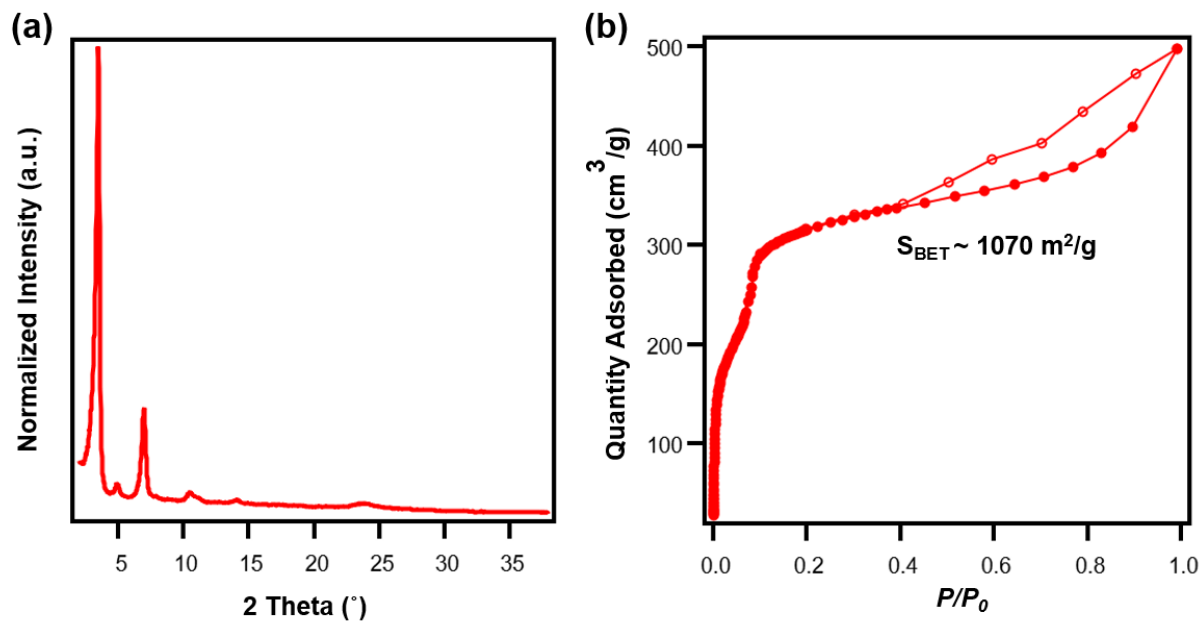


Figure 4.S5 (a) PXRD and (b) N₂ adsorption isotherm of **TAPPy-Thiophene COF**.

4.6.4 BET Plots for N₂ Isotherm

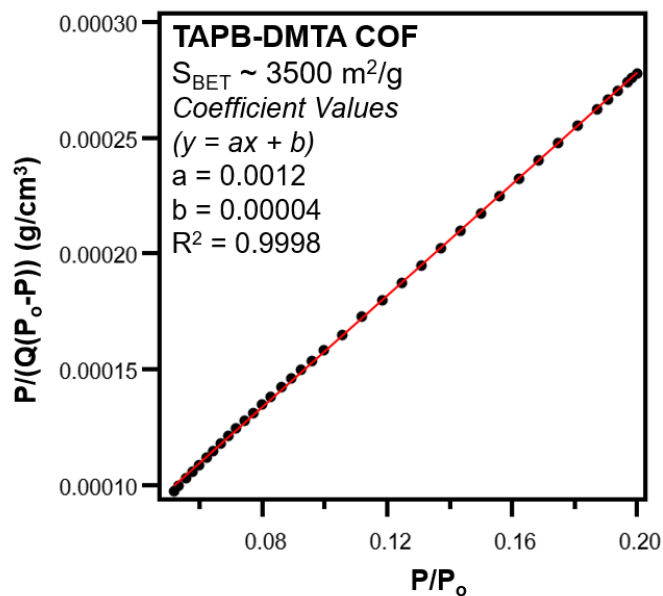


Figure 4.S6 BET plot of TAPB-DMTA COF.

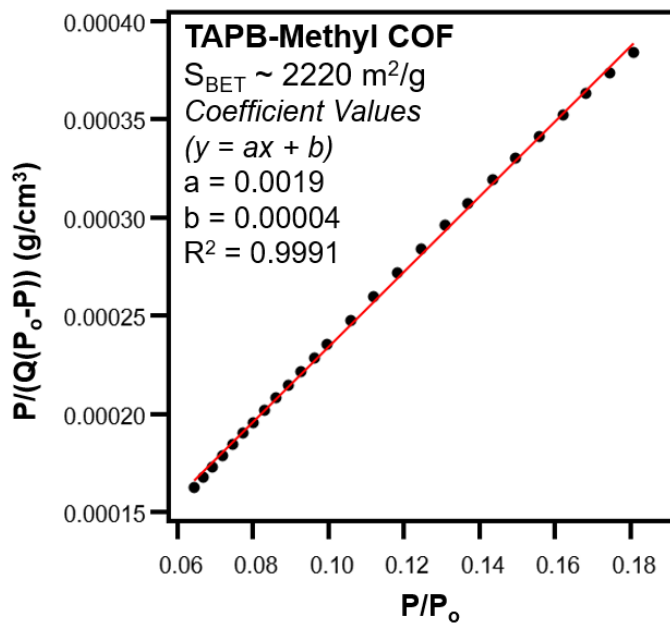


Figure 4.S7 BET plot of TAPB-Methyl COF.

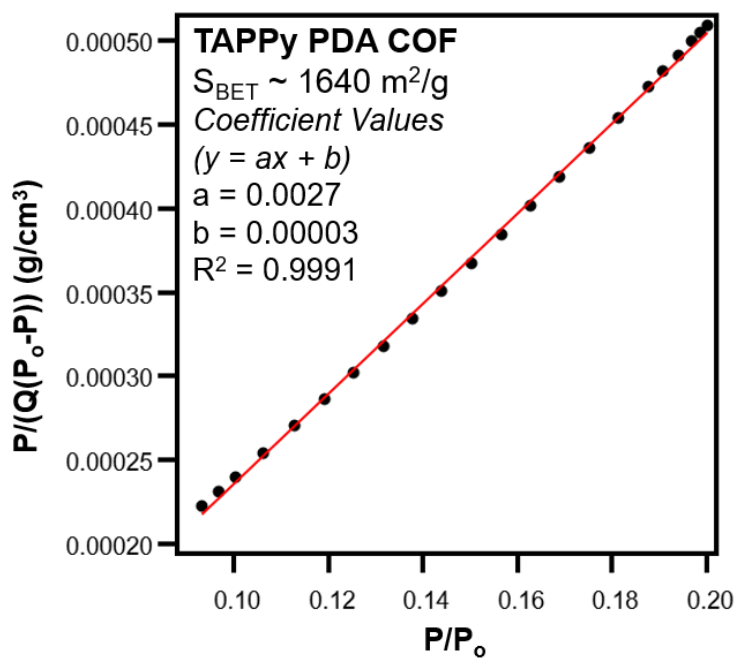


Figure 4.S8 BET plot of TAPPy-PDA COF.

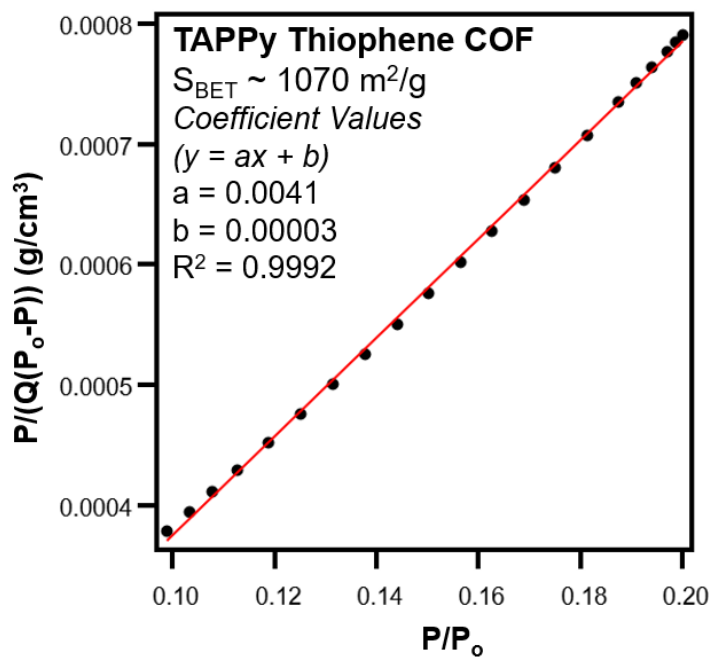


Figure 4.S9 BET plot of TAPPy-Thiophene COF.

5. References

1. Li, R. L.; Flanders, N. C.; Evans, A. M.; Ji, W.; Castano, I.; Chen, L. X.; Gianneschi, N. C.; Dichtel, W. R., Controlled growth of imine-linked two-dimensional covalent organic framework nanoparticles. *Chem. Sci.* **2019**, *10*, 3796-3801.
2. Evans, A. M.; Castano, I.; Brumberg, A.; Parent, L. R.; Corcos, A. R.; Li, R. L.; Flanders, N. C.; Gosztola, D. J.; Gianneschi, N. C.; Schaller, R. D.; Dichtel, W. R., Emissive Single-Crystalline Boroxine-Linked Colloidal Covalent Organic Frameworks. *J. Am. Chem. Soc.* **2019**, *141*, 19728-19735.
3. Evans, A. M.; Parent, L. R.; Flanders, N. C.; Bisbey, R. P.; Vitaku, E.; Chen, L. X.; Gianneschi, N. C.; Dichtel, W. R., Seeded growth of single-crystal two-dimensional covalent organic frameworks. *Science* **2018**, *361*, 52-57.
4. Han, X.; Zhang, J.; Huang, J.; Wu, X.; Yuan, D.; Liu, Y.; Cui, Y., Chiral induction in covalent organic frameworks. *Nat. Commun.* **2018**, *9*, 1-10.
5. Burke, D. W.; Sun, C.; Castano, I.; Flanders, N. C.; Evans, A. M.; Vitaku, E.; McLeod, D. C.; Lambeth, R. H.; Chen, L. X.; Gianneschi, N. C.; Dichtel, W., Acid Exfoliation of Imine-linked Covalent Organic Frameworks Enables Solution Processing into Crystalline Thin Films. *Angew. Chem. Int. Ed.* **2020**, *59*, 5165-5171.
6. Das, G.; Prakasam, T.; Addicoat, M. A.; Sharma, S. K.; Ravaux, F.; Mathew, R.; Baias, M.; Jagannathan, R.; Olson, M. A.; Trabolsi, A., Azobenzene-Equipped Covalent Organic Framework: Light-Operated Reservoir. *J. Am. Chem. Soc.* **2019**, *141*, 19078-19087.

7. Wang, P.; Chen, X.; Jiang, Q.; Addicoat, M.; Huang, N.; Dalapati, S.; Heine, T.; Huo, F.; Jiang, D., High-Precision Size Recognition and Separation in Synthetic 1D Nanochannels. *Angew. Chem. Int. Ed.* **2019**, *131*, 16069-16074.
8. Sick, T.; Rotter, J. M.; Reuter, S.; Kandambeth, S.; Bach, N. N.; Döblinger, M.; Merz, J.; Clark, T.; Marder, T. B.; Bein, T., Switching on and off Interlayer Correlations and Porosity in 2D Covalent Organic Frameworks. *J. Am. Chem. Soc.* **2019**, *141*, 12570-12581.
9. Vitaku, E.; Dichtel, W. R., Synthesis of 2D Imine-Linked Covalent Organic Frameworks through Formal Transimination Reactions. *J. Am. Chem. Soc.* **2017**, *139*, 12911-12914.
10. Li, Rebecca L.; Flanders, N. C.; Evans, A. M.; Ji, W.; Castano, I.; Chen, L. X.; Gianneschi, N. C.; Dichtel, W. R., Controlled growth of imine-linked two-dimensional covalent organic framework nanoparticles. *Chem. Sci.* **2019**, *10*, 3796-3801.
11. Ding, S.-Y.; Dong, M.; Wang, Y.-W.; Chen, Y.-T.; Wang, H.-Z.; Su, C.-Y.; Wang, W., Thioether-Based Fluorescent Covalent Organic Framework for Selective Detection and Facile Removal of Mercury(II). *J. Am. Chem. Soc.* **2016**, *138*, 3031-3037.
12. Cui, D.; MacLeod, J. M.; Ebrahimi, M.; Rosei, F., Selective binding in different adsorption sites of a 2D covalent organic framework. *CrystEngComm* **2017**, *19*, 4927-4932.
13. Lehn, J.-M.; Eliseev, A. V., Dynamic combinatorial chemistry. *Science* **2001**, *291*, 2331-2332.
14. Lehn, J. M., Dynamic combinatorial chemistry and virtual combinatorial libraries. *Chem. Eur. J.* **1999**, *5*, 2455-2463.
15. Lutz, J.-F.; Lehn, J.-M.; Meijer, E.; Matyjaszewski, K., From precision polymers to complex materials and systems. *Nat. Rev. Mater.* **2016**, *1*, 1-14.

16. Lehn, J.-M., From supramolecular chemistry towards constitutional dynamic chemistry and adaptive chemistry. *Chem. Soc. Rev.* **2007**, *36*, 151-160.
17. Rowan, S. J.; Cantrill, S. J.; Cousins, G. R. L.; Sanders, J. K. M.; Stoddart, J. F., Dynamic Covalent Chemistry. *Angew. Chem. Int. Ed.* **2002**, *41*, 898-952.
18. Fyfe, M. C.; Stoddart, J. F., Synthetic supramolecular chemistry. *Acc. Chem. Res.* **1997**, *30*, 393-401.
19. Fujita, M., *Molecular self-assembly: organic versus inorganic approaches*. Springer: 2003; Vol. 96.
20. Fujita, M., Metal-directed self-assembly of two-and three-dimensional synthetic receptors. *Chem. Soc. Rev.* **1998**, *27*, 417-425.
21. Tashiro, K.; Aida, T., Metalloporphyrin hosts for supramolecular chemistry of fullerenes. *Chem. Soc. Rev.* **2007**, *36*, 189-197.
22. Aida, T., On Supramolecular Polymerization: Interview with Takuzo Aida. *Adv. Mater.* **2020**, *32*, 1905445.
23. Hoeben, F. J.; Jonkheijm, P.; Meijer, E.; Schenning, A. P., About supramolecular assemblies of π -conjugated systems. *Chem. Rev.* **2005**, *105*, 1491-1546.
24. De Greef, T. F.; Smulders, M. M.; Wolfs, M.; Schenning, A. P.; Sijbesma, R. P.; Meijer, E., Supramolecular polymerization. *Chem. Rev.* **2009**, *109*, 5687-5754.
25. Brunsveld, L.; Folmer, B.; Meijer, E. W.; Sijbesma, R., Supramolecular polymers. *Chem. Rev.* **2001**, *101*, 4071-4098.
26. Diercks, C. S.; Yaghi, O. M., The atom, the molecule, and the covalent organic framework. *Science* **2017**, *355*, 923.

27. O'Keeffe, M.; Yaghi, O. M., Deconstructing the crystal structures of metal–organic frameworks and related materials into their underlying nets. *Chem. Rev.* **2012**, *112*, 675-702.
28. Liu, Y.; O'Keeffe, M.; Treacy, M. M.; Yaghi, O. M., The geometry of periodic knots, polycatenanes and weaving from a chemical perspective: a library for reticular chemistry. *Chem. Soc. Rev.* **2018**, *47*, 4642-4664.
29. Zhou, H.-C.; Long, J. R.; Yaghi, O. M., Introduction to metal–organic frameworks. *Chem. Rev.* **2012**.
30. Long, J. R.; Yaghi, O. M., The pervasive chemistry of metal–organic frameworks. *Chem. Soc. Rev.* **2009**, *38*, 1213-1214.
31. Ockwig, N. W.; Delgado-Friedrichs, O.; O'Keeffe, M.; Yaghi, O. M., Reticular chemistry: occurrence and taxonomy of nets and grammar for the design of frameworks. *Acc. Chem. Res.* **2005**, *38*, 176-182.
32. Tranchemontagne, D. J.; Mendoza-Cortés, J. L.; O'Keeffe, M.; Yaghi, O. M., Secondary building units, nets and bonding in the chemistry of metal–organic frameworks. *Chem. Soc. Rev.* **2009**, *38*, 1257-1283.
33. Robson, R.; Abrahams, B. F.; Batten, S. R.; Gable, R. W.; Hoskins, B. F.; Liu, J., Crystal engineering of novel materials composed of infinite two- and three-dimensional frameworks. ACS Publications: 1992.
34. Robson, R., A net-based approach to coordination polymers. *Dalton Trans.* **2000**, 3735-3744.
35. Abrahams, B. F.; Hoskins, B. F.; Robson, R., A new type of infinite 3D polymeric network containing 4-connected, peripherally-linked metalloporphyrin building blocks. *J. Am. Chem. Soc.* **1991**, *113*, 3606-3607.

36. Dresselhaus, M. S.; Araujo, P. T., Perspectives on the 2010 nobel prize in physics for graphene. ACS Publications: 2010.
37. Novoselov, K.; Mishchenko, A.; Carvalho, A.; Neto, A. C., 2D materials and van der Waals heterostructures. *Science* **2016**, *353*, aac9439.
38. Novoselov, K., Nobel lecture: Graphene: Materials in the flatland. *Rev. Mod. Phys.* **2011**, *83*, 837.
39. Geim, A. K., Random walk to graphene (Nobel Lecture). *Angew. Chem. Int. Ed.* **2011**, *50*, 6966-6985.
40. Zhang, H.; Cheng, H.-M.; Ye, P., 2D nanomaterials: beyond graphene and transition metal dichalcogenides. *Chem. Soc. Rev.* **2018**, *47*, 6009-6012.
41. Manzeli, S.; Ovchinnikov, D.; Pasquier, D.; Yazyev, O. V.; Kis, A., 2D transition metal dichalcogenides. *Nat. Rev. Mater.* **2017**, *2*, 17033.
42. Li, H.; Li, Y.; Aljarb, A.; Shi, Y.; Li, L.-J., Epitaxial growth of two-dimensional layered transition-metal dichalcogenides: growth mechanism, controllability, and scalability. *Chem. Rev.* **2017**, *118*, 6134-6150.
43. Ma, Y.; Li, B.; Yang, S., Ultrathin two-dimensional metallic nanomaterials. *Mater. Chem. Front.* **2018**, *2*, 456-467.
44. Han, G. H.; Duong, D. L.; Keum, D. H.; Yun, S. J.; Lee, Y. H., Van der Waals metallic transition metal dichalcogenides. *Chem. Rev.* **2018**, *118*, 6297-6336.
45. Zhu, Y.; Ji, H.; Cheng, H.-M.; Ruoff, R. S., Mass production and industrial applications of graphene materials. *Nat. Sci. Rev.* **2018**, *5*, 90-101.

46. Zhao, G.; Li, X.; Huang, M.; Zhen, Z.; Zhong, Y.; Chen, Q.; Zhao, X.; He, Y.; Hu, R.; Yang, T.; Ruoff, R., The physics and chemistry of graphene-on-surfaces. *Chem. Soc. Rev.* **2017**, *46*, 4417-4449.
47. Custelcean, R., Anions in crystal engineering. *Chem. Soc. Rev.* **2010**, *39*, 3675-3685.
48. Biradha, K.; Santra, R., Crystal engineering of topochemical solid state reactions. *Chem. Soc. Rev.* **2013**, *42*, 950-967.
49. Krishnamohan Sharma, C., Crystal engineering—where do we go from here? *Cryst. Growth Des.* **2002**, *2*, 465-474.
50. Desiraju, G., Crystal engineering: a holistic view. *Chem. Soc. Rev.* **2007**, *46*, 8342-8356.
51. Reichenbacher, K.; Süß, H. I.; Hulliger, J., Fluorine in crystal engineering—“the little atom that could”. *Chem. Soc. Rev.* **2005**, *34*, 22-30.
52. Moulton, B.; Zaworotko, M. J., From molecules to crystal engineering: supramolecular isomerism and polymorphism in network solids. *Chem. Rev.* **2001**, *101*, 1629-1658.
53. Aakeröy, C. B.; Seddon, K. R., The hydrogen bond and crystal engineering. *Chem. Soc. Rev.* **1993**, *22*, 397-407.
54. Desiraju, G. R., Supramolecular synthons in crystal engineering—a new organic synthesis. *Angew. Chem. Int. Ed.* **1995**, *34*, 2311-2327.
55. Cote, A. P.; Benin, A. I.; Ockwig, N. W.; O'Keeffe, M.; Matzger, A. J.; Yaghi, O. M., Porous, Crystalline, Covalent Organic Frameworks. *Science* **2005**, *310*, 1166-1170.
56. Chen, X.; Geng, K.; Liu, R.; Tan, K. T.; Gong, Y.; Li, Z.; Tao, S.; Jiang, Q.; Jiang, D., Covalent Organic Frameworks: Chemical Approaches to Designer Structures and Built-In Functions. *Angew. Chem. Int. Ed.* **2020**, *59*, 5050-5091.

57. Geng, K.; He, T.; Liu, R.; Dalapati, S.; Tan, K. T.; Li, Z.; Tao, S.; Gong, Y.; Jiang, Q.; Jiang, D., Covalent Organic Frameworks: Design, Synthesis, and Functions. *Chem. Rev.* **2020**.
58. Li, Y.; Chen, W.; Xing, G.; Jiang, D.; Chen, L., New synthetic strategies toward covalent organic frameworks. *Chem. Soc. Rev.* **2020**.
59. Jin, E.; Asada, M.; Xu, Q.; Dalapati, S.; Addicoat, M. A.; Brady, M. A.; Xu, H.; Nakamura, T.; Heine, T.; Chen, Q.; Jiang, D., Two-dimensional sp² carbon-conjugated covalent organic frameworks. *Science* **2017**, *357*, 673-676.
60. Zhang, B.; Wei, M.; Mao, H.; Pei, X.; Alshimri, S. A.; Reimer, J. A.; Yaghi, O. M., Crystalline dioxin-linked covalent organic frameworks from irreversible reactions. *J. Am. Chem. Soc.* **2018**, *140*, 12715-12719.
61. Jin, E.; Lan, Z.; Jiang, Q.; Geng, K.; Li, G.; Wang, X.; Jiang, D., 2D sp² Carbon-Conjugated Covalent Organic Frameworks for Photocatalytic Hydrogen Production from Water. *Chem* **2019**, *5*, 1632-1647.
62. Zhuang, X.; Zhao, W.; Zhang, F.; Cao, Y.; Liu, F.; Bi, S.; Feng, X., A two-dimensional conjugated polymer framework with fully sp²-bonded carbon skeleton. *Polym. Chem.* **2016**, *7*, 4176-4181.
63. Lyu, H.; Diercks, C. S.; Zhu, C.; Yaghi, O. M., Porous Crystalline Olefin-Linked Covalent Organic Frameworks. *J. Am. Chem. Soc.* **2019**, *141*, 6848-6852.
64. Lyle, S. J.; Waller, P. J.; Yaghi, O. M., Covalent organic frameworks: organic chemistry extended into two and three dimensions. *Trends in Chemistry* **2019**.
65. Waller, P. J.; Gandara, F.; Yaghi, O. M., Chemistry of Covalent Organic Frameworks. *Acc. Chem. Res.* **2015**, *48*, 3053-3063.

66. Waller, P. J.; Lyle, S. J.; Osborn Popp, T. M.; Diercks, C. S.; Reimer, J. A.; Yaghi, O. M., Chemical Conversion of Linkages in Covalent Organic Frameworks. *J. Am. Chem. Soc.* **2016**, *138*, 15519-15522.
67. Segura, J. L.; Mancheno, M. J.; Zamora, F., Covalent organic frameworks based on Schiff-base chemistry: synthesis, properties and potential applications. *Chem Soc Rev* **2016**, *45*, 5635-5671.
68. Zhao, W.; Xia, L.; Liu, X., Covalent Organic Frameworks (COFs): Perspectives of Industrialization. *CrystEngComm* **2018**, Ahead of Print.
69. Kandambeth, S.; Dey, K.; Banerjee, R., Covalent organic frameworks: chemistry beyond the structure. *J. Am. Chem. Soc.* **2018**, *141*, 1807-1822.
70. Banerjee, R.; Champness, N. R., Covalent organic frameworks and organic cage structures. *CrystEngComm* **2017**, *19*, 4866-4867.
71. Segura, J. L.; Mancheno, M. J.; Zamora, F., Covalent organic frameworks based on Schiff-base chemistry: synthesis, properties and potential applications. *Chem. Soc. Rev.* **2016**, *45*, 5635-5671.
72. Uribe-Romo, F. J.; Hunt, J. R.; Furukawa, H.; Klöck, C.; O’Keeffe, M.; Yaghi, O. M., A Crystalline Imine-Linked 3-D Porous Covalent Organic Framework. *J. Am. Chem. Soc.* **2009**, *131*, 4570-4571.
73. Ding, S.-Y.; Gao, J.; Wang, Q.; Zhang, Y.; Song, W.-G.; Su, C.-Y.; Wang, W., Construction of Covalent Organic Framework for Catalysis: Pd/COF-LZU1 in Suzuki-Miyaura Coupling Reaction. *J. Am. Chem. Soc.* **2011**, *133*, 19816-19822.

74. Kaleeswaran, D.; Vishnoi, P.; Murugavel, R., [3+3] Imine and β -ketoenamine tethered fluorescent covalent-organic frameworks for CO₂ uptake and nitroaromatic sensing. *J. Mater. Chem. C* **2015**, *3*, 7159-7171.
75. Chen, X.; Addicoat, M.; Jin, E.; Zhai, L.; Xu, H.; Huang, N.; Guo, Z.; Liu, L.; Irle, S.; Jiang, D., Locking Covalent Organic Frameworks with Hydrogen Bonds: General and Remarkable Effects on Crystalline Structure, Physical Properties, and Photochemical Activity. *J. Am. Chem. Soc.* **2015**, *137*, 3241-3247.
76. Wang, P.; Kang, M.; Sun, S.; Liu, Q.; Zhang, Z.; Fang, S., Imine-Linked Covalent Organic Framework on Surface for Biosensor. *Chin. J. Chem.* **2014**, *32*, 838-843.
77. Zhang, Y.-B.; Su, J.; Furukawa, H.; Yun, Y.; Gandara, F.; Duong, A.; Zou, X.; Yaghi, O. M., Single-Crystal Structure of a Covalent Organic Framework. *J. Am. Chem. Soc.* **2013**, *135*, 16336-16339.
78. Huang, W.; Jiang, Y.; Li, X.; Li, X.; Wang, J.; Wu, Q.; Liu, X., Solvothermal Synthesis of Microporous, Crystalline Covalent Organic Framework Nanofibers and Their Colorimetric Nanohybrid Structures. *ACS Appl. Mater. Interfaces* **2013**, *5*, 8845-8849.
79. Rabbani, M. G.; Sekizkardes, A. K.; Kahveci, Z.; Reich, T. E.; Ding, R.; El-Kaderi, H. M., A 2D mesoporous imine-linked covalent organic framework for high pressure gas storage applications. *Chem. - Eur. J.* **2013**, *19*, 3324-3328.
80. Daugherty, M. C.; Vitaku, E.; Li, R. L.; Evans, A. M.; Chavez, A. D.; Dichtel, W. R., Improved synthesis of β -ketoenamine-linked covalent organic frameworks via monomer exchange reactions. *Chem. Commun.* **2019**, *55*, 2680-2683.

81. Matsumoto, M.; Valentino, L.; Stiehl, G. M.; Balch, H. B.; Corcos, A. R.; Wang, F.; Ralph, D. C.; Marinas, B. J.; Dichtel, W. R., Lewis-Acid-Catalyzed Interfacial Polymerization of Covalent Organic Framework Films. *Chem.* **2018**, *4*, 308-317.
82. Smith, B. J.; Overholts, A. C.; Hwang, N.; Dichtel, W. R., Insight into the crystallization of amorphous imine-linked polymer networks to 2D covalent organic frameworks. *Chem. Commun.* **2016**, *52*, 3690-3693.
83. Corcos, A. R.; Levato, G. A.; Jiang, Z.; Evans, A. M.; Livingston, A. G.; Mariñas, B. J.; Dichtel, W. R., Reducing the Pore Size of Covalent Organic Frameworks in Thin-Film Composite Membranes Enhances Solute Rejection. *ACS Mater. Lett.* **2019**, *1*, 440-446.
84. de la Pena Ruigomez, A.; Rodriguez-San-Miguel, D.; Stylianou, K. C.; Cavallini, M.; Gentili, D.; Liscio, F.; Milita, S.; Roscioni, O. M.; Ruiz-Gonzalez, M. L.; Carbonell, C.; Maspoch, D.; Mas-Balleste, R.; Segura, J. L.; Zamora, F., Direct On-Surface Patterning of a Crystalline Lamellar Covalent Organic Framework Synthesized at Room Temperature. *Chem. - Eur. J.* **2015**, *21*, 10666-10670.
85. Liu, X.-H.; Guan, C.-Z.; Ding, S.-Y.; Wang, W.; Yan, H.-J.; Wang, D.; Wan, L.-J., On-Surface Synthesis of Single-Layered Two-Dimensional Covalent Organic Frameworks via Solid-Vapor Interface Reactions. *J. Am. Chem. Soc.* **2013**, *135*, 10470-10474.
86. Wu, Y.; Xu, H.; Chen, X.; Gao, J.; Jiang, D., A π -electronic covalent organic framework catalyst: π -walls as catalytic beds for Diels-Alder reactions under ambient conditions. *Chem. Commun.* **2015**, *51*, 10096-10098.
87. Sick, T.; Hufnagel, A. G.; Kampmann, J.; Kondofersky, I.; Calik, M.; Rotter, J. M.; Evans, A.; Doeblinger, M.; Herbert, S.; Peters, K.; Boehm, D.; Knochel, P.; Medina, D. D.;

Fattakhova-Rohlfing, D.; Bein, T., Oriented Films of Conjugated 2D Covalent Organic Frameworks as Photocathodes for Water Splitting. *J. Am. Chem. Soc.* **2018**, *140*, 2085-2092.

88. Liu, T.; Hu, X.; Wang, Y.; Meng, L.; Zhou, Y.; Zhang, J.; Chen, M.; Zhang, X., Triazine-based covalent organic frameworks for photodynamic inactivation of bacteria as type-II photosensitizers. *J. Photochem. Photobiol., B* **2017**, *175*, 156-162.

89. Dong, W.-l.; Wang, L.; Ding, H.-m.; Zhao, L.; Wang, D.; Wang, C.; Wan, L.-J., Substrate Orientation Effect in the On-Surface Synthesis of Tetrathiafulvalene-Integrated Single-Layer Covalent Organic Frameworks. *Langmuir* **2015**, *31*, 11755-11759.

90. Dalapati, S.; Addicoat, M.; Jin, S.; Sakurai, T.; Gao, J.; Xu, H.; Irle, S.; Seki, S.; Jiang, D., Rational design of crystalline supermicroporous covalent organic frameworks with triangular topologies. *Nat. Commun.* **2015**, *6*, 7786.

91. Banerjee, T.; Haase, F.; Savasci, G.; Gottschling, K.; Ochsenfeld, C.; Lotsch, B. V., Single Site Photocatalytic H₂ Evolution from Covalent Organic Frameworks with Molecular Cobaloxime Co-catalysts. *J. Am. Chem. Soc.* **2017**, Ahead of Print.

92. Sun, Q.; Aguila, B.; Ma, S., A bifunctional covalent organic framework as an efficient platform for cascade catalysis. *Mater. Chem. Front.* **2017**, *1*, 1310-1316.

93. Rozhko, E.; Bavykina, A.; Osadchii, D.; Makkee, M.; Gascon, J., Covalent organic frameworks as supports for a molecular Ni based ethylene oligomerization catalyst for the synthesis of long chain olefins. *J. Catal.* **2017**, *345*, 270-280.

94. Khattak, A. M.; Ali Ghazi, Z.; Liang, B.; Ali Khan, N.; Iqbal, A.; Li, L.; Tang, Z., A redox-active 2D covalent organic framework with pyridine moieties capable of faradaic energy storage. *J. Mater. Chem. A* **2016**, *4*, 16312-16317.

95. Aiyappa, H. B.; Thote, J.; Shinde, D. B.; Banerjee, R.; Kurungot, S., Cobalt-Modified Covalent Organic Framework as a Robust Water Oxidation Electrocatalyst. *Chem. Mater.* **2016**, *28*, 4375-4379.
96. Leng, W.; Peng, Y.; Zhang, J.; Lu, H.; Feng, X.; Ge, R.; Dong, B.; Wang, B.; Hu, X.; Gao, Y., Sophisticated Design of Covalent Organic Frameworks with Controllable Bimetallic Docking for a Cascade Reaction. *Chem. - Eur. J.* **2016**, *22*, 9087-9091.
97. Xu, S.-Q.; Zhan, T.-G.; Wen, Q.; Pang, Z.-F.; Zhao, X., Diversity of Covalent Organic Frameworks (COFs): A 2D COF Containing Two Kinds of Triangular Micropores of Different Sizes. *ACS Macro Lett.* **2016**, *5*, 99-102.
98. Zhou, T.-Y.; Xu, S.-Q.; Wen, Q.; Pang, Z.-F.; Zhao, X., One-Step Construction of Two Different Kinds of Pores in a 2D Covalent Organic Framework. *J. Am. Chem. Soc.* **2014**, *136*, 15885-15888.
99. Huang, W.; Ma, B. C.; Lu, H.; Li, R.; Wang, L.; Landfester, K.; Zhang, K. A. I., Visible-Light-Promoted Selective Oxidation of Alcohols Using a Covalent Triazine Framework. *ACS Catal.* **2017**, *7*, 5438-5442.
100. Keller, N.; Bessinger, D.; Reuter, S.; Calik, M.; Ascherl, L.; Hanusch, F. C.; Auras, F.; Bein, T., Oligothiophene-Bridged Conjugated Covalent Organic Frameworks. *J. Am. Chem. Soc.* **2017**, *139*, 8194-8199.
101. Li, C.; Li, P.; Chen, L.; Briggs, M. E.; Liu, M.; Chen, K.; Shi, X.; Han, D.; Ren, S., Pyrene-cored covalent organic polymers by thiophene-based isomers, their gas adsorption, and photophysical properties. *J. Polym. Sci., Part A: Polym. Chem.* **2017**, *55*, 2383-2389.

102. Chen, Y.; Cui, H.; Zhang, J.; Zhao, K.; Ding, D.; Guo, J.; Li, L.; Tian, Z.; Tang, Z., Surface growth of highly oriented covalent organic framework thin film with enhanced photoresponse speed. *RSC Adv.* **2015**, *5*, 92573-92576.
103. Diercks, C. S.; Lin, S.; Kornienko, N.; Kapustin, E. A.; Nichols, E. M.; Zhu, C.; Zhao, Y.; Chang, C. J.; Yaghi, O. M., Reticular Electronic Tuning of Porphyrin Active Sites in Covalent Organic Frameworks for Electrocatalytic Carbon Dioxide Reduction. *J. Am. Chem. Soc.* **2018**, *140*, 1116-1122.
104. Hynek, J.; Zelenka, J.; Rathousky, J.; Kubat, P.; Ruml, T.; Demel, J.; Lang, K., Designing Porphyrinic Covalent Organic Frameworks for the Photodynamic Inactivation of Bacteria. *ACS Appl. Mater. Interfaces* **2018**, *10*, 8527-8535.
105. Gole, B.; Stepanenko, V.; Rager, S.; Gruene, M.; Medina, D. D.; Bein, T.; Wuerthner, F.; Beuerle, F., Microtubular Self-Assembly of Covalent Organic Frameworks. *Angew. Chem. Int. Ed.* **2018**, *57*, 846-850.
106. Wang, K.; Qi, D.; Li, Y.; Wang, T.; Liu, H.; Jiang, J., Tetrapyrrole macrocycle based conjugated two-dimensional mesoporous polymers and covalent organic frameworks: From synthesis to material applications. *Coord. Chem. Rev.* **2017**, Ahead of Print.
107. Xu, K.; Dai, Y.; Ye, B.; Wang, H., Two dimensional covalent organic framework materials for chemical fixation of carbon dioxide: excellent repeatability and high selectivity. *Dalton Trans.* **2017**, *46*, 10780-10785.
108. Bhunia, S.; Das, S. K.; Jana, R.; Peter, S. C.; Bhattacharya, S.; Addicoat, M.; Bhaumik, A.; Pradhan, A., Electrochemical Stimuli-Driven Facile Metal-Free Hydrogen Evolution from Pyrene-Porphyrin-Based Crystalline Covalent Organic Framework. *ACS Appl. Mater. Interfaces* **2017**, *9*, 23843-23851.

109. Hou, Y.; Zhang, X.; Wang, C.; Qi, D.; Gu, Y.; Wang, Z.; Jiang, J., Novel imine-linked porphyrin covalent organic frameworks with good adsorption removing properties of RhB. *New J. Chem.* **2017**, *41*, 6145-6151.
110. Wang, H.; Ding, H.; Wang, C., Research progress in porphyrin-based covalent organic frameworks. *Huaxue Tongbao* **2017**, *80*, 132-138.
111. Fan, X.; Kong, F.; Kong, A.; Chen, A.; Zhou, Z.; Shan, Y., Covalent Porphyrin Framework-Derived Fe₂P@Fe₄N-Coupled Nanoparticles Embedded in N-Doped Carbons as Efficient Trifunctional Electrocatalysts. *ACS Appl. Mater. Interfaces* **2017**, *9*, 32840-32850.
112. Li, Z.-J.; Ding, S.-Y.; Xue, H.-D.; Cao, W.; Wang, W., Synthesis of -C=N- linked covalent organic frameworks via the direct condensation of acetals and amines. *Chem. Commun.* **2016**, *52*, 7217-7220.
113. Segura, J. L.; Royuela, S.; Ramos, M. M., Post-synthetic modification of covalent organic frameworks. *Chem. Soc. Rev.* **2019**, *48*, 3903-3945.
114. Wei, P.-F.; Qi, M.-Z.; Wang, Z.-P.; Ding, S.-Y.; Yu, W.; Liu, Q.; Wang, L.-K.; Wang, H.-Z.; An, W.-K.; Wang, W., Benzoxazole-linked ultrastable covalent organic frameworks for photocatalysis. *J. Am. Chem. Soc.* **2018**, *140*, 4623-4631.
115. Seo, J.-M.; Noh, H.-J.; Jeong, H. Y.; Baek, J.-B., Converting Unstable Imine-Linked Network into Stable Aromatic Benzoxazole-Linked One via Post-oxidative Cyclization. *J. Am. Chem. Soc.* **2019**, *141*, 11786-11790.
116. Pyles, D. A.; Coldren, W. H.; Eder, G. M.; Hadad, C. M.; McGrier, P. L., Mechanistic investigations into the cyclization and crystallization of benzobisoxazole-linked two-dimensional covalent organic frameworks. *Chem. Sci.* **2018**, *9*, 6417-6423.

117. Waller, P. J.; AlFaraj, Y. S.; Diercks, C. S.; Jarenwattananon, N. N.; Yaghi, O. M., Conversion of imine to oxazole and thiazole linkages in covalent organic frameworks. *J. Am. Chem. Soc.* **2018**, *140*, 9099-9103.
118. Pyles, D. A.; Crowe, J. W.; Baldwin, L. A.; McGrier, P. L., Synthesis of Benzobisoxazole-Linked Two-Dimensional Covalent Organic Frameworks and Their Carbon Dioxide Capture Properties. *ACS Macro Lett.* **2016**, *5*, 1055-1058.
119. Li, X.; Zhang, C.; Cai, S.; Lei, X.; Altoe, V.; Hong, F.; Urban, J. J.; Ciston, J.; Chan, E. M.; Liu, Y., Facile transformation of imine covalent organic frameworks into ultrastable crystalline porous aromatic frameworks. *Nat. Commun.* **2018**, *9*, 1-8.
120. Wang, P.-L.; Ding, S.-Y.; Zhang, Z.-C.; Wang, Z.-P.; Wang, W., Constructing Robust Covalent Organic Frameworks via Multicomponent Reactions. *J. Am. Chem. Soc.* **2019**, *141*, 18004-18008.
121. Liu, H.; Chu, J.; Yin, Z.; Cai, X.; Zhuang, L.; Deng, H., Covalent organic frameworks linked by amine bonding for concerted electrochemical reduction of CO₂. *Chem.* **2018**, *4*, 1696-1709.
122. Lyle, S. J.; Osborn Popp, T. M.; Waller, P. J.; Pei, X.; Reimer, J. A.; Yaghi, O. M., Multistep Solid-State Organic Synthesis of Carbamate-Linked Covalent Organic Frameworks. *J. Am. Chem. Soc.* **2019**, *141*, 11253-11258.
123. Haase, F.; Troschke, E.; Savasci, G.; Banerjee, T.; Duppel, V.; Dörfler, S.; Grundei, M. M.; Burow, A. M.; Ochsenfeld, C.; Kaskel, S.; Lotsch, B., Topochemical conversion of an imine-into a thiazole-linked covalent organic framework enabling real structure analysis. *Nat. Commun.* **2018**, *9*, 1-10.

124. Ji, W.; Xiao, L.; Ling, Y.; Ching, C.; Matsumoto, M.; Bisbey, R. P.; Helbling, D. E.; Dichtel, W. R., Removal of GenX and perfluorinated alkyl substances from water by amine-functionalized covalent organic frameworks. *J. Am. Chem. Soc.* **2018**, *140*, 12677-12681.
125. Chen, L.; Furukawa, K.; Gao, J.; Nagai, A.; Nakamura, T.; Dong, Y.; Jiang, D., Photoelectric covalent organic frameworks: converting open lattices into ordered donor-acceptor heterojunctions. *J. Am. Chem. Soc.* **2014**, *136*, 9806-9809.
126. Yang, F.; Cheng, S.; Zhang, X.; Ren, X.; Li, R.; Dong, H.; Hu, W., 2D Organic Materials for Optoelectronic Applications. *Adv. Mater.* **2018**, *30*, n/a.
127. Li, L.-l.; Liu, S.; Zhang, Q.; Hu, N.-t.; Wei, L.-m.; Yang, Z.; Wei, H., Advances in covalent organic frameworks. *Wuli Huaxue Xuebao* **2017**, *33*, 1960-1977.
128. Jin, Y. H.; Hu, Y. M.; Zhang, W., Tessellated multiporous two-dimensional covalent organic frameworks. *Nat Rev Chem* **2017**, *1*.
129. Bisbey, R. P.; Dichtel, W. R., Covalent Organic Frameworks as a Platform for Multidimensional Polymerization. *ACS Cent. Sci.* **2017**, *3*, 533-543.
130. Yaghi, O. M., Reticular Chemistry in All Dimensions. *ACS Cent. Sci.* **2019**.
131. Zhao, Y.; Guo, L.; Gandara, F.; Ma, Y.; Liu, Z.; Zhu, C.; Lyu, H.; Trickett, C. A.; Kapustin, E. A.; Terasaki, O.; Yaghi, O. M., A Synthetic Route for Crystals of Woven Structures, Uniform Nanocrystals, and Thin Films of Imine Covalent Organic Frameworks. *J. Am. Chem. Soc.* **2017**, *139*, 13166-13172.
132. Diercks, C. S.; Kalmutzki, M. J.; Yaghi, O. M., Covalent organic frameworks-organic chemistry beyond the molecule. *Molecules* **2017**, *22*, 1575/1-1575/6.
133. Ji, Q.; Lirag, R. C.; Miljanic, O. S., Kinetically controlled phenomena in dynamic combinatorial libraries. *Chem. Soc. Rev.* **2014**, *43*, 1873-1884.

134. Cougnon, F. B.; Sanders, J. K., Evolution of dynamic combinatorial chemistry. *Acc. Chem. Res.* **2012**, *45*, 2211-2221.
135. Hunt, R. A.; Otto, S., Dynamic combinatorial libraries: new opportunities in systems chemistry. *Chem. Commun.* **2011**, *47*, 847-858.
136. Matsumoto, M.; Dasari, R. R.; Ji, W.; Feriante, C. H.; Parker, T. C.; Marder, S. R.; Dichtel, W. R., Rapid, Low Temperature Formation of Imine-Linked Covalent Organic Frameworks Catalyzed by Metal Triflates. *J. Am. Chem. Soc.* **2017**, *139*, 4999-5002.
137. Chavez, A. D.; Evans, A. M.; Flanders, N. C.; Bisbey, R. P.; Vitaku, E.; Chen, L. X.; Dichtel, W. R., Equilibration of Imine-Linked Polymers to Hexagonal Macrocycles Driven by Self-Assembly. *Chem. - Eur. J.* **2018**, *24*, 3989-3993.
138. Stewart, D.; Antypov, D.; Dyer, M. S.; Pitcher, M. J.; Katsoulidis, A. P.; Blanc, F.; Rosseinsky, M. J.; Chater, P. A.; Blanc, F., Stable and ordered amide frameworks synthesised under reversible conditions which facilitate error checking. *Nat. Commun.* **2017**, *8*, 1102.
139. Tan, J.; Namuangruk, S.; Kong, W.; Kungwan, N.; Guo, J.; Wang, C., Manipulation of Amorphous-to-Crystalline Transformation: Towards the Construction of Covalent Organic Framework Hybrid Microspheres with NIR Photothermal Conversion Ability. *Angew. Chem. Int. Ed.* **2016**, *55*, 13979-13984.
140. Brus, J.; Kobera, L.; Urbanova, M.; Dousova, B.; Lhotka, M.; Kolousek, D.; Kotek, J.; Cuba, P.; Czernek, J.; Dedecek, J., Interface Induced Growth and Transformation of Polymer-Conjugated Proto-Crystalline Phases in Aluminosilicate Hybrids: A Multiple-Quantum ^{23}Na - ^{23}Na MAS NMR Correlation Spectroscopy Study. *Langmuir* **2016**, *32*, 2787-2797.

141. Kuecken, S.; Schmidt, J.; Zhi, L.; Thomas, A., Conversion of amorphous polymer networks to covalent organic frameworks under ionothermal conditions: a facile synthesis route for covalent triazine frameworks. *J. Mater. Chem. A* **2015**, *3*, 24422-24427.
142. Rambo, B. M.; Tilford, R. W.; Lanni, L. M.; Liu, J.; Lavigne, J. J., Boronate-linked materials: ranging from amorphous assemblies to highly structured networks. *Macromol. Containing Met. Met.-Like Elem.* **2009**, *9*, 255-294.
143. Zhang, G.; Tsujimoto, M.; Packwood, D.; Duong, N. T.; Nishiyama, Y.; Kadota, K.; Kitagawa, S.; Horike, S., Construction of a Hierarchical Architecture of Covalent Organic Frameworks via a Postsynthetic Approach. *J. Am. Chem. Soc.* **2018**, *140*, 2602-2609.
144. Koo, B. T.; Heden, R. F.; Clancy, P., Nucleation and growth of 2D covalent organic frameworks: polymerization and crystallization of COF monomers. *Phys. Chem. Chem. Phys.* **2017**, *19*, 9745-9754.
145. Wang, H.; He, B.; Liu, F.; Stevens, C.; Brady, M. A.; Cai, S.; Wang, C.; Russell, T. P.; Tan, T. W.; Liu, Y., Orientation transitions during the growth of imine covalent organic framework thin films. *J. Mater. Chem. C* **2017**, *5*, 5090-5095.
146. Feriante, C. H.; Jhulki, S.; Evans, A. M.; Dasari, R. R.; Slicker, K.; Dichtel, W. R.; Marder, S. R., Rapid Synthesis of High Surface Area Imine-Linked 2D Covalent Organic Frameworks by Avoiding Pore Collapse During Isolation. *Adv. Mater.* **2019**, 1905776.
147. Feriante, C.; Evans, A. M.; Jhulki, S.; Castano, I.; Strauss, M. J.; Barlow, S.; Dichtel, W. R.; Marder, S. R., New Mechanistic Insights into the Formation of Imine-Linked Two-Dimensional Covalent Organic Frameworks. *J. Am. Chem. Soc.* **2020**, *142*, 18637-18644.

148. Feriante, C. H.; Jhulki, S.; Evans, A. M.; Dasari, R. R.; Slicker, K.; Dichtel, W. R.; Marder, S. R., Rapid Synthesis of High Surface Area Imine-Linked 2D Covalent Organic Frameworks by Avoiding Pore Collapse During Isolation. *Advanced Materials* **2019**, 1905776.
149. Smith, B. J.; Dichtel, W. R., Mechanistic studies of two-dimensional covalent organic frameworks rapidly polymerized from initially homogenous conditions. *J Am Chem Soc* **2014**, *136*, 8783-9.
150. Medina, D. D.; Rotter, J. M.; Hu, Y.; Dogru, M.; Werner, V.; Auras, F.; Markiewicz, J. T.; Knochel, P.; Bein, T., Room temperature synthesis of covalent-organic framework films through vapor-assisted conversion. *J Am Chem Soc* **2015**, *137*, 1016-9.
151. Lanni, L. M.; Tilford, R. W.; Bharathy, M.; Lavigne, J. J., Enhanced Hydrolytic Stability of Self-Assembling Alkylated Two-Dimensional Covalent Organic Frameworks. *J. Am. Chem. Soc.* **2011**, *133*, 13975-13983.
152. Rodriguez-San-Miguel, D.; Zamora, F., Processing of covalent organic frameworks: an ingredient for a material to succeed. *Chem. Soc. Rev.* **2019**, Ahead of Print.
153. Sun, Q.; Aguila, B.; Perman, J.; Earl, L. D.; Abney, C. W.; Cheng, Y.; Wei, H.; Nguyen, N.; Wojtas, L.; Ma, S., Postsynthetically Modified Covalent Organic Frameworks for Efficient and Effective Mercury Removal. *J Am Chem Soc* **2017**, *139*, 2786-2793.
154. Huang, N.; Zhai, L.; Xu, H.; Jiang, D., Stable Covalent Organic Frameworks for Exceptional Mercury Removal from Aqueous Solutions. *J Am Chem Soc* **2017**, *139*, 2428-2434.
155. Ji, W.; Xiao, L.; Ling, Y.; Ching, C.; Matsumoto, M.; Bisbey, R. P.; Helbling, D. E.; Dichtel, W. R., Removal of GenX and Perfluorinated Alkyl Substances from Water by Amine-Functionalized Covalent Organic Frameworks. *J. Am. Chem. Soc.* **2018**, *140*, 12677-12681.

156. Li, Z.; Zhang, Y.; Xia, H.; Mu, Y.; Liu, X., A robust and luminescent covalent organic framework as a highly sensitive and selective sensor for the detection of Cu(2+) ions. *Chem Commun (Camb)* **2016**, *52*, 6613-6.
157. Wang, Y.; Li, G.; Yan, Y.; Hao, C.; Zhao, Z.; Hao, C., A 2D covalent organic framework as a sensor for detecting formaldehyde. *J Mol Model* **2018**, *24*, 153.
158. Wei, P.-F.; Qi, M.-Z.; Wang, Z.-P.; Ding, S.-Y.; Yu, W.; Liu, Q.; Wang, L.-K.; Wang, H.-Z.; An, W.-K.; Wang, W., Benzoxazole-Linked Ultrastable Covalent Organic Frameworks for Photocatalysis. *J Am Chem Soc* **2018**, *140*, 4623-4631.
159. Wang, X.; Chen, L.; Chong, S. Y.; Little, M. A.; Wu, Y.; Zhu, W. H.; Clowes, R.; Yan, Y.; Zwiijnenburg, M. A.; Sprick, R. S.; Cooper, A. I., Sulfone-containing covalent organic frameworks for photocatalytic hydrogen evolution from water. *Nat Chem* **2018**.
160. Zhao, S.; Dong, B.; Ge, R.; Wang, C.; Song, X.; Ma, W.; Wang, Y.; Hao, C.; Guo, X.; Gao, Y., Channel-wall functionalization in covalent organic frameworks for the enhancement of CO₂ uptake and CO₂/N₂ selectivity. *RSC Adv* **2016**, *6*, 38774-38781.
161. Zeng, Y.; Zou, R.; Zhao, Y., Covalent Organic Frameworks for CO₂ Capture. *Adv Mater* **2016**, *28*, 2855-73.
162. Zhai, L.; Huang, N.; Xu, H.; Chen, Q.; Jiang, D., A backbone design principle for covalent organic frameworks: the impact of weakly interacting units on CO₂ adsorption. *Chem Commun (Camb)* **2017**, *53*, 4242-4245.
163. Krishnaraj, C.; Kaczmarek, A. M.; Jena, H. S.; Leus, K.; Chaoui, N.; Schmidt, J.; Van Deun, R.; Van Der Voort, P., Triggering White-Light Emission in a 2D Imine Covalent Organic Framework Through Lanthanide Augmentation. *ACS Appl. Mater. Interfaces* **2019**, Ahead of Print.

164. Zhao, W.; Xia, L. Y.; Liu, X. K., Covalent organic frameworks (COFs): perspectives of industrialization. *Crystengcomm* **2018**, *20*, 1613-1634.
165. Mulzer, C. R.; Shen, L.; Bisbey, R. P.; McKone, J. R.; Zhang, N.; Abruna, H. D.; Dichtel, W. R., Superior Charge Storage and Power Density of a Conducting Polymer-Modified Covalent Organic Framework. *ACS Cent. Sci.* **2016**, *2*, 667-673.
166. Vitaku, E.; Gannett, C. N.; Carpenter, K. L.; Shen, L.; Abruña, H. D.; Dichtel, W. R., Phenazine-Based Covalent Organic Framework Cathode Materials with High Energy and Power Densities. *J. Am. Chem. Soc.* **2019**.
167. Smith, B. J.; Parent, L. R.; Overholts, A. C.; Beaucage, P. A.; Bisbey, R. P.; Chavez, A. D.; Hwang, N.; Park, C.; Evans, A. M.; Gianneschi, N. C.; Dichtel, W. R., Colloidal Covalent Organic Frameworks. *ACS Cent. Sci.* **2017**, *3*, 58-65.
168. Li, H.; Evans, A. M.; Castano, I.; Strauss, M. J.; Dichtel, W. R.; Brédas, J.-L., Nucleation-Elongation Dynamics of Two-Dimensional Covalent Organic Frameworks. *J. Am. Chem. Soc.* **2019**.
169. Evans, A.; Parent, L. R.; Flanders, N. C.; Bisbey, R. P.; Vitaku, E.; Chen, L. X.; Gianneschi, N. C.; Dichtel, W. R., Seeded Growth of Single-Crystal Two-Dimensional Covalent Organic Frameworks. *Science* **2018**.
170. Flanders, N. C.; Kirschner, M. S.; Kim, P.; Fauvell, T. J.; Evans, A. M.; Helweh, W.; Spencer, A. P.; Schaller, R. D.; Dichtel, W. R.; Chen, L. X., Large Exciton Diffusion Coefficients in Two-Dimensional Covalent Organic Frameworks with Different Domain Sizes Revealed by Ultrafast Exciton Dynamics. *J. Am. Chem. Soc.* **2020**.

171. Castano, I.; Evans, A. M.; Li, H.; Vitaku, E.; Strauss, M. J.; Brédas, J.-L.; Gianneschi, N. C.; Dichtel, W. R., Chemical Control over Nucleation and Anisotropic Growth of Two-Dimensional Covalent Organic Frameworks. *ACS Cent. Sci.* **2019**, *5*, 1892-1899.
172. Rao, C.; Kulkarni, G.; Thomas, P. J.; Edwards, P. P., Size-dependent chemistry: properties of nanocrystals. *Chem. Eur. J.* **2002**, *8*, 28-35.
173. Li, R. L.; Flanders, N. C.; Evans, A. M.; Ji, W.; Castano, I.; Dichtel, W. R., Formation and Controlled Particle Growth of Imine-Linked Colloidal Covalent Organic Frameworks.
174. Rodriguez-San-Miguel, D.; Yazdi, A.; Guillerm, V.; Perez-Carvajal, J.; Puentes, V.; Maspoch, D.; Zamora, F., Confining Functional Nanoparticles into Colloidal Imine-Based COF Spheres by a Sequential Encapsulation-Crystallization Method. *Chem Eur J* **2017**, *23*, 8623-8627.
175. Miro, P.; Audiffred, M.; Heine, T., An atlas of two-dimensional materials. *Chem. Soc. Rev.* **2014**, *43*, 6537-6554.
176. Cai, X.; Luo, Y.; Liu, B.; Cheng, H.-M., Preparation of 2D material dispersions and their applications. *Chem. Soc. Rev.* **2018**, *47*, 6224-6266.
177. Coleman, J. N.; Lotya, M.; O'Neill, A.; Bergin, S. D.; King, P. J.; Khan, U.; Young, K.; Gaucher, A.; De, S.; Smith, R. J., Two-dimensional nanosheets produced by liquid exfoliation of layered materials. *Science* **2011**, *331*, 568-571.
178. Nicolosi, V.; Chhowalla, M.; Kanatzidis, M. G.; Strano, M. S.; Coleman, J. N., Liquid exfoliation of layered materials. *Science* **2013**, *340*.
179. Dong, R.; Zhang, T.; Feng, X., Interface-assisted synthesis of 2D materials: Trend and challenges. *Chem. Rev.* **2018**, *118*, 6189-6235.

180. Moreno, C.; Vilas-Varela, M.; Kretz, B.; Garcia-Lekue, A.; Costache, M. V.; Paradinas, M.; Panighel, M.; Ceballos, G.; Valenzuela, S. O.; Peña, D., Bottom-up synthesis of multifunctional nanoporous graphene. *Science* **2018**, *360*, 199-203.
181. Colson, J. W.; Mann, J. A.; De Blase, C. R.; Dichtel, W. R., Patterned growth of oriented 2D covalent organic framework thin films on single-layer graphene. *J. Polym. Sci., Part A: Polym. Chem.* **2015**, *53*, 378-384.
182. Spitler, E. L.; Colson, J. W.; Uribe-Romo, F. J.; Woll, A. R.; Giovino, M. R.; Saldivar, A.; Dichtel, W. R., Lattice Expansion of Highly Oriented 2D Phthalocyanine Covalent Organic Framework Films. *Angew. Chem. Int. Ed.* **2012**, *51*, 2623-2627, S2623/1-S2623/41.
183. Colson, J. W.; Woll, A. R.; Mukherjee, A.; Levendorf, M. P.; Spitler, E. L.; Shields, V. B.; Spencer, M. G.; Park, J.; Dichtel, W. R., Oriented 2D Covalent Organic Framework Thin Films on Single-Layer Graphene. *Science* **2011**, *332*, 228-231.
184. Bessinger, D.; Ascherl, L.; Auras, F.; Bein, T., Spectrally Switchable Photodetection with Near-Infrared-Absorbing Covalent Organic Frameworks. *J. Am. Chem. Soc.* **2017**, *139*, 12035-12042.
185. Medina, D. D.; Petrus, M. L.; Jumabekov, A. N.; Margraf, J. T.; Weinberger, S.; Rotter, J. M.; Clark, T.; Bein, T., Directional Charge-Carrier Transport in Oriented Benzodithiophene Covalent Organic Framework Thin Films. *ACS Nano* **2017**, *11*, 2706-2713.
186. Sun, B.; Zhu, C.-H.; Liu, Y.; Wang, C.; Wan, L.-J.; Wang, D., Oriented Covalent Organic Framework Film on Graphene for Robust Ambipolar Vertical Organic Field-Effect Transistor. *Chem. Mater.* **2017**, *29*, 4367-4374.
187. Bisbey, R. P.; DeBlase, C. R.; Smith, B. J.; Dichtel, W. R., Two-dimensional Covalent Organic Framework Thin Films Grown in Flow. *J. Am. Chem. Soc.* **2016**, *138*, 11433-11436.

188. Kandambeth, S.; Biswal, B. P.; Chaudhari, H. D.; Rout, K. C.; Kunjattu H, S.; Mitra, S.; Karak, S.; Das, A.; Mukherjee, R.; Kharul, U. K.; Banerjee, R., Selective Molecular Sieving in Self-Standing Porous Covalent-Organic-Framework Membranes. *Adv. Mater.* **2017**, *29*, n/a.
189. Alahakoon, S. B.; Thompson, C. M.; Occhialini, G.; Smaldone, R. A., Design Principles for Covalent Organic Frameworks in Energy Storage Applications. *ChemSusChem* **2017**, *10*, 2116-2129.
190. Zeng, Y.; Zou, R.; Zhao, Y., Covalent Organic Frameworks for CO₂ Capture. *Adv. Mater.* **2016**, *28*, 2855-2873.
191. Gu, C.; Liu, D.; Huang, W.; Liu, J.; Yang, R., Synthesis of covalent triazine-based frameworks with high CO₂ adsorption and selectivity. *Polym. Chem.* **2015**, *6*, 7410-7417.
192. Gao, Q.; Bai, L.; Zhang, X.; Wang, P.; Li, P.; Zeng, Y.; Zou, R.; Zhao, Y., Synthesis of Microporous Nitrogen-Rich Covalent-Organic Framework and Its Application in CO₂ Capture. *Chin. J. Chem.* **2015**, *33*, 90-94.
193. Huang, N.; Chen, X.; Krishna, R.; Jiang, D., Two-Dimensional Covalent Organic Frameworks for Carbon Dioxide Capture through Channel-Wall Functionalization. *Angew. Chem. Int. Ed.* **2015**, *54*, 2986-2990.
194. Wu, S.; Gu, S.; Zhang, A.; Yu, G.; Wang, Z.; Jian, J.; Pan, C., A rational construction of microporous imide-bridged covalent-organic polytriazines for high-enthalpy small gas absorption. *J. Mater. Chem. A* **2015**, *3*, 878-885.
195. Tong, M.; Yang, Q.; Xiao, Y.; Zhong, C., Revealing the structure-property relationship of covalent organic frameworks for CO₂ capture from postcombustion gas: a multi-scale computational study. *Phys. Chem. Chem. Phys.* **2014**, *16*, 15189-15198.

196. Li, X.-D.; Guo, J.-H.; Zhang, H.; Cheng, X.-L.; Liu, X.-Y., Design of 3D 1,3,5,7-tetraphenyladamantane-based covalent organic frameworks as hydrogen storage materials. *RSC Adv.* **2014**, *4*, 24526-24532.
197. Yuan, R.; Ren, H.; Yan, Z.; Wang, A.; Zhu, G., Robust tri(4-ethynylphenyl)amine-based porous aromatic frameworks for carbon dioxide capture. *Polym. Chem.* **2014**, *5*, 2266-2272.
198. Ding, S.-Y.; Wang, W., Covalent organic frameworks (COFs). From design to applications. *Chem. Soc. Rev.* **2013**, *42*, 548-568.
199. Dawson, R.; Cooper, A. I.; Adams, D. J., Nanoporous organic polymer networks. *Prog. Polym. Sci.* **2012**, *37*, 530-563.
200. Wu, M. M.; Wang, Q.; Sun, Q.; Jena, P.; Kawazoe, Y., First-principles study of hydrogen adsorption in metal-doped COF-10. *J. Chem. Phys.* **2010**, *133*, 154706/1-154706/6.
201. Jelski, D. A.; George, T. F., *Computational Studies of New Materials*. World Scientific: 1999.
202. Lin, C.-Y.; Zhang, D.; Zhao, Z.; Xia, Z., Covalent Organic Framework Electrocatalysts for Clean Energy Conversion. *Adv. Mater.* **2018**, *30*, n/a.
203. Gao, Q.; Li, X.; Ning, G.-H.; Xu, H.-S.; Liu, C.; Tian, B.; Tang, W.; Loh, K. P., Covalent Organic Framework with Frustrated Bonding Network for Enhanced Carbon Dioxide Storage. *Chem. Mater.* **2018**, *30*, 1762-1768.
204. Zhao, L.; Shi, S.; Liu, M.; Zhu, G.; Wang, M.; Du, W.; Gao, J.; Xu, J., Covalent triazine framework catalytic oxidative cleavage of lignin models and organosolv lignin. *Green Chem.* **2018**, Ahead of Print.
205. Sharma, A.; Malani, A.; Medhekar, N.; Babarao, R., CO₂ Adsorption and Separation in Covalent Organic Frameworks with Interlayer Slipping. *CrystEngComm* **2017**, Ahead of Print.

206. Zhu, L.; Zhang, Y.-B., Crystallization of covalent organic frameworks for gas storage applications. *Molecules* **2017**, *22*, 1149/1-1149/29.
207. Zhan, X.; Chen, Z.; Zhang, Q., Recent progress in two-dimensional COFs for energy-related applications. *J. Mater. Chem. A* **2017**, *5*, 14463-14479.
208. Mandal, A. K.; Mahmood, J.; Baek, J.-B., Two-Dimensional Covalent Organic Frameworks for Optoelectronics and Energy Storage. *ChemNanoMat* **2017**, *3*, 373-391.
209. Xue, R.; Guo, H.; Wang, T.; Gong, L.; Wang, Y.; Ai, J.; Huang, D.; Chen, H.; Yang, W., Fluorescence properties and analytical applications of covalent organic frameworks. *Anal. Methods* **2017**, *9*, 3737-3750.
210. Wu, M.-X.; Yang, Y.-W., Applications of covalent organic frameworks (COFs): From gas storage and separation to drug delivery. *Chin. Chem. Lett.* **2017**, *28*, 1135-1143.
211. Dong, J.; Wang, Y.; Liu, G.; Cheng, Y.; Zhao, D., Isoreticular covalent organic frameworks for hydrocarbon uptake and separation: the important role of monomer planarity. *CrystEngComm* **2017**, *19*, 4899-4904.
212. Lee, G.-Y.; Lee, J.; Kim, S.; Park, T.; Vo, H. T.; Lee, H., Amine-Functionalized Covalent Organic Framework for Efficient SO₂ Capture with High Reversibility. *Sci Rep* **2017**, *7*, 557.
213. Liao, Y.; Li, J.; Thomas, A., General Route to High Surface Area Covalent Organic Frameworks and Their Metal Oxide Composites as Magnetically Recoverable Adsorbents and for Energy Storage. *ACS Macro Lett.* **2017**, *6*, 1444-1450.
214. Yang, H.; Kim, I.; Ko, Y.; Kim, S.; Kim, W., Studies on adsorption and desorption of ammonia using covalent organic framework COF-10. *Kongop Hwahak* **2016**, *27*, 265-269.
215. Zhang, C.-y.; Luo, J.-x.; Li, A.-y.; Jiang, M.-l.; Yu, G.-p.; Pan, C.-y., Progress in application research of covalent organic frameworks. *Gaofenzi Tongbao* **2016**, 32-39.

216. Pramudya, Y.; Mendoza-Cortes, J. L., Design Principles for High H₂ Storage Using Chelation of Abundant Transition Metals in Covalent Organic Frameworks for 0-700 bar at 298 K. *J. Am. Chem. Soc.* **2016**, *138*, 15204-15213.
217. Huang, L.; Cao, G., Two dimensional Squaraine-Bridged Covalent Organic Polymers with Promising CO₂ Storage and Separation Properties. *Chemistryselect* **2016**, *1*, 533-538.
218. Bai, L.; Gao, Q.; Zhao, Y., Two fully conjugated covalent organic frameworks as anode materials for lithium ion batteries. *J. Mater. Chem. A* **2016**, *4*, 14106-14110.
219. Vyas, V. S.; Vishwakarma, M.; Moudrakovski, I.; Haase, F.; Savasci, G.; Ochsenfeld, C.; Spatz, J. P.; Lotsch, B. V., Exploiting Noncovalent Interactions in an Imine-Based Covalent Organic Framework for Quercetin Delivery. *Adv. Mater.* **2016**, *28*, 8749-8754.
220. Ma, L.; Wang, S.; Feng, X.; Wang, B., Recent advances of covalent organic frameworks in electronic and optical applications. *Chin. Chem. Lett.* **2016**, *27*, 1383-1394.
221. DeBlase, C. R.; Dichtel, W. R., Moving Beyond Boron: The Emergence of New Linkage Chemistries in Covalent Organic Frameworks. *Macromolecules* **2016**, *49*, 5297-5305.
222. Liao, J.; Yazaydin, A. O.; Yang, S.; Li, F.; Ding, L., Molecular simulation studies of hydrogen enriched methane (HEM) storage in Covalent Organic Frameworks. *Microporous Mesoporous Mater.* **2016**, *231*, 138-146.
223. Zhen, J.; Ding, S.; Wang, W.; Liu, J.; Sun, J.; Huang, Z.; Zheng, Q., Undulated 2D Covalent Organic Frameworks Based on Bowl-Shaped Cyclotricatechylene. *Chin. J. Chem.* **2016**, *34*, 783-787.
224. Ge, R.; Hao, D.; Shi, Q.; Dong, B.; Leng, W.; Wang, C.; Gao, Y., Target Synthesis of an Azo (N=N) Based Covalent Organic Framework with High CO₂-over-N₂ Selectivity and Benign Gas Storage Capability. *J. Chem. Eng. Data* **2016**, *61*, 1904-1909.

225. Huang, Y.-B.; Pachfule, P.; Sun, J.-K.; Xu, Q., From covalent-organic frameworks to hierarchically porous B-doped carbons: a molten-salt approach. *J. Mater. Chem. A* **2016**, *4*, 4273-4279.
226. Niu, X.; Ding, S.; Wang, W.; Xu, Y.; Xu, Y.; Chen, H.; Chen, X., Separation of small organic molecules using covalent organic frameworks-LZU1 as stationary phase by open-tubular capillary electrochromatography. *J. Chromatogr. A* **2016**, *1436*, 109-117.
227. Trunk, M.; Herrmann, A.; Bildirir, H.; Yassin, A.; Schmidt, J.; Thomas, A., Copper-Free Sonogashira Coupling for High-Surface-Area Conjugated Microporous Poly(aryleneethynylene) Networks. *Chemistry* **2016**, *22*, 7179-83.
228. Li, Z.; Zhi, Y.; Feng, X.; Ding, X.; Zou, Y.; Liu, X.; Mu, Y., An Azine-Linked Covalent Organic Framework: Synthesis, Characterization and Efficient Gas Storage. *Chem. - Eur. J.* **2015**, *21*, 12079-12084.
229. Zhang, C.; Luo, J.; Zhang, D.; Wu, H.; Zhao, S., Progress in covalent organic frameworks. *Huagong Xinxing Cailiao* **2014**, *42*, 19-21.
230. Bai, C.; Li, J.; Liu, S.; Yang, X.; Yang, X.; Tian, Y.; Cao, K.; Huang, Y.; Ma, L.; Li, S., In situ preparation of nitrogen-rich and functional ultramicroporous carbonaceous COFs by "segregated" microwave irradiation. *Microporous Mesoporous Mater.* **2014**, *197*, 148-155.
231. Zhang, J.; Hou, S.-e.; Jin, H., Progress on porphyrin-based porous frameworks. *Huagong Xinxing Cailiao* **2013**, *41*, 24-26, 42.
232. Neti, V. S. P. K.; Wu, X.; Deng, S.; Echegoyen, L., Synthesis of a phthalocyanine and porphyrin 2D covalent organic framework. *CrystEngComm* **2013**, *15*, 6892-6895.
233. Zhang, J.; Hou, S.-e.; Jin, H., Progress on porous covalent organic frameworks based on polyimide. *Huagong Xinxing Cailiao* **2013**, *41*, 17-19.

234. Colson, J. W.; Dichtel, W. R., Rationally synthesized two-dimensional polymers. *Nat. Chem.* **2013**, *5*, 453-465.
235. Kunowsky, M.; Suarez-Garcia, F.; Linares-Solano, A., Adsorbent density impact on gas storage capacities. *Microporous Mesoporous Mater.* **2013**, *173*, 47-52.
236. Kahveci, Z.; Islamoglu, T.; Shar, G. A.; Ding, R.; El-Kaderi, H. M., Targeted synthesis of a mesoporous triptycene-derived covalent organic framework. *CrystEngComm* **2013**, *15*, 1524-1527.
237. Wang, F.; Zhao, J.; Gong, J.; Wen, L.; Zhou, L.; Li, D., New Multifunctional Porous Materials Based on Inorganic-Organic Hybrid Single-Walled Carbon Nanotubes: Gas Storage and High-Sensitive Detection of Pesticides. *Chem. - Eur. J.* **2012**, *18*, 11804-11810, S11804/1-S11804/8.
238. Guo, J.-H.; Zhang, H.; Liu, Z.-P.; Cheng, X.-L., Multiscale Study of Hydrogen Adsorption, Diffusion, and Desorption on Li-Doped Phthalocyanine Covalent Organic Frameworks. *J. Phys. Chem. C* **2012**, *116*, 15908-15917.
239. Ono, K., Porous organic cage crystals. *Yuki Gosei Kagaku Kyokaishi* **2012**, *70*, 653-654.
240. Liu, J.; Ge, C.; Zhang, X.; Zhang, M., Progress on the covalent organic frameworks based on organic boronic acid. *Huaxue Tongbao* **2012**, *75*, 432-440.
241. Yu, J.-T.; Chen, Z.; Sun, J.; Huang, Z.-T.; Zheng, Q.-Y., Cyclotricatechylene based porous crystalline material: Synthesis and applications in gas storage. *J. Mater. Chem.* **2012**, *22*, 5369-5373.
242. Kalidindi, S. B.; Oh, H.; Hirscher, M.; Esken, D.; Wiktor, C.; Turner, S.; Van, T. G.; Fischer, R. A., Metal@COFs: covalent organic frameworks as templates for Pd nanoparticles and hydrogen storage properties of Pd@COF-102 hybrid material. *Chemistry* **2012**, *18*, 10848-56.

243. Xu, S.; Liang, L.; Li, B.; Luo, Y.; Liu, C.; Tan, B., Research progress on microporous organic polymers. *Huaxue Jinzhan* **2011**, *23*, 2085-2094.
244. Choi, J. H.; Choi, K. M.; Jeon, H. J.; Choi, Y. J.; Lee, Y.; Kang, J. K., Acetylene Gas Mediated Conjugated Microporous Polymers (ACMPs): First Use of Acetylene Gas as a Building Unit. *Macromolecules* **2010**, *43*, 5508-5511.
245. Germain, J.; Frechet, J. M. J.; Svec, F., Nanoporous polymers for hydrogen storage. *Small* **2009**, *5*, 1098-1111.
246. Lino, M. A.; Lino, A. A.; Mazzoni, M. S. C., Porous nanotubes and fullerenes based on covalent organic frameworks. *Chem. Phys. Lett.* **2007**, *449*, 171-174.
247. Wang, Y.; Liu, H.; Pan, Q.; Wu, C.; Hao, W.; Xu, J.; Chen, R.; Liu, J.; Li, Z.; Zhao, Y., Construction of Fully Conjugated Covalent Organic Frameworks via Facile Linkage Conversion for Efficient Photoenzymatic Catalysis. *J. Am. Chem. Soc.* **2020**, *142*, 5958-5963.
248. Wang, S.; Yang, L.; He, G.; Shi, B.; Li, Y.; Wu, H.; Zhang, R.; Nunes, S.; Jiang, Z., Two-dimensional nanochannel membranes for molecular and ionic separations. *Chem. Soc. Rev.* **2020**, *49*, 1071-1089.
249. Zhang, C.; Wu, B.-H.; Ma, M.-Q.; Wang, Z.; Xu, Z.-K., Ultrathin metal/covalent-organic framework membranes towards ultimate separation. *Chem. Soc. Rev.* **2019**, *48*, 3811-3841.
250. Fenton, J. L.; Burke, D. W.; Qian, D.; Cruz, M. O. d. l.; Dichtel, W. R., Polycrystalline Covalent Organic Framework Films Act as Adsorbents, Not Membranes. *J. Am. Chem. Soc.* **2021**, *143*, 1466-1473.
251. Wang, J.; Zhuang, S., Covalent organic frameworks (COFs) for environmental applications. *Coord. Chem. Rev.* **2019**, *400*, 213046.

252. Huang, N.; Zhai, L.; Xu, H.; Jiang, D., Stable Covalent Organic Frameworks for Exceptional Mercury Removal from Aqueous Solutions. *J. Am. Chem. Soc.* **2017**, *139*, 2428-2434.
253. Sun, Q.; Aguila, B.; Perman, J.; Earl, L. D.; Abney, C. W.; Cheng, Y.; Wei, H.; Nguyen, N.; Wojtas, L.; Ma, S., Postsynthetically Modified Covalent Organic Frameworks for Efficient and Effective Mercury Removal. *J. Am. Chem. Soc.* **2017**, *139*, 2786-2793.
254. Meri-Bofi, L.; Royuela, S.; Zamora, F.; Ruiz-Gonzalez, M. L.; Segura, J. L.; Munoz-Olivas, R.; Mancheno, M. J., Thiol grafted imine-based covalent organic frameworks for water remediation through selective removal of Hg(II). *J. Mater. Chem. A* **2017**, *5*, 17973-17981.
255. Zhu, Y.; Qiao, M.; Peng, W.; Li, Y.; Zhang, G.; Zhang, F.; Li, Y.; Fan, X., Rapid exfoliation of layered covalent triazine-based frameworks into N-doped quantum dots for the selective detection of Hg²⁺ ions. *J. Mater. Chem. A* **2017**, *5*, 9272-9278.
256. Sahiner, N.; Demirci, S.; Sel, K., Covalent organic framework based on melamine and dibromoalkanes for versatile use. *J. Porous Mater.* **2016**, *23*, 1025-1035.
257. Ge, J.; Xiao, J.; Liu, L.; Qiu, L.; Jiang, X., Facile microwave-assisted production of Fe₃O₄ decorated porous melamine-based covalent organic framework for highly selective removal of Hg²⁺. *J. Porous Mater.* **2016**, *23*, 791-800.
258. Zuo, H.; Li, Y.; Liao, Y., Europium ionic liquid grafted covalent organic framework with dual luminescence emissions as sensitive and selective acetone sensor. *ACS Appl. Mater. Interfaces* **2019**, *11*, 39201-39208.
259. Sun, Q.; Aguila, B.; Earl, L. D.; Abney, C. W.; Wojtas, L.; Thallapally, P. K.; Ma, S., Covalent organic frameworks as a decorating platform for utilization and affinity enhancement of chelating sites for radionuclide sequestration. *Adv. Mater.* **2018**, *30*, 1705479.

260. Aguila, B.; Sun, Q.; Cassady, H.; Abney, C. W.; Li, B.; Ma, S., Design strategies to enhance amidoxime chelators for uranium recovery. *ACS Appl. Mater. Interfaces* **2019**, *11*, 30919-30926.
261. Zhou, Z.; Zhong, W.; Cui, K.; Zhuang, Z.; Li, L.; Li, L.; Bi, J.; Yu, Y., A covalent organic framework bearing thioether pendant arms for selective detection and recovery of Au from ultra-low concentration aqueous solution. *Chem. Commun.* **2018**, *54*, 9977-9980.
262. Chen, L.; He, Y.; Lei, Z.; Gao, C.; Xie, Q.; Tong, P.; Lin, Z., Preparation of core-shell structured magnetic covalent organic framework nanocomposites for magnetic solid-phase extraction of bisphenols from human serum sample. *Talanta* **2018**, *181*, 296-304.
263. Ren, J.-Y.; Wang, X.-L.; Li, X.-L.; Wang, M.-L.; Zhao, R.-S.; Lin, J.-M., Magnetic covalent triazine-based frameworks as magnetic solid-phase extraction adsorbents for sensitive determination of perfluorinated compounds in environmental water samples. *Anal. Bioanal. Chem.* **2018**, *410*, 1657-1665.
264. Zhao, W.; Qiao, J.; Ning, T.-L.; Liu, X.-K., Scalable ambient pressure synthesis of covalent organic frameworks and their colorimetric nanocomposites through dynamic imine exchange reactions. *Chin. J. Polym. Sci.* **2018**, *36*, 1-7.
265. Wang, R.; Chen, Z., A covalent organic framework-based magnetic sorbent for solid phase extraction of polycyclic aromatic hydrocarbons, and its hyphenation to HPLC for quantitation. *Microchim. Acta* **2017**, *184*, 3867-3874.
266. Lan, Y.; Tong, M.; Yang, Q.; Zhong, C., Computational screening of covalent organic frameworks for the capture of radioactive iodine and methyl iodide. *CrystEngComm* **2017**, *19*, 4920-4926.

267. Yu, S.-B.; Lyu, H.; Tian, J.; Wang, H.; Zhang, D.-W.; Liu, Y.; Li, Z.-T., A polycationic covalent organic framework: a robust adsorbent for anionic dye pollutants. *Polym. Chem.* **2016**, *7*, 3392-3397.
268. Stegbauer, L.; Hahn, M. W.; Jentys, A.; Savasci, G.; Ochsenfeld, C.; Lercher, J. A.; Lotsch, B. V., Tunable Water and CO₂ Sorption Properties in Isostructural Azine-Based Covalent Organic Frameworks through Polarity Engineering. *Chem. Mater.* **2015**, *27*, 7874-7881.
269. Lee, J. K.; Shin, J.; Ahn, N. H.; Turrina, A.; Park, M. B.; Byun, Y.; Cho, S. J.; Wright, P. A.; Hong, S. B., A Family of Molecular Sieves Containing Framework-Bound Organic Structure-Directing Agents. *Angew. Chem. Int. Ed.* **2015**, *54*, 11097-11101.
270. Huang, N.; Krishna, R.; Jiang, D., Tailor-Made Pore Surface Engineering in Covalent Organic Frameworks: Systematic Functionalization for Performance Screening. *J. Am. Chem. Soc.* **2015**, *137*, 7079-7082.
271. Li, J.; Yang, X.; Bai, C.; Tian, Y.; Li, B.; Zhang, S.; Yang, X.; Ding, S.; Xia, C.; Tan, X.; Ma, L.; Li, S., A novel benzimidazole-functionalized 2-D COF material: Synthesis and application as a selective solid-phase extractant for separation of uranium. *J. Colloid Interface Sci.* **2015**, *437*, 211-218.
272. Wang, T.; Kailasam, K.; Xiao, P.; Chen, G.; Chen, L.; Wang, L.; Li, J.; Zhu, J., Adsorption removal of organic dyes on covalent triazine framework (CTF). *Microporous Mesoporous Mater.* **2014**, *187*, 63-70.
273. Liu, J.; Zong, E.; Fu, H.; Zheng, S.; Xu, Z.; Zhu, D., Adsorption of aromatic compounds on porous covalent triazine-based framework. *J. Colloid Interface Sci.* **2012**, *372*, 99-107.
274. Pei, C.-Y.; Qu, F.-Y., Preparation and characterization of hydroxyl functional compound with covalent organic framework. *Chem. J. Chin.* **2011**, *32*, 1234-1238.

275. Wang, W.; Deng, S.; Ren, L.; Li, D.; Wang, W.; Vakili, M.; Wang, B.; Huang, J.; Wang, Y.; Yu, G., Stable covalent organic frameworks as efficient adsorbents for high and selective removal of an aryl-organophosphorus flame retardant from water. *ACS Appl. Mater. Interfaces* **2018**, *10*, 30265-30272.
276. Gao, C.; Lin, G.; Lei, Z.; Zheng, Q.; Lin, J.; Lin, Z., Facile synthesis of core-shell structured magnetic covalent organic framework composite nanospheres for selective enrichment of peptides with simultaneous exclusion of proteins. *J. Mater. Chem. B* **2017**, *5*, 7496-7503.
277. Zhang, X.; Qing, G.; Yu, L.; Kang, H.; Chen, C.; Li, X.; Liang, X., Novel nanoporous covalent organic frameworks for the selective extraction of endogenous peptides. *RSC Adv.* **2018**, *8*, 37528-37533.
278. Ward, T. J.; Ward, K. D., Chiral separations: fundamental review 2010. *Anal. Chem.* **2010**, *82*, 4712-4722.
279. Qian, H.-L.; Yang, C.-X.; Wang, W.-L.; Yang, C.; Yan, X.-P., Advances in covalent organic frameworks in separation science. *J. Chromatogr. A* **2018**, *1542*, 1-18.
280. Qian, H.-L.; Yang, C.-X.; Yan, X.-P., Bottom-up synthesis of chiral covalent organic frameworks and their bound capillaries for chiral separation. *Nat. Commun.* **2016**, *7*, 12104.
281. Bai, L.; Phua, S. Z. F.; Lim, W. Q.; Jana, A.; Luo, Z.; Tham, H. P.; Zhao, L.; Gao, Q.; Zhao, Y., Nanoscale covalent organic frameworks as smart carriers for drug delivery. *Chem. Commun.* **2016**, *52*, 4128-4131.
282. Hoffmann, R., How should chemists think? *Scientific American* **1993**, *268*, 66-73.
283. Côté, A. P.; Benin, A. I.; Ockwig, N. W.; Keeffe, M.; Matzger, A. J.; Yaghi, O. M., Porous, Crystalline, Covalent Organic Frameworks. *Science* **2005**, *310*, 1166.

284. Huang, N.; Wang, P.; Jiang, D., Covalent organic frameworks: a materials platform for structural and functional designs. *Nature Reviews Materials* **2016**, *1*, 16068.
285. Bisbey, R. P.; Dichtel, W. R., Covalent Organic Frameworks as a Platform for Multidimensional Polymerization. *ACS Central Science* **2017**, *3*, 533-543.
286. Huang, N.; Krishna, R.; Jiang, D., Tailor-Made Pore Surface Engineering in Covalent Organic Frameworks: Systematic Functionalization for Performance Screening. *J. Am. Chem. Soc.* **2015**, *137*, 7079-7082.
287. Sun, Q.; Aguila, B.; Perman, J.; Earl, L. D.; Abney, C. W.; Cheng, Y.; Wei, H.; Nguyen, N.; Wojtas, L.; Ma, S., Postsynthetically Modified Covalent Organic Frameworks for Efficient and Effective Mercury Removal. *J. Am. Chem. Soc.* **2017**, *139*, 2786-2793.
288. Sun, Q.; Aguila, B.; Earl Lyndsey, D.; Abney Carter, W.; Wojtas, L.; Thallapally Praveen, K.; Ma, S., Covalent Organic Frameworks as a Decorating Platform for Utilization and Affinity Enhancement of Chelating Sites for Radionuclide Sequestration. *Adv. Mater.* **2018**, *0*, 1705479.
289. Furukawa, H.; Yaghi, O. M., Storage of Hydrogen, Methane, and Carbon Dioxide in Highly Porous Covalent Organic Frameworks for Clean Energy Applications. *J. Am. Chem. Soc.* **2009**, *131*, 8875-8883.
290. Han, S. S.; Furukawa, H.; Yaghi, O. M.; Goddard, W. A., Covalent Organic Frameworks as Exceptional Hydrogen Storage Materials. *J. Am. Chem. Soc.* **2008**, *130*, 11580-11581.
291. Doonan, C. J.; Tranchemontagne, D. J.; Glover, T. G.; Hunt, J. R.; Yaghi, O. M., Exceptional ammonia uptake by a covalent organic framework. *Nature Chem.* **2010**, *2*, 235-238.

292. Huang, N.; Chen, X.; Krishna, R.; Jiang, D., Two-Dimensional Covalent Organic Frameworks for Carbon Dioxide Capture through Channel-Wall Functionalization. *Angew. Chem. Int. Ed.* **2015**, *54*, 2986-2990.
293. Ding, S.-Y.; Dong, M.; Wang, Y.-W.; Chen, Y.-T.; Wang, H.-Z.; Su, C.-Y.; Wang, W., Thioether-Based Fluorescent Covalent Organic Framework for Selective Detection and Facile Removal of Mercury(II). *J. Am. Chem. Soc.* **2016**, *138*, 3031-3037.
294. Huang, N.; Zhai, L.; Xu, H.; Jiang, D., Stable Covalent Organic Frameworks for Exceptional Mercury Removal from Aqueous Solutions. *J. Am. Chem. Soc.* **2017**, *139*, 2428-2434.
295. Sun, M.; Arevalo, E.; Strynar, M.; Lindstrom, A.; Richardson, M.; Kearns, B.; Pickett, A.; Smith, C.; Knappe, D. R. U., Legacy and Emerging Perfluoroalkyl Substances Are Important Drinking Water Contaminants in the Cape Fear River Watershed of North Carolina. *Environ. Sci. Technol. Lett.* **2016**, *3*, 415-419.
296. Cousins, I. T.; Vestergren, R.; Wang, Z.; Scheringer, M.; McLachlan, M. S., The precautionary principle and chemicals management: The example of perfluoroalkyl acids in groundwater. *Environment International* **2016**, *94*, 331-340.
297. Gebbink, W. A.; van Asseldonk, L.; van Leeuwen, S. P. J., Presence of Emerging Per- and Polyfluoroalkyl Substances (PFASs) in River and Drinking Water near a Fluorochemical Production Plant in the Netherlands. *Environmental Science & Technology* **2017**, *51*, 11057-11065.
298. Barzen-Hanson, K. A.; Roberts, S. C.; Choyke, S.; Oetjen, K.; McAlees, A.; Riddell, N.; McCrindle, R.; Ferguson, P. L.; Higgins, C. P.; Field, J. A., Discovery of 40 Classes of Per- and Polyfluoroalkyl Substances in Historical Aqueous Film-Forming Foams (AFFFs) and AFFF-Impacted Groundwater. *Environmental Science & Technology* **2017**, *51*, 2047-2057.

299. Hu, X. C.; Andrews, D. Q.; Lindstrom, A. B.; Bruton, T. A.; Schaidler, L. A.; Grandjean, P.; Lohmann, R.; Carignan, C. C.; Blum, A.; Balan, S. A.; Higgins, C. P.; Sunderland, E. M., Detection of Poly- and Perfluoroalkyl Substances (PFASs) in U.S. Drinking Water Linked to Industrial Sites, Military Fire Training Areas, and Wastewater Treatment Plants. *Environ. Sci. Technol. Lett.* **2016**, *3*, 344-350.
300. Kataria, A.; Trachtman, H.; Malaga-Diequez, L.; Trasande, L., Association between perfluoroalkyl acids and kidney function in a cross-sectional study of adolescents. *Environmental Health* **2015**, *14*, 89.
301. Melzer, D.; Rice, N.; Depledge, M. H.; Henley, W. E.; Galloway, T. S., Association between Serum Perfluorooctanoic Acid (PFOA) and Thyroid Disease in the U.S. National Health and Nutrition Examination Survey. *Environ. Health Perspect.* **2010**, *118*, 686-692.
302. Gomis, M. I.; Vestergren, R.; Borg, D.; Cousins, I. T., Comparing the toxic potency in vivo of long-chain perfluoroalkyl acids and fluorinated alternatives. *Environment International* **2018**, *113*, 1-9.
303. Sheng, N.; Cui, R.; Wang, J.; Guo, Y.; Wang, J.; Dai, J., Cytotoxicity of novel fluorinated alternatives to long-chain perfluoroalkyl substances to human liver cell line and their binding capacity to human liver fatty acid binding protein. *Arch. Toxicol.* **2018**, *92*, 359-369.
304. Wang, Z.; Cousins, I. T.; Scheringer, M.; Hungerbühler, K., Fluorinated alternatives to long-chain perfluoroalkyl carboxylic acids (PFCAs), perfluoroalkane sulfonic acids (PFSAAs) and their potential precursors. *Environment International* **2013**, *60*, 242-248.
305. Wang, Z.; Cousins, I. T.; Scheringer, M.; Hungerbuehler, K., Hazard assessment of fluorinated alternatives to long-chain perfluoroalkyl acids (PFAAs) and their precursors: Status quo, ongoing challenges and possible solutions. *Environment International* **2015**, *75*, 172-179.

306. Barzen-Hanson, K. A.; Field, J. A., Discovery and Implications of C2 and C3 Perfluoroalkyl Sulfonates in Aqueous Film-Forming Foams and Groundwater. *Environ. Sci. Technol. Lett.* **2015**, *2*, 95-99.
307. Strynar, M.; Dagnino, S.; McMahan, R.; Liang, S.; Lindstrom, A.; Andersen, E.; McMillan, L.; Thurman, M.; Ferrer, I.; Ball, C., Identification of Novel Perfluoroalkyl Ether Carboxylic Acids (PFECAs) and Sulfonic Acids (PFESAs) in Natural Waters Using Accurate Mass Time-of-Flight Mass Spectrometry (TOFMS). *Environmental Science & Technology* **2015**, *49*, 11622-11630.
308. Eschauzier, C.; Beerendonk, E.; Scholte-Veenendaal, P.; De Voogt, P., Impact of Treatment Processes on the Removal of Perfluoroalkyl Acids from the Drinking Water Production Chain. *Environmental Science & Technology* **2012**, *46*, 1708-1715.
309. Xiao, L.; Ling, Y.; Alsaiee, A.; Li, C.; Helbling, D. E.; Dichtel, W. R., β -Cyclodextrin Polymer Network Sequesters Perfluorooctanoic Acid at Environmentally Relevant Concentrations. *J. Am. Chem. Soc.* **2017**, *139*, 7689-7692.
310. Lee, M.-T.; Ferguson, G. S., Stepwise Synthesis of a Well-Defined Silicon (Oxide)/Polyimide Interface. *Langmuir* **2001**, *17*, 762-767.
311. Guerin, D.; Lenfant, S.; Godey, S.; Vuillaume, D., Synthesis and electrical properties of fullerene-based molecular junctions on silicon substrate. *J. Mater. Chem.* **2010**, *20*, 2680-2690.
312. Xu, H.; Gao, J.; Jiang, D., Stable, crystalline, porous, covalent organic frameworks as a platform for chiral organocatalysts. *Nature Chem.* **2015**, *7*, 905-912.
313. Abellan-Flos, M.; Tanc, M.; Supuran, C. T.; Vincent, S. P., Exploring carbonic anhydrase inhibition with multimeric coumarins displayed on a fullerene scaffold. *Organic & Biomolecular Chemistry* **2015**, *13*, 7445-7451.

314. Okada, Y.; Sugai, M.; Chiba, K., Hydrogen-Bonding-Induced Fluorescence: Water-Soluble and Polarity-Independent Solvatochromic Fluorophores. *J. Org. Chem.* **2016**, *81*, 10922-10929.
315. Kolb, H. C.; Finn, M. G.; Sharpless, K. B., Click Chemistry: Diverse Chemical Function from a Few Good Reactions. *Angew. Chem. Int. Ed.* **2001**, *40*, 2004-2021.
316. Senevirathna, S. T. M. L. D.; Tanaka, S.; Fujii, S.; Kunacheva, C.; Harada, H.; Shivakoti, B. R.; Dinh, H.; Ariyadasa, T., Adsorption of four perfluorinated acids on non ion exchange polymer sorbents. *Water Sci. Technol.* **2011**, *63*, 2106-2113.
317. Zhang, D.; Luo, Q.; Gao, B.; Chiang, S.-Y. D.; Woodward, D.; Huang, Q., Sorption of perfluorooctanoic acid, perfluorooctane sulfonate and perfluoroheptanoic acid on granular activated carbon. *Chemosphere* **2016**, *144*, 2336-2342.
318. Ho, Y. S.; McKay, G., Pseudo-second order model for sorption processes. *Process Biochem.* **1999**, *34*, 451-465.
319. Matsumoto, M.; Dasari, R. R.; Ji, W.; Feriante, C. H.; Parker, T. C.; Marder, S. R.; Dichtel, W. R., Rapid, Low Temperature Formation of Imine-Linked Covalent Organic Frameworks Catalyzed by Metal Triflates. *J. Am. Chem. Soc.* **2017**, *139*, 4999-5002.
320. Leffler, J. E.; Temple, R. D., Staudinger reaction between triarylphosphines and azides. Mechanism. *J. Am. Chem. Soc.* **1967**, *89*, 5235-5246.
321. Lin, F. L.; Hoyt, H. M.; van Halbeek, H.; Bergman, R. G.; Bertozzi, C. R., Mechanistic Investigation of the Staudinger Ligation. *J. Am. Chem. Soc.* **2005**, *127*, 2686-2695.
322. Geng, K.; He, T.; Liu, R.; Dalapati, S.; Tan, K. T.; Li, Z.; Tao, S.; Gong, Y.; Jiang, Q.; Jiang, D., Covalent Organic Frameworks: Design, Synthesis, and Functions. *Chem. Rev.* **2020**.

323. Alahakoon, S. B.; Diwakara, S. D.; Thompson, C. M.; Smaldone, R. A., Supramolecular design in 2D covalent organic frameworks. *Chem. Soc. Rev.* **2020**, *49*, 1344-1356.
324. Huang, N.; Wang, P.; Jiang, D., Covalent organic frameworks: a materials platform for structural and functional designs. *Nat. Rev. Mater.* **2016**, *1*, 16068.
325. Li, Y.; Chen, W.; Xing, G.; Jiang, D.; Chen, L., New synthetic strategies toward covalent organic frameworks. *Chem. Soc. Rev.* **2020**, *49*, 2852-2868.
326. Guan, X.; Chen, F.; Fang, Q.; Qiu, S., Design and applications of three dimensional covalent organic frameworks. *Chem. Soc. Rev.* **2020**, *49*, 1357-1384.
327. Doonan, C. J.; Tranchemontagne, D. J.; Glover, T. G.; Hunt, J. R.; Yaghi, O. M., Exceptional ammonia uptake by a covalent organic framework. *Nat. Chem.* **2010**, *2*, 235-238.
328. Ma, H.; Ren, H.; Meng, S.; Yan, Z.; Zhao, H.; Sun, F.; Zhu, G., A 3D microporous covalent organic framework with exceedingly high C₃H₈/CH₄ and C₂ hydrocarbon/CH₄ selectivity. *Chem. Commun.* **2013**, *49*, 9773-9775.
329. Xu, H.; Gao, J.; Jiang, D., Stable, crystalline, porous, covalent organic frameworks as a platform for chiral organocatalysts. *Nat. Chem.* **2015**, *7*, 905-912.
330. Wei, P.-F.; Qi, M.-Z.; Wang, Z.-P.; Ding, S.-Y.; Yu, W.; Liu, Q.; Wang, L.-K.; Wang, H.-Z.; An, W.-K.; Wang, W., Benzoxazole-Linked Ultrastable Covalent Organic Frameworks for Photocatalysis. *J. Am. Chem. Soc.* **2018**, *140*, 4623-4631.
331. Chen, R.; Shi, J.-L.; Ma, Y.; Lin, G.; Lang, X.; Wang, C., Designed Synthesis of a 2D Porphyrin-Based sp² Carbon-Conjugated Covalent Organic Framework for Heterogeneous Photocatalysis. *Angew. Chem., Int. Ed.* **2019**, *58*, 6430-6434.

332. Wang, Y.; Liu, H.; Pan, Q.; Wu, C.; Hao, W.; Xu, J.; Chen, R.; Liu, J.; Li, Z.; Zhao, Y., Construction of Fully Conjugated Covalent Organic Frameworks via Facile Linkage Conversion for Efficient Photoenzymatic Catalysis. *J. Am. Chem. Soc.* **2020**, *142*, 5958-5963.
333. Li, Z.; Huang, N.; Lee, K. H.; Feng, Y.; Tao, S.; Jiang, Q.; Nagao, Y.; Irle, S.; Jiang, D., Light-Emitting Covalent Organic Frameworks: Fluorescence Improving via Pinpoint Surgery and Selective Switch-On Sensing of Anions. *J. Am. Chem. Soc.* **2018**, *140*, 12374-12377.
334. Wu, X.; Han, X.; Xu, Q.; Liu, Y.; Yuan, C.; Yang, S.; Liu, Y.; Jiang, J.; Cui, Y., Chiral BINOL-Based Covalent Organic Frameworks for Enantioselective Sensing. *J. Am. Chem. Soc.* **2019**, *141*, 7081-7089.
335. Yuan, C.; Wu, X.; Gao, R.; Han, X.; Liu, Y.; Long, Y.; Cui, Y., Nanochannels of Covalent Organic Frameworks for Chiral Selective Transmembrane Transport of Amino Acids. *J. Am. Chem. Soc.* **2019**, *141*, 20187-20197.
336. Jhulki, S.; Evans, A. M.; Hao, X.-L.; Cooper, M. W.; Feriante, C. H.; Leisen, J.; Li, H.; Lam, D.; Hersam, M. C.; Barlow, S.; Brédas, J.-L.; Dichtel, W. R.; Marder, S. R., Humidity Sensing through Reversible Isomerization of a Covalent Organic Framework. *J. Am. Chem. Soc.* **2020**, *142*, 783-791.
337. Burke, D. W.; Sun, C.; Castano, I.; Flanders, N. C.; Evans, A. M.; Vitaku, E.; McLeod, D. C.; Lambeth, R. H.; Chen, L. X.; Gianneschi, N. C.; Dichtel, W. R., Acid Exfoliation of Imine-linked Covalent Organic Frameworks Enables Solution Processing into Crystalline Thin Films. *Angew. Chem., Int. Ed.* **2020**, *59*, 5165-5171.
338. Corcos, A. R.; Levato, G. A.; Jiang, Z.; Evans, A. M.; Livingston, A. G.; Mariñas, B. J.; Dichtel, W. R., Reducing the Pore Size of Covalent Organic Frameworks in Thin-Film Composite Membranes Enhances Solute Rejection. *ACS Mater. Lett.* **2019**, *1*, 440-446.

339. Fan, H.; Mundstock, A.; Feldhoff, A.; Knebel, A.; Gu, J.; Meng, H.; Caro, J., Covalent Organic Framework–Covalent Organic Framework Bilayer Membranes for Highly Selective Gas Separation. *J. Am. Chem. Soc.* **2018**, *140*, 10094-10098.
340. Sasmal, H. S.; Aiyappa, H. B.; Bhange, S. N.; Karak, S.; Halder, A.; Kurungot, S.; Banerjee, R., Superprotonic Conductivity in Flexible Porous Covalent Organic Framework Membranes. *Angew. Chem., Int. Ed.* **2018**, *57*, 10894-10898.
341. Wang, M.; Ballabio, M.; Wang, M.; Lin, H.-H.; Biswal, B. P.; Han, X.; Paasch, S.; Brunner, E.; Liu, P.; Chen, M.; Bonn, M.; Heine, T.; Zhou, S.; Cánovas, E.; Dong, R.; Feng, X., Unveiling Electronic Properties in Metal–Phthalocyanine-Based Pyrazine-Linked Conjugated Two-Dimensional Covalent Organic Frameworks. *J. Am. Chem. Soc.* **2019**, *141*, 16810-16816.
342. Bi, S.; Yang, C.; Zhang, W.; Xu, J.; Liu, L.; Wu, D.; Wang, X.; Han, Y.; Liang, Q.; Zhang, F., Two-dimensional semiconducting covalent organic frameworks via condensation at arylmethyl carbon atoms. *Nat. Commun.* **2019**, *10*, 2467.
343. Jhulki, S.; Kim, J.; Hwang, I.-C.; Haider, G.; Park, J.; Park, J. Y.; Lee, Y.; Hwang, W.; Dar, A. A.; Dhara, B.; Lee, S. H.; Kim, J.; Koo, J. Y.; Jo, M. H.; Hwang, C.-C.; Jung, Y. H.; Park, Y.; Kataria, M.; Chen, Y.-F.; Jhi, S.-H.; Baik, M.-H.; Baek, K.; Kim, K., Solution-Processable, Crystalline π -Conjugated Two-Dimensional Polymers with High Charge Carrier Mobility. *Chem* **2020**, *6*, 2035-2045.
344. Day, R. W.; Bediako, D. K.; Rezaee, M.; Parent, L. R.; Skorupskii, G.; Arguilla, M. Q.; Hendon, C. H.; Stassen, I.; Gianneschi, N. C.; Kim, P.; Dincă, M., Single Crystals of Electrically Conductive Two-Dimensional Metal–Organic Frameworks: Structural and Electrical Transport Properties. *ACS Cent. Sci.* **2019**, *5*, 1959-1964.

345. Evans, A. M.; Parent, L. R.; Flanders, N. C.; Bisbey, R. P.; Vitaku, E.; Kirschner, M. S.; Schaller, R. D.; Chen, L. X.; Gianneschi, N. C.; Dichtel, W. R., Seeded growth of single-crystal two-dimensional covalent organic frameworks. *Science* **2018**, *361*, 52.
346. Ma, T.; Kapustin, E. A.; Yin, S. X.; Liang, L.; Zhou, Z.; Niu, J.; Li, L.-H.; Wang, Y.; Su, J.; Li, J.; Wang, X.; Wang, W. D.; Wang, W.; Sun, J.; Yaghi, O. M., Single-crystal x-ray diffraction structures of covalent organic frameworks. *Science* **2018**, *361*, 48.
347. Beaudoin, D.; Maris, T.; Wuest, J. D., Constructing monocrystalline covalent organic networks by polymerization. *Nat. Chem.* **2013**, *5*, 830-834.
348. Smith, B. J.; Overholts, A. C.; Hwang, N.; Dichtel, W. R., Insight into the crystallization of amorphous imine-linked polymer networks to 2D covalent organic frameworks. *Chem. Commun.* **2016**, *52*, 3690-3693.
349. Feriante, C.; Evans, A. M.; Jhulki, S.; Castano, I.; Strauss, M. J.; Barlow, S.; Dichtel, W. R.; Marder, S. R., New Mechanistic Insights into the Formation of Imine-Linked Two-Dimensional Covalent Organic Frameworks. *J. Am. Chem. Soc.* **2020**, *142*, 18637-18644.
350. Feriante, C. H.; Jhulki, S.; Evans, A. M.; Dasari, R. R.; Slicker, K.; Dichtel, W. R.; Marder, S. R., Rapid Synthesis of High Surface Area Imine-Linked 2D Covalent Organic Frameworks by Avoiding Pore Collapse During Isolation. *Adv. Mater.* **2020**, *32*, 1905776.
351. Smith, B. J.; Parent, L. R.; Overholts, A. C.; Beaucage, P. A.; Bisbey, R. P.; Chavez, A. D.; Hwang, N.; Park, C.; Evans, A. M.; Gianneschi, N. C.; Dichtel, W. R., Colloidal Covalent Organic Frameworks. *ACS Cent. Sci.* **2017**, *3*, 58-65.
352. Castano, I.; Evans, A. M.; Li, H.; Vitaku, E.; Strauss, M. J.; Brédas, J.-L.; Gianneschi, N. C.; Dichtel, W. R., Chemical Control over Nucleation and Anisotropic Growth of Two-Dimensional Covalent Organic Frameworks. *ACS Cent. Sci.* **2019**, *5*, 1892-1899.

353. Wang, S.; Zhang, Z.; Zhang, H.; Rajan, A. G.; Xu, N.; Yang, Y.; Zeng, Y.; Liu, P.; Zhang, X.; Mao, Q.; He, Y.; Zhao, J.; Li, B.-G.; Strano, M. S.; Wang, W.-J., Reversible Polycondensation-Termination Growth of Covalent-Organic-Framework Spheres, Fibers, and Films. *Matter* **2019**, *1*, 1592-1605.
354. Wang, S.; Chavez, A. D.; Thomas, S.; Li, H.; Flanders, N. C.; Sun, C.; Strauss, M. J.; Chen, L. X.; Markvoort, A. J.; Bredas, J.-L.; Dichtel, W. R., Pathway Complexity in the Stacking of Imine-Linked Macrocycles Related to Two-Dimensional Covalent Organic Frameworks. *Chem. Mater.* **2019**, *31*, 7104-7111.
355. Evans, A. M.; Castano, I.; Brumberg, A.; Parent, L. R.; Corcos, A. R.; Li, R. L.; Flanders, N. C.; Gosztola, D. J.; Gianneschi, N. C.; Schaller, R. D.; Dichtel, W. R., Emissive Single-Crystalline Boroxine-Linked Colloidal Covalent Organic Frameworks. *J. Am. Chem. Soc.* **2019**, *141*, 19728-19735.

6. Vita

Woojung Ji was born in Daejeon, South Korea on November 15th, 1991, to Dr. June Keun Ji and Dr. Chaisun Oh. She grew up in this suburban town filled with doctors in philosophy and medicine with her younger sister Heeseo. Her first experience in science was at Verde Valley School where she was taught by her high school biology teacher, Andy Gill. While she enjoyed many disciplines in science, she was especially intrigued by chemistry, in which she decided to major at Trinity College. At Trinity, she gained experience in physical chemistry with Prof. Maria Krisch, analytical chemistry with Prof. Michelle Kovarik, inorganic chemistry with Prof. Maria Parr, and organic chemistry with Prof. Timothy P. Curran and Prof. Cheyenne Brindle, all of whom touched upon her scientific interest and inspired her to pursue a career in Chemistry. From the Winter of 2013 of to Spring of 2015, she conducted chemical research on cyclic tungsten bis-alkyne complexes with Prof. Curran. She then graduated Trinity College with a B.S in Chemistry and was accepted to the doctoral program in Chemistry at Northwestern University to start in the Fall of 2015. She subsequently joined and completed her doctoral work on two-dimensional imine-linked covalent organic frameworks under the guidance of Prof. William R. Dichtel in the department of Chemistry. Beyond Chemistry, Woojung enjoys spending time with her family and friends, writing journals, playing Hearthstone and Cookierun, listening to Rich Roll podcast series, and practicing yoga and meditation.

7. List of Publications

- (1) Ji, W.; Hamachi, L. S.; Flanders, N. C.; Li, R. L.; Natraj, A.; Chen, L. X.; Dichtel, W. R., Thermal Depolymerization and Recrystallization of Two-Dimensional Imine-Linked Covalent Organic Frameworks. *In Preparation*.
- (2) Evans, A. M.; Strauss, M. R.; Corcos, A. R.; Hirani, Z.; Ji, W.; Hamachi, L. S.; Aguilar-Enriquez, X.; Chavez, A. D.; Smith, B. J.; Dichtel, W. R., Two-Dimensional Polymers and Polymerization. *In Review*.
- (3) Yu, C.-J.; von Kugelgen, S.; Krzyaniak, M. D.; Ji, W.; Dichtel, W. R.; Wasielewski, M. R.; Freedman, D. E., Spin and Phonon Design in Modular Arrays of Molecular Qubits. *Chem. Mater.* **2020**, *32*, 10200-10206.
- (4) Evans, A. M.; Ryder, M. R.; Ji, W.; Strauss, M. J.; Corcos, A. R.; Vitaku, E.; Flanders, N. C.; Bisbey, R. P.; Dichtel, W. R., Trends in the Thermal Stability of Two-Dimensional Covalent Organic Frameworks. *Faraday Discuss.* **2021**, *225*, 226-240.
- (5) Li, R. L.; Flanders, N. C.; Evans, A. M.; Ji, W.; Castano, I.; Gianneschi, N. C.; Dichtel, W. R., Formation and Controlled Growth of Imine-Linked Covalent Organic Framework Nanoparticles. *Chem. Sci.* **2019**, *10*, 3796-3801.
- (6) Ji, W.; Xiao, L.; Ling, Y.; Matsumoto, M.; Bisbey, R. P.; Helbling, D. E.; Dichtel, W. R., Removal of GenX and Perfluorinated Alkyl Substances from Water by Amine-Functionalized Covalent Organic Frameworks. *J. Am. Chem. Soc.* **2018**, *140*, 12677-12681.
- (7) Matsumoto, M.; Dasari, R. R.; Ji, W.; Feriante, C. H.; Parker, T. C.; Marder, S. R.; Dichtel, W. R., Rapid, Low Temperature Formation of Imine-Linked Covalent Organic Frameworks Catalyzed by Metal Triflates. *J. Am. Chem. Soc.* **2017**, *139*, 4999-5002.

- (8) Curran, T. P.; Lawrence, A. P.; Murtaugh, T. S.; Ji, W.; Pokharel, N.; Gober, C. B.; Sutor, J., Conformationally Rigid Cyclic Tungsten Bis-alkyne Complexes Derived From 1,1'-dialkynylferrocenes. *J. Organomet. Chem.* **2017**, *846*, 24-32.